

New Methods in X-ray Imaging

Torsten Lauridsen

February 1, 2018

This thesis has been submitted to:

The PhD School,
The Faculty of Science,
University of Copenhagen,
Denmark

For the PhD degree

by

Torsten Lauridsen,
Niels Bohr Institute,
University of Copenhagen,
Universitetsparken 5,
2100 Copenhagen,
Denmark

Supervisors:

Robert Feidenhans'l and Kell Mortensen

Abstract

A couple of decades ago, x-ray tomography was a technique largely reserved for a few specialists from the hospitals' diagnostic departments and university based research groups. But during the last 20 years x-ray imaging has become much more available outside these narrow circles as a method to help the advancement of many different academic and industrial fields.

In this thesis I describe my work on developing the techniques within the field and studying their possible applications as well as my collaboration with external researchers, applying x-ray imaging methods to answer scientific questions within their particular fields.

For the sake of completeness I start my thesis from the electric field equation. From there I derive the transport of intensity equation, the Fresnel propagator function and the basic formula of propagated intensity used in holotomography. I also sketch the principles behind the magnification effect and interactions between x-rays and matter.

From these fundamental formulas and principles, I move on to describe the practical aspects of x-ray imaging in more detail. I describe the basis of the different contrast mechanisms in absorption, holotomography and grating interferometry. I have also included a description of the basic principles behind tomogram reconstruction.

Next, I describe my work relating to image construction from grating interferometer data, both the adaptive-period sine fitting method and the anisotropic tomogram reconstruction algorithm I have developed.

Thereafter I move on to describe my work investigating the applicability of the grating interferometer dark-field signal for detecting sub-resolution sized cracks in a solid material and for detecting misaligned fibers in a fiber composite material.

In the next chapter I introduce the ideas and main conclusions from my collaboration with researchers from other academic fields. Finally, I sum up my work and give my view on the future possibilities and challenges within the field.

Dansk resumé

For blot et par årtier siden var røntgentomografi hovedsageligt en metode for få indviede specialister fra hospitalernes diagnostiske afdelinger og specialiserede forskningsgrupper ved universiteterne. Men gennem de sidste 20 år er røntgenbilleddannelse blevet meget mere tilgængeligt uden for disse snævre cirkler, som en metode der skaber fremskridt på diverse akademiske og industrielle områder.

I denne afhandling beskriver jeg mit arbejde med at udvikle teknikker inden for feltet og undersøge deres mulige anvendelser, samt mit samarbejde med eksterne forskere, hvor vi anvender røntgenbilleddannelsesmetoder til at besvare videnskabelige spørgsmål inden for deres respektive felter.

For fuldkommenhedens skyld starter jeg min afhandling fra den elektriske feltligning. Derfra udleder jeg intensitetsstransportligningen, Fresnels propagationsfunktion og den grundlæggende funktion for propageret intensitet, som bruge i holotomografi. Jeg skitserer også principperne bag forstørrelseseffekten og vekselvirkning mellem røntgenstråling og stof.

Ud fra disse fundamentale formler og principper, bevæger jeg mig videre til at beskrive de praktiske aspekter af røntgenbilleddannelse mere grundigt. Jeg beskriver grundlaget for de forskellige kontrastmekanismer i absorption, holotomografi og gitterinterferometri. Jeg har også medtaget en beskrivelse af de grundlæggende principper bag tomogramrekonstruktion. Dernæst beskriver jeg mit arbejde med billeddannelse fra gitterinterferometerdata, både den adaptive sinus-fit metode og den anisotropiske tomogramrekonstruktionsmetode jeg har udviklet.

Derefter bevæger jeg mig videre til at beskrive mit arbejde med at undersøge egnetheden af gitterinterferometerets mørkefeltsignal til at detektere revner mindre end den rumlige opløsning i et fast stof, samt til at detektere fejlorienterede fibre i et fiberkompositmateriale.

I det næste kapitel introducerer jeg ideerne og de vigtigste konklusioner fra mit samarbejde med forskere fra andre akademiske områder. Til sidst opsummerer jeg mit arbejde og giver mit blik på fremtidens muligheder og udfordringer inden for feltet.

Acknowledgements

I would like to thank my supervisors Robert Feidenhans'l and Kell Mortensen for letting me enjoy a level of academic freedom that is seldomly seen these days. Robert, who was my supervisor for most of the time, has been very open to all my ideas and suggestions, and has let me explore them extensively. It is worth noting that this freedom has payed off; two of the papers presented in this thesis are a direct consequence of this freedom, and the two image formation algorithms I invented and tested would not have been realised, if it wasn't for this great degree of freedom. I would also like to thank the IT support at the Niels Bohr Institute for helping me out with the server and network requirements for all my projects. Especially Jannis Bouchikas deserves credit for accommodating all my extraordinary wishes for server space, LAN access, user rights, etc. On the IT-side of things, I also owe a big thanks to the eScience center at the Niels Bohr Institute for hosting all my data and making computation ressources available to me and the rest of the group. Without their help, simply handling all of the enormous data amounts would have been a PhD thesis on its own. I would also like to thank Højteknologifonden and Region Hovedstaden for funding my research. Finally, there's a large number of people whom I've been collaborating and sharing ideas with. At the risk of having forgotten someone, the main collaborators have been: Kristian Rix, Mikkel Schou Nielsen, Carsten Gundlach, Brian Vinter, Martin Rehr, Jonas Bardino, Alexander Rack, Ole Pedersen, Else Marie Pinholt, Camilla Neldam, Erik Mejdal Lauridsen and Jessica Pingel.

Contents

Contents	11
1 Introduction	13
1.1 Project description	13
1.2 Current state of the field	14
1.2.1 Lab-source microtomography	14
1.2.2 Grating interferometry	14
1.2.3 Absorption tomography using directly converting detectors	15
1.2.4 Raster scanning tomography methods	15
1.2.5 Holotomography	15
1.3 Outline of the thesis	16
1.3.1 Background knowledge chapters	16
1.3.2 Specific work chapters	16
2 X-ray theory	19
2.1 Photonic wave functions	19
2.2 Fourier optics	20
2.3 Rayleigh-Sommerfeld diffraction integral	22
2.4 Paraxial regime	22
2.4.1 Paraxial wave equation	24
2.5 Matter	24
2.6 Magnification effect	26
2.7 Intensity Fourier transform	28
3 Imaging theory	31
3.1 2D absorption imaging	31
3.1.1 absorption assumption	31
3.1.2 Absorption projections	31
3.1.3 Absorption contrast optimization	32
3.1.4 Refraction correction	32
3.2 2D non-interferometric phase imaging	34
3.2.1 The case against phase	35
3.3 2D grating interferometer imaging	37
3.3.1 Grating interferometer modalities	41
3.4 Tomographic reconstruction	42
3.4.1 Inverse Radon transform	42
3.4.2 Differential phase contrast reconstruction	45
3.4.3 Cone beam reconstruction	46
4 Image formation algorithms	49
4.1 Reducing the effects of instabilities in x-ray grating interferometers	49
4.1.1 Algorithm	49
4.1.2 Method test	52
4.1.3 Conclusion and outlook	55
4.2 Regularized iterative reconstruction of an angularly dependent x-ray dark-field tomogram	56

4.2.1	Introduction	56
4.2.2	Experimental setup	56
4.2.3	Sample	58
4.2.4	Method	59
4.2.5	Tomogram model	60
4.2.6	Algorithm	60
4.2.7	Regularizations	61
4.2.8	Experimental results	62
4.2.9	Conclusion and Outlook	63
5	Dark-field modality application tests	67
5.1	Introduction to publication A.1	67
5.2	Introduction to publication A.2	68
6	Applied high resolution synchrotron imaging	71
6.1	Introduction to publication A.3	71
6.1.1	scientific motivation	72
6.1.2	Experimental setup	72
6.1.3	Reconstruction	72
6.1.4	Data analysis and results	73
6.2	Introduction to publication A.4	73
6.2.1	scientific motivation	74
6.2.2	Experimental setup	74
6.2.3	Results	75
6.3	Introduction to publication A.5	75
6.4	Introduction to publication A.6	76
6.5	Introduction to publication A.7	76
6.5.1	Experiment and results	77
7	Conclusion	79
8	Outlook	81
8.1	Lab tomography	81
8.2	Synchrotron tomography	82
8.3	Data analysis challenges	82
	Bibliography	85
A	Main publications	89
A.1	90
A.2	99
A.3	105
A.4	116
A.5	138
A.6	145
A.7	156
B	Other publications	171
B.1	X-ray tomography using the full complex index of refraction	171
B.2	X-ray dark-field imaging for detection of foreign bodies in food	181

Chapter 1

Introduction

The finalization of my thesis has been delayed significantly due to a number of factors, among others the above mentioned pursuit of new ideas. Though this delay is of course not appreciated by the university, I have been very grateful for all the scientific and personal adventures I have experienced on my prolonged journey through the academic world. I cannot imagine anything more exiting and challenging than what I have experienced in the last seven years. In this thesis I have tried to give an overview of the diverse subjects I have covered during this time. Though “New Methods in X-ray Imaging” may seem a narrow subject to the outsider, the challenges and possibilities within this field are truly diverse, and I have worked in many different areas within this spectrum. I have worked with different experimental methods, optimized 2D image extraction, developed a new method for 3D reconstruction and performed image analysis on reconstructed 3D tomograms for external 'clients'.

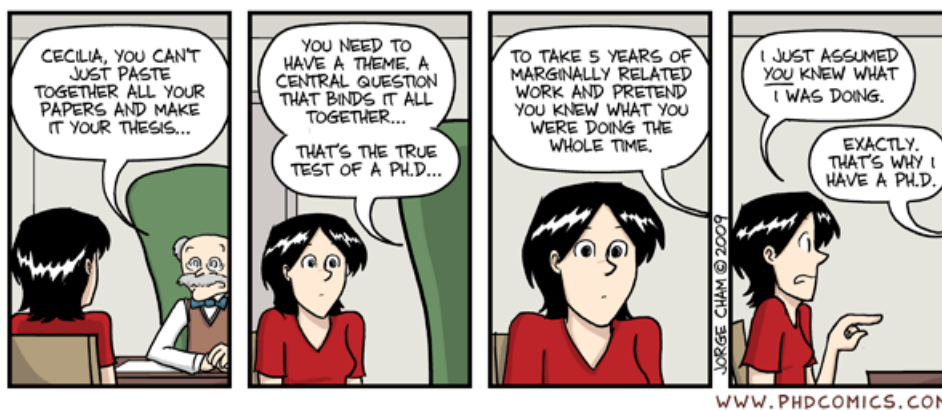


Figure 1.1: *The thesis you are reading is an attempt to bind together the very different areas and applications of x-ray imaging that I have been working with for the last seven years. I have done so by putting each of them into one of three categories; Image formation algorithms, Dark-field modality application tests and Applied high resolution synchrotron imaging.*

1.1 Project description

The project description for my PhD is:

New Methods in X-ray Imaging

The project will focus on work in the field of X-ray Imaging using phase contrast and dark field methods. The aim of the project will be to develop and improve the x-ray imaging methods in these fields. These new methods are well suited to perform imaging of soft tissue. The focus will be on developing a labora-

tory based system at the Niels Bohr Institute for applications within meat and other food products, but synchrotron radiation experiments at large scale international facilities must also be foreseen.

The only part of this project description that is not thoroughly covered in this thesis is the part about food products. I have worked on imaging of food products in many different projects during the last seven years, but in the projects that actually gave scientifically interesting results, I have only contributed on a discussion level and by participation in beamtimes. The actual data analysis in the successful food projects has been carried out by my colleague Mikkel Schou Nielsen, and hence I have put the articles representing this work in the final appendix of my thesis for the sake of completeness.

1.2 Current state of the field

Originally microtomography was predominantly a synchrotron based method, using absorption as the contrast modality. Today, the field has expanded greatly, both into other contrast modalities and away from the synchrotrons and into the laboratories. Even in the presence of all these new possibilities, the original synchrotron based absorption tomography method is still alive and thriving - and in my opinion, no less impressive in its capabilities than all the other methods; synchrotron absorption tomography today is fast, typical acquisition times are around ten minutes, but they can be done much faster if needed - at the cost of noise, of course. In these ten minutes you typically get a 3D image with ten billion voxels (voxel is just the fancy word for 3D pixel) with a voxel size as small as a few hundred nanometers. That means that within a cube one mm on either side, you measure the absorption coefficient at ten billion points within a few minutes. Isn't that impressive?

1.2.1 Lab-source microtomography

Within the later years, x-ray microtomography equipment for laboratory use has become widely commercially available. This has helped tremendously in spreading the use and general awareness of the possibilities within x-ray imaging to a much broader audience. Several companies today offer fully functional closed-hutch scanners with intuitive software interfaces. Along with a reasonable price (less than one million euro) this has brought x-ray microtomography scanners to wide use in academic and commercial circles, that most likely would otherwise not have punched through the barrier to the synchrotrons. With a single exception, these commercial lab-microtomography scanners are all based on absorption as the contrast mechanism, since this type of scanner is the simplest to build, and the method puts the least requirements on stability and alignment of the equipment. The typical commercial CT-scanner has a micro-focus source with a W-anode, a spot size of a few μm , a power of 5 - 500 W and an acceleration voltage up to around 200 kV. The detector is of the scintillator-based type, and as such, offers no tunable energy-sensitivity. Instead the software might implement some sort of beam-hardening correction. Reconstruction is performed using a standard FDK-backprojection algorithm. One manufacturer offers a fully equipped closed-hutch grating interferometer allowing the user to retrieve phase-contrast and dark-field tomograms. This scanner is specifically designed to image small animals such as mice. But apart from this exception, we need to go to specialized labs and synchrotrons at universities and research institutions in order to find applications of other imaging modalities than full-spectrum anode source absorption contrast.

1.2.2 Grating interferometry

X-ray grating interferometers were originally developed at synchrotrons, but have quickly moved to laboratories where the introduction of a source grating has allowed researchers to produce phase-contrast and dark-field tomograms using low-brilliance sources that would otherwise not have the coherence necessary for grating interferometry. The advantage of the grating interferometer is the addition of two new contrast modalities. One is phase contrast, which potentially offer increased sensitivity to low-Z materials, and the other is the very interesting sub-resolution structure-sensitive dark-field modality. The disadvantage of the grating interferometer is the increased stability requirement and the increased measurement times. Lately, a lot of work has been done to simplify the original 3-grating setup and the stepwise scan procedure initially used with it. Some of this work seeks to remove one of the gratings and

to replace the stepping procedure with a single exposure by having sufficient resolution on the detector screen to directly map the intensity pattern created by a single absorption grating [35, 26, 5, 18]. The grating does not necessarily have to be a regular absorption grating, you can even use sandpaper [19]. Often, these setups still require quite small source sizes, and hence still need either a micro focus source or a source grating to produce the necessary coherence. Either way, the resulting beam intensity is reduced compared to setups allowing for a larger spot size. The direct mapping of the interference pattern can require quite high spatial resolution on the detector in order to get sufficient sensitivity. Since there's a limit to the total number of pixels in available detectors, the small pixel size requirement limits the total field of view. To counter the small field of view allowed by this method, another single-shot approach can be taken, which retains all of the original 3 gratings and then seeks to produce a Moiré pattern on the detector screen through small deliberate misalignments of the gratings [31]. By analysing shifts in the Moiré pattern, dark-field and differential phase images can be achieved.

1.2.3 Absorption tomography using directly converting detectors

Another possibility for improving the standard lab-CT setup is simply exchanging the scintillator-based detector in commercial scanners for a directly converting and possibly energy-dispersive one. The reduced noise and the increased energy-sensitivity offers an increased (or tunable, if you like) material-density sensitivity. Increased sensitivity, especially to low-Z materials, has been the main motivation for many efforts to increase the applicability of phase-contrast methods. Thus, the two methods are in some ways competing about the future market for commercial soft matter imaging equipment. With the reduced prices and improved availability of directly converting detectors that we have seen over the last years, the balance of the two seems to be shifting towards the grating-free absorption contrast setup using directly converting detectors. When detectors become energy-dispersive, as is technically possible with directly converting systems, the polychromaticity of lab sources can suddenly become an advantage, rather than being a disadvantage, as is the case for their scintillator-based counterparts.

1.2.4 Raster scanning tomography methods

Methods where projections of the full sample volume are achieved in one go are called full-field methods. Achieving very high spatial resolution with full-field imaging has some practical challenges. Typically, the lower limit of the spatial resolution is determined by the pixel size of the detector, and since it can be hard to construct detector systems with very small pixel sizes, this is a challenge when trying to achieve very high spatial resolution in full-field imaging. Another practical challenge is that as the pixel size goes down, so must the sample-detector distance in order to avoid phase effects disturbing the projected intensities in absorption imaging. If some sort of phase contrast sensitive imaging, such as holotomography, is applied instead of absorption, there's an increase in the requirements for precision of the propagation distance and an increase in measurement times, because several exposures are now necessary at every rotation angle. To avoid these challenges of full-field imaging, we can instead seek to achieve very high spatial resolution by using some sort of raster scanning method. In these methods, the sample is projected one bit at a time with a narrowly focused beam. Characteristic for these methods is that the phase is generally the imaged modality. The most used raster scanning tomography technique is ptychography [8], where the raster scanned areas are so closely spaced that they overlap. The overlapping scan areas then counters the underdetermined nature of retrieving the phase, the so-called *phase problem*. In some cases ptychography currently allows imaging down to a spatial resolution of 16 nanometers [12]. A downside to this technique is the long acquisition times; a full tomogram typically takes several hours to acquire.

1.2.5 Holotomography

Holotomography offers the simplest conceivable full-field imaging phase-contrast setup, at least in principle. Phase-sensitivity is simply achieved by moving the detector and acquiring the intensity-distributions at different distances behind the sample. Interference-effects will then shift the intensity-distribution as the beam propagates downstream from the sample. The shifting intensity-distributions will indirectly reveal the underlying phase-distribution that gives rise to the intensity shifts. In principle, all a holotomography setup requires is a source, a sample rotation stage and a movable detector. But what this

seemingly simple method lacks in hardware components it makes up for in requirements on coherence, stability and motor precision. Especially the strict coherence-requirements exclude lab sources from being implemented in any useful realisations of this method. The method has been tested at synchrotrons, and has attracted significant attention from people within the field of x-ray imaging. But so far it has not been used to any significant extent by people outside the field (i.e. what you could call the *users* or even *customers* from other scientific fields and industry), except from cases of very high resolution imaging. The reason for the lacking breakthrough of this method is two-fold. The first reason is simply the fact that holotomography-measurements are both cumbersome and time-consuming due to the requirement for multi-distance measurements at very accurate positions. When synchrotron users are allocated a certain amount of beamtime, it is essential for them to make best use of the time given, and hence holotomography stands at a disadvantage compared to absorption tomography. The second reason is that because holotomography can only be realised at synchrotron setups, and synchrotrons also typically offer monochromatic light with a tunable energy within quite a broad spectrum, users have the alternative possibility to tune the x-ray energy to fit the absorption of even very low-Z materials. Increased low-Z sensitivity has otherwise been one of the main motivating factors in the development of phase-contrast tomography.

1.3 Outline of the thesis

If we disregard the introduction, conclusion and outlook chapters my thesis can basically be divided in two main parts. The first part consists of chapters 2 and 3. It gives a theoretical and practical background for understanding my work. The second part consists of the three chapters 4, 5 and 6. It describes the work I have done more specifically. Chapters 5 and 6 are quite brief, but they rely heavily on referencing the various articles I have contributed to. These articles are included in Appendix A.

1.3.1 Background knowledge chapters

In chapter 2 I give a general outline of the relevant theoretical background and I derive the most necessary formulas for describing the propagation of electromagnetic fields. I have chosen to start out from the electric field equation, and deduce the necessary equations from there. Some might argue that this is an unnecessarily long way back to start out, and that I could have skipped at least some of chapter 2. I have chosen this approach for two reasons: First of all I think it is a good thing to be aware of the theoretical background and the implicit assumptions behind the formulas we use. And even for those of us who have done the derivations before, and have worked in the field for some time, we tend to forget the finer details, and I think refreshing them every once in a while can be beneficial. It is my experience that going through the basics sometimes opens up new perspectives on the broader field. The second reason is a purely subjective one: I find it quite satisfactory to start out from one of the fundamental equations of nature to stress that this is not all just speculations built on shaky grounds. This also makes it easier to explain some of the derivations and assumptions in chapter 3, where I use the results from chapter 2 to give a more specific overview of the relevant imaging techniques and contrast formation mechanisms. In this chapter I derive the principles and formulas necessary for understanding the imaging work described in the specific work chapters.

1.3.2 Specific work chapters

Chapter 4 contains my image formation algorithm-related work. One of the two algorithms I have developed is a new algorithm to analyze interferometer grating scans with a four-parameter sine fitting algorithm, rather than the traditional Fourier transform, thus avoiding the discrete-period limitation implicitly imposed on the grating scan analysis by the Fourier transform method. This allowed us to take the setup instabilities into account already in the first step of the initial data analysis, and thus improve 2D and 3D image quality. The other algorithm in chapter 4 is a new image reconstruction algorithm seeking to take the orientational dependence of the dark-field signal into account. This leaves the reconstruction heavily underdetermined. The underdeterminedness is counteracted by imposing heavy regularizations. In chapter 5 I focus on the exploration of possible useful applications of the interesting new contrast modality represented by the dark-field signal. The first article in this chapter explores the possibility of utilizing the sensibility of the dark-field signal to sub-resolution structures to

determine cracks so small that they would have been undetectable by absorption and phase contrast methods, unless the pixel size was very small. A small pixel size on the other hand would mean a reduced field of view, and the dark field signal in this way may become the best method for detecting the desired properties without sacrificing field of view. The second article in chapter 5 explores the possible advantages of aligning the tomographic rotation axis with the probed scattering direction. Such a geometry allows us to mask out fibrous microstructures aligned with the rotation axis, which could be useful in settings where only deviations from a certain main fiber orientation are of interest. The final of the three chapters presenting my work is chapter 6. All work presented in this chapter was performed with a scientific aim outside of physics and in collaboration with people from other institutes. The articles referenced here are aimed at an audience outside the x-ray imaging community, and x-ray imaging only serves as a tool to explore some set of samples that are of interest to my external collaborators. All these articles are based on synchrotron measurements, and my work here has mainly been focused on the image analysis of the reconstructed tomograms.

Chapter 2

X-ray theory

This chapter is focused on the fundamental theoretical background of x-ray imaging. Though all the equations in this chapter play a role, and many build on each other, I find the most important equation in this chapter to be equation (2.18). This equation is the Fourier space version of the Fresnel diffraction integral, whose last exponential term is called the paraxial wavefront propagator. This propagator function describes how electromagnetic waves propagate through space in the paraxial regime (with current detector technology the paraxial requirement is typically met for practically realizable full-field x-ray imaging methods). In some form, most theoretical aspects of direct x-ray imaging revolve around this function and the many interesting inverse problems it gives rise to.

2.1 Photonic wave functions

The behaviour of electromagnetic fields is described by the four Maxwell equations. These can be combined to form two differential equations, one regarding the magnetic field and one regarding the electric field. In vacuum the electric field equation is:

$$\nabla^2 \mathbf{E} = \frac{1}{c^2} \frac{\partial \mathbf{E}}{\partial t^2} \quad (2.1)$$

Where ∇^2 is the Laplacian operator. The magnetic field-equivalent of equation (2.1) substitutes \mathbf{E} with \mathbf{B} . Equation (2.1) is a vector equation, but can be separated into three equations, each depending only on one spatial dimension and time. If we disregard polarization we can assume each of these single-coordinate equations to be proportional to the others, and hence replace the vector field by a scalar field:

$$\nabla^2 E = \frac{1}{c^2} \frac{\partial E}{\partial t^2} \quad (2.2)$$

For our applications polarization is not an important property, and thus the wave behaviour in our experiments is well described by scalar fields rather than vector fields as in the original field equation. Working with scalar fields is a great computational simplification, so from this point on we will simply treat the electric field as a scalar field. The scalar field equation (2.2) can be solved by:

$$E(\mathbf{r}, t) = \frac{E_s}{r} e^{i(kr - \omega t)} \quad (2.3)$$

$\left(\frac{\omega}{k} = c \right)$

Where $r = |\mathbf{r}|$ and k is the wave number (and not a wave *vector*, since the propagation direction of the spherical wave in this equation depends on position, i.e. talking about a wave *vector* in the context of this wave only makes sense in a local neighbourhood where it can be approximated by a plane wave). ω is the angular frequency (in time domain). Equation (2.3) describes the free space propagation of an electromagnetic field from a point source. We can see that any ω can be chosen, but to maintain the

correct wavespeed, c , the wave length (and thus k) follows once ω is set. Equation (2.3) is not the only solution to the wave equation, but we choose it over other solutions (e.g. a plane wave or an inward propagating spherical wave) because it is physically meaningful; it describes the outward propagating wave emitted from a point source. Note that it isn't defined at the source point $\mathbf{r}=0$. Before we move on to consider more interesting solutions to the scalar field equation (2.2) we perform a separation of variables. We do this by assuming that the solution to equation (2.2) is separable:

$$E(\mathbf{r}, t) = E(\mathbf{r})T(t) \quad (2.4)$$

The separability assumption is physically reasonable, since this is often, to good approximation, the case for the electric field equations relevant for us; for instance all monochromatic fields, such as the point source field in equation (2.3) are separable. If we substitute this expression into equation (2.2) things can be rearranged so that:

$$\frac{\nabla^2 E(\mathbf{r})}{E(\mathbf{r})} = \frac{1}{c^2 T} \frac{\partial T}{\partial t^2} \quad (2.5)$$

Each side of this equation is only dependent on either space or time. As a result, all general solutions must have either side equal to a constant value. For obvious reasons we will call this constant value $-k^2$. Setting the left side equal to our constant value we get:

$$\nabla^2 E(\mathbf{r}) = -k^2 E(\mathbf{r}) \quad (2.6)$$

This equation is the Helmholtz wave equation, and the task of solving this equation (or similar versions of it) for some set of boundary conditions will be the general theme for the remainder of this chapter.

2.2 Fourier optics

In this section I introduce the concept of Fourier optics. Simply put, Fourier optics is just a shift of basis; instead of viewing electric field waves as real space functions, we may view them as Fourier space functions. The motivation for this basis shift is that computation of solutions to the Helmholtz wave equation (2.6) are greatly simplified when viewing the problem in Fourier space instead of in real space. Our first step is to recognize that all Fourier basis functions are in fact eigenvectors of the Laplacian operator ∇^2 :

$$\begin{aligned} \nabla^2 e^{i2\pi\mathbf{f}\cdot\mathbf{r}} &= \left(\frac{\partial^2}{\partial x^2} + \frac{\partial^2}{\partial y^2} + \frac{\partial^2}{\partial z^2} \right) e^{i2\pi(f_x, f_y, f_z)\cdot(x, y, z)} \\ &= \left(-(2\pi f_x)^2 - (2\pi f_y)^2 - (2\pi f_z)^2 \right) e^{i2\pi(f_x, f_y, f_z)\cdot(x, y, z)} \\ &= -(2\pi f)^2 e^{i2\pi\mathbf{f}\cdot\mathbf{r}} \end{aligned} \quad (2.7)$$

Note the use of the convention that the use of a non-bold font to annotate a vector indicates euclidean norm; $f = |\mathbf{f}|$. From equation (2.7) it is obvious that Fourier basis functions of appropriate frequency ($f = k/(2\pi)$) have the correct eigenvalue and hence solve the Helmholtz equation. Having found an appropriate basis to express the solution to the Helmholtz wave equation, we turn to the other restriction on our solutions, namely the boundary conditions. We will assume that the electric field is well-defined in some plane (in the typical imaging or diffraction setup, this plane will be defined as the plane going through the sample while being orthogonal to the centre of the source-sample beam), but unknown downstream from this plane (in the space between the sample and the detector), see Figure 2.1.

We will call the known electric field at the aperture E_a . E_a is a 2D function, and can be 2D Fourier transformed. From this point on, the propagation direction, z , of the field will play a special role, and I will treat it separately from the perpendicular plane coordinates, which will be grouped together in the vector $\mathbf{r}_\perp = (x, y)$. Correspondingly, the Fourier space vector $\mathbf{f}_\perp = (f_x, f_y)$ will also be a 2D vector in the corresponding plane in Fourier space. Note that both \mathbf{r} and \mathbf{f} still represent 3D functions.

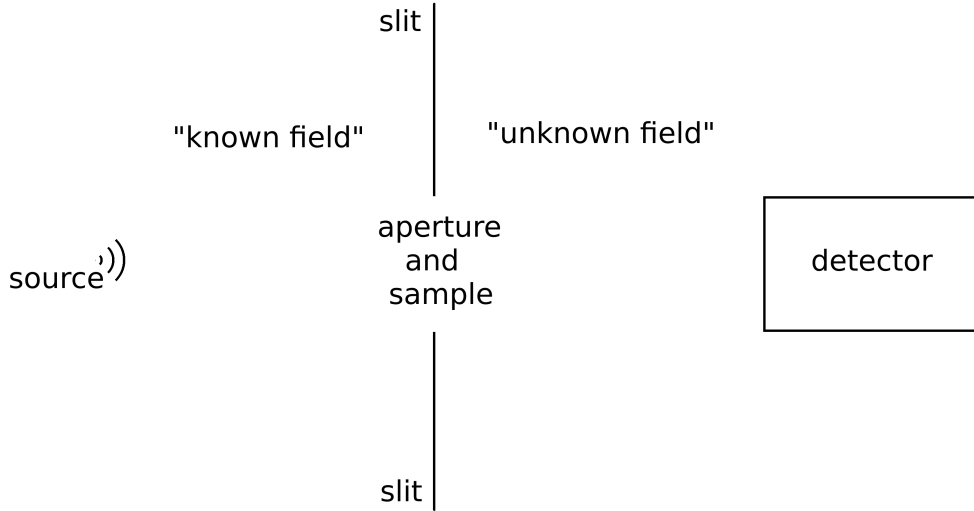


Figure 2.1: Sketch of typical imaging setup.

Anyway, the dimensionality of the relevant variables should hopefully also be clear from the context. I define the Origo of the z -dimension to be at the aperture plane, which means that the Fourier transform of the electric field in the aperture plane looks like this:

$$\tilde{E}_a(\mathbf{f}_\perp) = \iint E(\mathbf{r}_\perp, z = 0) e^{i2\pi\mathbf{f}_\perp \cdot \mathbf{r}_\perp} d\mathbf{r}_\perp \quad (2.8)$$

In principle the integral goes to infinity, but since we assume the slits to only allow radiation to pass through the narrow aperture, we only need to integrate over the aperture area. Looking at the Fourier components of E_a individually, we can easily solve the diffraction problem (i.e. satisfy the aperture boundary condition and behave according to the Helmholtz equation in the free space between aperture and detector). We know that 3D exponential basis functions of appropriate frequency solve the Helmholtz equation, so for a given set of f_x and f_y we only need to find the correct f_z :

$$f_z = \sqrt{\left(\frac{k}{2\pi}\right)^2 - f_\perp^2} \quad (2.9)$$

The z -dimension frequency above could equally well be the negative number with the same absolute value. But a negative f_z would imply a negative propagation direction, and we choose to disregard this solution. Having found an appropriate f_z we now know *where* in 3D Fourier space our solution is non-zero. Now we just need to find out *what* it is. This is trivial because of our definition of the z -axis as being zero at the aperture:

$$\tilde{E}(\mathbf{f}_\perp, f_z) = \tilde{E}_a(\mathbf{f}_\perp) \quad (2.10)$$

The Fourier basis function above solves the diffraction problem for the component of E_a represented by $\tilde{E}_a(\mathbf{f}_\perp)$. Since we can solve the diffraction problem for any Fourier component of E_a , the sum of all these solutions will solve the diffraction problem for the complete aperture field (E_a). If we look at a plane some distance downstream from the aperture ($z=d$), the 2D Fourier transform of the electric field in this plane \tilde{E}_d will then be:

$$\begin{aligned} \tilde{E}_d(\mathbf{f}_\perp) &= \tilde{E}(\mathbf{f}_\perp, f_z) e^{i2\pi d f_z} \\ &= \tilde{E}_a(\mathbf{f}_\perp) e^{i2\pi d f_z} \end{aligned} \quad (2.11)$$

We choose to call $e^{i2\pi df_z}$ the *propagator function* because it allows us to propagate a plane wavefront through free space. Before we move on to applying the propagator function to different special geometrical cases, I will make a short remark regarding high frequencies in the aperture plane. I only do this for the sake of completeness, since such high frequencies will neither be occurring to any significant degree in imaging setups, nor will the effects be detectable due to the high spatial frequencies and the short propagation distances involved (as will be seen in the following). If the wave in the aperture plane has non-zero components for frequencies higher than the frequency dictated by the Helmholtz equation, the wavefront can still be propagated but it will produce a decaying wave, a so-called *evanescent wave*. This is easily seen by noting that for $f > \frac{k}{2\pi}$, equation (2.9) gives us an imaginary f_z . This again means that the propagated wave will be of the following form:

$$\tilde{E}_d(\mathbf{f}) = \tilde{E}_a(\mathbf{f})e^{-2\pi d|f_z|} \quad (2.12)$$

Which is an exponentially decaying function of d .

2.3 Rayleigh-Sommerfeld diffraction integral

The real space equivalent of equation(2.11) is the *Rayleigh-Sommerfeld diffraction formula*. To find it we first take the inverse Fourier transform of equation(2.11):

$$E_d = E_a \otimes \mathcal{F}^{-1} [e^{i2\pi df_z}] \quad (2.13)$$

Where \otimes denotes a convolution operation. The inverse fourier transform of the last term in the above equation is not trivial, but it can be shown [11] to be:

$$\begin{aligned} \mathcal{F}^{-1} [e^{i2\pi df_z}] &= \iint e^{i2\pi d\sqrt{(\frac{k}{2\pi})^2 - f_{\perp}^2}} e^{i\mathbf{f}_{\perp} \cdot \mathbf{r}_{\perp}} d\mathbf{r}_{\perp} \\ &= \frac{2\pi}{k} \left(\frac{1}{kr} - i \right) \frac{d}{r} \frac{e^{i2\pi kr}}{r} \end{aligned} \quad (2.14)$$

Where $r = |\mathbf{r}|$ is the 3-Dimensional vector norm. This equation is the real space propagator function, or what is sometimes called the *impulse response* of the electric field for an oscillation of time-frequency $\omega = kc$. Written out in full, the convolution in equation (2.13) then becomes:

$$\begin{aligned} E(\mathbf{r}_{\perp}, d) &= \iint E(\mathbf{r}'_{\perp}, 0) \frac{2\pi}{k} \left(\frac{1}{kl} - i \right) \frac{d}{l} \frac{e^{i2\pi kl}}{l} d\mathbf{r}'_{\perp} \\ &\quad \left(l = \sqrt{d^2 + (x - x')^2 + (y - y')^2} \right) \end{aligned} \quad (2.15)$$

This is the *Rayleigh-Sommerfeld diffraction formula*. From it can be derived the very intuitive and very well-known *Huygen's principle*. In my own words it goes something like this: *Every point on a wavefront may be considered an emitter of a spherical second order wavefront. It is the interference of all these second order wavefronts that determines the further propagation of the wave.* The shape of these second order wavefronts is given by the impulse response in equation (2.14). Solving the Rayleigh-Sommerfeld diffraction integral directly is typically much harder than propagating the field using the Fourier space propagator function, so I will not use it in the following, and its only use in the context of my work is as an intuitive description of wave propagation (though I would argue that, as you get used to the Fourier propagation concept, this also becomes a very intuitive framework).

2.4 Paraxial regime

So far we have looked at very general setup geometries and we have imposed no conditions on the wavefronts. In equation (2.12) we have even briefly considered the very exotic (and local, as we saw in that equation) case of wavefront oscillations of higher frequencies than the natural oscillation frequency dictated by the Helmholtz equation. But now we will turn to a very common assumption within optics; the *paraxial approximation*. The reasoning behind the approximation comes from the fact that most optical setups (e.g. x-ray imaging setups) have a very well determined primary propagation axis (conventionally

called z , a convention that I adhere to in this thesis). This means that the electric field's oscillation frequency in the z -direction is very close to the eigenfrequency dictated by the Helmholtz equation, and we may Taylor expand the expression for f_z we found in equation (2.9):

$$\begin{aligned} f_z &= \frac{k}{2\pi} \sqrt{1 - \left(\frac{2\pi f_\perp}{k}\right)^2} \\ &\approx \frac{k}{2\pi} + \frac{\pi f_\perp^2}{k} - \frac{\pi^3 f_\perp^4}{k^3} + \dots \end{aligned} \quad (2.16)$$

At this point we will make the *paraxial assumption* that the aperture-plane frequencies are sufficiently small compared to the Helmholtz-frequency for us to ignore the fourth-order term above. This of course raises the question of when it is reasonable to ignore the fourth order term. When dealing with Taylor expansion approximations in physics, the usual restriction applied is that the ignored higher-order terms should be much smaller than the included lower-order terms. However, in our case this is not a sufficient requirement since we are dealing with a Taylor expansion of the input to a periodic function (the exponential in equation (2.11)). So in order to ignore the fourth-order term in the equation above, we must require it to produce an input to the propagator exponential that is much smaller than 2π . I choose to set the limit at one degree i.e. $\pi/180$ radians. Leaving a one-degree term out of a complex exponential results in an error of 1.7 %, which I deem acceptable.

$$\begin{aligned} 2\pi d \frac{\pi^3 f_\perp^4}{k^3} &< \frac{\pi}{180} \\ df_\perp^4 &< \frac{k^3}{360\pi^3} \end{aligned} \quad (2.17)$$

We should of course also consider all terms of higher order than 4, but since the spatial resolution of our detector will always be much smaller than the wave number ($f_\perp \ll k$) higher order terms in equation (2.16) will always be much smaller than the fourth-order term. The paraxial assumption in equation (2.17) above is not a very strict requirement for most imaging setups. For instance, if we assume we have photons with a one Å wavelength (i.e. an energy of 12 keV) and a detector with a one μm pixel size (i.e. a maximum f of 10^6m^{-1}), the paraxial assumption holds for propagation distances smaller than 2.8 km! The reason that the paraxial assumption holds so well for typical x-ray imaging setups is that the pixel sizes are usually much larger than the photon wavelengths. With our new second order expression for f_z and the corresponding propagator function, we can express the wavefront at some distance d from the aperture as:

$$\begin{aligned} E_d &= \mathcal{F}^{-1} \left[e^{i2\pi f_z d} \tilde{E}_a \right] \\ &\approx \mathcal{F}^{-1} \left[e^{ikd} e^{i\pi\lambda df_\perp^2} \tilde{E}_a \right] \\ &= e^{ikd} \mathcal{F}^{-1} \left[e^{i\pi\lambda df_\perp^2} \tilde{E}_a \right] \end{aligned} \quad (2.18)$$

Where I have used that $k = 2\pi/\lambda$ when inserting the expression for f_z . The last exponential in the equation above is called the Fresnel propagator. In real space the expression above becomes the Fresnel diffraction integral:

$$E(\mathbf{r}_\perp, d) = \frac{e^{ikd}}{i\lambda d} \iint E(\mathbf{r}'_\perp, 0) e^{\frac{ik}{2d} |\mathbf{r}'_\perp - \mathbf{r}_\perp|^2} d\mathbf{r}'_\perp \quad (2.19)$$

Sometimes the Fresnel diffraction integral is derived from real space integrals such as the Rayleigh Sommerfeld (equation 2.15) or Kirchhoff (which is an approximation of the Rayleigh Sommerfeld integral) diffraction integrals. As the name suggests, the key assumption in the paraxial approximation is that the propagation directions are all very close to the principal propagation axis z . This is achieved very simply in Fourier space by requiring the frequencies in the transverse plane (f_\perp) to be small. But to achieve it in a real space derivation (i.e. to substitute the ' r_\perp '-dependencies in the denominators of equation (2.15) with d), it is necessary to assume d to be much larger than the width of the detector. This assumption

is not necessary when using the Fourier optics approach, and thus we are allowed to view the Fresnel propagation in equation (2.18) in the limit of infinitesimal propagation distances, which is what we will do in the following section.

2.4.1 Paraxial wave equation

In the following I will disregard the high-frequency pre-factor e^{ikd} in equation (2.18), since this is just a constant phase contribution across the 2D plane of the propagating wave. Let's have a look at the derivative of the electric field along the propagation direction:

$$\begin{aligned}\frac{\partial E}{\partial d} &= \frac{\partial}{\partial d} \left[\mathcal{F}^{-1} \left[e^{i\pi\lambda d f_{\perp}^2} \tilde{E} \right] \right] \\ &= \mathcal{F}^{-1} \left[i\pi\lambda f_{\perp}^2 e^{i\pi\lambda d f_{\perp}^2} \tilde{E} \right]\end{aligned}\tag{2.20}$$

We now remember that multiplying with $i2\pi f_{\perp}$ in Fourier space is equivalent to differentiating in real space. We can use this to get rid of the frequency prefactor:

$$\begin{aligned}\frac{\partial E}{\partial d} &= \mathcal{F}^{-1} \left[\frac{\lambda}{i4\pi} (i2\pi f_{\perp})^2 e^{i\pi\lambda d f_{\perp}^2} \tilde{E} \right] \\ &= -\frac{i}{2k} \nabla_{\perp}^2 E\end{aligned}\tag{2.21}$$

The result is the *paraxial wave equation*. It is called so because it is the paraxial regime's equivalent to the Helmholtz wave equation (2.6). The paraxial wave equation is often written in the form:

$$\left(\nabla_{\perp}^2 + i2k \frac{\partial}{\partial z} \right) E = 0\tag{2.22}$$

Note that the nabla (∇) in the equation above is only taken on the transverse plane, and not in z -direction. The omission of the z -directional component of ∇ in the equation above is actually equivalent to making the paraxial assumption. And the paraxial wave equation shows one of the reasons why the paraxial assumption is so useful; it decouples the terms, so that one term (the curvature) only considers the transverse plane, and the other term only considers the propagation direction. A function closely related to the paraxial wave function is the transport of intensity function. To get from the paraxial wave equation to the transport of intensity equation no further assumptions are necessary. All we have to do is to separate our spatial wave modulation into its amplitude and phase parts:

$$E = e^{i\phi} \sqrt{I}\tag{2.23}$$

Where \sqrt{I} is chosen instead of $|E|$ for later notational simplicity and for convenience reasons, since the intensity I is the measured property of the electric field. After a lot of rearrangements, which I will spare the reader from, we will arrive at:

$$\nabla_{\perp} \cdot (I \nabla_{\perp} \phi) = -k \frac{\partial I}{\partial z}\tag{2.24}$$

This is the transport of intensity equation, which we will use for correcting our images for refraction artefacts in section 3.1.4.

2.5 Matter

So far we have only considered free space propagation. Now we will consider what happens when x-rays encounter matter. Matter affects the phase speed c in equation (2.2):

$$\begin{aligned}\nabla^2 E &= \left(\frac{n}{c} \right)^2 \frac{\partial E}{\partial t^2} \\ (n &= 1 + i\beta - \delta)\end{aligned}\tag{2.25}$$

Where n is the refractive index. δ and β are both real numbers. For x-rays δ and β are both quite small, even for dense materials. They are typically on the order of 10^{-6} for δ and 10^{-9} for β . This leaves

us with a refractive index very close to unity, and explains why x-ray reflectivity only occurs at very shallow angles, and why x-rays penetrate matter so well. The equation above can be stated in different forms. In the form we have chosen, the vacuum light speed, c , is kept, and we express the material-dependency via the refractive index. Just like in section 2.1 we make the Helmholtz assumption that the electric field can be separated into a time-dependent and a space-dependent part. The space-dependent part becomes:

$$\nabla^2 E(\mathbf{r}) = -n(\mathbf{r})^2 k^2 E(\mathbf{r}) \quad (2.26)$$

Where we have kept the squared refractive index in the spatial part of the equation. In other words; for a fixed time frequency, (e.g. a constant source), the presence of matter will influence the wave propagation as stated in the equation above. Without loss of generality we can rewrite the electric field as the product of a plane wave travelling along z and a perturbation function, E_p :

$$E(\mathbf{r}) = E_p(\mathbf{r}) e^{ikz} \quad (2.27)$$

Strictly speaking we have not required anything of E_p , but the formulation above of course implicitly suggests that E_p is slowly varying. Now, let's insert 2.27 in 2.26:

$$\left(\nabla^2 E_p + 2ik \frac{\partial}{\partial z} E_p - k^2 E_p \right) e^{ikz} = -n^2 k^2 E_p e^{ikz} \quad (2.28)$$

Moving a little around, we get:

$$2ik \frac{\partial}{\partial z} E_p = (1 - n^2) k^2 E_p - \nabla^2 E_p \quad (2.29)$$

Which, apart from the inclusion of the z -directional component of ∇ , is just the paraxial wave equation in (2.22) generalized to apply in matter. Hence, as it was hinted at in the previous section, it follows from the derivation in this section, that the paraxial wave function can be derived directly from the Helmholtz wave equation by assuming the wave function to be the product of a plane wave and a perturbation function, and then afterwards making the paraxial assumption by omitting the z -component of ∇ . In a sense, the two terms on the right of the equation above represent the two different domains of x-ray imaging; wave-matter interaction and free space propagation. The equation also serves to demonstrate one of the fundamental challenges in x-ray imaging; it is very hard to take both interactions on the right side into account. This problem is typically tackled by only considering them one at a time, which is where the thin-film-at-aperture-approximation comes into play. This approximation simply states that we can assume all the matter in the sample to be projected onto a thin film at the aperture plane. This film is so thin, that we don't need to consider the propagation term (the curvature term in the equation above) while the wave passes it, and everywhere else except within this thin aperture plane, we have just removed all matter, so we can ignore wave-matter interactions (the left term on the right side of the equation above). Voila, we've just made everything much easier! We move on by writing out n and remembering that δ and β are both much smaller than one, so we disregard the resulting squared $(i\beta - \delta)$ term. We also get rid of the z -component of ∇ which is equivalent to making the paraxial assumption in equation (2.21):

$$2ik \frac{\partial}{\partial z} E_p = -2(i\beta - \delta) k^2 E_p - \nabla_{\perp}^2 E_p \quad (2.30)$$

Then we make the domain-distinction of neglecting the propagation-term on the right. First we note that the inclusion of the x - y -curvature terms in equation (2.30) corresponds to applying a paraxial wave propagation as done in equation (2.18). We now want to ignore the propagation altogether, meaning that we must require the exponential in equation (2.18) to be approximately one. Adhering to the previous standard we do this by requiring the exponent to be less than 1 degree:

$$\begin{aligned}\pi\lambda df_{\perp}^2 &< \frac{\pi}{180} \\ d &< \frac{1}{180\lambda f_{\perp}^2}\end{aligned}\tag{2.31}$$

For a 12 keV beam and a one μm pixel size, this leaves us with a propagation distance smaller than 55 μm . That's quite a thin film, and illustrates why the thin-film-at-aperture approximation is not always sound. Assuming the approximation holds, we can ignore the curvature term in equation (2.30) and we get:

$$\frac{\partial}{\partial z} E_p = ik(i\beta - \delta)E_p\tag{2.32}$$

This equation is easily solvable by using:

$$E_p = e^{ik(i\beta - \delta)z}\tag{2.33}$$

Which leads us to the very nice aperture field for the thin-film-at-aperture-assumption:

$$E_p = e^{ik(iB - D)}\tag{2.34}$$

$$(2.35)$$

Where:

$$\begin{aligned}B &= \int \beta dz \\ D &= \int \delta dz\end{aligned}\tag{2.36}$$

The E_p in equation (2.35) is also sometimes called the transmittance function or the transmission function, and then usually denoted by T . The thin-film-at-aperture-plane approximation can also be reached more directly from the Helmholtz wave equation in matter in equation (2.26) by ignoring the transverse-plane components of the curvature. But I've chosen the line going over equation (2.30), since I find this equation to be quite instructive and since I will refer to it in a later section (3.2.1).

2.6 Magnification effect

Real-life beams are seldomly parallel. Even the large distances from source to sample at synchrotron beamlines are not enough to completely erase the effect of the non-parallelity of the source beam. Luckily, we can find a very simple mechanism, called image magnification, that describes this effect under certain assumptions. Unfortunately, these assumptions, are quite restrictive and in general the magnification effect only holds for synchrotron beams. Consider a point source a distance d_s from the aperture plane (we have defined the z-axis so the aperture plane is at $z=0$). If the beam propagates freely from source to aperture plane, the source will produce the following field:

$$E(\mathbf{r}_{\perp}, z = 0) = E_s \frac{e^{ikr_s}}{r_s}\tag{2.37}$$

Where we have introduced the source distance r_s

$$r_s = \sqrt{d_s^2 + r_{\perp}^2}\tag{2.38}$$

At the aperture plane, the Taylor expansion of the expression above with respect to r_{\perp} , looks like this:

$$r_s = d_s + \frac{r_{\perp}^2}{2d_s} - \frac{r_{\perp}^4}{8d_s^3} + \dots\tag{2.39}$$

Let's require the fourth order term to be sufficiently small not to produce a significant effect on the phase, i.e. we require the input to the exponential in equation (2.37) to vary less than one degree when we omit the fourth order term (corresponding to an error of 1.7 %):

$$\begin{aligned} k \frac{r_{\perp}^4}{8d_s^3} &< \frac{2\pi}{360} \\ r_{\perp} &< \sqrt[4]{\frac{d_s^3 \lambda}{45}} \end{aligned} \quad (2.40)$$

The requirement above secures the fourth-order term in the Taylor expansion of r_s to be sufficiently small for us to ignore it. Because our wavelengths are always much smaller than the source-sample distances, higher-order terms are always much smaller than the fourth order term, and the inequality above is sufficient to allow us to exclude fourth-order and higher terms in the source field equation (2.37). Note that the requirement in equation (2.40) typically doesn't hold for lab setups. Assuming that equation (2.40) is fulfilled, we can make the quadratic approximation of the source field:

$$E(\mathbf{r}_{\perp}, z = d_s) = E_s \frac{e^{ik\left(d_s + \frac{r_{\perp}^2}{2d_s}\right)}}{d_s} \quad (2.41)$$

Where we have ignored the second order term in the denominator, since it is typically orders of magnitude smaller than d_s as long as equation (2.40) holds. Now let's consider a thin sample with a transmission function T . This will produce the following field just as the beams exits the sample:

$$E_{s,a}(\mathbf{r}_{\perp}) = \frac{e^{ikd_s}}{d_s} T E_s e^{ik\frac{r_{\perp}^2}{2d_s}} \quad (2.42)$$

If the frequencies of the field at the aperture plane (i.e. the product of the source field and the transmission function) are low enough to satisfy equation (2.17), we can propagate the field expression above using the Fresnel diffraction integral from equation (2.19):

$$E(\mathbf{r}_{\perp}, d) = \frac{e^{ikd}}{i\lambda d} \frac{e^{ikd_s}}{d_s} E_s \iint T(r'_{\perp}) e^{ik\left(\frac{r'_{\perp}{}^2}{2d_s} + \frac{|\mathbf{r}'_{\perp} - \mathbf{r}_{\perp}|^2}{2d}\right)} d\mathbf{r}' \quad (2.43)$$

Defining the magnification as:

$$M \equiv \frac{d + d_s}{d_s} \quad (2.44)$$

We can rewrite the second order distance terms in the integral of equation (2.43):

$$\frac{r'_{\perp}{}^2}{2d_s} + \frac{|\mathbf{r}'_{\perp} - \mathbf{r}_{\perp}|^2}{2d} = \frac{r'_{\perp}{}^2}{2(d + d_s)} + \frac{1}{2d_M} |\mathbf{r}'_{\perp} - \mathbf{r}_M|^2 \quad (2.45)$$

Where we have used the magnification variables:

$$\begin{aligned} d_M &\equiv \frac{d}{M} \\ \mathbf{r}_M &\equiv \frac{\mathbf{r}_{\perp}}{M} \end{aligned} \quad (2.46)$$

Making the substitution suggested by equation (2.45) in equation (2.43), we get:

$$\begin{aligned} E(\mathbf{r}_{\perp}, d) &= \frac{e^{ikd}}{i\lambda d} \frac{e^{ikd_s}}{d_s} E_s e^{\frac{ik}{2(d+d_s)} r_{\perp}^2} \iint T(r'_{\perp}) e^{\frac{ik}{2d_M} |\mathbf{r}'_{\perp} - \mathbf{r}_M|^2} d\mathbf{r}' \\ &= E_s \frac{e^{ik\left(d+d_s + \frac{r_{\perp}^2}{2(d+d_s)}\right)}}{d + d_s} \frac{1}{i\lambda d_M} \iint T(r'_{\perp}) e^{\frac{ik}{2d_M} |\mathbf{r}'_{\perp} - \mathbf{r}_M|^2} d\mathbf{r}' \end{aligned} \quad (2.47)$$

We see that the first part of the expression above is just the quadratic approximation of the undisturbed source field from equation (2.41). The last part of the equation above corresponds to equation (2.19), i.e. it describes the propagation of a plane wave incident on the sample. This means that the intensity distribution at distance d is just a scaled up (magnified) version of the intensity distribution that would be seen at d_M if T had been the transmission function resulting from an incident plane wave illumination. Note however that T is not exactly the same as in the plane wave case, since the field has a slightly different (longer or equal) propagation distance through the sample than it would have had in the plane wave case. But this effect is negligible just as the quadratic term in the denominator of equation (2.41) is. Due to equation (2.40) the magnification effect typically doesn't hold for lab setups per se. But since lab setups often have propagation distances too short for phase effects to play a significant role, we don't need to worry about Fresnel propagation. Regarding grating interferometers, the phase contrast modality is based on a "local plane wave approximation", which I will also briefly mention in section 3.3.

2.7 Intensity Fourier transform

I will now derive an expression for the Fourier transform of the intensity at the detector screen. This is a very useful expression since the intensity, unlike the electric field E , is directly measurable. First, we note that the intensity is the product of the electric field and its complex conjugate. Given a sufficiently well behaved aperture field (equation (2.17)) the electric field at the detector is found using the Fresnel propagator in equation (2.18). The complex conjugate of the electric field then becomes:

$$\bar{E}(\mathbf{r}_\perp, d) = e^{-ikd} \mathcal{F}^{-1} \left[e^{-i2\pi f_\perp' d} \tilde{E}_a \right] \quad (2.48)$$

So we can find the intensity at the detector as:

$$\begin{aligned} I_d &= E_d \bar{E}_d \\ &= F^{-1} \left[\tilde{E}_a e^{i2\pi f_\perp' d} \right] F^{-1} \left[\tilde{E}_a e^{-i2\pi f_\perp' d} \right] \end{aligned} \quad (2.49)$$

The equation above suggests that we might simplify the expression by considering the Fourier transform of I_d :

$$\tilde{I}_d(\mathbf{f}_\perp) = \left[\tilde{E}_0 e^{i2\pi f_\perp' d} \right] \otimes \left[\tilde{E}_0 e^{-i2\pi f_\perp' d} \right] \quad (2.50)$$

The next step becomes notationally simpler if we insert the full expression for f_\perp' :

$$\tilde{I}_d(\mathbf{f}_\perp) = \left[\tilde{E}_0 e^{i\pi\lambda d f_\perp^2} \right] \otimes \left[\tilde{E}_0 e^{-i\pi\lambda d f_\perp^2} \right] \quad (2.51)$$

Let's write out the convolution integral:

$$\tilde{I}_d(\mathbf{f}_\perp) = \int \tilde{E}_0(\mathbf{p}_\perp) e^{i\pi\lambda d p_\perp^2} \tilde{E}_0(\mathbf{f}_\perp - \mathbf{p}_\perp) e^{-i\pi\lambda d |\mathbf{f}_\perp - \mathbf{p}_\perp|^2} d\mathbf{p}_\perp \quad (2.52)$$

Using that the Fourier transform of the complex conjugate is the complex conjugate of the flipped Fourier transform ($E(\tilde{\mathbf{f}}_\perp) = E(-\mathbf{f}_\perp)$) we can rewrite the integral:

$$\tilde{I}_d(\mathbf{f}_\perp) = e^{-i\pi\lambda d f_\perp^2} \int \tilde{E}_0(\mathbf{p}_\perp) \tilde{E}_0(\mathbf{p}_\perp - \mathbf{f}_\perp) e^{2i\pi\lambda d \mathbf{f}_\perp \cdot \mathbf{p}_\perp} d\mathbf{p}_\perp \quad (2.53)$$

Parseval's theorem allows us to change an integral over Fourier space products to an integral over real space products:

$$\tilde{I}_d(\mathbf{f}_\perp) = e^{-i\pi\lambda d f_\perp^2} \int F^{-1} \left[\tilde{E}_0(\mathbf{p}_\perp) e^{2i\pi\lambda d \mathbf{f}_\perp \cdot \mathbf{p}_\perp} \right] (\mathbf{r}_\perp) F^{-1} \left[\tilde{E}_0(\mathbf{p}_\perp - \mathbf{f}_\perp) \right] (\mathbf{r}_\perp) d\mathbf{r}_\perp \quad (2.54)$$

Note that there's a bar above the last of the two inverse Fourier transforms, meaning that after the transformation, the function needs to be complex conjugated. To make things less messy I will write out the two integrals from the inverse Fourier transforms above separately:

$$F^{-1} \left[\tilde{E}_0(\mathbf{p}_\perp) e^{2i\pi\lambda d \mathbf{f}_\perp \cdot \mathbf{p}_\perp} \right] = \int \tilde{E}_0(\mathbf{p}_\perp) e^{2i\pi\lambda d \mathbf{f}_\perp \cdot \mathbf{p}_\perp} e^{i2\pi \mathbf{p}_\perp \cdot \mathbf{r}_\perp} d\mathbf{p}_\perp \quad (2.55)$$

$$= \int \tilde{E}_0(\mathbf{p}_\perp) e^{i2\pi \mathbf{p}_\perp \cdot (\mathbf{r}_\perp + \lambda d \mathbf{f}_\perp)} d\mathbf{p}_\perp \quad (2.56)$$

$$= E_0(\mathbf{x} + \lambda d \mathbf{f}) \quad (2.57)$$

and the other transform looks like this:

$$F^{-1} \left[\tilde{E}_0(\mathbf{p}_\perp - \mathbf{f}_\perp) \right] = \int \tilde{E}_0(\mathbf{p}_\perp - \mathbf{f}_\perp) e^{i2\pi \mathbf{p}_\perp \cdot \mathbf{r}_\perp} d\mathbf{p}_\perp \quad (2.58)$$

Substituting $\mathbf{q}_\perp = \mathbf{p}_\perp - \mathbf{f}_\perp$:

$$F^{-1} \left[\tilde{E}_0(\mathbf{p}_\perp - \mathbf{f}_\perp) \right] = \int \tilde{E}_0(\mathbf{q}_\perp) e^{i2\pi(\mathbf{q}_\perp + \mathbf{f}_\perp) \cdot \mathbf{r}_\perp} d\mathbf{q}_\perp \quad (2.59)$$

$$= e^{i2\pi \mathbf{f}_\perp \cdot \mathbf{r}_\perp} E_0(\mathbf{r}_\perp) \quad (2.60)$$

Inserting both in equation 2.54 above:

$$\tilde{I}_d(\mathbf{f}_\perp) = e^{-i\pi\lambda d f^2} \int E_0(\mathbf{r}_\perp + \lambda d \mathbf{f}_\perp) E_0(\bar{\mathbf{r}}_\perp) e^{-i2\pi \mathbf{f}_\perp \cdot \mathbf{r}_\perp} d\mathbf{r}_\perp \quad (2.61)$$

$$= \int E_0(\mathbf{r}_\perp + \lambda d \mathbf{f}_\perp) E_0(\bar{\mathbf{r}}_\perp) e^{-i2\pi \mathbf{f}_\perp \cdot (\mathbf{r}_\perp + \frac{\lambda d \mathbf{f}_\perp}{2})} d\mathbf{r}_\perp \quad (2.62)$$

The exponential term is almost begging for the substitution $\mathbf{r}'_\perp = \mathbf{r}_\perp + \frac{\lambda d \mathbf{f}_\perp}{2}$:

$$\tilde{I}_d(\mathbf{f}_\perp) = \int E_0(\mathbf{r}_\perp + \frac{\lambda d \mathbf{f}_\perp}{2}) \bar{E}_0(\mathbf{r}_\perp - \frac{\lambda d \mathbf{f}_\perp}{2}) e^{-i2\pi \mathbf{f}_\perp \cdot \mathbf{r}_\perp} d\mathbf{r}_\perp \quad (2.63)$$

And this is our final result, which directly gives us the intensity distribution after a propagation distance d . This equation will be used in the derivation of the propagation based phase-retrieval, or *holotomography*, method described in the next chapter. Now I have derived the different basic formulas needed for the following work, and I will proceed to look more specifically at different imaging methods.

Chapter 3

Imaging theory

Before proceeding with the imaging theory I will explain my definition of certain terms used later in this chapter. I do this for the sake of clarity, because the meaning of these terms is not always consistent within the field of x-ray imaging.

term	definition
exposure	a single detector readout, i.e. a 2D map of photon flux
projection	a 2D projection of physical properties built from a number of exposures at a given projection angle, e.g. an absorption projection
tomogram	a 3D map of physical properties built from a number of projections
image	umbrella term covering both projections and tomograms
flatfield	exposure or projection with no sample in the beam, used as a reference, e.g. a differential phase contrast flatfield projection

3.1 2D absorption imaging

3.1.1 absorption assumption

Absorption imaging is both the most common and the oldest form of x-ray imaging. In absorption imaging, interference phenomena are ignored. Under this assumption, the intensity distribution at the detector will be the same as it was when the beam exited the sample (except for geometrical magnification). As seen in equation (2.18) the Fresnel propagator function is close to unity for sufficiently small propagation distances. To ignore phase effects, let's require the exponential of the propagator function to be less than 1 degree:

$$\begin{aligned} 2\pi^2 f^2 \frac{d}{k} &< \frac{\pi}{180} \\ d &< \frac{k}{360\pi f^2} \end{aligned} \tag{3.1}$$

If we assume a wavelength of 1 Å, and a pixelsize of 5 μm, the absorption assumption holds within propagation distances less than 5 mm. For synchrotron setups, the absorption-only requirement can usually be met, by making sure the detector is placed as close to the sample as possible. For laboratory setups, especially micro-CT systems that have become widespread in the later years, the absorption-only requirement can sometimes be hard to meet, but they are often saved by the relatively high energies (and hence large wave number, k) they use.

3.1.2 Absorption projections

Two detector readouts are required to create an absorption projection; a flatfield exposure, and a sample exposure. From the two exposures, the transmission T can be defined. Since refraction effects are

ignored, the transmission is only dependent on the absorption coefficient distribution along the photon path. Transmission is related to the absorption coefficient by Lambert-Beer's law:

$$T = \frac{I_{sample}}{I_0} = e^{-\int \mu dz} \quad (3.2)$$

If the flatfield exposure I_0 is taken with nothing but air in the beam path, I_0 can be assumed to be equal to the incident photon flux. If the flatfield is taken with some sort of reference medium (e.g. a water bath) in the beam path, the incident photon flux is unknown, and in this case the μ in equation (3.2) is a relative absorption coefficient ($\mu = \mu_{sample} - \mu_0$), rather than an absolute one.

3.1.3 Absorption contrast optimization

In absorption contrast imaging, the energy is usually tunable in some way: On a synchrotron the beam is approximately monochromatic, and the energy can be selected by tuning the monochromator. On lab sources, the bremsstrahlung spectrum can be shifted up or down by tuning the acceleration voltage. For simplicity, we will consider the case of a monochromatic parallel beam and a single-material sample, and we will disregard statistical uncertainty of the count rates. The sample has a projected thickness $\rho(\mathbf{r}_\perp)$ and an energy-dependent absorption coefficient μ . The transmitted intensity is given by Lambert-Beer's law in equation (3.2):

$$I = I_0 e^{-\mu\rho} \quad (3.3)$$

We assume I_0 to be constant across the projection plane. The transmission intensity varies across the projection plane as:

$$\frac{\partial I}{\partial \mathbf{r}_\perp} = -\mu I_0 \frac{\partial \rho}{\partial \mathbf{r}_\perp} e^{-\mu\rho} \quad (3.4)$$

We may call this quantity the contrast variation. It is this quantity that we will try to maximize. Let's see what effect shifting the absorption coefficient has on the contrast variation:

$$\frac{\partial^2 I}{\partial \mathbf{r}_\perp \partial \mu} = (\rho\mu - 1) I_0 \frac{\partial \rho}{\partial \mathbf{r}_\perp} e^{-\mu\rho} \quad (3.5)$$

The maximum value of the contrast variation must be where the equation above is zero. Except for exotic cases like constant material thickness across the projection plane or infinite absorption coefficient, this requirement is fulfilled only for $\rho\mu = 1$, which corresponds to a transmission of:

$$T_{max\ contrast} = e^{-1} = 37\% \quad (3.6)$$

A number of factors can shift the actual optimal transmission rate either up or down, e.g. counting statistics improve for bigger counts, which pushes us towards higher count rates, whereas a very varying sample thickness of course pushes us towards lower transmission rates in the thickest regions of the sample. But in general, a transmission rate of 37 % is often a good number to aim for.

3.1.4 Refraction correction

Taking both refraction and absorption into account in propagation-based imaging with only a single sample-detector distance, is generally not possible in a strict mathematical sense. Simply put, it is not possible to know if the photon distribution across the detector screen is the result of absorption or refraction effects, or, more realistically, to what degree it is the result of each of the two effects. If we want to find a solution to the problem (i.e. determine both β and δ from the refractive index), we need to make an assumption about β and δ . There are many different assumption possibilities [7]. Here we choose to assume that the ratio of β and δ is constant [21] throughout the sample, as this is what was

used in some of my publications. We will also apply the thin-film-at-aperture assumption from section 2.5, i.e. assume the sample to be of such a small thickness ρ that interference effects during the wave's propagation through the sample can be neglected. With these assumptions the electric field just as the beam exits the sample becomes:

$$E(\mathbf{r}_\perp, 0) = E_s(\mathbf{r}_\perp, 0)e^{ik(i\beta - \delta)\rho(\mathbf{r}_\perp)} \quad (3.7)$$

Where E_s is the undisturbed field emitted from the source and β and δ are the imaginary and real parts of the deviation of the refractive index from unity (i.e. $n = 1 + i\beta - \delta$). From this equation it is clear that we can express the intensity I and phase ϕ as the beam exits the sample like this:

$$\begin{aligned} \phi_0 &= -k\delta\rho + \phi_s \\ I_0 &= I_s e^{-2k\beta\rho} \end{aligned} \quad (3.8)$$

Where ϕ_s and I_s are the phase and intensity of the flatfield beam at the aperture plane, and $\rho(\mathbf{r}_\perp)$ is the projected sample thickness. Inserting these expressions in the transport of intensity equation (2.24) we get:

$$-k \frac{\partial}{\partial z} I = \nabla_\perp \cdot (I_s e^{-2k\beta\rho} \nabla_\perp [-k\delta\rho + \phi_s]) \quad (3.9)$$

If we assume the source field to be planar, we can ignore ϕ_s and move I_s outside the differentiation in the equation above:

$$\begin{aligned} -k \frac{\partial}{\partial z} I &= I_s \nabla_\perp \cdot (e^{-2k\beta\rho} \nabla_\perp (-k\delta\rho)) \\ &= -k\delta I_s \nabla_\perp \cdot (e^{-2k\beta\rho} \nabla_\perp \rho) \\ &= -k\delta I_s \nabla_\perp \cdot \left(\frac{1}{-2k\beta} \nabla_\perp e^{-2k\beta\rho} \right) \\ &= \frac{\delta}{2\beta} I_s \nabla_\perp^2 e^{-2k\beta\rho} \\ &= \frac{\delta}{2\beta} \nabla_\perp^2 I_0 \end{aligned} \quad (3.10)$$

Equation (3.10) gives us the first order derivative of I as it propagates downstream. For appropriately small propagation distances, the development in I is approximately determined by the first order contribution only. To evaluate the validity region for the first order approximation, we must turn to the derivation of the paraxial wave equation. The first order approximation holds within 1.5 % as long as the exponent in equation (2.20) is smaller than $\pi/18$ (i.e. "10 degrees"):

$$\begin{aligned} 2\pi f_\perp' d &< \pi/18 \\ 2\pi \frac{\pi f_\perp^2}{k} d &< \pi/18 \\ d &< \frac{k}{36\pi f_\perp^2} \end{aligned} \quad (3.11)$$

If the condition above is fulfilled, we can express the intensity distribution at a distance d as:

$$\begin{aligned} I_d &= d \frac{\partial}{\partial z} I_0 + I_0 \\ &= -d \frac{\delta}{2k\beta} \nabla_\perp^2 I_0 + I_0 \\ &= \left(-d \frac{\delta}{\mu} \nabla_\perp^2 + 1 \right) e^{-\mu\rho} \end{aligned} \quad (3.12)$$

Where I have inserted $I_0 = e^{-\mu\rho}$. The quantity we are looking for is the projected sample thickness ρ . Taking the Fourier transform on both sides of the equation above we get:

$$\begin{aligned}\tilde{I}_0 &= \left(1 - d \frac{\delta}{\mu} (i2\pi f)^2\right) \mathcal{F} [e^{-\mu\rho}] \\ e^{-\mu\rho} &= \mathcal{F}^{-1} \left[\frac{\tilde{I}_0}{1 + d \frac{\delta}{\mu} (2\pi f_\perp)^2} \right]\end{aligned}\tag{3.13}$$

To get the projected thickness ρ we just need to take the logarithm and divide by $-\mu$. The equation above is sometimes called a phase retrieval algorithm or a phase contrast method. I object to this naming, since it is misleading. The derived quantity is not a phase projection, and the main contrast formation mechanism is absorption, not phase. In fact, the inequality in equation (3.11) works to assure that the propagation distance is so small that phase effects only play a minor role, even at the highest frequencies, which are most affected by phase modulations. In a sense, the equation above is the opposite of a phase retrieval algorithm, since what it seeks to accomplish is to remove phase-induced intensity modulations by suppressing the higher order Fourier terms most affected by phase effects. It is also worth noting that the equation above effectively acts as a low-pass filter, leading to reduced statistical noise at the cost of reduced spatial resolution. This means that the filter above can sometimes serve as a convenient excuse for applying some low-pass filtering to images.

3.2 2D non-interferometric phase imaging

Simply put, x-ray detectors count photons, but are indifferent to the phase of the photons counted. If we want to map the δ -distribution of a sample, this poses a challenge, since the part of the x-ray wave function directly affected by δ cannot be measured. The problem with the lacking phase information is called the *phase problem*. Instead of directly measuring the phase, propagation based phase imaging relies on phase dependent interference effects which modulate the (measurable) intensity distribution of the beam. To map the full complex electric field at the aperture plane (see Fig. 2.1) we may choose to place the detector at different distances from the aperture. This will allow us to map the evolution of the wave intensity as the beam propagates. This evolution is an interference effect and it depends on the phase of the beam. So the intensity evolution allows us to derive information about the phase distribution. But the derivation or *phase retrieval* is not straightforward; it requires some work to arrive at a suitable algorithm. It is the derivation of such an algorithm that I will sketch in the following. We will start by writing out the amplitude (A) and phase (ϕ) parts of the electric field, so that $E = Ae^{i\phi}$, and insert this in the intensity Fourier transform in equation 2.63:

$$\tilde{I}_d(\mathbf{f}_\perp) = \int E_0(\mathbf{r}_\perp + \frac{\lambda d \mathbf{f}_\perp}{2}) E_0(\mathbf{r}_\perp - \frac{\lambda d \mathbf{f}_\perp}{2}) e^{i\phi(\mathbf{r}_\perp - \frac{\lambda d \mathbf{f}_\perp}{2}) - i\phi(\mathbf{r}_\perp + \frac{\lambda d \mathbf{f}_\perp}{2})} e^{-i2\pi \mathbf{f}_\perp \cdot \mathbf{r}_\perp} d\mathbf{r}_\perp \tag{3.14}$$

If the phase varies sufficiently slowly ($\phi(\mathbf{r}_\perp + \frac{\lambda d \mathbf{f}_\perp}{2}) - \phi(\mathbf{r}_\perp - \frac{\lambda d \mathbf{f}_\perp}{2}) < \pi/180$), we can linearize the phase term. Note that this assumption is often quite dubious. E.g. for a 1 Å wavelength (i.e. an energy of 12 keV) and a detector with a 1 μm pixel size (i.e. a maximum f of almost 10^6m^{-1}) and a propagation distance of a few centimeters, $\lambda d f$ will be a few μm corresponding to a few pixels. If our sample varies less than one degree over several pixels, it certainly isn't producing much effect on the beam, and we should probably consider increasing the contrast in some way, which would then render our assumption of a slowly varying phase invalid - and now we're going in circles, suddenly tied to a very low-contrast scenario. This is one of the problems with propagation based phase contrast imaging:

$$\begin{aligned}\tilde{I}_d(\mathbf{f}_\perp) &= \int E_0(\mathbf{r}_\perp + \frac{\lambda d \mathbf{f}_\perp}{2}) E_0(\mathbf{r}_\perp - \frac{\lambda d \mathbf{f}_\perp}{2}) \left[1 + i\phi(\mathbf{r}_\perp - \frac{\lambda d \mathbf{f}_\perp}{2}) - i\phi(\mathbf{r}_\perp + \frac{\lambda d \mathbf{f}_\perp}{2}) \right] e^{-i2\pi \mathbf{f}_\perp \cdot \mathbf{r}_\perp} d\mathbf{r}_\perp \\ &= I_d^{\phi=0} + ie^{-i\pi \lambda d f_\perp^2} \int E_0(\mathbf{r}_\perp) E_0(\mathbf{r}_\perp + \lambda d \mathbf{f}_\perp) \phi(\mathbf{r}_\perp) e^{-i2\pi \mathbf{f}_\perp \cdot \mathbf{r}_\perp} d\mathbf{r}_\perp \\ &\quad - ie^{i\pi \lambda d f_\perp^2} \int E_0(\mathbf{r}_\perp - \lambda d \mathbf{f}_\perp) E_0(\mathbf{r}_\perp) \phi(\mathbf{r}_\perp) e^{-i2\pi \mathbf{f}_\perp \cdot \mathbf{r}_\perp} d\mathbf{r}_\perp\end{aligned}\tag{3.15}$$

With $I_d^{\phi=0}$ being the propagated beam intensity if the phase at the aperture was zero. The exponential prefactors can be expressed by trigonometric functions rather than exponentials:

$$\begin{aligned}
ie^{-i\pi\lambda df_{\perp}^2} &= i \cos(\pi\lambda df_{\perp}^2) + \sin(\pi\lambda df_{\perp}^2) \\
- ie^{i\pi\lambda df_{\perp}^2} &= -i \cos(\pi\lambda df_{\perp}^2) + \sin(\pi\lambda df_{\perp}^2)
\end{aligned} \tag{3.16}$$

Inserting in equation (3.15) and rearranging:

$$\begin{aligned}
\tilde{I}_d(\mathbf{f}_{\perp}) &= I_d^{\phi=0} + i \cos(\pi\lambda df_{\perp}^2) \int A_0(\mathbf{r}_{\perp}) (A_0(\mathbf{r}_{\perp} - \lambda d\mathbf{f}_{\perp}) - A_0(\mathbf{r}_{\perp} + \lambda d\mathbf{f}_{\perp})) \phi(\mathbf{r}_{\perp}) e^{-i2\pi\mathbf{f}_{\perp} \cdot \mathbf{r}_{\perp}} d\mathbf{r}_{\perp} \\
&\quad + \sin(\pi\lambda df_{\perp}^2) \int A_0(\mathbf{r}_{\perp}) (A_0(\mathbf{r}_{\perp} - \lambda d\mathbf{f}_{\perp}) + A_0(\mathbf{r}_{\perp} + \lambda d\mathbf{f}_{\perp})) \phi(\mathbf{r}_{\perp}) e^{-i2\pi\mathbf{f}_{\perp} \cdot \mathbf{r}_{\perp}} d\mathbf{r}_{\perp}
\end{aligned} \tag{3.17}$$

The intensity will be assumed to have no significant contribution from higher order Fourier components, i.e. it is slowly varying, so that:

$$\begin{aligned}
A_0(\mathbf{r}_{\perp} - \lambda d\mathbf{f}_{\perp}) - A_0(\mathbf{r}_{\perp} + \lambda d\mathbf{f}_{\perp}) &= 2\lambda d\mathbf{f}_{\perp} \cdot \nabla A_0(\mathbf{r}_{\perp}) \\
A_0(\mathbf{r}_{\perp} - \lambda d\mathbf{f}_{\perp}) + A_0(\mathbf{r}_{\perp} + \lambda d\mathbf{f}_{\perp}) &= 2A_0(\mathbf{r}_{\perp})
\end{aligned} \tag{3.18}$$

Inserting in equation (3.17):

$$\begin{aligned}
\tilde{I}_d(\mathbf{f}_{\perp}) &= I_d^{\phi=0} + 2i \cos(\pi\lambda df_{\perp}^2) \lambda d\mathbf{f}_{\perp} \cdot \int A_0 \phi \nabla A_0 e^{-i2\pi\mathbf{f}_{\perp} \cdot \mathbf{r}_{\perp}} d\mathbf{r}_{\perp} \\
&\quad + 2 \sin(\pi\lambda df_{\perp}^2) \int A_0^2 \phi e^{-i2\pi\mathbf{f}_{\perp} \cdot \mathbf{r}_{\perp}} d\mathbf{r}_{\perp}
\end{aligned} \tag{3.19}$$

Where I have omitted noting the x-dependencies, since we have gotten rid of all the shifts in x-dependencies. The two integrals can now be identified as Fourier transforms. For notational simplicity we can introduce $\psi = A_0^2 \phi$ and rewrite the equation above:

$$\tilde{I}_d(\mathbf{f}_{\perp}) = I_d^{\phi=0} + 2 \sin(\pi\lambda df_{\perp}^2) \tilde{\psi} + 2i \cos(\pi\lambda df_{\perp}^2) \lambda d\mathbf{f}_{\perp} \cdot \mathcal{F}[A_0 \phi \nabla A_0] \tag{3.20}$$

The last term can be manipulated into a more compact form by considering:

$$\begin{aligned}
\mathbf{f}_{\perp} \cdot \mathcal{F}[A_0 \phi \nabla A_0] &= \frac{1}{2} \mathbf{f}_{\perp} \cdot \mathcal{F}[\phi \nabla I_0] \\
&= \frac{1}{i4\pi} \mathcal{F}[\nabla \cdot \phi \nabla I_0] \\
&= \frac{1}{i4\pi} \mathcal{F}[\nabla \cdot \psi \nabla \ln(I_0)]
\end{aligned} \tag{3.21}$$

Inserting in equation (3.20) we get:

$$\tilde{I}_d(\mathbf{f}_{\perp}) = I_d^{\phi=0} + 2 \sin(\pi\lambda df_{\perp}^2) \tilde{\psi} + \cos(\pi\lambda df_{\perp}^2) \frac{\lambda d}{2\pi} \mathcal{F}[\nabla \cdot \psi \nabla \ln(I_0)] \tag{3.22}$$

Which gives us a compact description of the intensity some distance downstream as a function of the two distribution I_0 and ψ . I_0 is measured directly at the first detector distance (as close to the sample as possible), leaving only ψ left to be determined. To do this the last term is treated as a perturbation, which allows $\tilde{\psi}$ to be found directly. It is obvious that the prefactor $2 \sin(\pi\lambda df_{\perp}^2)$ (often called the *contrast transfer function*) is zero at some critical frequencies, depending on d. Since we are dividing through with the contrast transfer function when finding $\tilde{\psi}$ near-zero values of the contrast transfer function will make our $\tilde{\psi}$ vulnerable to noise. We can avoid this by introducing several propagation distances with different contrast transfer functions each having different critical frequencies.

3.2.1 The case against phase

I have included this small section as a small protest against what I feel is a sometimes overly enthusiastic view on phase imaging. "Phase" has become quite a buzzword, and everyone seems to want to do "phase contrast imaging". In my opinion phase imaging is overrated, and absorption imaging is generally preferable, though there are of course several cases where phase contrast is useful. I will not make any concrete references in this section because I don't think that would serve any constructive purpose. My goal is merely to point out what I think is a slightly incorrect perspective, that I often observe. I will base

my comments on the holotomographic method, but many of the arguments also hold when considering other phase imaging methods.

More is not always better

The first and most serious notion is the claim that because the δ -part (i.e. the phase part) of the refractive index is typically several orders of magnitude bigger than β , phase imaging offers several orders of magnitude "more contrast". But this is a very elusive contrast if you consider it. There is no inherent rule stating that more projected δ or β is necessarily better. On the contrary, as we saw in section 3.1.3, there exists a certain sweet spot for absorption imaging around which we are most sensitive to variations in projected sample density. A similar thing goes for phase imaging, where phase wrapping can become a problem (phase wrapping means that the phase is shifted an integer number of periods. This shift is then indistinguishable from the case of any other integer number of periods). Phase wrapping presents a problem if there is too much projected δ , which will lead to phase wrapping in the image plane, meaning that even if we could correctly reconstruct the complex electric field at the aperture plane, we still don't know with certainty what absolute phase shift produced that field.

Contrast transfer

Another problem relates to the contrast transfer function $2 \sin(\pi \lambda d f_{\perp}^2)$ of equation (3.22). Not only do we become very dependent on correct d and f (remember that the magnification effect from equation (2.47) means that f is not simply the frequency at the detector screen) for determining the correct contrast transfer function, but the contrast transfer function also has zeropoints that we need to take care of. We also need to consider that the larger the argument of the contrast transfer function gets, the faster the transfer function oscillates, and the more sensitive we get to inaccuracies in its argument. All these issues mean that in order to get reliable phase retrieval, we must keep the argument of the contrast transfer function within quite a narrow interval for it to be useful, which again means that we need several different distances, d , to appropriately cover frequency space (and on a side note, we can never determine the zero order contribution).

d-accuracy and sample thickness

As we noted above, the contrast transfer function dependence requires us to be very careful in determining the correct propagation distance d , if we want to retrieve the phase accurately. This leads to yet another concern; the thin-film-at-aperture assumption. When propagation distance is so critical for correct phase retrieval, assuming all phase shifts happen at exactly the same z-position (the aperture plane) is not necessarily appropriate. But shedding the thin-sample-at-aperture assumption also means the tomographic reconstruction needs to be changed, since this typically assumes knowledge of the z-projected distribution. I.e. the reconstruction algorithm would have to abandon the domain distinction mentioned in section 2.5 and take both terms on the right side of equation (2.30) into account at the same time. Considering all these points it is clear that phase imaging is inherently cumbersome, and since there is not necessarily an advantage from it, absorption should generally be considered the superior method if applicable.

Absorption to the rescue

Absorption on the other hand is in many ways an ideal contrast mechanism; by varying the photon energy it is tunable (so you can usually get transmission rates around the optimal 37 %) and monotonic in its response (i.e. no phase wrapping problems). It is also not directly propagation distance dependent. But, propagation distance can play a role, since we need to place the detector sufficiently close to the sample to avoid phase-induced intensity shifts. This can be difficult, and unwanted phase effects can occur. Thus, I think of phase more as an inconvenient effect that we must take into account out of necessity, rather than some superior imaging modality. Of course there are cases where phase contrast is advantageous over absorption imaging. For instance, if beam damage is a big concern, e.g. in medical imaging, we can turn the photon energy up very high, so that there's hardly any absorption, but the phase shift is on the order of $\approx \pi/2$. We can also imagine cases where the added contrast modality from phase is beneficial, and of course, when samples get very small (and frequencies very high), it can

be hard to get the detector close enough to avoid phase effects. Raster scanning techniques such as ptychography could be said to represent the extreme case of very high resolution, and on this scale, phase effects inherently dominate.

3.3 2D grating interferometer imaging

The grating interferometer technique is designed to measure phase disturbances using pixel sizes much too big to directly detect the intensity shifts associated with the phase disturbances. This is achieved by introducing a set of gratings between the source and the detector. One grating, the phase grating (G1), produces periodic phase shifts in the beam, leading to a well defined interference pattern downstream from the grating. At certain characteristic *fractional Talbot distances*, the periodic intensity shift of the interference pattern across the beam is at its maximum. At one such distance a second grating (G2) is placed. This grating is an absorption grating with a period designed to match the period of the intensity pattern of the beam. By moving the phase grating sideways it can be positioned so that it matches the intensity pattern, allowing either minimal or maximal intensity to pass through it. The detector is put just after the absorption grating. Lets have a look at the interference pattern produced by G1. We will use the paraxial propagator function:

$$E_d = \mathcal{F}^{-1} \left[e^{i2\frac{d(\pi f_x)^2}{k}} E_{G1} \right] \quad (3.23)$$

The grating is only periodic in one direction (let's call it 'x'). In the other direction (y) it is constant. If we assume the incident field on the grating to be constant, then E_{G1} will also be periodic along x and constant along y. This then means that \tilde{E}_{G1} is non-zero only along f_x , effectively making \tilde{E}_{G1} a discrete 1-dimensional function, see Figure 3.1.

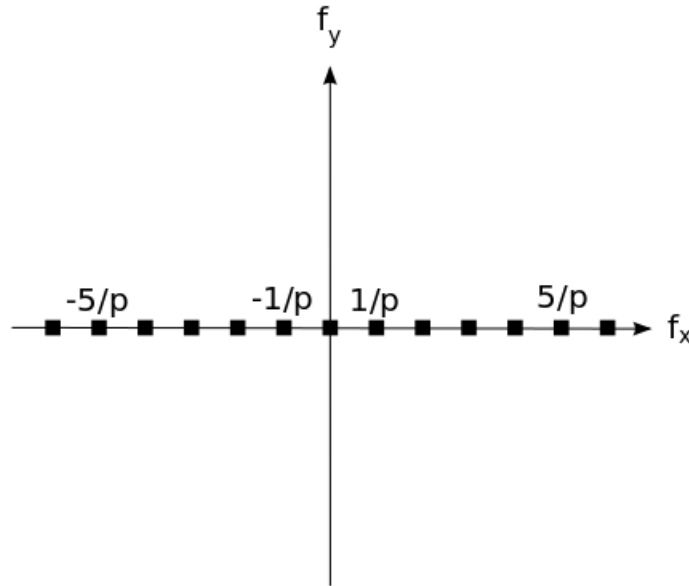


Figure 3.1: *Non-zero components of the Fourier transform of some phase grating G1. If G1 is p-periodic along x and constant along y, it will only have non-zero components at the points marked above. The π -shift 0.5 duty cycle-pattern in Figure 3.2 only has non-zero components at the odd points along f_x above ($\dots, -1/p, 1/p, 3/p, \dots$).*

If we call the period of the phase grating p, all nonzero components of \tilde{E}_{G1} will be at f_x -values being integer multiples of $1/p$. The periodic discreteness of \tilde{E}_{G1} allows us to require the exponent of the paraxial propagator function (equation 2.18) to be some multiple of 2π for all the interesting f_x values at the same time:

$$\begin{aligned}
2 \frac{d_T \pi^2}{k p^2} &= 2\pi \\
d_T &= \frac{p^2 k}{\pi}
\end{aligned}
\tag{3.24}$$

The distance d_T above is called the Talbot distance. At this distance the wave is exactly the same as it was when it had just passed G1. It can easily be seen that all integer multiples of d_T also produce recurring similar wavefronts. Though it is of course an interesting phenomenon, the recurring phase shifted wave front is in itself useless, since we cannot measure phase shifts directly. However, if the shift-pattern produced by G1 is of the correct sort it will also produce periodic intensity-modulated interference patterns at certain *fractional Talbot distances*. One such G1 phase shift pattern is an equal length rectangular function with a relative shift of π , see Figure 3.2. We may call this pattern a π -shift 0.5 duty cycle-pattern.

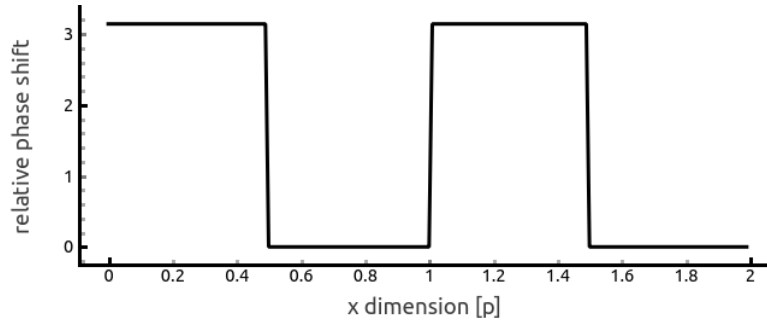


Figure 3.2: *Example of a phase shift introduced by G1. This is a π -shift 0.5 duty cycle-pattern*

If we propagate the π -shift 0.5 duty cycle-pattern from Figure 3.2, the resulting intensity pattern will look as seen in Figure 3.3.



Figure 3.3: *Intensity of the interference pattern produced by the π -shift 0.5 duty cycle-pattern in Figure 3.2. Notice the recurring maximal intensity variations at fractional Talbot distances*

In Figure 3.3, the maximum intensity variations at the fractional Talbot distances are clearly visible. In the transverse direction, the maximum intensity-pattern has a period corresponding to half the G1-period (i.e. it is $p/2$ -periodic). We can see that the pattern occurs eight times between G1 and the first Talbot distance, which leads us to define the odd fractional Talbot distances:

$$d = \frac{m p^2 k}{16\pi} \quad , \quad (m \text{ is odd})
\tag{3.25}$$

If we place an absorption grating G2 at a fractional distance d , and make sure its period matches the interference pattern period, stepping G2 in the transverse direction will result in a triangular intensity function at the detector just behind G2, see Figure 3.4

The triangular intensity transmission function in Figure 3.4 is the result of convolving the two rectangular functions in Figure 3.4. According to the convolution theorem, instead of convolving the two real space functions we can multiply their Fourier transforms. Since the functions are $p/2$ -periodic, their Fourier transforms are discrete with non-zero components only at:

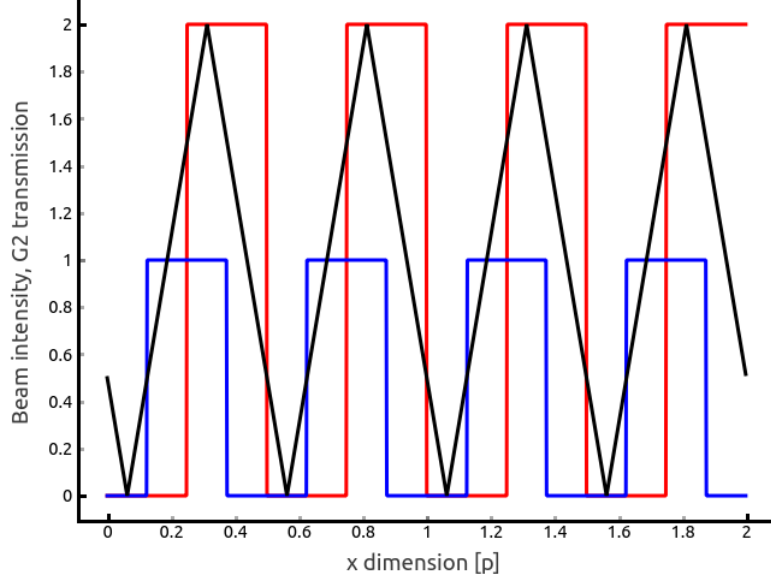


Figure 3.4: *Transverse profiles at some fractional Talbot distance d . Red line: Relative beam intensity before G2. Blue line: Transmission profile of G2. Black line: Total intensity transmission through G2 as it is stepped along x . Note that the beam intensity is $p/2$ -periodic, as is also seen in Figure 3.3*

$$f_n = \frac{2n}{p} \quad (3.26)$$

Where n is an integer. The Fourier transform of a rectangular function is a sinc function:

$$\mathcal{F}[\text{rect}_p](f) = p \text{sinc}(\pi f p) \quad (3.27)$$

Where I have used the definition of the *sinc* function (also called the cardinal sine function) without the factor of π :

$$\text{sinc}(x) = \begin{cases} 1 & \text{if } x = 0 \\ \frac{\sin(x)}{x} & \text{if } x \neq 0 \end{cases} \quad (3.28)$$

The equation in (3.27) is the Fourier transform of a single p -width rectangle centered around zero. For a periodic 0.5 duty cycle rectangular function of period $p/2$ (i.e. with a $p/4$ -width rectangle as in Figure 3.4) and a height of 1, the Fourier Transform becomes:

$$\mathcal{F}[\text{rect}_{p/4}^\infty](f) = \begin{cases} \frac{p}{4} \text{sinc}(\frac{\pi f p}{4}) & \text{if } f = \frac{2n}{p} \\ 0 & \text{else} \end{cases} \quad (3.29)$$

Our rectangle functions differ from the rectangle function above in one way (actually, the intensity function also differs in a second way; scaling. But that is just a matter of a constant factor of 2): The rectangle function above is assumed to be symmetric around zero, which is not the case for the rectangular functions in Figure 3.4. But since this is just a matter of zero-point definition, we will ignore the shift-factors that should otherwise have been applied to the Fourier transform. So, apart from an x -shift, the product of the Fourier transformed rectangular functions in Figure 3.4 is:

$$\begin{aligned} \tilde{I}_{G2}(f_n) &= \frac{2}{p} \tilde{I}_d(f_n) \tilde{T}_{G2}(f_n) \\ &= \frac{p}{4} \text{sinc}^2\left(\frac{\pi f_n p}{4}\right) \end{aligned} \quad (3.30)$$

The factor of $2/p$ in the first line comes from the convolution theorem (because I divide by the interval length ($p/2$ in this case) during the inverse Fourier transform. If I had instead divided during

forward transform, as is used in some definitions, the prefactor should have been inverted (i.e. $p/2$). The squared cardinal sine function above is the Fourier transform of a triangle function, so applying the inverse Fourier transform to $I_{G2}^{\sim}(f)$ we get:

$$\begin{aligned} I_{G2} &= \mathcal{F}^{-1} \left[I_{G2}^{\sim} \right] \\ &= 2\text{tri}_{p/2}^{\infty}(x) \end{aligned} \quad (3.31)$$

Which is the $p/2$ -periodic triangle function in Figure 3.4. In reality, the wavefront intensity just before G2 (red line in Figure 3.4) will not be a perfect step function, simply because of the non-perfect coherence of the incident beam on G1. I.e. the pattern in Figure 3.3 will look increasingly blurred as the beam propagates downstream. Let's assume a Gaussianly distributed source intensity, s , with a width ω_s :

$$s_{source}(x) = \frac{1}{\omega_s \sqrt{2\pi}} e^{-\frac{x^2}{2\omega_s^2}} \quad (3.32)$$

The Gaussianly distributed source intensity will lead to a Gaussianly distributed smearing of the intensity at G2. The width of the Gaussian smearing at G2 will depend on the distance L from the source to G1, and the distance d from G1 to G2:

$$s_d(x) = \frac{1}{\omega \sqrt{2\pi}} e^{-\frac{x^2}{2\omega^2}} \quad , \quad \omega = \frac{\omega_s d}{L} \quad (3.33)$$

We can now find the intensity at the detector as G2 is stepped by convolving the Gaussian distribution in equation (3.33) with the triangular intensity function from the perfectly coherent beam in equation 3.31. Again we will use the convolution theorem and instead of actually performed the convolution, we will multiply the Fourier transforms of the two functions. Remembering that the Fourier transform of a Gaussian function is again a Gaussian we get:

$$\begin{aligned} I_{G2}^{\sim}(f_n) &= I_{G2}^{\sim}(f_n) \tilde{s}_d(f_n) \\ &= \frac{p}{4} \text{sinc}^2\left(\frac{\pi f_n p}{4}\right) e^{-2(\pi \omega f_n)^2} \end{aligned} \quad (3.34)$$

Now, we just need to inversely Fourier transform the function above:

$$\begin{aligned} I_{G2}^s &= \mathcal{F}^{-1} \left[I_{G2}^{\sim} \right] \\ &= \frac{2}{p} \sum_{f_n} I_{G2}^{\sim}(f_n) e^{i2\pi x f_n} \\ &= \frac{1}{2} \sum_{n=-\infty}^{\infty} \text{sinc}^2\left(\frac{\pi n}{2}\right) e^{-8\left(\frac{\pi \omega n}{p}\right)^2} e^{i\frac{4\pi x n}{p}} \end{aligned} \quad (3.35)$$

We can use that the *sinc* function above is only evaluated for arguments that are integer multiples of $\pi/2$. Looking at the definition of *sinc* in equation 3.28 it becomes clear that except for $n=0$, only odd values of n contribute to the sum above. For odd values of n we have:

$$\text{sinc}^2\left(\frac{\pi n}{2}\right) = \frac{4}{(\pi n)^2} \quad \text{if } n \text{ is odd} \quad (3.36)$$

So we can rewrite the sum in equation 3.35:

$$I_{G2}^s = \frac{1}{2} + \frac{1}{2} \sum_{n \text{ odd}} \frac{4}{(\pi n)^2} e^{-8\left(\frac{\pi \omega n}{p}\right)^2} e^{i\frac{4\pi x n}{p}} \quad (3.37)$$

Collecting all $(n,-n)$ -pairs in the sum above we can rewrite the last term as a cosine:

$$\begin{aligned}
I_{G2}^s &= \frac{1}{2} + \frac{1}{2} \sum_{n=1,3,\dots} \frac{4}{(\pi n)^2} e^{-8(\frac{\pi \omega n}{p})^2} 2 \cos(\frac{4\pi x n}{p}) \\
&= \frac{1}{2} + \frac{4}{\pi^2} e^{-8(\frac{\pi \omega}{p})^2} \cos(\frac{4\pi}{p} x) \\
&\quad + \frac{4}{9\pi^2} e^{-71(\frac{\pi \omega}{p})^2} \cos(\frac{36\pi}{p} x) \\
&\quad + \frac{4}{25\pi^2} e^{-200(\frac{\pi \omega}{p})^2} \cos(\frac{100\pi}{p} x) \\
&\quad + \dots
\end{aligned} \tag{3.38}$$

From the equation above it is clear that the transmitted intensity as G2 is stepped can be approximated as a $p/2$ -period cosine function plus the zero-order contribution. Higher order terms decay quite rapidly. For point sources ($\omega = 0$) higher order terms decay as the inverse square of n . For finite source sizes they decay even faster, due to the exponential term.

3.3.1 Grating interferometer modalities

So far, we've assumed the wave function to be unaffected by the sample. We have also assumed the incident wave function on G1 to be perfectly plane and of constant intensity equal to one. We now assume that small deviations in intensity and shifts in phase and coherence occur. We will assume these deviations to be so small that the overall mechanics of the equations remain the same (i.e. this corresponds to assuming that the wave is still approximately plane in any local neighbourhood). Taking such small deviations into account, we will rewrite equation (3.38) to be:

$$I_{G2} \approx C + A \cos\left(\frac{4\pi}{p} x - \phi\right) \tag{3.39}$$

Three parameters have been introduced in the equation above, each of them corresponding to one of the three fundamental *modalities* or *signals* from a grating interferometer; Intensity, C (absorption), amplitude, A (incoherent scattering) and phase, ϕ (differential phase contrast). Putting a sample anywhere in front of G2 will affect each of these three parameters. To distinguish the effect produced by the sample from the signal from the undisturbed beam, a *flatfield phase scan* (i.e. a phase scan with no sample in the beam) is taken. From the flatfield scan, the parameters C_0 , A_0 and ϕ_0 are found. We will now look at how to deduce some of the physical properties of the sample by comparing the parameters from the flatfield scan with those from the sample scan. The absorption of the sample will affect the average intensity, C , in the same way that we saw in section 3.1.1:

$$T = \frac{C}{C_0} = e^{-\int \mu dz} \tag{3.40}$$

Just like the finite source spot size produces a decoherent beam in equation (3.32), any non-uniform microstructure of the sample will have a decoherence effect on the beam. Any decoherence of the beam leads to a reduced relative amplitude (A/C). Since A/C is the parameter directly affected by the decoherence, this ratio has a name, and is often called the *visibility*, which I denote with a V . The decoherence from the sample is often assumed to be represented by a decoherence coefficient ϵ , creating a clear analogy to the absorption coefficient:

$$\begin{aligned}
T_V &= \frac{V}{V_0} = e^{-\int \epsilon dz} \\
&\quad \left(V = \frac{A}{C}\right)
\end{aligned} \tag{3.41}$$

The final parameter to consider is the phase shift ϕ . This parameter represents small angular shifts in the propagation direction of the beam. Such shifts can occur due to phase gradients induced by the sample. For a phase gradient $\frac{\partial\Phi}{\partial x}$ and a wavelength λ , the propagation angle will shift by α :

$$\tan(\alpha) = \frac{\partial\Phi}{\partial x} \frac{\lambda}{2\pi} \left(\Phi = \frac{2\pi}{\lambda} \int \delta dz \right) \quad (3.42)$$

Where δ is the real part of the refractive index's deviation from unity, see equation (2.25). We note that a shift in ϕ of 2π corresponds to a physical shift of one period, $p2$, leading us to this expression for the relation between α and ϕ :

$$\tan(\alpha) = \frac{(\phi - \phi_0)p2}{2\pi d_{a-G2}} \quad (3.43)$$

Where d_{a-G2} is the distance from the sample (or the aperture plane), where Φ is measured, to G2. Let's put together equations (3.42) and (3.43):

$$\phi - \phi_0 = \frac{\partial\Phi}{\partial x} \frac{\lambda d_{a-G2}}{p2} \quad (3.44)$$

Hereby, we have linked all three parameters of the grating interferometer intensity oscillation equation (3.39) to integrals over physical constants in the sample: μ , ϵ and δ . This leads us naturally to the next next section.

3.4 Tomographic reconstruction

In section 3.1.1 we saw that using Lambert-Beer's law in equation (3.2) we can project the μ -distribution of a 3D-object on to a 2D-plane simply by measuring the transmission rate. And in section 3.3 we saw that we can also use x-rays to obtain integrals over other physical properties. But for simplicity I will focus on absorption tomography in the following. If we alternate between rotating the sample a little bit and acquiring 2D projections, we end up with a set of 2D projections from all sides of the sample (note, we only have one rotation axis, so 'from all sides' implicitly means 'from any direction in the plane perpendicular to the rotation axis'). For parallel beams (i.e. plane waves), this set of 2D projections can be shown to contain enough information to *reconstruct* the 3D-distribution of μ in the sample (assuming full and continuous projection angle coverage and noiseless data). The problem of reconstructing μ is an inverse problem, i.e. it is quite straightforward to calculate the expected projections from some distribution of μ , but a bit harder, or at least a bit less intuitive, to perform the inverse operation. It is this inverse problem that we will have a brief look at in this section. The most common type of tomogram reconstruction algorithm is the filtered backprojection algorithm. It comes in several forms, the simplest of which is the plane-wave filtered backprojection algorithm called the inverse Radon transform. All of the more advanced forms build on the inverse Radon transform. In the following I will first go through the inverse Radon transform and afterwards one of the more advanced forms; the so-called FDK-filtered backprojection.

3.4.1 Inverse Radon transform

The central part in the mathematics of the inverse Radon transform is the projection-slice theorem. The theorem works on some 2D distribution $\mu(x, y)$. It relates projection lines of this distribution (because μ is 2D, projections are 1D) to slices through the 2D-Fourier transform of μ . Letting P_ω denote the projection operator at an angle ω , S_ω the slicing operator along a line through origo at angle ω and letting $\mathcal{F}_1, \mathcal{F}_2$ denote 1D and 2D Fourier transforms respectively, the projection-slice theorem says that:

$$\mathcal{F}_1 P_\omega \mu = S_\omega \mathcal{F}_2 \mu \quad (3.45)$$

I will not prove the projection-slice theorem above, but it is quite easily shown that the theorem holds by inserting the appropriate full expressions for the operations involved. Equation (3.45) tells us that from the projection lines of μ , we can obtain corresponding lines in Fourier space. If the density of lines in Fourier space is large enough to cover the highest significant frequencies in μ well, the function is well covered in Fourier space and we can reconstruct a map of μ from the known Fourier coefficients. In practical applications, the reconstruction is usually performed in real space through filtered backprojections of the measured projection lines. A schematic overview of the Fourier space coverage from a set of projection lines is shown in Figure 3.5:

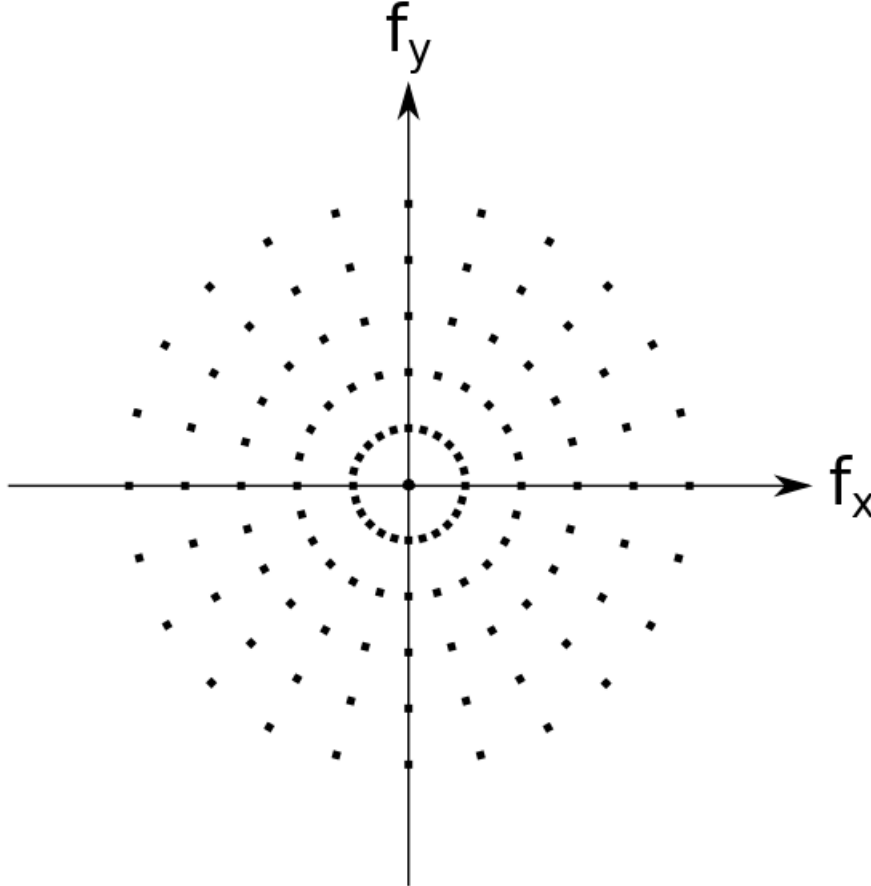


Figure 3.5: Schematic overview of the points in Fourier space that have been found by applying the projection-slice theorem in equation (3.45) to a set of 12 projection lines. Because the projection lines are discrete (they are pixel based) and have finite width, the corresponding Fourier space lines are finite and discrete. And because the angular sampling is discrete (e.g. here we have 12 projection angles) so is the angular coverage in Fourier space. The sampling density is higher for Fourier space points closer to Origo, and Origo itself (i.e. the zero-order component) is probed everytime a projection is performed.

From Figure 3.5 it is obvious that the density of points is inversely proportional to the radial distance from Origo. To avoid over-weighting low frequency components we must therefore apply a Fourier space weighting before we backproject each line. In the continuous case this Fourier space weighting is simply a ramp-filter, g , so the reconstruction becomes the integral shown in equation (3.46):

$$\begin{aligned} \mu &= \int_0^{2\pi} (g \otimes P_\omega) (y \cos \omega - x \sin \omega) d\omega \\ g(x) &= \frac{1}{2} \int_{-\infty}^{\infty} |f| e^{i2\pi f x} df \end{aligned} \quad (3.46)$$

Real measurements are of course discrete and finite, so in reality the integrals above will be sums.

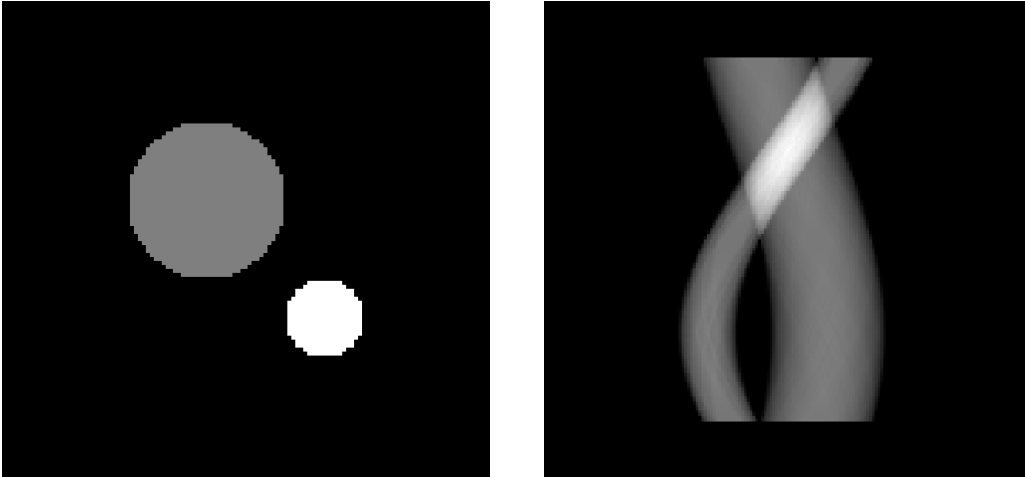
Changing the integral signs to sums in the backprojection integral (the top-most of the two integrals above) is quite trivial, but the discreteness of our sampling also has a non-trivial effect on the filter function g (the bottom-most integral above), which must be redined. The discrete real space sampling means that we will have a frequency cut-off. For a pixel width of Δx the real space version of the filter becomes [32]:

$$\begin{aligned} g_{\Delta x}(x) &= \frac{1}{2} \int_{-\frac{1}{2\Delta x}}^{\frac{1}{2\Delta x}} |f| e^{i2\pi fx} df \\ &= \frac{1}{2(\Delta x)^2} \text{sinc} \left(\frac{2x}{2\Delta x} \right) - \frac{1}{4(\Delta x)^2} \text{sinc}^2 \left(\frac{x}{2\Delta x} \right) \end{aligned} \quad (3.47)$$

The expression above may look a bit overwhelming. But if we utilize the discrete sampling along x , we can make a nice expression for the n 'th pixel:

$$g_{\Delta x}(n\Delta x) = \begin{cases} \frac{1}{4(\Delta x)^2} & \text{if } n = 0 \\ 0 & \text{if } n \text{ is even} \\ -\frac{1}{(n\pi\Delta x)^2} & \text{if } n \text{ is odd} \end{cases} \quad (3.48)$$

In practical applications, the filter function is defined in real space as described above and then Fourier transformed and applied to the projection line in Fourier space. Having found the necessary expressions for performing filtered backprojection reconstructions, let's look at an example. In Figure 3.6 we have projected a phantom at 128 different angles, giving rise to the sinogram in Figure 3.6b.



(a) Phantom 2D slice.

(b) Sinogram of the phantom.

Figure 3.6: The phantom slice is 101×101 pixels. The rotation axis is assumed to go through the center. Black corresponds to $\mu = 0$, gray corresponds to $\mu = 1 \text{ pixel}^{-1}$, and white to $\mu = 2 \text{ pixel}^{-1}$. The small circle has a radius of 10, and the big has a radius of 20. The sinogram covers 180 degrees in 128 projection. Note how the two circles in the phantom slice give rise to each a sinusoidal shape in the sinogram and that the two sine curves are in counter-phase, since the circles are positioned opposite to each other relative to the rotation axis in phantom slice. Also note how the small circle gives rise to a curve of half the width of the big circle, but that the gray levels in the two curves are the same since the small circle has twice the μ -value of the big circle.

To reconstruct the phantom slice in Figure 3.6a, we just need to filter all the projection lines in the sinogram using the ramp filter in equation (3.48). The effect of the ramp filter is illustrated in Figure 3.7.

Having performed the filtering, it is time to backproject the results. In Figure 3.8 we look at the result of using different numbers of backprojection angles.

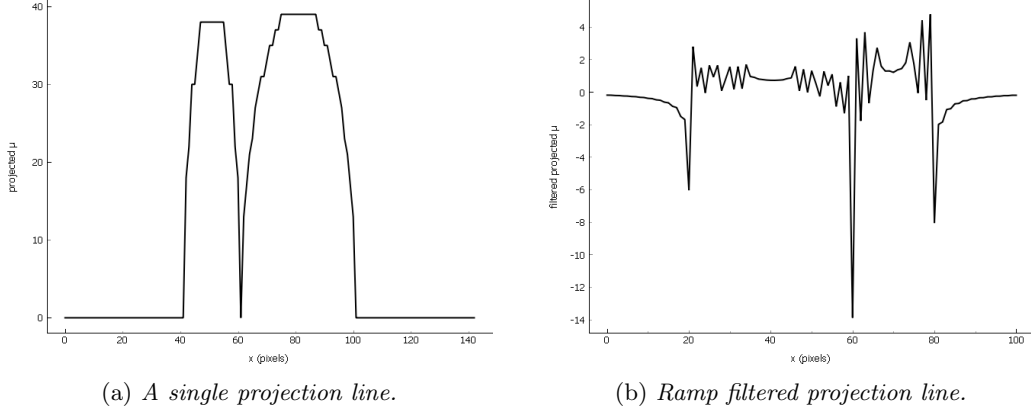


Figure 3.7: The projection line is the last line of the sinogram in Figure 3.6b. At this projection angle, the two circle contours just meet. Note how the contour widths and projected μ -values correspond with the radii and μ -values mentioned in the text of Figure 3.6. That the ramp filter acts as a high-pass filter can be illustrated by the many small oscillations in Figure 3.7b.

3.4.2 Differential phase contrast reconstruction

The filtered backprojection algorithm in section 3.4.1 assumed that we knew the projections of the parameter we're reconstructing (μ in the case of an absorption tomogram). But as we saw in section 3.3.1, in the case of grating interferometer imaging, we don't retrieve the projection of the phase-part of the refractive index δ directly. Instead we get the differential (with respect to x) of the projection (along z) of δ . So, since the phase contrast signal from grating interferometer projections is a *differential* signal, we should integrate it somewhere along the reconstruction process. One possibility would of course be to integrate directly in the differential phase contrast projections, but another approach is usually taken: Since we are already Fourier transforming the signal in order to apply the ramp-filter during the reconstruction process we might as well perform the integration in Fourier space where it corresponds to a simple multiplication:

$$\mathcal{F}[\Phi] = \frac{1}{i2\pi f_x} \mathcal{F}\left[\frac{d\Phi}{dx}\right] \quad (3.49)$$

I have included the x -index on f_x to underline that it is just the x -component of the Fourier space vector that we are considering, since this is the axis along which the grating is stepped. Introducing the phase integration in the filtered backprojection of equation (3.46), we get the following expression for reconstructing δ from differential phase contrast data:

$$\begin{aligned} \delta &= \frac{\lambda}{2\pi} \int_0^{2\pi} (g \otimes P_\omega[\Phi]) (y \cos \omega - x \sin \omega) d\omega \\ &= \frac{\lambda}{2\pi} \int_0^{2\pi} \left(g \otimes h_x \otimes P_\omega\left[\frac{\partial\Phi}{\partial x}\right] \right) (y \cos \omega - x \sin \omega) d\omega \\ g &= \frac{1}{2} \int_{-\infty}^{\infty} |f| e^{i2\pi f x} df \\ h_x &= \int_{-\infty}^{\infty} \frac{1}{i2\pi f} df \end{aligned} \quad (3.50)$$

The double convolution operation in equation (3.50) suggests that we should combine g and h_x to give a single *differential phase contrast backprojection filter*, that we will call g_x :

$$\begin{aligned} g_x &= g \otimes h_x \\ &= \int_{-\infty}^{\infty} \frac{e^{i2\pi f x}}{i2\pi} df \end{aligned} \quad (3.51)$$

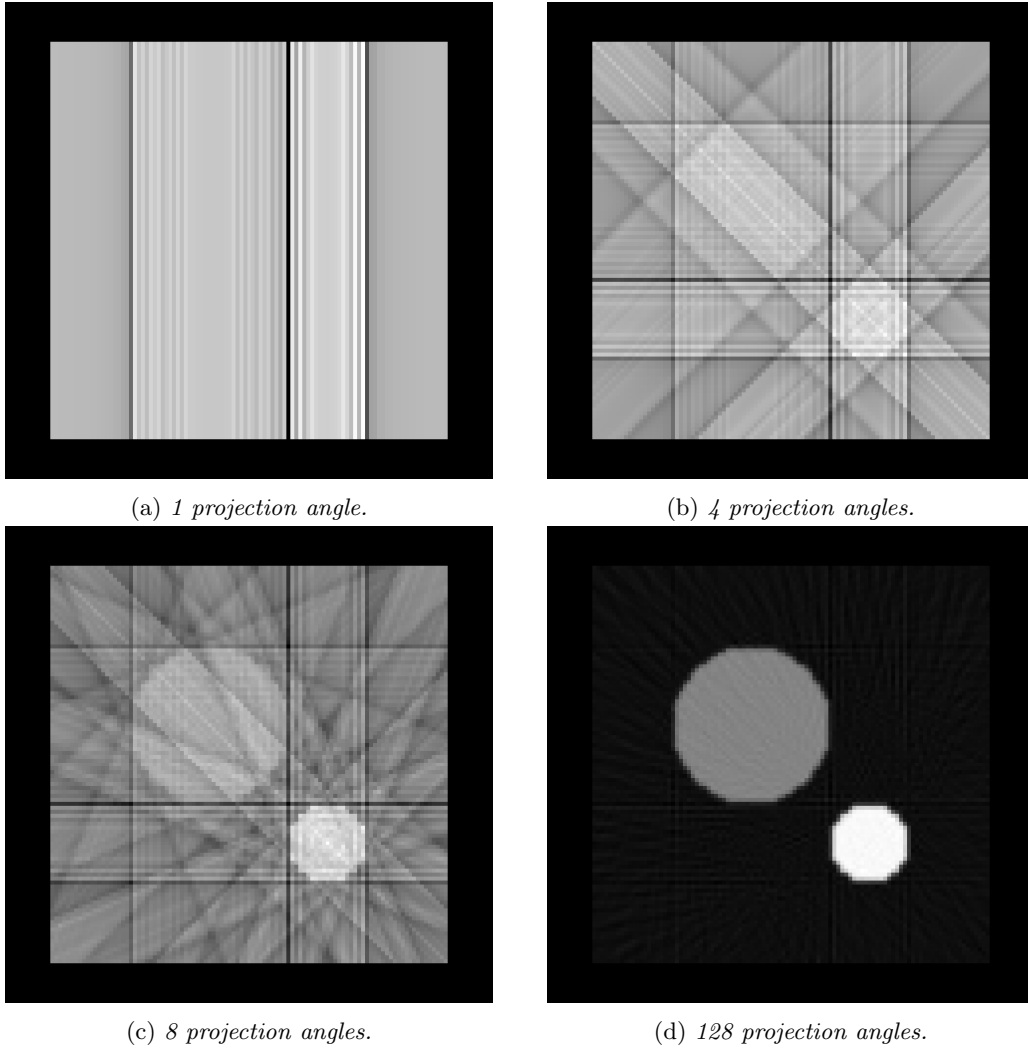


Figure 3.8: Ramp filtered backprojections of the sinogram in Figure 3.6b. Except from being flipped left-right, the single-angle backprojection is just the projection line in Figure 3.7b smeared out along the backprojection direction. Compare the 128-angle backprojection in Figure 3.8d to the original phantom in Figure 3.6a.

We see that the two Fourier distance components, f in g and h_x cancel out. Now we have a single backprojection filter, and from here everything proceeds just like in the case of absorption contrast tomography. The easiest way to handle the integration operator is to construct g (the normal absorption backprojection filter) in real space as described in equation (3.48), then Fourier transform it and multiply with the x-integration operator in Fourier space. This means that the end result for our differential phase contrast filtered backprojection becomes:

$$\delta = \frac{\lambda}{2\pi} \int_0^{2\pi} \mathcal{F}^{-1} \left[\tilde{g}_x P_\omega \tilde{[\Phi]} \right] (y \cos \omega - x \sin \omega) d\omega \quad (3.52)$$

$$\tilde{g}_x = \mathcal{F} [g_{\Delta x}] \frac{1}{i2\pi f_x}$$

And this equation gives us a method for reconstructing δ from grating interferometer projection data.

3.4.3 Cone beam reconstruction

In the previous sections we looked at parallel beam projections and how to reconstruct tomograms from such projections. But in reality, experimental setups produce perfectly parallel x-ray beams. Syn-

chrotrons come quite close; due to their large source-detector distances and small detector sizes, the beam cone angles at synchrotrons are typically very small, and it is appropriate to treat these measurements as parallel beam measurements in the reconstruction (a bit more care should be taken when considering propagation distances in phase retrieval, as seen from section 2.6 and 3.2.1. But we will just assume a pure absorption contrast measurement, since this is by far the most common modality, especially in lab source setups, which is where cone beam angles are large enough that they should be taken into account. There is no mathematically exact algorithm to reconstructing tomograms from cone beam measurements (assuming a so-called circular scanning geometry, i.e. the sample is rotated around the z-axis, as is the common case in laboratory micrCT systems). But an algorithm that comes close if the cone beam angle is not too big is the FDK-algorithm. Arguably, this algorithm comes *as close as possible* to a mathematically exact reconstruction, since in the limit of zero cone z-angle it converges to the mathematically exact (fan-beam) back projection algorithm. The FDK-algorithm can be seen as a generalisation of the inverse Radon transform in equation (3.46). The only difference consists of the multiplication the cone-angular pre-weighting factor w and a flux-density post-weighting factor U :

$$\begin{aligned} \mu &= \int_0^{2\pi} U^2 (g_\infty \otimes (wP_\omega)) (y \cos \omega - x \sin \omega) d\omega \\ w &= \frac{R}{\sqrt{R^2 + a^2 + b^2}} \\ U &= \frac{R}{(R + y \sin \omega + x \cos \omega)} \end{aligned} \tag{3.53}$$

It can be shown that except from possible intensity shifts in the z-direction, the FDK-algorithm is mathematically exact, i.e. the integral along z of the reconstructed tomogram will be correct, except for measurement uncertainties, of course. In the case of a cone beam differential phase contrast reconstruction, the Fourier space integration multiplication in equation (3.49) is incorporated in the convolution in above integral.

Chapter 4

Image formation algorithms

This chapter is concerned with two algorithms applied to grating interferometer data. Unlike the previous chapters, this chapter presents my original work. The data presented in section 4.1 were acquired at our in-house grating interferometer setup at the Niels Bohr Institute. This was the same setup used in the experiments described in publication A.2. The measurements that produced the data used in section 4.2 were performed at a lab-source grating interferometer at Technical University of München. This setup was also where we acquired the data for publication A.1. The two algorithms in this chapter are examples of attempts to optimize the quality of the images produced by the grating interferometer without changing the physical setup. Loosely speaking, this chapter can be said to represent my suggestions for improvements of the existing proposed solution to the optimization problem that could be framed: *given a set of detector readouts from a grating interferometer setup, how do we produce the images of highest possible quality?* One algorithm attempts to increase the image quality by improving the way the sinusoidal intensity oscillation is described. The other algorithm proposes a new tomographic reconstruction technique that takes the anisotropic nature of the dark-field signal into account without imposing extra complexity on the experimental setup.

4.1 Reducing the effects of instabilities in x-ray grating interferometers

The algorithm that is the subject of this section is the product of my attempts to solve a practical problem originating from the observed mechanical instability of our setup (see Figure 4.1). So, interestingly, this could be said to be a case of inferior equipment leading to a new methodological development. The algorithm improves image quality in 2- and 3-dimensional x-ray grating interferometer based images. I have substituted the normally used Fourier transform of the grating stepping images with an iterative 4-parameter sine fit. The sine fit model provides a better representation of the photon counts measured in the detector than the sinusoidal curve represented by the Fourier transform (The Fourier transform is just a linear transformation and not necessarily a good best fit estimator for a single sine curve). In a series of 2D test images, the photon counts modelled with the fitting method yielded a 53% lower deviation from the measurement. When comparing tomographic reconstructions produced by the two methods, the fitting method reduced the noise in the reconstructed phase image by up to 10%. However, the computation time of the fitting method is approximately 30 times longer than that of the Fourier based method.

4.1.1 Algorithm

Let's have a look at the intensity oscillation described in equation (3.39). This equation tells us that we should expect a sinusoidal behaviour of the beam intensity I , as we step one of the gratings (it could be any of the three gratings, but here we'll just assume that we are stepping G2). Let's perform a number of equidistant phase steps. In this case, the image intensity in the n 'th grating position can be described as:

$$\begin{aligned}
I_{G2}(n) &\approx C + A \cos\left(\frac{4\pi}{p}\Delta x \cdot n - \phi\right) \\
&= C + A \cos(\omega_{\Delta} \cdot n - \phi)
\end{aligned}
\tag{4.1}$$

Where Δx is the step length. Note that by building on equation (3.39), we have assumed that this is a parallel beam setup. If we want to adapt to a cone beam case, the G1 period (p) in equation (4.1) should be magnified by $(d+L)/L$, where d is the distance from G1 to G2 and L is the distance from source to G1. In the latter part of equation (4.1) we have introduced the phase step length ω_{Δ} . In real-world experiments, it can often be very difficult to control the step length Δx , meaning that we need to fit it (along with A , C and ϕ) in our algorithm. For this purpose, the last part of equation (4.1) is the most convenient form. In the Fourier transform method, the steps in a phase scan are usually assumed to cover an integer number of grating periods (typically one period), and the step length is assumed known and constant throughout the entire scan, which could last for hours in the case of a tomography scan. In this case, the oscillation in photon counts can be described by just two (complex) Fourier coefficients, or, alternatively, by the three real numbers (A , C and ϕ). But keeping ω_{Δ} constant throughout a whole tomography scan, which may last for hours, can be hard in an experimental setup due to mechanical instabilities and variations in temperature (see Figure 4.1).

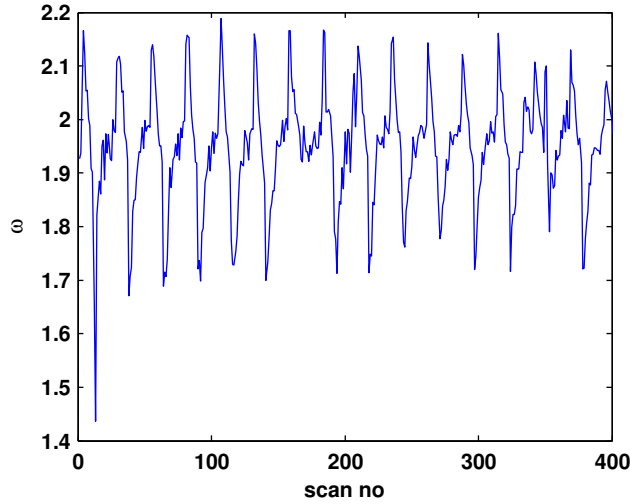


Figure 4.1: Plot of the phase step length ω_{Δ} from equation (4.1) as a function of phase scan number during a tomogram measurement. The first axis gives the phase scan number (i.e. it is an approximate measure of time - each scan is approximately two minutes). The second axis gives the phase step length for the oscillations of the photon counts in the detector. Each scan consisted of four grating steps. The ω plotted here is the result of the fitting routine described later in this article. The median phase step length is 1.96, corresponding to an oscillation period of 3.21. As seen, the oscillation frequency is far from stable over time. The variations have a general periodic structure, which was later determined to match the periodicity with which the thermostatically controlled air condition in the laboratory was turned on.

To account for an unknown, and possibly time-varying, phase step length, I propose to replace the Fourier transform by a fitting method taking the variations in ω_{Δ} over time into account. The parameter ω_{Δ} is not used directly in the image construction, but it is used as a helping parameter in the fitting routine, improving the estimates of the three relevant parameters A , C and ϕ . The routine fits all three parameters A , C and ϕ for each pixel, and furthermore fits one global ω_{Δ} (i.e. the fitting model forces all pixel oscillation frequencies in a given phase scan to be identical, so the model only introduces a single extra degree of freedom in a system which typically has on the order of 100.000 degrees of freedom - each pixel has three degrees of freedom coming from A , C and ϕ). The fitted phase step lengths are shown in Figure 4.1.

The fitting method

The sine fitting algorithm is an extension of the fitting method described in [13]. It builds on a linearization of a rewritten form of equation (4.1). We extend the algorithm outlined in [13] by imposing the requirement of constant ω_Δ across the entire detector screen. Each phase scan is treated independently. First, we rewrite equation (4.1) to make it a product of two real sinusoidal functions:

$$\begin{aligned} I_{G2}(n) &= a \cos(\omega_\Delta \cdot n) + b \sin(\omega_\Delta \cdot n) + C \\ a &= A \sin(\phi) \\ b &= A \cos(\phi) \end{aligned} \quad (4.2)$$

Keeping equation (4.2) in mind, we introduce the matrix D :

$$D = \begin{bmatrix} \cos(\omega_\Delta) & \sin(\omega_\Delta) & 1 \\ \cos(2\omega_\Delta) & \sin(2\omega_\Delta) & 1 \\ \dots & \dots & \dots \\ \cos(N\omega_\Delta) & \sin(N\omega_\Delta) & 1 \end{bmatrix} \quad (4.3)$$

Using D , we can express the beam intensity by $I_{model} = D \cdot v$, where $v = (a, b, C)$ is the parameter vector. If ω_{Delta} is known, the the least squares solution to a set of measured intensities can be found (for $N \geq 3$) by solving the matrix equation $I \approx D \cdot v$:

$$v = (D^T D)^{-1} D^T I_{measured} \quad (4.4)$$

Equation (4.4) gives the best fit of v for a known phase step length. If we want to take the variable ω_Δ into account, equation (4.2) is no longer linear in all parameters, and the least squares minimization problem can no longer be solved analytically (for over-determined systems). Instead of trying to solve equation (4.2) for unknown phase step lengths directly, we expand equation it to first order with respect to ω_Δ :

$$I_{G2}(n) = a \cos(\omega_{\Delta,j} n) + b \sin(\omega_{\Delta,j} n) + C + \Delta\omega_\Delta (-an \sin(\omega_{\Delta,j} n) + bn \cos(\omega_{\Delta,j} n)) \quad (4.5)$$

With the expanded expression above, we can define the corresponding matrix D_j :

$$D_j = \begin{bmatrix} \cos(\omega_{\Delta,j}) & \sin(\omega_{\Delta,j}) & 1 & -a_{j-1} \sin(\omega_{\Delta,j}) + b_{j-1} \cos(\omega_{\Delta,j}) \\ \cos(2\omega_{\Delta,j}) & \sin(2\omega_{\Delta,j}) & 1 & -2a_{j-1} \sin(2\omega_{\Delta,j}) + 2b_{j-1} \cos(2\omega_{\Delta,j}) \\ \dots & \dots & \dots & \dots \\ \cos(N\omega_{\Delta,j}) & \sin(N\omega_{\Delta,j}) & 1 & -Na_{j-1} \sin(N\omega_{\Delta,j}) + Nb_{j-1} \cos(N\omega_{\Delta,j}) \end{bmatrix} \quad (4.6)$$

The system $I_{model,j} = D_j \cdot v_j$ is linear in the four parameters $v_j = (a, b, C, \Delta\omega_\Delta)$, and like previously, we can solve the minimization the squared deviation from some measured set of intensities by:

$$v_j = (D_j^T D_j)^{-1} D_j^T I_{measured} \quad (4.7)$$

v_j above solves equation (4.5). But we still need to estimate the values $\omega_{\Delta,j}$, a_{j-1} and b_{j-1} to construct D_j . As hinted by the indexing, this is done in an iterative manner. The process of finding (a, b, C, ϕ) can be described by the following schematic:

Algorithm 1 Interferometer intensity sine fit algorithm

- 1: Set initial phase step length guess $\omega_{\Delta,0}$
 - 2: Find initial (a, b, C) estimate using equation (4.4)
 - 3: Set $\Delta\omega_\Delta = 0$ for all pixels
 - 4: Check convergence criteria
 - 5: **while** Convergence criteria not met **do**
 - 6: $j=j+1$
 - 7: Set $\omega_{\Delta,j} = \omega_{\Delta,j-1} + \text{median}(\Delta\omega_{\Delta,j-1})$
 - 8: Set D_j from equation 4.6 using the estimates $\omega_{\Delta,j}$, a_{j-1} and b_{j-1}
 - 9: From equation (4.7), estimate v_j
 - 10: Check convergence criteria
-

For my analysis, the convergence criterion is met if the 49th percentile of the $\Delta\omega_{\Delta,j}$ -values are negative and the 51st percentile of the $\Delta\omega_{\Delta,j}$ -values are positive (i.e. for the latest ω_{Δ} at least 49 percent of the pixels returned negative $\Delta\omega_{\Delta}$ -values and at least 49 percent of the pixels returned positive $\Delta\omega_{\Delta}$ -values). The algorithm converges quite fast (usually around 4 iterations is enough). Sometimes it can get stuck in an infinite loop of shifting over- and underestimating ω_{Δ} . This can be helped by introducing a relaxation parameter in the estimation of ω_{Δ} (line 7 of the algorithm) after a set number of iterations.

4.1.2 Method test

As a test sample we used a polypropylene (PP) cylinder (see Figure 4.2). The sample was chosen because the geometry is simple, and the material is stable and uniform. The polypropylene in our sample has an electron density of 0.514 mol/cm³.



Figure 4.2: *The polypropylene (PP) cylinder used as sample in the sine fit algorithm test experiment.*

The experiments were carried out at the x-ray tomography lab at the Niels Bohr Institute. The Rigaku rotating anode tube had a copper target and was set at an acceleration voltage of 40 kV and a filament current of 150 mA. Due to a downward angle of the setup of 6 degrees the source of size 1 mm x 10 mm had a reduced footprint giving an effective source size of 1 mm x 1 mm. The interferometer used a π -phase grating with a duty cycle of 0.5 and a period of 3.5 μm for G1. The G0 and G2 gratings had periods of 14.1 m and 2.0 m. In the setup the G0-to-G1 distance was 139 cm. The G1-to-G2 distance was 20 cm, which matched the fifth fractional Talbot distance. The phase grating was optimized for 28 keV (i.e. this is the photon energy at which the Talbot pattern produced by G1 has interference maximum exactly at the position of G2). 28 keV is approximately the peak flux photon energy at 40 kV acceleration voltage. The images were recorded with a 300 μm Dectris Pilatus 100k detector with 195x487 pixels. An example of a raw detector readout is seen in Figure 4.3.

401 phase scans were recorded: First 20 reference phase scans with no sample (for flat field correction) were recorded, then 361 phase scans with the sample covering 360 degrees of rotation, and finally another 20 reference phase scans with no sample. Each phase scan consisted of four grating steps. Each exposure lasted 10 seconds. For each of the 401 phase scans (40 flatfields and 361 rotational scans), both the iterative fitting method and the Fourier transform method were applied, see Figure 4.4. The transmission, dark field and phase contrast images were constructed for the 361 sample phase scans using the 40 flatfield phase scans as reference.

Differential phase contrast images from the two methods are compared in Figure 4.5. The images in Figure 4.5 are from the 95th phase scan, which, according to the ITER algorithm, had $\omega_{\Delta} = 1.883$ corresponding to a period of 3.34 grating steps. The Fourier transform method requires an integer oscillation, so an assumed period of 3 steps was used. Note how the Fourier image has some more or less periodic noise that might come from the Moiré shifts. Also note how this noise is reduced in the sine fit image.

From the differential phase contrast projections phase tomograms were reconstructed for both methods. As the sample was homogeneous, all the tomogram voxels in the sample should have the same electron density, and thereby the same value in the phase tomogram. The values of the plastic voxels

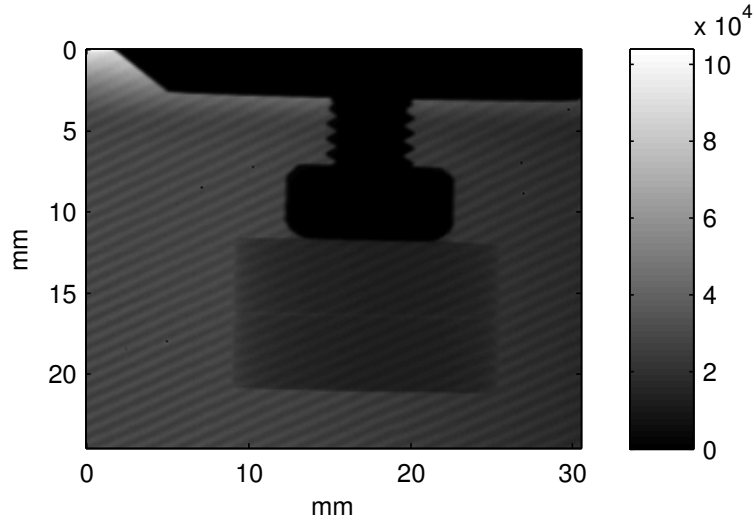


Figure 4.3: Photon count in one of the sample exposures. The exposure time was 10 seconds. The completely black area in the top center of the image is the steel sample holder, which has almost no x-ray penetration. The plastic sample is the two rectangular areas that are slightly darker than the surrounding pixels. Note the nice Moiré fringe pattern across the whole detector screen stemming from the slight misalignment of the gratings relative to each other.

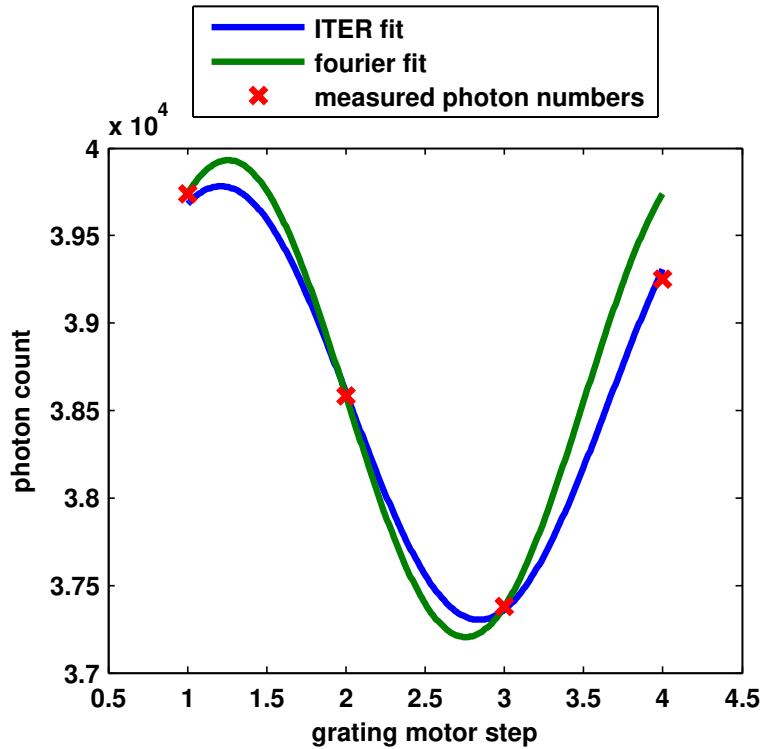


Figure 4.4: Intensity oscillation in a single pixel. The results for the traditional Fourier transform method and the proposed fitting method are plotted with solid lines. The first axis is the step number, n , and the second axis is the photon count number. Standard deviations for the four pixel counts for the fitted curve and the Fourier curve were 42 and 246 photons respectively.

in the phase tomograms were normalised to the expected electron density for the polypropylene in our sample ($\rho_e = 0.514N_A/cm^3$, where N_A is Avogadro's number)). To compare the two tomograms, a

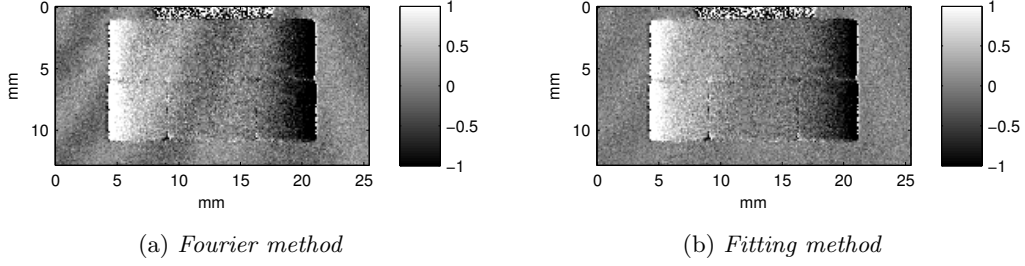


Figure 4.5: Comparison of differential phase contrast projections of the sample in Figure 4.2. The projection are constructed based on the same phase scan data, the only difference lies in the analysis, which is done using a traditional fast Fourier transform algorithm for one image and using the previously sketched iterative sine fitting algorithm for the other.

histogram of voxel values within the upper half of the plastic sample is shown in Figure 4.6.

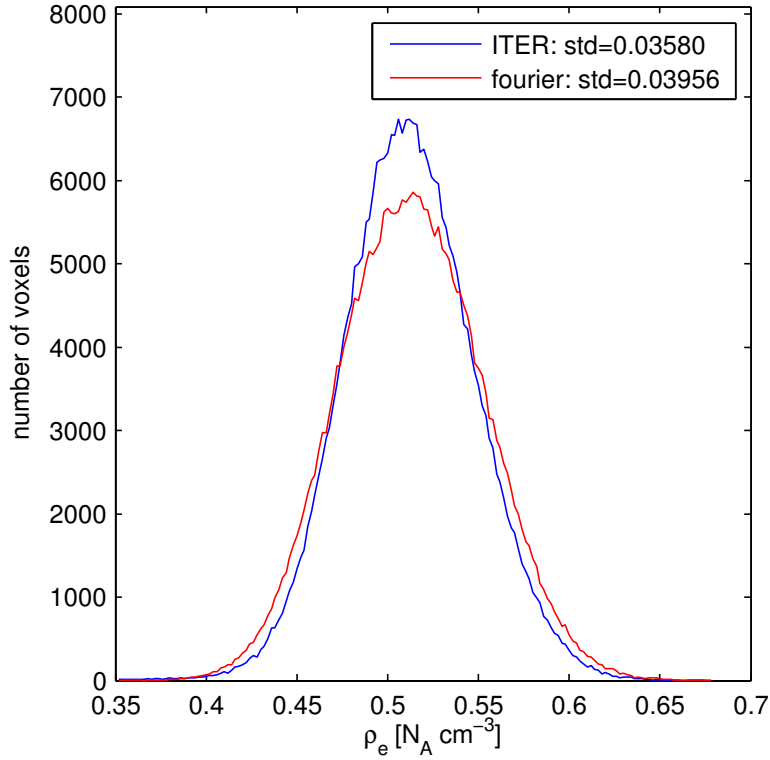


Figure 4.6: Histogram of the voxel values in the sample. The first axis is the electron density in units of NA/cm^3 The two methods were normalised to give the same mean voxel values ($0.514 NA/cm^3$). The tomogram from fitting method had a lower standard deviation in the voxel values ($0.0358 NA/cm^3$ compared to $0.0396 NA/cm^3$ for the Fourier method).

Table 4.1 gives the computation times and two measures of the accuracy of the two analysis methods. The models' deviations from the photon counts (I) measure how close the sinusoidal curves corresponding to the analysis method comes to the actual photon counts (see Figure 4.4). The standard deviations of the sample voxels indicates how uniformly dispersed the voxels values of the sample voxels were in the reconstructed phase tomograms. Computation times are also included to show that the improved performance of the fitting method comes at the price of an increased computation time. The analysis was performed on a 2GHz laptop using a MATLAB script. Analysis time could be optimized both soft- and hardwarewise, however that is not the scope of this article. The purpose is just to give an idea of the

method	Analysis time	from I	of sample voxels
FFT	59 s	215 photons	0.0358
ITER	1743 s	100 photons	0.0396

Table 4.1: *Key numbers for the two algorithms. The analysis time gives the time it took to perform the construction of modality projections for all 401 phase scans. Thus, this number does not include the time for reconstructing the tomogram, which is the same for both methods. The standard deviation of the photon counts for all exposures in the 401 phase scans is given, and so is the standard deviation of the voxel values in the sample. The analysis was performed on a 2GHz laptop and using a MATLAB script. Analysis time could probably be optimized both soft- and hardwarewise, however that is not the scope of this article. The purpose is just to give an idea of the differences in computation time.*

differences in computation time. The fitting method is clearly superior to the FFT-method in creating smaller standard deviations, but also more costly in computation time. But since the acquisition time is typically much longer than the 30 minutes calculation time in the fitting method, this will usually not be a problem.

4.1.3 Conclusion and outlook

Using an iterative sine fitting we were able to reduce the noise in a reconstructed tomogram from a grating based interferometry setup but increasing the computation time relative to the traditional Fourier transform method by a factor of 5. The fitting method allows us to take varying and non-integer stepping periods into account. These variations can occur as a result of temperature variations and mechanical instabilities. This could lead to lower stability requirements and reduce the need for time consuming alignments, and thereby allow installation in less controlled and stable environments than the typical x-ray lab, for instance in a production line for non-destructive testing. The iterative fitting method presented in this article might help introducing the x-ray grating interferometer to a wider commercial use than seen today, where commercial systems are available, but only in the form of closed-cabinet scanners. Production line applications have not yet been realized, but the analysis method described in this article might be a step in that direction. It is worth noting that the method could also be relevant for synchrotron measurements with non-integer stepping periods.

4.2 Regularized iterative reconstruction of an angularly dependent x-ray dark-field tomogram

In this section I present a tomographic reconstruction method, which takes into account the anisotropic nature of the decoherence measure known as the grating interferometer dark-field signal. I demonstrate that the method is superior to the traditional FDK-reconstruction method [9] in describing the measured data. Unlike the tensor field reconstruction method [17, 33], this method requires only one sample rotation axis, thus the setup and the acquired measured dataset are just the same as used for the absorption and phase tomogram reconstruction methods, keeping measurement times lower than what would be needed for reconstructing the full tensor field distribution. The simplicity of the experimental setup relative to the tensor field method comes at the cost of reduced sample information; the method only maps scattering as a function of orientation within the rotation plane of the sample, instead of the full spherical angular dependency mapped by the tensor field method. A method to describe the anisotropic dark-field signal produced by a sample in a classical single-rotation-axis setup has been proposed before [3]. However, this method only includes zeroth and first-order components, which I show is insufficient to describe the measured data. In this method, I include higher order frequency-components, which in turn makes the reconstruction problem severely underdetermined. I counter the underdetermination of the problem by enforcing regularizations and restrictions on the tomogram.

4.2.1 Introduction

The grating interferometer dark-field signal has been shown to be able to detect sub-pixel sized non-uniformities [24, 36, 16]. The magnitude of the dark-field signal is dependent on variations in the projected refractive index [38]. As a given non-uniform feature is projected at different angles, the fluctuations in the projected refractive index will vary [2], and hence the dark-field signal will be dependent on the projection angle. So far the problem of reconstructing the angularly varying tomogram has been solved by taking one of two approaches; either ignoring the angular dependency, which is a feasible assumption for some samples (By choosing an appropriate rotation axis, the error introduced by this assumption may be minimized [15]), or increasing the volume of the angular space covered by the measurement by introducing more angular dimensions in the form of rotation axes to the scanning procedure [17]. We propose a different approach, retaining the simplicity of the experimental setup from the first approach, while giving some information about the angular dependence as in the second approach. The problem of solving the angularly dependency in this case becomes heavily underdetermined, and hence relies on heavy regularizations to provide useful results.

The paper is organized as follows. Our measurement setup and test sample are described in sections 4.2.2 and 4.2.3. The tomogram model and the algorithm used to construct it is described in section 4.2.4. In section 4.2.8, the tomograms constructed using the algorithm are evaluated.

4.2.2 Experimental setup

The measurement setup is a standard lab-based x-ray grating interferometer tomography setup at Technische Universität München, E17, Lehrstuhl für Medizinische Physik [22, 4, 34, 23] with a single sample rotation axis. The source was a rotating Mo-anode run at 40 kV and 70 mA. The design energy of the gratings was 23 keV. Three gratings are used in order to produce the dark-field and differential phase-contrast signals. In order of appearance for the propagating photon, the gratings are: G0, or the source grating, is an Au-based absorption grating placed close to the x-ray source, in order to increase beam coherence. G1, or the phase grating, is a Ni-grating introducing a periodic pattern of relative phase shifts of π . G2, or the detector grating, is an Au-based absorption grating just in front of the detector. All three gratings had a grating pattern period of $5.4\mu\text{m}$. The detector was a photon-counting Pilatus II (Dectris, Switzerland) with a pixel size of $172 \times 172 \mu\text{m}^2$ and a resolution of 487×195 (horizontal x vertical).

To produce a tomogram, the sample was imaged at 801 equidistantly spaced rotation angles (θ_{rot} , see Fig. 4.7) covering 2π . At each angle a phase scan is made by stepping G1 in the horizontal direction transverse to the beam propagation direction. Each phase scan consisted of detector readouts at 12 equidistantly placed G1 positions covering one grating period. Stepping the phase grating in this direction shifts the interference pattern produced by G1 correspondingly. The shifted interference pattern

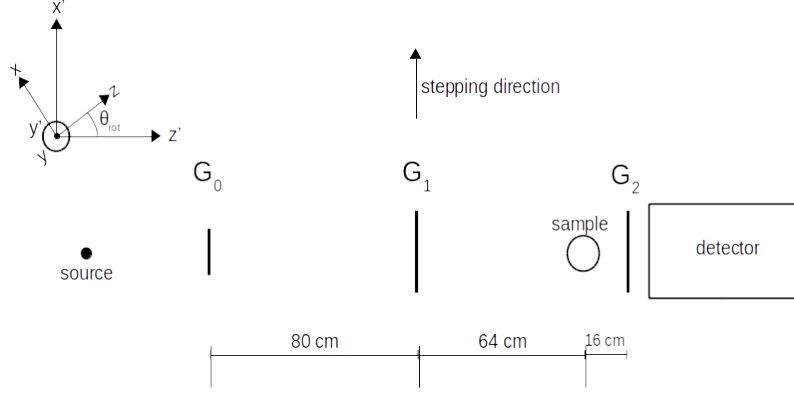


Figure 4.7: Sketch of the x-ray grating interferometer setup. Three gratings are used: The source grating (G0) is placed close to the source. It functions to decrease the effective source size. The phase grating (G1) creates a characteristic interference pattern called a Talbot pattern downstream from G1. G1 can be stepped transversely to the beam propagation direction which then again shifts the Talbot pattern. The detector grating (G2) is an absorption grating designed to match the interference pattern produced by G1, so that the transmitted intensity through G2 oscillates as the Talbot patterns shift when G1 is stepped. The distance from source to G0 was 50 cm, and the distance from G2 to the detector was 8 cm. The lab coordinate system (x', y', z') is shown along with the sample coordinate system (x, y, z) , which is rotated by θ_{rot} around y .

will then in turn result in oscillating intensity transmissions at the absorption grating G2. It is the shift and relative amplitude of this oscillation that creates the differential phase-contrast and dark-field images respectively. If the decoherence is represented by Gaussian distributed phase shifts, the intensity oscillation in a given detector pixel is well modelled by a sinusoidal function [22]:

$$I(x'_g) = a_0 + a_1 \sin(kx'_g + \phi) \quad (4.8)$$

Where x'_g is the position of grating G1 as it is stepped transversely to the beam direction. a_0 is the average photon count, a_1 is the amplitude of the intensity oscillation, k is the angular oscillation frequency ($2\pi / \text{G1-period}$) and ϕ is the phase shift of the intensity oscillation. The visibility is defined as the relative oscillation amplitude in Eq. 4.8:

$$V = \frac{a_1}{a_0} \quad (4.9)$$

And the dark-field signal is defined from the relative visibility according to Eq. 4.9:

$$d_f = -\ln \frac{V}{V_{ref}} \quad (4.10)$$

Where V_{ref} is the reference image without sample, a.k.a. the flatfield image. We will assume the dark-field signal to be introduced by a linear diffusion coefficient ϵ [4, 25, 2]:

$$d_f = \int \epsilon dt \quad (4.11)$$

Where the integral is taken along the beam propagation path, parametrized by t (for a parallel beam setup t would be equal to z'). This makes the measured visibility an exponentially decaying function of the integral over ϵ (see Eq. 4.10). With this exponential dependence, visibility (V) and ϵ are dark-field analogs to intensity (I) and absorption coefficient μ , see Eq. 4.12 where the two are compared:

$$\begin{aligned} V &= V_{ref} \exp\left(-\int \epsilon dt\right) \\ I &= I_{ref} \exp\left(-\int \mu dt\right) \end{aligned} \quad (4.12)$$

The only respect in which the analogy breaks down is that ϵ is angularly dependent and μ is not.

4.2.3 Sample

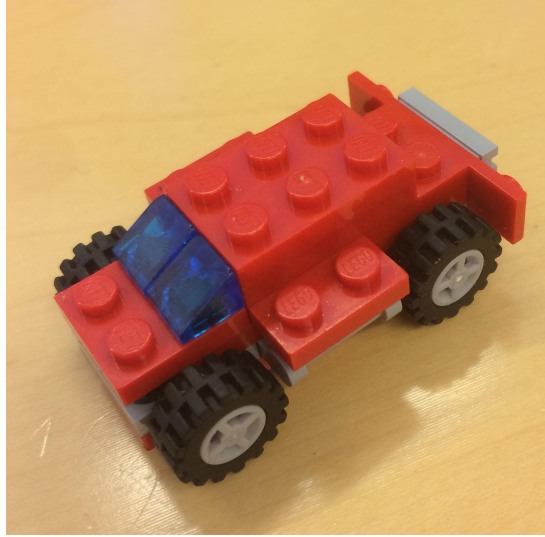


Figure 4.8: The imaged sample was a LEGO Toy car. The car has many internal (plastic-plastic) and external (plastic-air) interfaces which produce a decoherence signal.

The sample was a toy LEGO car (see Fig. 4.8). The car is a well defined and, due to the many edges and interfaces, quite anisotropically scattering sample [37], making it difficult to model. To illustrate the degree of anisotropy we can plot the total projected dark-field signal, E (see Eq. 4.13), as a function of the sample's rotation angle. E is found as the integral of d_f (see Eq. 4.11) across the entire detector screen, as shown below:

$$\begin{aligned}
 E &= \iint d_f dx' dy' \\
 &= \iint \left[\int \epsilon dt \right] dx' dy' \\
 &\approx \iiint \epsilon dV
 \end{aligned}
 \tag{4.13}$$

Since the beam in our lab setup is not parallel, the integral in Eq. 4.11 is not along z , but it does come quite close. For our setup, the beam cone angle at the detector corners is 1.5 degrees, making the total projected dark-field signal a good estimate of the total linear diffusion coefficient in the sample at the current projection angles. The total projected dark-field signal as a function of sample rotation angle is shown in Fig. 4.9.

The signal shows distinct peaks for each $\pi/2$ rotation. This is in accordance with the basic rectangular shape of the LEGO blocks. By close examination it can be seen that each of the $\pi/2$ -periodic peaks is split into two narrowly spaced peaks. This peak splitting effect arises from the decoherence signal being largest for beam propagation angles slightly different from the orientation of the plane surfaces in the car. This effect is more closely examined in Fig. 4.10.

As seen in Fig. 4.10 it seems that the dark-field signal has at least a very prominent refraction contribution. Seen in Fig. 4.9 the total projected dark-field signal varied by up to a factor of 2 depending on the sample rotation, meaning that the signal produced by the individual volume elements (voxels) within the sample must also be expected to vary with at least the same factor of 2 (at least on average: It is of course possible that some voxels produce a constant non-zero contribution, which would then be countered by other voxels producing a signal varying by more than a factor of 2). Furthermore, the curve in Fig. 4.9 is obviously not sinusoidal, and thus can not be the sum of a number of sinusoidal functions of the same period, as would be expected from the (first order only) model in [3, 25, 2]. Due to the large

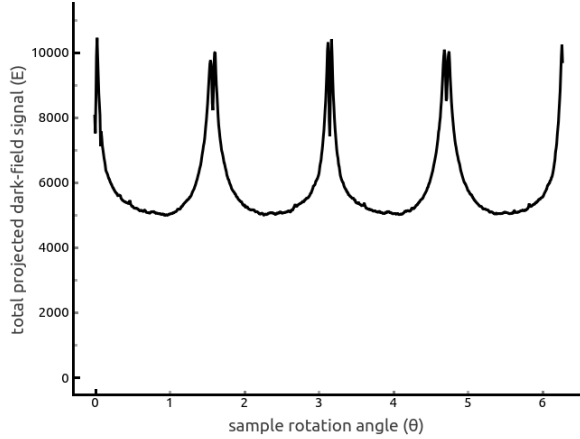


Figure 4.9: Total projected dark-field signal, ϵ , (see Eq. 4.12) integrated over the whole detector screen, as a function of sample rotation, θ . The signal is not sinusoidal as would be expected from the pure zero- and first-order model from [3, 25, 2]. Simply by observing the shape of this curve we thus have a strong argument for the inclusion of higher-order terms.

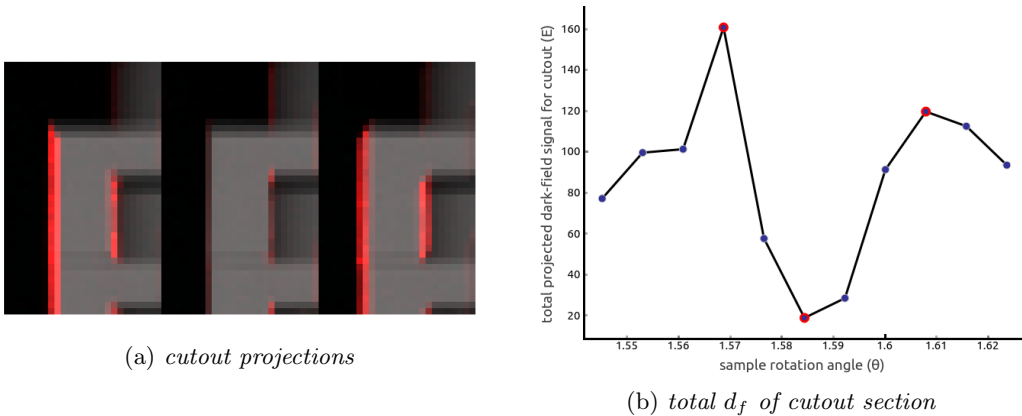


Figure 4.10: *Illustration of the peak splitting effect. The projections in 4.10a combine the absorption projections (in grayscale) with the dark-field projections d_f (in red). The projection cutouts cover a small section of the rear end of the Lego car. The three projections represent the two peak orientations and the minimum in between them. The plot in 4.10b shows the total d_f signal for the whole cutout as a function of θ . The projection angles represented in 4.10a are marked with red. It is clear from the figures above that the maximal value of d_f is not encountered when the beam propagation is parallel to the brick surfaces, but rather when it is at a very shallow angle to the surface.*

higher order contribution to the total signal, our sample could be said to be “more anisotropic” than the first order model allows. Thus, due to the strong anisotropy, this sample provides quite a challenging (higher order) test dataset.

4.2.4 Method

Our method only differs from standard grating interferometer tomography methods in the reconstruction algorithm, which takes the angular dependence of the produced dark-field signal into account. Since only a single rotation axis is used, the dark-field signal for each voxel is only probed in a single (1D) curve through the (2D) spherical angle space. In the case of a parallel beam or fan beam setup, the probed (1D) curve is simply a circle in the plane perpendicular to the orientation of the rotation axis. In the more general case of a cone beam setup, the curve deviates from this rotation axis-perpendicular circle. The larger the cone angle, the bigger the deviation is. Since only scattering along directions in this 1D-curve through angle space is probed, our model will only depend on a single angular variable.

4.2.5 Tomogram model

In this section, we will introduce the sample coordinate system (x,y,z) and the photon propagation direction θ in the sample coordinate system. We will also introduce the detector coordinates (x',y',z') . To avoid coordinate system confusion, all the equations in this section are centered around the tomogram coordinate system (x,y,z) and the fourth tomogram dimension, θ . The detector coordinates are only used for illustrating the backward and forward projection operations. The transition from tomogram coordinate system to the lab (and detector) coordinate system is straightforward (and exactly the same as for other cone-beam tomography setups), but tends to make equations messy, so these have been absorbed in the forward and backward projection operators. To accommodate for the angular dependence of the dark-field signal we introduce the dimension θ , to the tomogram model. θ describes the propagation direction of the x-rays through a given volume element (voxel). Since we only rotate the sample around a single rotation axis, only one angular variable is needed. The introduction of a θ -dependence makes our tomogram, ϵ , four-dimensional (three spatial dimensions, and one angular), rather than just three-dimensional (only spatial dimensions) as is the case for traditional absorption tomograms. We can expand ϵ into its θ -Fourier components, essentially giving us a set of 3D-spatial tomograms ϵ_f :

$$\epsilon_f(x, y, z) = \frac{1}{2\pi} \int_0^{2\pi} \epsilon(x, y, z, \theta) e^{-i\theta f} d\theta \quad (4.14a)$$

$$\epsilon(x, y, z, \theta) = \epsilon_0(x, y, z) + \sum_{f=1}^{N-1} 2\text{Re} [\epsilon_f(x, y, z) e^{i\theta f}] \quad (4.14b)$$

The equations above are the Fourier transform (Eq. 4.14a) and inverse Fourier transform (Eq. 4.14b) with respect to θ . In Eq. 4.14b we utilize the fact that ϵ is real (and hence that its Fourier transform is hermitian) by omitting negative f 's and instead taking the real part and multiplying with two. Since ϵ is periodic, its Fourier transform is discrete (aka. a Fourier series). For the case $N=2$ Eq. 4.14b is similar to the model in [3, 25, 2]. Note that θ is the actual propagation angle through the sample coordinate system at a given point in space, and not simply the sample rotation angle (in cases of a parallel beam the two are identical, except for the sign ($\theta_{prop} = -\theta_{rot}$), but in the general cone beam case the cone angle should be taken into account; $\theta_{prop} = -\theta_{rot} + \theta_{cone}$).

4.2.6 Algorithm

The 4D-tomogram model is iteratively optimized through a residual backprojection process similar to the Simultaneous Algebraic Reconstruction Technique (SART) algorithm [1], sometimes used in reconstruction of traditional absorption-tomograms:

$$\mu_{res}(x, y, z) = \frac{R}{R + x\cos\theta + y\sin\theta} P_{res}(x'(x, y, z, \theta), y'(x, y, z, \theta)) \quad (4.15)$$

The relationship between the projection coordinates on the detector screen (x', y') and the sample coordinates (x, y, z) depend on the sample rotation θ :

$$x'(x, y, z, \theta) = D_{det} \frac{x\cos\theta + z\sin\theta}{D_s - x\sin\theta + z\cos\theta} \quad (4.16a)$$

$$y'(x, y, z, \theta) = D_{det} \frac{y}{D_s - x\sin\theta + z\cos\theta} \quad (4.16b)$$

Where D_{det} is the source-detector distance and D_s is the source-sample distance. Eq. 4.15 describes the spatial backprojection in the SART algorithm, where P_{res} is the residual of the current model projection, R is the source-sample distance and (a,b) are the detector coordinates. The only difference between our new algorithm and SART is the modifications necessitated by the introduction of a fourth dependent variable .

To accommodate for the angular dependence, we backproject the residuals from many projection angles at once (either the full set of recorded angles or a subset evenly distributed over θ_{rot} . The

backprojection operation is both a spatial and angular-Fourier-component (see Eq. 4.14b) distributor. Expressed in continuous variables, the backprojection looks like:

$$\epsilon_{f,res}(x, y, z) = \int \frac{R}{R + x\cos\theta + y\sin\theta} P_{res}(x'(x, y, z, \theta), y'(x, y, z, \theta)) e^{-i\theta f} d\theta \quad (4.17)$$

Comparing Eq. 4.17 and 4.15, we see that Eq. 4.17 is just an angular Fourier transform of the traditional spatial SART-backprojector. For practical implementations we have a finite number of discrete measurements, and the integral in Eq. 4.17 is substituted with a summation. The model optimization algorithm is sketched below:

Algorithm 2 tomogram optimization

```

Check convergence criteria
while Convergence criteria not meet do
  Choose set of M projection angles
  for M projection angles do
    forward project the current 4D-model at the m'th projection angle
    compare with the measured projection and calculate residual
    backproject the projection residual according to Eq. 4.17
  Update the 4D-model according to the results of all M residual backprojections
  Apply regularizations
  Check convergence criteria

```

4.2.7 Regularizations

The 4D-tomogram in Eq. 4.14b is heavily underdetermined (by a factor of app. 100) by the 3D measured dataset (2 spatial detector dimensions and one angular dimension). So, to reduce overfitting and restrict the solution space, we can introduce a number of regularizations. Since our model is so heavily underdetermined, regularization is absolutely necessary, and careful selection of the appropriate regularizations is key to arriving at meaningful solutions.

Frequency cut-off

As a first general regularization, we will assume the dark-field signal to be sufficiently "well-behaved" for it to be well represented by the first few elements in the Fourier series of Eq. 4.14b. Our tests have shown as low as 5'th order models to be able to describe the measured data quite well, with only a few percent improvement in the tomogram's ability to model the measured data achieved by increasing the frequency cut-off from 5 to 10. The frequency cut-off represents a significant reduction of the solution space volume (from possibly several hundred Fourier components representing the hundreds of projection angles to only around a handful of Fourier components).

Positivity constraint

We also impose a positivity constraint, requiring ϵ to be positive for all angles and spatial coordinates. This constraint is considered generally sound for all types of samples, since negative ϵ -values would imply increased beam coherence, which is unphysical, except in the case of carefully designed x-ray optics.

Higher order Fourier component suppression

To reduce overfitting, we can penalize the higher order Fourier components. To penalize according to real space (θ -space) curvature of the given Fourier component contribution, we penalize according to the square of the Fourier component number (f). For each algorithm iteration we introduce a driving force lowering the higher order Fourier components. The magnitude of the force is controlled by the suppression parameter s :

$$\epsilon_{f,s}(x, y, z) = \epsilon_f(x, y, z) e^{-s f^2} \quad (4.18)$$

Periodicity requirement

As an appendix to the assumption of a Gaussian-spread angular distribution lying behind the introduction of the linear diffusion coefficient in Eq. 4.11, we will also assume the Gaussian spread to be the same for parallel but opposite propagation angles. For parallel beams this assumption translates to requiring ϵ to be π -periodic with respect to θ .

For cone-beam geometries, this reverse-propagation-angle-similarity assumption generally doesn't translate to a π -periodic ϵ (due to the out-of-plane deviations of the probed propagation angles, as discussed in section 4.2.4), but if the cone angles are small enough (or if the sample is invariant with respect to angular heights), the deviations may be small enough for the periodicity-assumption to hold.

Symmetry requirement

We can impose a symmetry requirement, so the signal from a given voxel is required to have some symmetry angle θ_{sym} . This is equivalent to requiring the Fourier Components to be purely real after rotating them according to s and their Fourier component number f :

$$\epsilon_f = e^{i\theta_{sym}f} \text{Re} [\epsilon_f e^{i\theta_{sym}f}] \quad (4.19)$$

Note that θ_{sym} and ϵ_f in Eq. 4.19 are of course both dependent on the spatial coordinates (x,y,z) , which have been omitted in order to reduce notational complexity.

Similarity constraint

If the sample is sufficiently "uniform" we may introduce a similarity constraint, requiring all voxels to be of a similar "type". E.g. they must all be identical up to rotation and scaling. This is of course a very strict requirement, reducing the model parameters to just two spatially dependent parameters (rotation and scaling) and the (spatially independent) Fourier components describing the generic angular dependence of ϵ on θ .

Absorption and phase-regularization

We can utilize the fact that the grating interferometer images inherently come in sets of three modalities; phase-shift, absorption and dark-field, and regularize our dark-field tomogram using information from the two other modalities, e.g. requiring absorption or phase-tomogram values above some threshold in order to allow non-zero. This requirement would be founded in the fact that a decoherence effect can only be introduced by the sample material (air also introduces some small decoherence, but this is already accounted for in the flatfield images used to normalise the sample images).

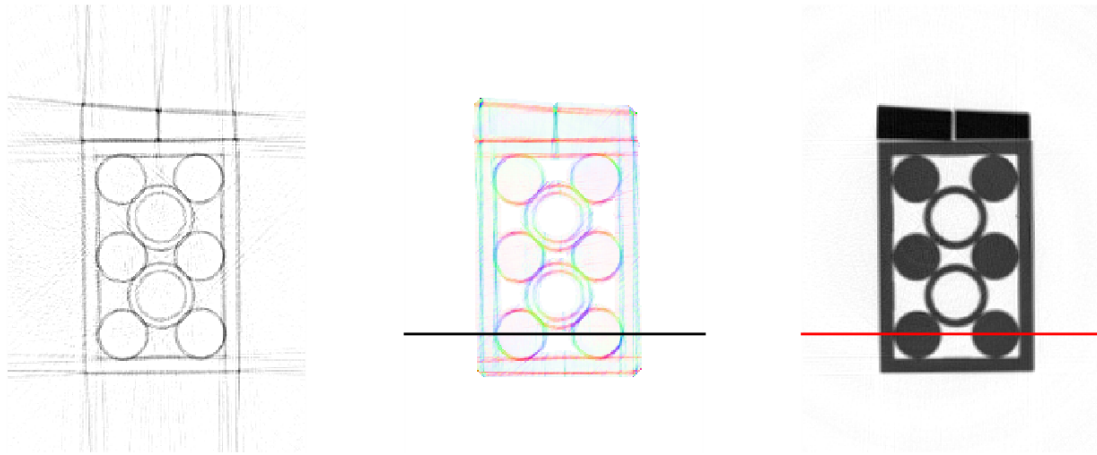
4.2.8 Experimental results

After a number of iterations (typically around 10, depending on how strongly regularized the model is), the model converges at a stable 4D-model. This convergence limit will be referred to as the 4D-tomogram. A 2D slice through the first order tomogram and the corresponding FDK-filtered backprojection-reconstructed tomogram are shown in Fig. 4.11

In the absorption tomogram slice in Fig. 4.11c, two graytone levels can be identified. The part with the lightest gray color consists of a rectangular shape, six circular disks and two circles. All these shapes have a lot of interfaces. Two of these interfaces are crossed by the red line. From the absorption tomogram it can be hard to see if the different shapes are actually connected or not. Plotting the line profile along the red line through the absorption tomogram, the disk shapes seem to be connected to the rectangular shape (see the red line in Fig. 4.12), i.e. the interfaces seem to actually be connections and not interfaces. Plotting the corresponding line profile through the first order dark-field tomogram (black line in Fig. 4.12), two large peaks reveal that the shapes are actually not connected.

The model fit was evaluated using the standard deviation of the projected -model in Eq. 4.11 from the measured dark-field signal calculated as in Eq. 4.10. The standard deviation is simply the square root of the variance, which is described in Eq. 4.20:

$$\sigma_{d_f}^2 = \sum_{x',y',\theta} (d_{f,measured} - d_{f,model})^2 \quad (4.20)$$



(a) *FDK dark-field tomogram* (b) *iterative dark-field tomogram* (c) *absorption tomogram*

Figure 4.11: *Corresponding 2D-slices through three different tomographic reconstructions Left: the traditional scalar FDK-filtered backprojected tomogram of the dark-field signal. Middle: The first order component of the regularized iteratively reconstructed 4D-tomogram of the dark-field signal. Right: FDK-reconstructed absorption tomogram. As can be seen, the 4D dark-field tomogram suffers less from streak artefacts than the corresponding FDK-tomogram. In the two latter slices, the line profile plotted in Fig. 4.12 is marked.*

The projection model errors were reduced in the 4D-tomogram ($\sigma = 0.05191$) model when compared to the FDK-reconstruction model ($\sigma = 0.07535$).

Virtual phantom test

The iterative reconstruction method was tested on a virtual dataset. First, an anisotropic virtual sample was created. The sample had fifth order angular variations in the voxel signals, see Fig. 4.13. The virtual sample simulated a rectangular structure producing a large signal at angles parallel (or close to parallel) to the propagation axis.

The virtual tomogram was forward projected at 101 angles. The resulting projection stack was used as input to two reconstruction algorithms; the FDK-algorithm and the iterative anisotropic reconstruction method described in this paper. To compare the two methods we only looked at the zero-order part of the iteratively reconstructed tomogram. The centre slice of all three tomograms is shown in Fig. 4.14.

As is seen from Fig. 4.14, the FDK-tomogram overestimates the positive values of the samples edges, while underestimating the values of the neighbouring voxels. This effect is due to the backprojections at edge-parallel propagation angles dominating the reconstructed tomogram. The standard deviation of the reconstructed tomograms were 0.257 and 0.017 for the FDK and iterative methods respectively. The iterative method was able to model the angular dependence on the phantom tomogram voxels quite well, as is seen in Fig. 4.13.

4.2.9 Conclusion and Outlook

Our sample produced a very angle dependent dark-field signal. The signal is strongest at shallow beam propagation angles relative to the surface, indication that refraction effects contribute to the decoherence. This angular dependence poses a challenging reconstruction problem. We have demonstrated an improved data modelling capability using an angle sensitive tomogram model. Using an iterative optimization, we arrived at a local minimum in the solution space, which represented a weighted compromise between data modelling capability and model “niceness” measured as the degree of anisotropy. Visual inspection of the resulting angularly dependent tomogram confirmed that this tomogram had reduced streak artifacts compared to the traditional FDK-filtered backprojected tomogram. A virtual phantom tomogram test

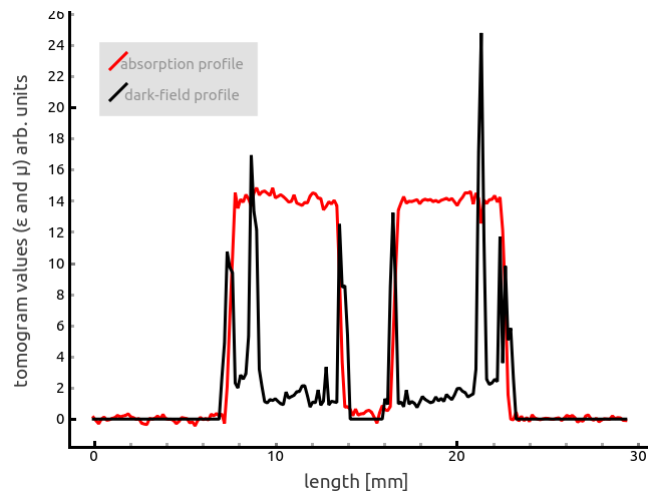


Figure 4.12: Profile plot of a line through the FDK-filtered backprojected absorption tomogram and the first order component of the regularized 4D-tomogram of the dark-field signal (i.e. ϵ_1 from Eq. 4.14a). The dark-field tomogram reveals two interfaces (i.e. peaks) not visible in the absorption tomogram

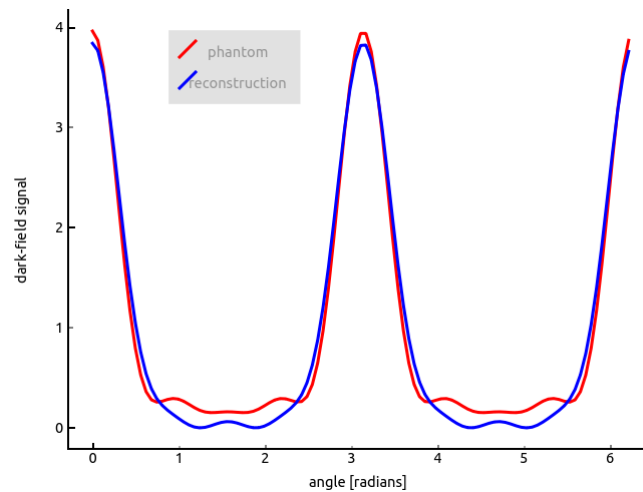


Figure 4.13: Angular dependence of the dark-field signal from a single voxel in the virtual sample (red) and the reconstructed tomogram (blue) respectively.

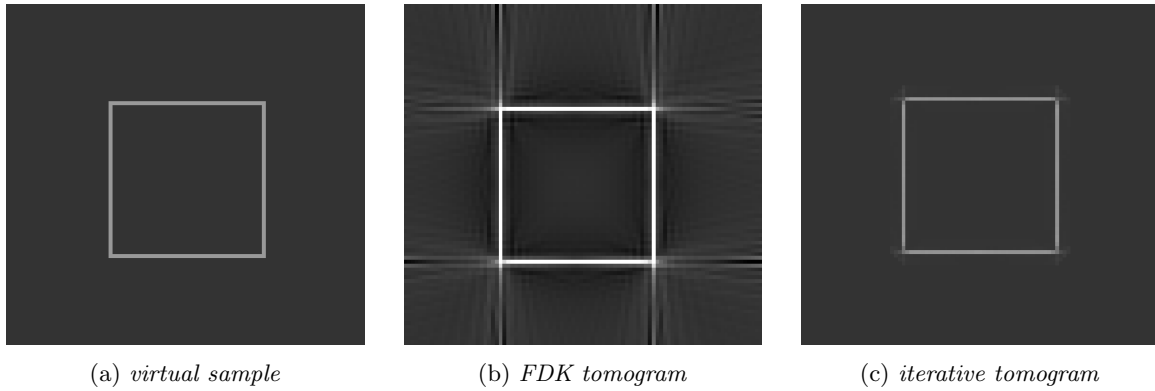


Figure 4.14: *Phantom test tomograms. Left: original virtual phantom. Middle: FDK-reconstruction. Right: iterative anisotropic reconstruction. Only zero-order components are shown here. Color scale is the same for all images.*

showed more than a 10-fold increase in reconstruction precision compared to the FDK-method. Another aspect of the algorithm's applicability is the convergence of the iterative fitting algorithm, both in terms of speed and stability. Improving convergence speed and reducing sensitivity to noise through smarter iterative optimization would be obvious goals for further developments.

Chapter 5

Dark-field modality application tests

The hard x-ray grating interferometer based dark-field contrast modality was described for the first time 10 years ago [22]. With its relatively recent first demonstration, the full spectrum of possible applications of this interesting new image formation modality is still being explored. Further adding to a lack of a complete overview of its possible applications is its unique nature. Unlike the differential phase contrast signal, which also is a product of the newly demonstrated grating interferometer, the physical contrast formation mechanism behind dark field signal is not simply a density property of the sample in question (i.e. phase and absorption contrast mechanisms depend on electron and elemental densities: They can both be calculated if you know the elemental densities of the sample). The 'density modalities', phase and absorption, are based on an implicit uniformity assumption; we assume that the relevant densities are uniform within the individual voxel. This assumption holds quite well, simply for statistical reasons; What ever sub-resolution density variations that exist will approximately cancel each other out on average. In contrast to the two density modalities, the contrast mechanism behind the dark-field modality is directly micro-structurally dependent[38]. More precisely, it is dependent on *transverse micrometer-scale scattering length density variations*. This fundamentally different contrast formation mechanism gives some interesting new possibilities for applications of the dark-field imaging modality. The two publications in the following are examples of such possible applications.

5.1 Introduction to publication A.1

Detection of sub-pixel fractures in X-ray dark-field tomography

My contribution to the work

The idea to this study was conceived by Robert Feidenhans'l and me. The measurements were performed at one of the lab setups at Technische Universität München, with the help of Marian Willner, Martin Bech and Franz Pfeiffer. Upon return from Munich, I performed all the data analysis and I produced all the figures. I was the main author of the paper we submitted to Applied Physics A.

In this article I have utilized the microstructural origin of the dark-field signal to detect sub-resolution-sized crack formation in a solid material. In order to be visible with density-contrast methods such as phase and absorption tomography, cracks must be of such a large size that the overall density of the individual voxel has changed enough to be detectable. In other words, the voxel size, along with the sensitivity of the setup, sets a lower limit to the size of cracks that can be detected in a tomogram. This lower size limit means that the desire to detect the formation of very small cracks in a sample sets a limit to the size of the sample that can be scanned, since using detector resolutions above approximately 2048x2048 pixels (detectors with a width of 2560 pixels have started to appear at synchrotron imaging beamlines) produces a lot of difficulties. By utilizing the microstructural sensitivity I have shown that the dark-field signal can push the lower limit on crack detectability size lower than the density contrast modalities of the same setup, and thus allow a larger sample to be scanned for a given critical crack size limit.

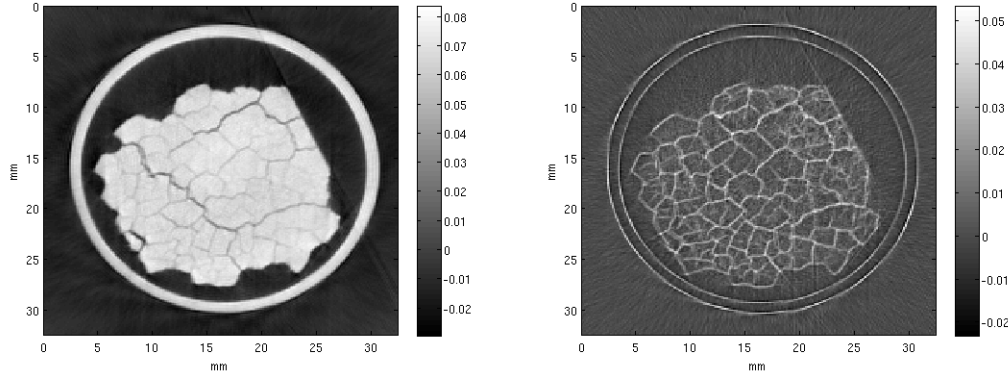


Figure 5.1: Corresponding absorption (left) and dark-field (right) tomogram slices. Many cracks clearly visible in the dark-field slice are hardly seen in the absorption slice. Illustrations from publication A.1

5.2 Introduction to publication A.2

Mapping misoriented fibers using X-ray dark field tomography

My contribution to the work

The design of this study was conceived jointly by Erik Mejdal Lauridsen, Robert Feidenhans'l and me. The measurements were performed at our own grating interferometer lab setup at the Niels Bohr Institute. Erik delivered the samples and I performed the setup modification and the measurements. I performed the data analysis and produced all the figures. Erik and Robert contributed extensively, but I was the main author of the paper we submitted to Applied Physics A.

In this publication I have tried to utilize the angular dependence of the dark-field signal to mask out a certain fiber orientation in the sample. This is done by changing the rotation axis in the setup, see Figure 5.2.

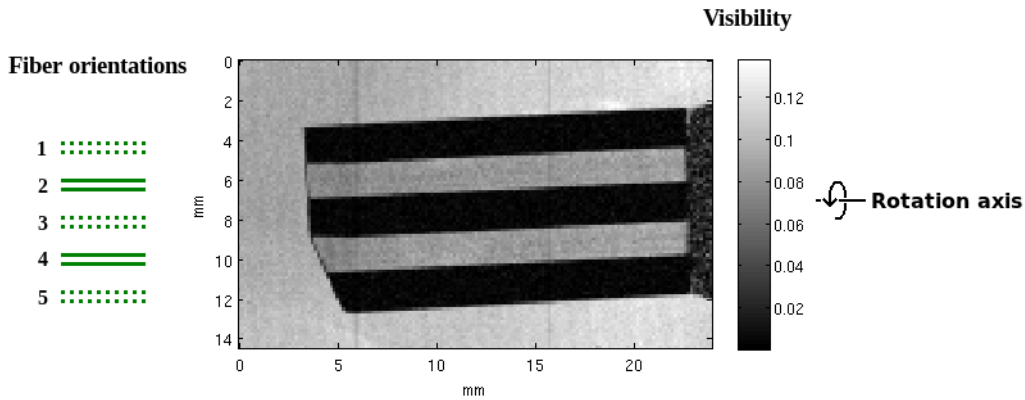


Figure 5.2: Dark-field projection of a carbon fiber sample. The sample consists of five identical layers. Within each layer, the fibers are all aligned. Layers 1, 3 and 5 have fibers aligned parallel to the beam propagation direction. Layers 2 and 4 have fibers aligned parallel to the grating stepping position. The fiber orientations are illustrated in the left part of the figure. Note that layers 2 and 4 produce almost no dark-field signal. Illustration from publication A.2

As stated in the beginning of this chapter the dark-field signal originates from transverse density variations. The “transverse” part of the previous sentence refers to the beam propagation direction and the grating slit direction. Since, in tomography measurements, we rotate the sample, the beam propaga-

tion direction relative to the sample changes during measurement. In traditional grating interferometer tomography setups the rotation axis is parallel to the grating slits. This means that the transverse density variations, and hence also the dark-field signal, must generally be expected to vary during the measurements. By changing the rotation axis, so it was parallel with the probed scattering direction, we were able to mask out all fibers aligned along the rotation axis; due to their 1-dimensional shape, fibers have no density variations along their length-dimension, and thus produce no dark field signal when their are oriented along the probed scattering direction.

Chapter 6

Applied high resolution synchrotron imaging

A part of my work has been on what I have called “Applied” imaging. Another description could be “servicing” or “requested scientific work”. This work is characterized by being performed on the initiative of some external “client”. By definition, the scientific aim of this kind of work lies outside of the area of x-ray imaging (in the cases I present here it even lies outside the field of physics and relates to such exotic scientific fields as biology, odontology and neurology). Though imaging in this kind of work merely serves as a tool to investigate the subject of “real” academic interest, it can still be of interest to the x-ray imaging expert (e.g. me) both because the analysis often brings up interesting challenges and new question I would not otherwise have found a reason to ask, and because imaging is by its nature very “client-driven”: The big synchrotrons around the world are not spending millions of euro, yen and dollars because x-ray imaging is inherently interesting (Though I think it *is* inherently interesting, this is not the *reason* for the big spendings around the world), but rather because imaging can serve as a tool to advance other scientific fields. With the emergence of the state-of-the-art synchrotron MAX IV in Lund, Sweden just across the water from my office in Copenhagen and the planned construction of at least a couple of dedicated full-field imaging beamlines, one of these being build for danish money, the “client service”-aspect of x-ray imaging seems extra relevant.

6.1 Introduction to publication A.3

Visualisation by high resolution synchrotron X-ray phase contrast micro-tomography of gas films on submerged superhydrophobic leaves

My contribution to the work

Most of the people in the author list contributed to the discussion about the design of this study. The measurements were performed at the TOMCAT beamline at SLS. All the authors contributed to the measurements. Upon return from Switzerland, I performed all the tomogram data analysis and I produced all the x-ray related figures. Ole was the main author of most of the paper’s text, though I was the main contributor to the x-ray relevant parts. We submitted this paper to the Journal of Structural Biology.

Publication A.3 represents my collaboration with a number of biologists from within the field of freshwater biology, most notably professor Ole Pedersen from the Freshwater Biological Laboratory at the University of Copenhagen. Ole studies gas and water transport in periodically submerged plants. We performed our measurements on submerged *Spartina* leaves at the TOMCAT beamline at the Swiss Light Source. During the initial attempts to derive qualitative results from the pure absorption tomograms in this data set, it became clear that heavy refraction artefacts prevented a good segmentation, at least without involving advanced segmentation algorithms. The solution became to apply the refraction correction algorithm described in section 3.1.4 (a.k.a. the “Paganin” method), which proved to give satisfactory segmentation results using only thresholding.

6.1.1 scientific motivation

The project studied plants of the genus *Spartina* (danish name: vadehavsgræs) native to the salt marshes of the Wadden Sea of southwestern Denmark. The salt marsh is a type of biological region found in some coastal areas. It is characterized by frequent flooding due to tidal changes in the water level. As an adaptation to the frequent floodings, the plant has developed mechanisms to preserve some amount of air within the plant itself as well as at its surface. The presence of free air increases the plants respiratory capacity while submerged at high tide, since oxygen diffusion across the cellular walls is faster in air than in water. The internal air pockets are simply cavities within the plants structure, i.e. a hollow stem or leave. The external air pockets are found on the bottom side of the leaves. The bottom side of these leaves is highly hydrophobic and quite curved. The curvature of the leaves is shaped such that it creates ridges along the leaves in which air is trapped when the plant is submerged. The primary goal of the analysis was to make a 3-dimensional in-situ visualisation of the plant and its air pockets when submerged in water.

6.1.2 Experimental setup

The TOMCAT beamline at SLS receives its photons from a bending magnet. It has a double crystal multilayer monochromator which for these measurements was set to select an energy of 12 keV. Multilayer monochromators typically give energy bandwidths of a couple of percent, which is fine for imaging purposes, and gives a much higher flux and, as a result of the higher flux, a shorter measurement time than what would have been achieved with the typical 10^{-4} energy bandwidths of single crystal monochromators. The detector resolution was 2048x2048, and the visible light optics behind the scintillator screen of the detector system included a 20X magnification resulting in an effective pixel size of $0.375 \mu\text{m}$.

6.1.3 Reconstruction

The SLS software provided us with both the unprocessed detector readouts, and corresponding tomogram reconstructions. These reconstructions were traditional absorption-only reconstructions, using a Parzen-filter (also known as a de la Vallée Poussin filter) [10]. The reconstructions showed quite heavy refraction artefacts (see Figure 6.1), which made a good segmentation difficult, because the refraction edges shadowed out the details of the leaf and air pocket interfaces.

To get rid of the refraction artefacts, we attempted to take refraction effects into account during the reconstruction by applying equation (3.13). Since the leaf was submerged in water, and the main constituent of plant cells is water, we assumed a δ/β ratio corresponding to that of water. When first testing the refraction correction algorithm it became clear that in addition to this we needed what was essentially a “locality correction”: In order for the inverse Radon transform in equation (3.46) to work, the mapped (absorption)-field must be go to zero at the tomogram edges, i.e. the entire sample should be contained in the tomogram. This criterion was not met in our case, since during measurements, the leaf was contained in a water filled plastic tube with a diameter of approximately 6 mm. With a detector pixel size of $0.375 \mu\text{m}$, we had a 0.77 mm field of view, far less than the width of the sample container, making the tomography local. The locality results in what can be considered a low order additive background contribution to the projection images. Essentially the background is just a projection of the cylindrical container added to the leaf signal. In the radon transform, the tomogram is assumed to go to zero at the edges of the tomogram, so the locality will give rise to low order errors as well as high frequency oscillations at the tomogram edge. Furthermore, when a paganin filter is applied, the locality error is wrapped across the image edges if no zero padding is applied (e.g. if there is a discontinuity going from the left side of a projection image to the right, this discontinuity will be smeared out, distorting the edges of the projection). This edge wrapping will affect the reconstruction, leading to further low order errors in the tomogram, complicating a meaningful analysis. The simplest and most general correction for this error would be to fit some low order polynomial to the projection edge values. This fit would then act as a background model, which could be subtracted from the projection image. But since the background in our case was so well-defined, I chose to apply a more specific model. In order to compensate for locality effects, a cylindrical background model was fitted to the full projections. Since the absorption from the cylinder was by far the dominating contribution to the total absorption signal, the cylinder model was simply fitted to the full absorption signal, ignoring the leaf’s contribution.

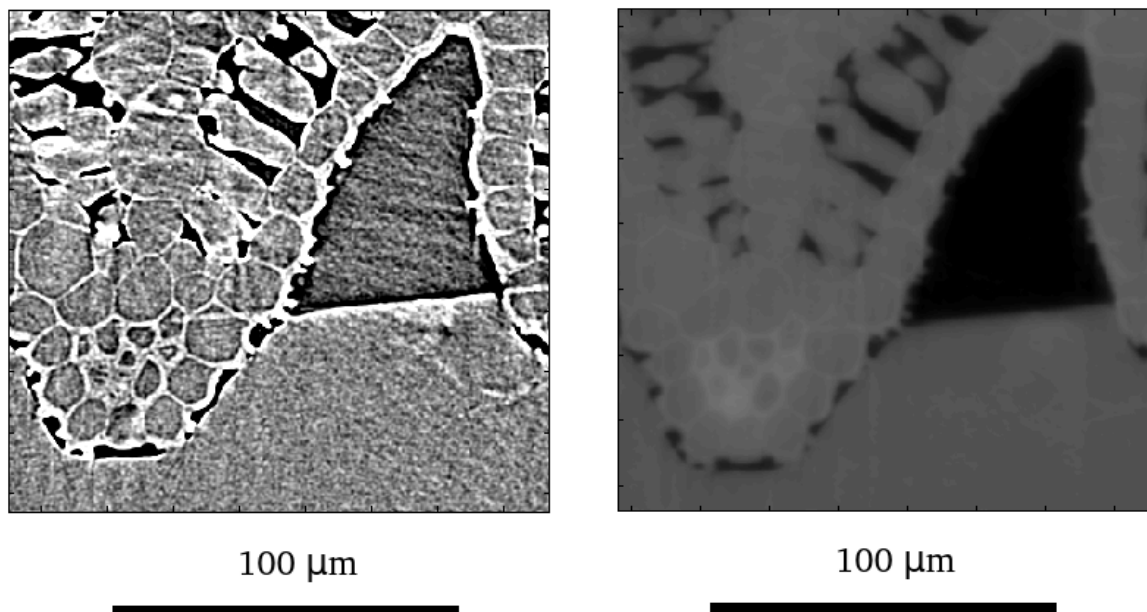


Figure 6.1: *Corresponding slices through an absorption-only tomogram (left slice) and a refraction corrected tomogram (right slice). The darker areas correspond to air pockets. The lighter areas in the top are plant cells, and the grey area in the bottom is surrounding water. The cellular walls are visible, especially in the absorption-only tomogram. Refraction artefacts in the form of edge-enhancement are quite pronounced in the absorption-only tomogram, especially at air pocket edges.*

6.1.4 Data analysis and results

Segmentation was basically performed as a simple threshold algorithm, except for a few logical and morphological postprocessing steps. The following data analysis derived a number of more or less trivial parameters for the internal and external air distribution. A distinction was made between internal and external air, and relative fractions of the two were compared at different positions along the leaf. Mean and maximal gas film thicknesses were also derived, and compared between the different leaf segments. Some of the derived parameters had been estimated before using other techniques such as visible light microscopy, others had never been measured before. The found values for the previously estimated parameters were in agreement with most literature values, and thus worked to confirm the validity of our results.

6.2 Introduction to publication A.4

Virtual histology uncertainty in Synchrotron x-ray micro-Computed Tomography evaluation

My contribution to the work

The scanings at ESRF were performed before we decided on this study. After having seen the tomograms, and the results of the analysis presented in papers A.4 and A.5 we decided to perform this investigation. The analysis methods were discussed between all three authors, but the actual analysis was performed by me. I also produced all the figures. Else was the primary author of most of the text, though I also contributed extensively.

Note that at the time of writing this article has gone through first review and a revised manuscript has been submitted, but the article has not yet been accepted for publication. Publication A.4 represents one of the three articles resulting from my collaboration with researchers within the field of dental surgery,

most notably Else Pinholt. Like the two other dental implant-related articles I contributed to, this article studies the integration of dental implants in the native bone of the jaw and maxilla (i.e. the lower and upper bones of the mouth, where the teeth have their roots). In this article we focused on examining the advantage of using a 3D sampling such as in x-ray tomography, instead of a 2D sampling technique such as microscopic histology, which is traditionally used for evaluating dental implant integration.

6.2.1 scientific motivation

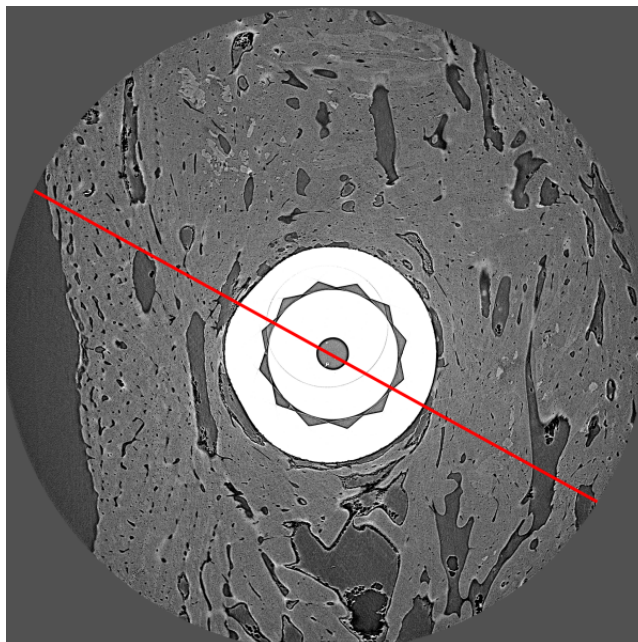


Figure 6.2: *Horizontal slice through one of the samples. The diameter of the image disc is 10.3 mm. The implant is the white part in the middle, and the bone is the lighter gray surrounding the implant. The darker gray areas are the cavities. The red line illustrates one possible histology cross section.*

The traditional evaluation method for studying the integration of dental implants in bone is by microscopy of histological cross sections [6]. This method has the disadvantage that it is both 2-dimensional and destructive; the sample is cut or grounded to expose an internal cross-section through the implant. The exposed cross-section can then be investigated by traditional visible-light microscopy. Typically, the sample is coloured using different colouring agents sensitive to different tissues in the sample. In this way it is possible to get very accurate images of the distribution of some particular tissue. Unfortunately, once the sample has been cut and ground, we cannot go back and choose another cross section for our analysis. If we examine the bone surrounding the implant in Figure 6.2 closely, we can see that in some areas the bone follows the implant closely, but in other areas, there is quite a big gap between the two. If we had only investigated one cross section, we might have ended up with either a very narrow or a very wide gap. In either way, we would not be able to tell whether our result was a good representation of the full implant surface. The tomogram allows us to construct many different virtual histology cross sections, and for each of them we can derive relevant parameters. If we then compare these parameters across different cross sections, we can get an idea how much the histology results can be expected to deviate depending on choice of cross section.

6.2.2 Experimental setup

The measurements were done at the ID19 beamline at the European Synchrotron Radiation Facility (ESRF). ID19 receives its photons from one of five different insertion devices (four undulators and a wiggler). ESRF is a 6 GeV storage ring. Such a high electron energy allows the beamline to produce quite high energy radiation. For these experiments, we used a 67 keV peak energy and a multilayer double monochromator. The samples were prepared by surgically placing implants in a goat mandible

for 20 weeks. The implants were placed in different environments; some were simply just screwed into the jaw bone, some were partially covered with *autologous* bone (i.e. bone taken from the hip bone of the same goat). Half the autologous bone implants were also covered by a membrane to keep the autologous bone in place. 20 weeks after implementation, the goats were sacrificed; and the samples were harvested, cleaned and embedded in acrylic material.

6.2.3 Results

Unless there is no variation across different choices of cross sections, a full 3D analysis will always give a better representation of the data than a single 2D cross section. The question then is how much better the 3D analysis will be than the 2D analysis. This will depend on how much the samples vary as a function of cross section choice. We examined this difference by studying the variations in bone fraction. For the 6 samples with uncovered implants, the mean bone fraction was 50.9%. When comparing the six full volume results the standard deviation was 7.6%. For the virtual histology cross sections the standard deviation was 14.9%. For the implants covered with autologous bone, but with no membrane the mean bone fraction was 56.1%. The standard deviations for the full volume results and the histology results respectively were 10.6% and 14.4%. Assuming these numbers to be constant, we investigated how many samples would be necessary to produce statistically significant differences between the two sample types. We assumed the results to be normal distributed with different variances for the two sample types. To determine whether two such sample sets are significantly different, a Welch t-test is used. The p-values as a function of number of samples is plotted in Figure 6.3.

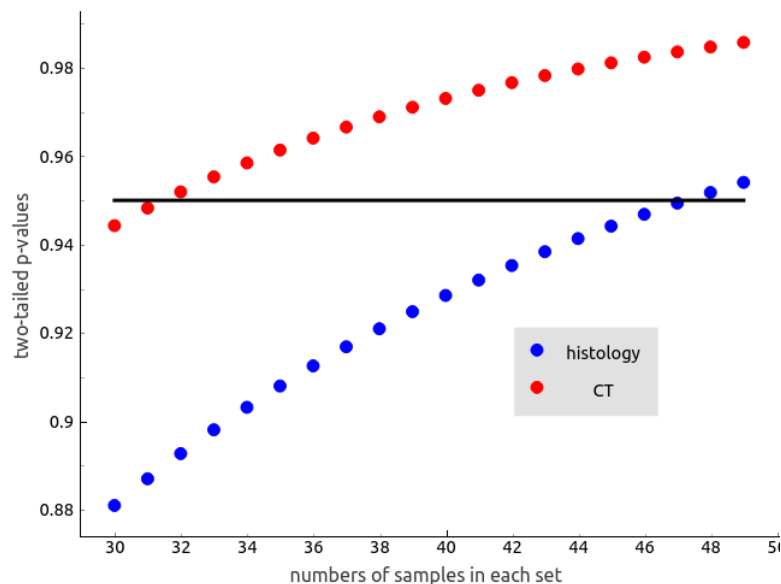


Figure 6.3: *Expected p-values for Welch’s t-test, based on the means and the unbiased variance estimates from the analysis of our six samples. Analysing a given sample set using either 2D histology or 3D CT, the 3-dimensional CT analysis gives less variance than the 2D histology. For a fixed number of samples, the lower variance of the CT analysis produces increased p-values, and a 95 % confidence will be reached with 32 samples. For histology analysis, it must be expected that 48 samples would be necessary to reach 95 % confidence.*

For a 95% confidence interval, we need 32 full volume analyses or 48 histological analyses, i.e. we will need 16 extra samples if we only perform the analysis in 2D.

6.3 Introduction to publication A.5

Application of high resolution synchrotron micro-CT radiation in dental implant osseointegration

My contribution to the work

I did not contribute to the measurements at ESRF, on which this project was based, but I performed all the tomogram analysis, after discussing the methods with Camilla, Tore, Robert and Else. I also produced the tomogram-related figures. I contributed to some of the tomography-relevant parts of the article text.

This and the following publication are both based on the same dataset as the one investigated in the article described in the previous section. In this study we looked at the volumetric bone fraction as a function of distance from the implants. The study found a much lower bone fraction close to the implant than what the literature traditionally suggests. We found bone fractions as low as 3-4 % right at the interface, where some studies find bone-to-implant contact ratios as high as 60-80%. This difference could be explained by segmentation errors induced by the refraction-induced edge-enhancement: The interface between the low-density bone/cavity segment and the comparatively very dense Titanium implant presents quite a strong electron-density gradient, and thus must be expected to give rise to refraction artefacts, see section 3.1.4. But the refraction effect can hardly explain the dip in bone fraction beginning typically extending all the way to a distance of 200 μm . By examining the tomograms visually (see Figure 6.3 for an example slice), I also see no suspicious features. Furthermore, there obviously is an increased occurrence of cavities close to the implant. Actually these cavities seem to almost fully enclose the implant at short distances. This tendency might be slightly visible if Figure 6.3 is inspected closely. So, my conclusion is that the bone fraction certainly seems to be much lower near the implant, though the contact value of 4% might be too low due to edge-enhancement artefacts. To my knowledge, this effect has not been described previously. As mentioned in the article, this previously undescribed effect might be a result of the design of this particular study.

6.4 Introduction to publication A.6

Synchrotron radiation μCT and histology evaluation of bone-to-implant contact

My contribution to the work

For this project, my contribution to the analysis was solely on a discussion level. I also contributed some to the article text.

Again, the same dataset was used as in the previous two publications. Motivated by the findings in article A.5, the focus in this study was on the comparison between traditional 2D histology and 3D tomography. Since the tomography analysis in article A.5 produced results that were very different from what is traditionally found using 2D histology we wanted to compare the two methods directly by analysing the same samples using both methods. The study also sought to investigate and compare the quality of the implant integration for different sample types. Unfortunately, the study found quite a weak correlation between the two analysis methods ($r=0.34$ for one area of the implants and $r=0.39$ for the other). One explanation for the weak correlation is the sampling effect; the histology method only investigated a cross section of the sample, whereas the tomography investigated the full volume. We would be very lucky if these cross sections all were perfectly representative of the full volumes. So the sampling effect alone must be expected to result in a lowered correlation even if the measurements were perfectly noise free. The problem of the limited sampling in 2D histology was the subject of the latest study of this dataset described in publication A.5. A further factor that must be taken into account is that the tomogram analysis for these particular samples used a 4-binned version of the data, i.e. the voxel size was 20 μm rather than the original 5 μm .

6.5 Introduction to publication A.7

Injection of high dose botulinum-toxin A leads to impaired skeletal muscle function and damage of the fibrillar and non-fibrillar structures

My contribution to the work

I participated in the discussions about design of this study as well as the measurements. But for the analysis my contribution was solely on a discussion level. I also contributed some to the article text.

During our work related to this study I learned, to my surprise, that Botulinum-toxin A, commonly known as Botox, is one of the strongest toxins known. It is apparently so toxic that a working group on civilian biodefense has published an article describing the possible threat from using it as a biological weapon [29]. With a lethal dose of around a few nanogram per kilogram of bodyweight (i.e. a single gram could kill the entire population of Denmark) you might wonder how such a compound has ever been approved for medical use. And furthermore, the fact that this compound is even used for purely cosmetic purposes was quite thought provoking, at least to me. The reason for the approval of the use of botox in medical treatments is that it offers relief to patients suffering from sometimes very impairing, and otherwise untreatable, illnesses, such as cerebral palsy, migraine and depression. However, the relief offered by botox treatment might come at a high price, as we showed in this study, where 60 picograms (i.e. $60 \cdot 10^{-12}g$) were injected to one of the the triceps surae (the calf muscle of the lower leg) of a number of rats. Only one leg was injected with botox, the other functioned as a control. 21 days after the injections, the rats were sacrificed and their triceps surae were harvested.

6.5.1 Experiment and results

We went to the TOMCAT beamline to perform the absorption tomography measurements. The tomograms allowed us to distinguish the higher density fibrillar tissue (i.e. the muscle fibers) from the non-fibrillar tissue (i.e. veins, fat, and other tissue). A strong and healthy muscle is characterized by a higher fraction of fibrillar tissue. The botox-injected legs showed a significantly reduced fraction of fibrous tissue and a correspondingly increased fraction of non-fibrous tissue. Furthermore, the weight of the botox-injected muscles was reduced by 45%. To measure the anisotropy of the muscles, a star length distribution [28] was mapped for a small subvolume of each tomogram. A star length distribution simply records how long you can move in a given direction before you hit an interface, in this case an interface between fibrous and non-fibrous tissue. These lengths are then recorded for a lot of different directions and a lot of different random points (or simply all voxel points in a given volume). From the star length distributions a number of parameters can be derived [20]. One of them is the isotropy index [14], which basically just fits an ellipsoid to the star length distribution and divides the length of the ellipsoid's minor axis with the length of its major axis. This results in a number between 0 and 1, with 0 representing an infinitely long rod and 1 representing a perfect sphere. The isotropy index is a relevant measure of muscle tissue quality, since, as mentioned above, strong and healthy muscle tissue is dominated by rod-like muscle fibers. So we would expect healthy muscle tissue to score lower in the isotropy index than unhealthy muscle tissue. The botox-injected muscles showed a significantly increased isotropy index, indicating that these muscles had been negatively affected by the botox injection.

Chapter 7

Conclusion

In this thesis I have suggested two algorithms for improving the image formation from grating interferometer data. One is directly concerned with the fundamental derivation of the oscillation parameters that give rise to the three distinct grating interferometer signals. By replacing the traditional Fourier transform with a sine fit, the restrictions on the data acquisition are relaxed a bit, and the derived model is shown to be a better representation of the data. The other algorithm deals with the problem of the angular dependence of the dark-field signal. Since traditional reconstruction algorithms rely upon an assumption of the sample as a scalar field independent of propagation angle, this angular dependence renders these algorithms invalid. I have shown that it is possible to derive a better tomogram by shedding the scalar field-assumption, and countering the resulting underdetermination of the reconstruction problem by heavy regularisations. I have also tested two practical applications of the dark-field signal, where the unique structural origin of this contrast modality might be of use. In the first application, I have shown that we can use the sub-resolution structure dependence of the dark-field signal to image cracks in a solid material at a scale below the spatial resolution of the tomogram. In the other application, I introduced a slight modification to the grating interferometer tomography setup by shifting the rotation axis, to become aligned with the stepping direction of the grating. This shift of rotation axis removes the dark-field signal at all projection angles from fibers oriented along the stepping direction, leaving only a signal from any fibers not oriented along this direction. Finally, through my external collaborations, I have demonstrated the usefulness of synchrotron based absorption tomography in a number of fields. I have shown that synchrotron tomography allows us to visualize and quantify the very thin gas films at the leaves of certain periodically water-submerged plants in-situ. Within the field of dental implant integration evaluation, I have contributed to a couple of studies, most notably a study evaluating the effect of the decreased statistical uncertainty that is achieved when traditional 2-dimensional evaluation methods are replaced by high-resolution tomography.

Chapter 8

Outlook

As you have seen from the previous chapters, I believe that absorption is generally the preferable contrast modality in full-field x-ray imaging, and I expect absorption to remain the most widespread contrast modality in the immediate future, though I also expect that we will see both single-shot grating methods and raster scanning techniques being used for samples requiring either special contrast modalities or very high spatial resolution. If prices continue to go down, I also expect that directly converting detectors could be introduced in many lab-scale CT systems, which would offer improved contrast through reduced statistical noise and beam hardening artefacts. But most likely the biggest challenge as well as the biggest potential scientific gain lies in improving the data analysis. Already today, surveys show that by far the most time consuming part of the total work hours spent on a scientific project regarding a tomographic investigation at a synchrotron are spent on the data analysis. And unless the processes are somehow standardized and made more efficient, the time required for performing the data analysis will most likely only increase in the future, due to the increases in the size of datasets and the number of samples. A final point I have not touched upon is the possibility for the introduction of greatly improved lab scale x-ray sources. At this point, the most probable breakthrough of a radically new technology in this field seems to be the compact light source [27, 30]. The possibilities within this field have been investigated for some years without a decisive breakthrough, but the perspectives are very big if the efforts are successful. In the best case, this technology could essentially offer a lab-sized synchrotron source. The brilliance of such a source would of course be much lower than what full-scale synchrotrons can offer, but it could still be orders of magnitude higher than what traditional anode sources can offer. I'm aware of at least two projects currently working experimentally with a compact light source system, one at a private company in California, USA and one at the Technical University of Munich, Germany.

8.1 Lab tomography

One simple improvement of the typical commercial lab-based CT-scanner would be the exchange of the scintillator-based detector for a directly converting type. These detectors inherently come with some degree of energy-tunability in the form of at least one energy-threshold. Photons with energies below the selected threshold will not be included in the detector counts. Running several scans at different energy-thresholds would allow the user to measure photon flux for several different energy-intervals. The energy dispersivity will reduce the problem of beam-hardening artefacts that can severely distort the gray values of lab-source tomograms. This will be especially valuable for tomograms of samples spanning a wide spectrum of atomic numbers. In such tomograms, the beam-hardening artefacts between high-Z or high-density regions will tend to dominate the low-Z or low-density regions in between them, shadowing out the features of the low-Z (/-density) areas. Thus, the exchange of the scintillator detector for a directly converting one will significantly improve the imaging capabilities of such scanners. It is also feasible that some of the single-shot phase and dark-field methods could be implemented in mass produced laboratory CT-scanners, although I don't expect these methods to become the norm; their possible application will probably be limited to special cases where absorption contrast doesn't suffice. One such case could be the mapping of a sample with sub-resolution structural features not detectable in absorption tomography. For such a case dark-field tomography could prove useful. An exciting project that should be mentioned here is the Modular Dark Field Detector project hosted at Teknologisk Institut, Høje Taastrup, Denmark,

where an industry-ready dark field detector is being produced. The detector is being designed to function in an industrial production line environment, which is far from having the high stabilities we are used to in the labs.

8.2 Synchrotron tomography

Though synchrotron radiation, due to its high coherence and possible monochromaticity, offers the possibility of various elaborate phase-contrast techniques, these techniques are rarely applied. In most cases, simple absorption contrast tomography suffices to map the structural features of the sample, making the cumbersome and time-consuming phase-contrast techniques irrelevant. In most cases, the high brilliance offered at a synchrotron beamline is best utilized by reducing measurement times (i.e. increasing sample throughput) and increasing spatial resolution (i.e. decreasing pixel size) of an absorption contrast measurement. I don't expect voxel resolutions at synchrotrons to increase rapidly in the future. The beamlines of today typically use detectors with a resolution between 2000 and 3000 pixels, and going much higher puts some high demands on computation and storage resources. E.g. a typical tomogram of $2048 \times 2048 \times 2048$ voxels (i.e. a *2k cubed* tomogram) using a 32-bit float datatype requires 32 GB of storage space. If we increase the resolution to 4k cubed, the tomogram will require 256 GB of storage space. The storage itself of such a tomogram (or a series of tomograms, often several dozens of tomograms are obtained at a single beamtime) would probably not be our biggest challenge. The very large tomogram size would put huge demands on any computing resource performing calculations on it. Most calculations become orders of magnitude slower if we are not able to hold the entire tomogram (and possibly several versions or transforms of it) in memory, meaning that we now need a computing resource with at the very least half a TB of memory. Along with the large memory we will need a very powerful array of CPUs or GPUs to perform calculations. All of this trouble will only yield an increase in resolution of a factor of two, and for most cases will probably not be worth the effort. Instead, our efforts are probably best spent on tackling the challenges of high-throughput tomography. Automation of sample exchanges has already been implemented in some preliminary form on some beamlines, but it still isn't the norm and there is still much throughput to be gained by making automatic sample exchange a standard. This potential for improvement increases as the measurement times go down due to the increasing brilliance at beamlines. E.g. on a typical beamtime the measurement time for a single tomogram could be ten minutes. But the time it takes to close the shutter, walk into the experiment hutch, exchange samples, perform the hutch search and open the shutter easily takes several minutes as well. In addition to this comes the time it takes to align the new sample, typically several minutes. Because of all these tasks relating to the sample exchange, we often end up spending less than half the beamtime actually doing measurements. Last, but not least, the very high resolution of the raster scanning techniques become increasingly attractive as measurement times go down due to the increasing brilliance, and I imagine that we will see an increase in the number of publications using ptychography and similar methods in the future. The combination of traditional full-field imaging with ptychography offers interesting multiscale mapping that will probably also produce interesting results.

8.3 Data analysis challenges

I have included the small subsection you are now reading to elaborate on the solutions I see to the challenges regarding data amounts mentioned in section 8.2. The large data sizes and number of tomograms pose challenges to both the hardware and the analysis running on the hardware. I will focus here on the analysis. Today, tomogram analysis is largely ad hoc; segmentation methods and their variables are typically chosen based on a combination of experience, currently available methods and visual evaluation of their results. Likewise, the quantification parameters derived from the segmented tomogram are largely up to the individual authors, without any agreed standards within the individual scientific fields. It is obvious that for the sake of result comparison and reproducibility, it is highly preferable to have some standardization of the analysis methods. The lack of such methods can probably to a large degree be explained by the relatively recent introduction of x-ray tomography in many fields. By time, some methods will probably be generally accepted as the de facto standards within different fields. But there is nothing wrong with us x-ray scientists speeding up this process by encouraging this standardization both within individual fields and across different fields that share themes in their analysis. Especially

the last point of standardization across sample types offers great potential for improving data analysis efficiency. And, notably, this standardization must, at least partly, be up to us as x-ray scientists, since we can not expect the experts within individual sample types to have the necessary overview and experience to decide on the optimal analysis strategies across very general investigation fields. Along with this standardization comes the potential for automatization.

Bibliography

- [1] A. ANDERSEN AND A. KAK, *Simultaneous algebraic reconstruction technique (sart): A superior implementation of the art algorithm*, Ultrasonic Imaging, 6 (1984), pp. 81 – 94.
- [2] F. BAYER, S. ZABLER, C. BRENDEL, G. PELZER, J. RIEGER, A. RITTER, T. WEBER, T. MICHEL, AND G. ANTON, *Projection angle dependence in grating-based x-ray dark-field imaging of ordered structures*, Opt. Express, 21 (2013), pp. 19922–19933.
- [3] F. L. BAYER, S. HU, A. MAIER, T. WEBER, G. ANTON, T. MICHEL, AND C. P. RIESS, *Reconstruction of scalar and vectorial components in x-ray dark-field tomography*, Proceedings of the National Academy of Sciences, 111 (2014), pp. 12699–12704.
- [4] M. BECH, O. BUNK, T. DONATH, R. FEIDENHANS’L, C. DAVID, AND F. PFEIFFER, *Quantitative x-ray dark-field computed tomography*, Physics in Medicine and Biology, 55 (2010), p. 5529.
- [5] E. E. BENNETT, R. KOPACE, A. F. STEIN, AND H. WEN, *A grating-based single-shot x-ray phase contrast and diffraction method for in vivo imaging*, Medical Physics, 37 (2010), pp. 6047–6054.
- [6] P.-I. BRÅNEMARK, U. BREINE, R. ADELL, B. O. HANSSON, J. LINDSTRÖM, AND OHLSSON, *Intra-osseous anchorage of dental prostheses: i. experimental studies*, Scandinavian Journal of Plastic and Reconstructive Surgery, 3 (1969), pp. 81–100. PMID: 4924041.
- [7] A. BURVALL, U. LUNDSTRÖM, P. A. C. TAKMAN, D. H. LARSSON, AND H. M. HERTZ, *Phase retrieval in x-ray phase-contrast imaging suitable for tomography*, Opt. Express, 19 (2011), pp. 10359–10376.
- [8] M. DIEROLF, A. MENZEL, P. THIBAUT, P. SCHNEIDER, C. M. KEWISH, R. WEPF, O. BUNK, AND F. PFEIFFER, *Ptychographic x-ray computed tomography at the nanoscale*, Nature, 467 (2010), pp. 436–439.
- [9] L. A. FELDKAMP, L. C. DAVIS, AND J. W. KRESS, *Practical cone-beam algorithm*, J. Opt. Soc. Am. A, 1 (1984), pp. 612–619.
- [10] F. J. HARRIS, *On the use of windows for harmonic analysis with the discrete fourier transform*, Proceedings of the IEEE, 66 (1978), pp. 51–83.
- [11] J. E. HARVEY, *Fourier treatment of nearfield scalar diffraction theory*, American Journal of Physics, 47 (1979), pp. 974–980.
- [12] M. HOLLER, A. DIAZ, M. GUIZAR-SICAIROS, P. KARVINEN, E. FÄRM, E. HÄRKÖNEN, M. RITALA, A. MENZEL, J. RAABE, AND O. BUNK, *X-ray ptychographic computed tomography at 16nm isotropic 3d resolution*, Scientific Reports, 4 (2014), p. 3857.
- [13] P. HÄNDEL, *Properties of the ieee-std-1057 four-parameter sine wave fit algorithm*, IEEE Transactions on Instrumentation and Measurement, 49 (2000), pp. 1189–1193.
- [14] R. A. KETCHAM AND T. M. RYAN, *Quantification and visualization of anisotropy in trabecular bone*, Journal of Microscopy, 213 (2004), pp. 158–171.
- [15] T. LAURIDSEN, E. M. LAURIDSEN, AND R. FEIDENHANS’L, *Mapping misoriented fibers using x-ray dark field tomography*, Applied Physics A, 115 (2014), pp. 741–745.

- [16] T. LAURIDSEN, M. WILLNER, M. BECH, F. PFEIFFER, AND R. FEIDENHANS'L, *Detection of sub-pixel fractures in x-ray dark-field tomography*, Applied Physics A, 121 (2015), pp. 1243–1250.
- [17] A. MALECKI, G. POTDEVIN, T. BIERNATH, E. EGGL, K. WILLER, T. LASSER, J. MAISENBACHER, J. GIBMEIER, A. WANNER, AND F. PFEIFFER, *X-ray tensor tomography*, EPL (Europhysics Letters), 105 (2014), p. 38002.
- [18] K. S. MORGAN, D. M. PAGANIN, AND K. K. W. SIU, *Quantitative single-exposure x-ray phase contrast imaging using a single attenuation grid*, Opt. Express, 19 (2011), pp. 19781–19789.
- [19] ———, *X-ray phase imaging with a paper analyzer*, Applied Physics Letters, 100 (2012), p. 124102.
- [20] A. ODGAARD, J. KABEL, B. VAN RIETBERGEN, M. DALSTRA, AND R. HUISKES, *Fabric and elastic principal directions of cancellous bone are closely related*, Journal of Biomechanics, 30 (1997), pp. 487 – 495.
- [21] D. PAGANIN, S. C. MAYO, T. E. GUREYEV, P. R. MILLER, AND S. W. WILKINS, *Simultaneous phase and amplitude extraction from a single defocused image of a homogeneous object*, Journal of Microscopy, 206 (2002), pp. 33–40.
- [22] F. PFEIFFER, M. BECH, O. BUNK, P. KRAFT, E. F. EIKENBERRY, C. BRÖNNIMANN, C. GRÜNZWEIG, AND C. DAVID, *Hard-X-ray dark-field imaging using a grating interferometer*, Nature Materials, 7 (2008), pp. 134–137.
- [23] F. PFEIFFER, T. WEITKAMP, O. BUNK, AND C. DAVID, *Phase retrieval and differential phase-contrast imaging with low-brilliance X-ray sources*, Nature Physics, 2 (2006), pp. 258–261.
- [24] V. REVOL, I. JERJEN, C. KOTTLER, P. SCHÜTZ, R. KAUFMANN, T. LÜTHI, U. SENNHAUSER, U. STRAUMANN, AND C. URBAN, *Sub-pixel porosity revealed by x-ray scatter dark field imaging*, Journal of Applied Physics, 110 (2011), p. 044912.
- [25] V. REVOL, C. KOTTLER, R. KAUFMANN, A. NEELS, AND A. DOMMANN, *Orientation-selective x-ray dark field imaging of ordered systems*, Journal of Applied Physics, 112 (2012), p. 114903.
- [26] G. SATO, H. ITOH, K. NAGAI, T. NAKAMURA, K. YAMAGUCHI, T. KONDOH, S. HANDA, C. OUCHI, T. TESHIMA, Y. SETOMOTO, AND T. DEN, *Single-shot x-ray phase-contrast imaging using two-dimensional gratings*, AIP Conference Proceedings, 1466 (2012), pp. 29–34.
- [27] G. SHAMUILOV AND K. ZOLOTAREV, *The project of a magnetic system for compact x-ray light source*, Physics Procedia, 84 (2016), pp. 118 – 125. Proceedings of the International Conference "Synchrotron and Free electron laser Radiation: generation and application" (SFR-2016), July 4 - 7, 2016, Novosibirsk, Russia.
- [28] T. H. SMIT, E. SCHNEIDER, AND A. ODGAARD, *Star length distribution: a volume-based concept for the characterization of structural anisotropy*, Journal of Microscopy, 191 (1998), pp. 249–257.
- [29] A. SS, S. R, I. TV, AND ET AL, *Botulinum toxin as a biological weapon: Medical and public health management*, JAMA, 285 (2001), pp. 1059–1070.
- [30] A. STREUN AND A. WRULICH, *Compact low emittance light sources based on longitudinal gradient bending magnets*, Nuclear Instruments and Methods in Physics Research Section A: Accelerators, Spectrometers, Detectors and Associated Equipment, 770 (2015), pp. 98 – 112.
- [31] D. STUTMAN, M. P. VALDIVIA, AND M. FINKENTHAL, *X-ray moiré deflectometry using synthetic reference images*, Appl. Opt., 54 (2015), pp. 5956–5961.
- [32] H. TURBELL, *Cone-Beam Reconstruction Using Filtered Backprojection*, PhD thesis, Linköpings universitet, 2001.
- [33] J. VOGEL, F. SCHAFF, A. FEHRINGER, C. JUD, M. WIECZOREK, F. PFEIFFER, AND T. LASSER, *Constrained x-ray tensor tomography reconstruction*, Opt. Express, 23 (2015), pp. 15134–15151.

- [34] T. WEITKAMP, C. DAVID, C. KOTTLER, O. BUNK, AND F. PFEIFFER, *Tomography with grating interferometers at low-brilliance sources*, Proceedings of the SPIE, 6318 (2006), p. 63180S.
- [35] H. H. WEN, E. E. BENNETT, R. KOPACE, A. F. STEIN, AND V. PAI, *Single-shot x-ray differential phase-contrast and diffraction imaging using two-dimensional transmission gratings*, Opt. Lett., 35 (2010), pp. 1932–1934.
- [36] F. YANG, F. PRADE, M. GRIFFA, I. JERJEN, C. D. BELLA, J. HERZEN, A. SARAPATA, F. PFEIFFER, AND P. LURA, *Dark-field x-ray imaging of unsaturated water transport in porous materials*, Applied Physics Letters, 105 (2014), p. 154105.
- [37] W. YASHIRO AND A. MOMOSE, *Effects of unresolvable edges in grating-based x-ray differential phase imaging*, Opt. Express, 23 (2015), pp. 9233–9251.
- [38] W. YASHIRO, Y. TERUI, K. KAWABATA, AND A. MOMOSE, *On the origin of visibility contrast in x-ray talbot interferometry*, Opt. Express, 18 (2010), pp. 16890–16901.

Appendix A

Main publications

This appendix contains the publications that represent the bulk of my work during my PhD-study. I have first-authored all of them except one. I have been the sole contributor to the actual analysis of x-ray imaging data in all of them (i.e. I have written the Matlab/Python code), but I have of course been guided by all the people around me in deciding the course of analysis. Four of the listed seven articles are published, and the remaining three are submitted at the time of writing. I have also contributed to a few other articles than the ones mentioned in this chapter. These secondary articles are listed in chapter B.

A.1

Detection of sub-pixel fractures in X-ray dark-field tomography

Applied Physics A (2015)

T. Lauridsen, M. Willner, M. Bech, F. Pfeiffer, R. Feidenhans'l

Appl. Phys. A (2015) 121: 1243–1250 DOI:0.1007/s00339-015-9496-2

Detection of sub-pixel fractures in X-ray dark-field tomography

Torsten Lauridsen¹ · Marian Willner² · Martin Bech³ · Franz Pfeiffer² · Robert Feidenhans¹

Received: 22 June 2015 / Accepted: 15 September 2015 / Published online: 23 September 2015
© Springer-Verlag Berlin Heidelberg 2015

Abstract We present a new method for detecting fractures in solid materials below the resolution given by the detector pixel size by using grating-based X-ray interferometry. The technique is particularly useful for detecting sub-pixel cracks in large samples where the size of the sample is preventing high-resolution μ CT studies of the entire sample. The X-ray grating interferometer produces three distinct modality signals: absorption, phase and dark field. The method utilizes the unique scattering features of the dark-field signal. We have used tomograms reconstructed from each of the three signals to detect cracks in a model sample consisting of stearin.

1 Introduction

Computer aided X-ray tomography (also called CT scanning) is a powerful technique for revealing the three-dimensional structure of materials and is used in a widespread range of technical applications [1–4]. However, the lateral resolution of the reconstructed images is limited by the pixel size of the X-ray detector, typically 50 microns or more. CT systems offering smaller pixel sizes exist, but a smaller pixel size results in a correspondingly smaller field of view. Thus, the desire to scan large objects (on the order of several cm) leads to large pixel sizes, limiting the

sensitivity of CT scanning to detect failures like cracks in materials or delaminations in the junction between two materials. Having a technique that could detect such failures at a very small scale while retaining a large field of view would give new possibilities, e.g. for improving the lifetime of functional materials.

Grating-based interferometry offers this possibility [5–9]. In normal CT scanning, the X-ray absorption signal is used to reconstruct the three-dimensional structure of the sample using variations in the materials' X-ray absorption coefficients as contrast mechanism. In grating-based interferometry, two more signals can be obtained: the differential phase contrast and the dark-field signal [10, 11]. The differential phase contrast is measured indirectly by detecting small distortions in an interference pattern that is produced by an X-ray grating placed in the beam path [12–16]. This contrast modality can further be used to quantify the electron density distribution of the material [17–19].

The dark-field signal is a measure of the visibility of this interference pattern. If a strongly scattering sample is placed behind the grating, the visibility of the interference pattern is reduced, which can be used to obtain information about variations in the microstructure of the sample [5–9, 20, 21]. Hence, it is sensitive to sub-pixel phase structures, such as air bubbles in metal which give rise to scattering [8]. The degree of decoherence introduced by a given small volume is generally anisotropic. A sub-pixel crack will scatter the X-ray beam at certain orientations and produce a different dark-field signal, depending on whether the X-ray beam passes along the crack orientation or perpendicular to it. This anisotropy is opposite to the absorption signal, which is isotropic for homogenous volumes. The isotropy of the absorption signal is a prerequisite of the filtered back-projection algorithm used for the reconstruction of absorption tomograms. In this paper, we have neglected the

✉ Torsten Lauridsen
torstenl@nbi.ku.dk

¹ Niels Bohr Institute, University of Copenhagen, Copenhagen, Denmark

² Department of Physics and Institute of Medical Engineering, Technische Universität München, Garching, Germany

³ Medical Radiation Physics, Lund University, Lund, Sweden

anisotropy of the dark-field signal and performed a filtered back-projection of the dark-field signal. This approach has been shown to lead to meaningful dark-field tomograms in earlier studies [6–8]. It has been shown [22] that it is possible to reconstruct an orientation tensor map of the dark-field signal, but the method is time-consuming. Here, we demonstrate that the filtered back-projection dark-field tomogram reveals sub-pixel cracks much more efficiently than the absorption signal and, hence, justifies its application in technical areas.

2 Experimental

2.1 Sample

As a model sample, we have chosen stearin, which is easy to handle and makes many cracks upon rapid cooling. The stearic acid (C₁₈H₃₆O₂) was heated to 70 °C (melting point is 69.6 °C). Molten stearic acid was poured in an aluminium container placed in a liquid nitrogen bath (boiling temperature is 196 °C). The rapid freezing causes the stearin to form cracks as it deforms under the tension created by the molecular rearrangements at low temperatures [23–25]. The resulting piece of stearic acid (size $\sim 2 \times 2 \times 4$ cm³) was scanned in the X-ray grating interferometer. During measurements, the sample was held in a cylindrical plastic container.

2.2 Set-up

The X-ray grating interferometer laboratory set-up consists of three gratings (G0, G1 and G2), an X-ray source and a detector (see Fig. 1).

The first grating, G0, is placed close to the source and represents an array of slits, which increases the beam coherence. The second grating, G1, is a phase grating that creates an interference pattern downstream by inducing a periodically varying phase shift to the X-rays. The resulting

intensity modulations can be resolved by another absorption grating, G2, which is installed in front of the detector. It is of the same period as the interference pattern and translated perpendicular to the beam, while several images are acquired. During this phase-stepping process, a sinusoidal intensity oscillation is recorded in each detector pixel and small shifts in the interference pattern arising from refraction effects in the sample can be mapped. A detailed description of the principle of X-ray grating interferometry at laboratory X-ray sources is given by [26].

A rotating molybdenum anode X-ray tube with an acceleration voltage of 40 kV and a current of 70 mA was used in the measurements. A photon-counting Pilatus II (Dectris, Switzerland) with a pixel size of 172×172 μm^2 was employed as detector. The gratings were fabricated by the Karlsruhe Institute of Technology and Microworks GmbH (Karlsruhe, Germany) and are described in Table 1.

The set-up distances are listed in Table 2.

2.3 Scan procedure

Each phase scan consisted of 12 detector exposures, each exposure lasting 3 s. For each exposure, the phase grating was stepped one-eleventh of the grating period, making the first and last exposure identical. Fifty flat-field phase scans were performed before the sample scans and another 50

Table 1 Descriptions of the three gratings used

Gratings	G0	G1	G2
Period	5.4 μm	5.4 μm	5.4 μm
Material	Au	Ni	Au

Table 2 Set-up distances

G0–G1	G1–G2	Sample mount G2	G2 detector
80 cm	80 cm	16 cm	8 cm

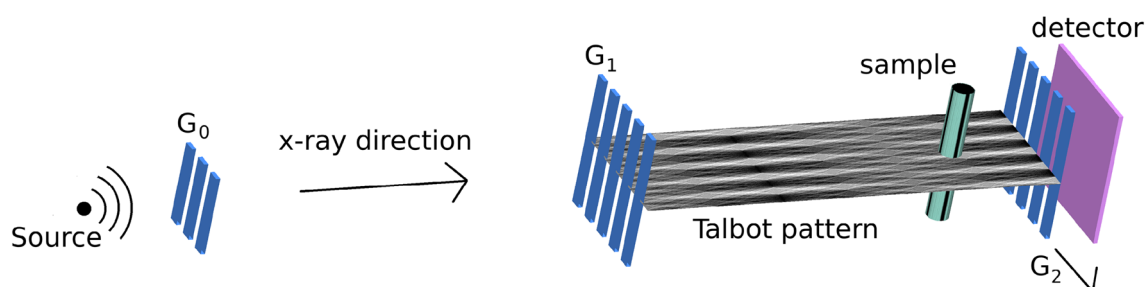


Fig. 1 Experimental set-up. X-ray photons enter through the source grating G0, pass the phase grating G1 and the sample before exiting through the absorption grating G2 and hit the detector screen. Grating periods are not to scale, and the figure disregards magnification and

intensity loss in the interference pattern due to incoherence. The translation direction for the phase scanning motion of G2 is marked by an arrow

after the sample scans. The sample was scanned in 501 phase scans, covering 360° of sample rotation.

2.4 Theory

2.4.1 Reconstruction

To reconstruct the dark-field signal of the stearin sample, we have assumed a Gaussian angular distribution of the beam. The sample is considered as a distribution of a divergence-introducing coefficient ϵ , named the linear diffusion coefficient, giving rise to a Gaussianly distributed increase in beam divergence [10]. For X-rays passing through a certain distance of the sample, the resulting angular beam distribution will be a convolution of the initial distribution and the distribution introduced by the linear diffusion coefficient ϵ [10]. Since both distributions are assumed to be Gaussian, the convolution product will be another Gaussian with a divergence given by an integral along the beam path z :

$$\sigma^2 = \sigma_0^2 + \int \epsilon(z)dz \tag{1}$$

In the ideal case of no beam divergence, the phase step scan function of the grating interferometer will be a triangle function. But in the presence of beam divergence, this triangular function should be convoluted with the angular beam distribution, which we have assumed to be Gaussian. The convolution of a triangle function and a Gaussian distribution is:

$$\frac{I(x)}{I_0} = 1 + \frac{8}{\pi^2} e^{-\pi^2 2(\sigma/p)^2} \cos\left(\frac{2\pi}{p}x\right) + \dots \tag{2}$$

where I_0 is the average beam intensity across the phase step scan, and x is the grating position in the scanning direction. The next term in the sum is the third-order term, which is much smaller than the first-order term, and is hence disregarded, as are all higher-order terms. The amplitude of the cosine oscillation in Eq. (2) is called the visibility. As can be seen from Eq. (2), it falls off with increased beam decoherence (σ). To quantify the decoherence-induced visibility loss, the dark-field signal is defined as the relative visibility (using a phase step scan with no sample, i.e. a flat field, as reference). Using this dark field definition and Eq. (2), we get:

$$\begin{aligned} DF &= \frac{V_{\text{sample}}}{V_{\text{flat}}} \\ &= \frac{e^{-\pi^2 2(\sigma_{\text{sample}}/p)^2}}{e^{-\pi^2 2(\sigma_{\text{flat}}/p)^2}} \\ &= e^{-\pi^2 2((\sigma_{\text{sample}} - \sigma_{\text{flat}})/p)^2} \end{aligned} \tag{3}$$

This result is analogous to the absorption signal, and hence, the filtered back-projection procedure used for retrieving the absorption coefficient distribution can also be used to find the linear diffusion coefficient distribution.

The reconstruction was performed with an inverse radon transform and a Hamming filter. Figure 2 illustrates two reconstructions of the same slice, mapping the absorption coefficient and the linear diffusion coefficient, respectively.

2.4.2 Detecting cracks

It is clear from both slices in Fig. 2 that structures have formed within the stearin sample. From the absorption slice, we can see that these structures have lower

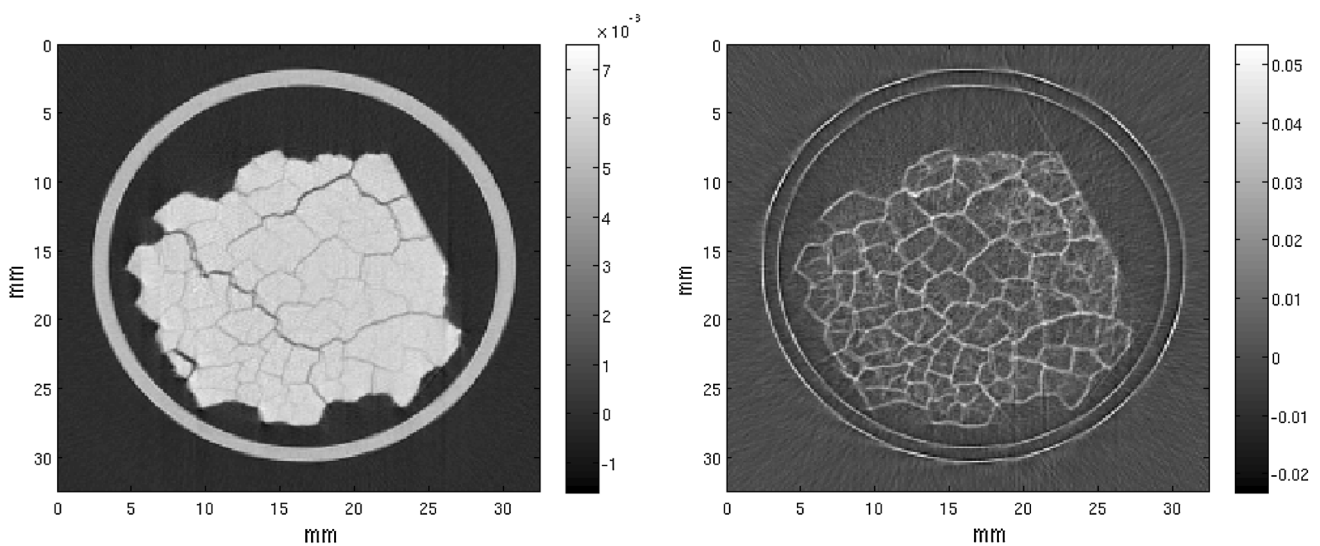


Fig. 2 Reconstructions of a 2D slice. *Left*: absorption signal, *right*: dark-field signal. The circular object surrounding the stearin sample is the sample container. The resolution is (among other factors) limited by the pixel size of the detector, which is 172 μm

absorption coefficients than the surrounding stearin, and in some cases, the coefficient is as low as in the air surrounding the stearin. This indicates that the structures we see in the absorption slice are indeed cracks. Absorption coefficient values in an absorption reconstruction can be considered volume averages. As a consequence, sub-pixel variations in the absorption coefficient are not resolved in the reconstruction. Instead the reconstruction gives the average absorption coefficient over the particular pixel volumes. This means that small cracks only taking up a fraction of the pixel volume will only reduce the signal by a corresponding fraction. This explains the very different absorption coefficients seen in the cracks in the absorption slice. Some cracks are so wide that they span entire pixels and give the absorption coefficient of the pixels the same value as the surrounding air. Other cracks are so narrow that the absorption coefficient reduction is so small that it is not detectable. Detecting cracks by absorption μ CT of the entire sample would be a formidably time-consuming task and would lead to impractically large data sets that cannot be handled efficiently by today's computers.

By comparing the dark-field slice with the absorption slice, we can see that there is a large overlap between the crack structure in the absorption slice and the structures in the dark-field image. It is also clear that the diffusion coefficient intensities of these cracks are not proportional to the absorption coefficient reductions in the corresponding pixels in the absorption slice: some cracks that are barely visible in the absorption slice are clearly visible in

the dark-field slice. For some cracks, this tendency is so strong that these cracks are not visible in the absorption slice at all, but clearly visible in the dark-field slice. Other cracks are clearly visible in the absorption image, but barely visible in the dark-field image. These cracks typically have a width spanning a pixel length or more. Such wide cracks will have a very low absorption coefficient in the centre (i.e. the absorption coefficient of air), but produce no dark-field signal in terms of decoherence of the X-ray beam from the scattering.

2.4.3 Origin of the dark-field signal

Our interpretation is that the dark-field signal created by the cracks originates from a scattering from edges (including surface roughness) at the sub-pixel length scale at the crack/stearin interface [8, 9] and hence gives rise to a loss of coherence.

It is obvious from Fig. 3 that the degree of decoherence introduced by scattering from a crack is anisotropic. If the sample is rotated 90° (corresponding to the X-ray beam being horizontal in Fig. 3), only some of the photons will cross the stearin/air interface. This means that the majority of the X-ray beam will not experience a coherence loss, and the dark-field signal induced by the pixels at this sample orientation will probably be lower than in the orientation depicted in Fig. 3. This is the anisotropy we have disregarded by using a traditional radon transform in the reconstruction of the dark-field slice. Generally, the cracks

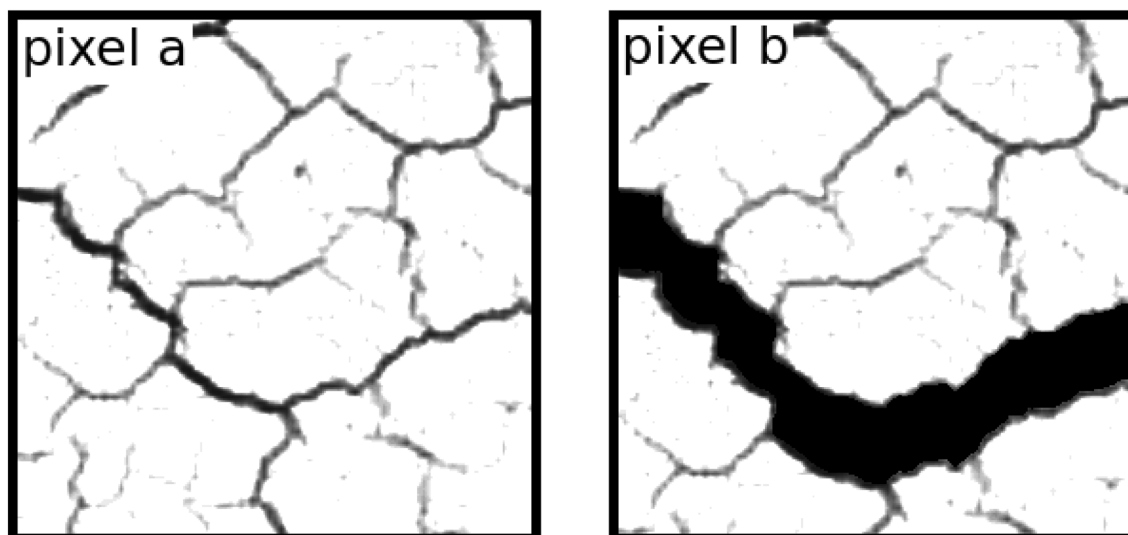


Fig. 3 Illustration of our sub-pixel surface roughness model. According to this model, surface roughness at the crack/stearin interface creates scattering in the beam direction. Pixel **a** has a narrow crack and will have an absorption coefficient close to that of stearin. Pixel **b** has a wide crack, which will lower its absorption coefficient more than for pixel **a**. Though the cracks have different widths, their

surface roughness in the figure is assumed to be the same. This means that the roughness-induced scattering in the beam is the same for the two pixels (illustrated by the *arrows*). Thus, the coherence loss will be the same for the two pixels, and the dark-field signal will hence also be the same. In the study at hand, the effective pixel size was $147 \mu\text{m}$

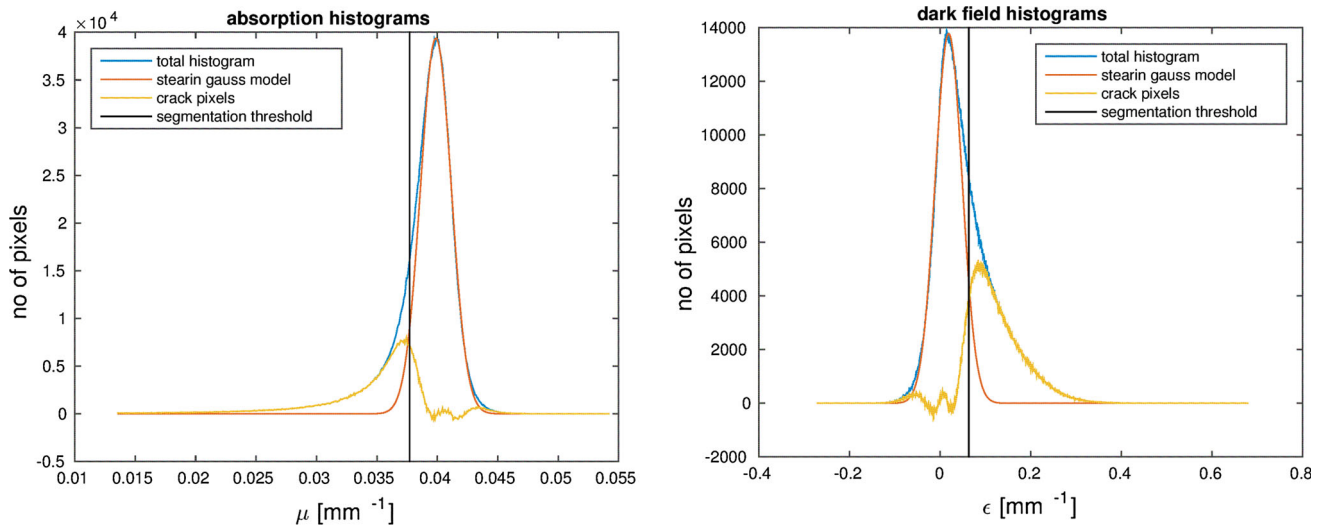


Fig. 4 Histograms of the pixel value distributions within the masked volume (*left*: absorption histograms, *right*: dark-field histograms). The *blue line* is the actual pixel value histogram. The *red line* is the fitted

Gaussian distribution, and the *yellow line* is the residual histogram (the difference between the actual histogram and the Gaussian model.)

have no preferred orientation, and furthermore, all larger cracks seem to have smaller perpendicular cracks running away from them. This complex structure of cracks with many different directions, even on a small length scale, suggests that the assumption of anisotropy is approximately valid.

2.5 Calculations

2.5.1 Masking

To detect the cracks in the reconstructed slices, we first have to determine the outer edge of the stearin sample (i.e. the mask). This was done by applying a threshold segmentation to the absorption slice. Pixels having an absorption coefficient above a certain value were segmented as ones, the rest as zeroes. A dilation operation was then performed to connect all stearin components. Finally, the plastic tube pixels were removed manually. This gave a binary mask defining the outer extent of the stearin sample.

2.5.2 Crack segmentation

Having determined the outer edge of the stearin sample, we now segment the cracks by applying a threshold filter to either the absorption slice or the dark-field slice. Pixels having an absorption coefficient below a certain value or a linear diffusion coefficient above a certain value were segmented as cracks if they lay within the stearin mask. To determine the relevant threshold values, we investigated the histograms of the pixel value distributions within the masked volume.

A simple threshold segmentation was applied to each of the two tomograms (dark field and absorption) to identify the crack pixels. The thresholds were chosen based on the level of skewness of the histogram distributions of the masked pixels (the blue lines in Fig. 4). To determine a segmentation threshold value, we made two assumptions: the first assumption was that the narrow side of each histogram only contained values from pixels with insignificant levels of crack formation. The other assumption was that the experimental uncertainty leads to Gaussian distributed values for a homogeneous sample. Based on these assumptions, we could fit a Gaussian distribution to the narrow side of each histogram (the red lines in Fig. 4). From the Gaussian distributions and the total histograms, the crack pixel histograms could be estimated (yellow lines in Fig. 4), and from the estimated crack pixel histograms, the number of crack pixels could be found as the integrated area under the curves. The threshold values were now chosen so that they led to the estimated number of crack pixels.

3 Results

The segmentations led to the number of detected crack voxels shown in Table 3.

As can be seen from the numbers in Table 3, there is a big overlap between the segmentations of each of the two tomograms. Of all the absorption-segmented pixels, 83 % are also found in the dark-field segmentation (Table 4). A 2D histogram of the distribution of absorption and dark-field values within the sample is shown in Fig. 5.

From the histogram in Fig. 5 and the numbers in Table 3, it is clear that the dark-field segmentation contains

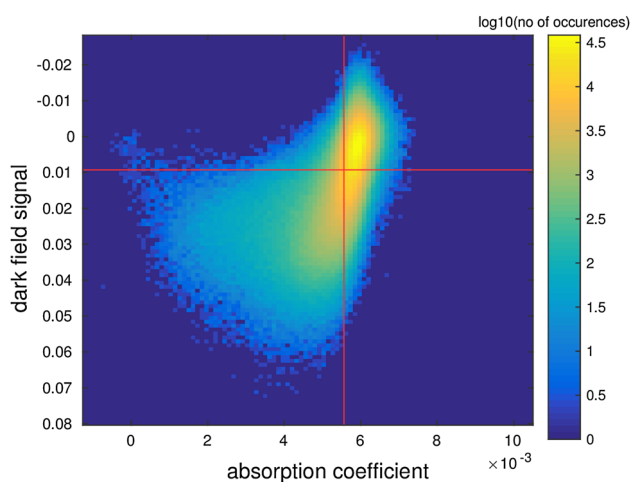
Table 3 Number of segmented pixels

	Absorption only	Dark field only	Both
No. of crack pixels	92.623	446.243	449.220

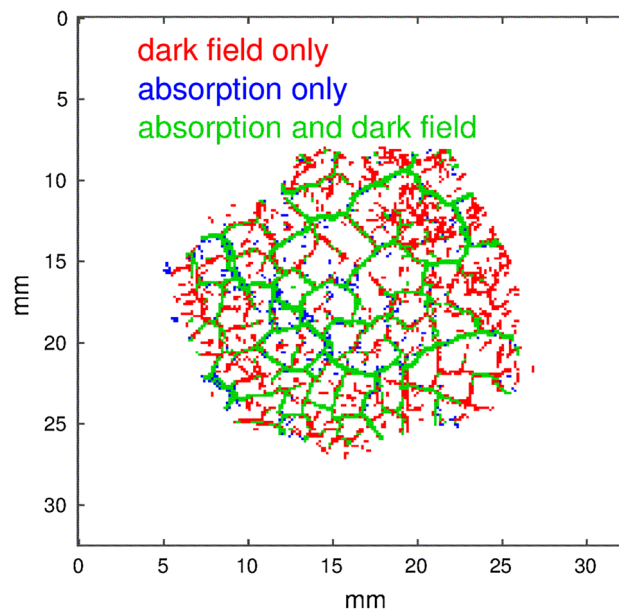
Left: number of segmented pixels found in the absorption segmentation, but not the dark-field segmentation. Centre: number of segmented pixels found in the dark-field segmentation, but not the absorption segmentation. Right: number of segmented pixels found in both the absorption segmentation and the dark-field segmentation

Table 4 Connectivities and average number of exposed voxel faces for the two segmentation methods. Each voxel has 6 faces, and each voxel face is considered exposed if its neighbouring voxel is not a crack voxel

	Absorption-detected voxels	Dark-field-detected voxels
Rel. size of largest conn comp	96.6 %	98.7 %
Average number of exposed faces per voxel	2.36	1.83

**Fig. 5** 2D Histogram showing the distribution of absorption and dark-field values within the tomograms. Segmentation threshold values are indicated with red lines

a lot of voxels with relatively high absorption coefficient values. These voxels can be interpreted as narrow-gapped cracks with a width too small to be recognizable in the absorption tomogram. This interpretation seems to be in agreement with the impression from Fig. 6, where the bigger central cracks are generally detected by both segmentations, but the smaller more peripheral cracks are only detected in the dark-field segmentation. These smaller dark-field-detected cracks tend to lie in connection with the absorption-detected ones, indicating that they are probably just narrower continuations of the broader absorption-detected parts of the same crack lines. This interpretation is

**Fig. 6** One slice combining the segmented dark field and absorption tomograms. The slice is the same as shown in Fig. 2

further supported by the numbers in Table 4, which show that the dark-field-detected cracks are generally more interconnected than their absorption-detected counterparts.

The cracks in all tomograms are highly connected, as can be seen from Table 4. For the dark-field tomogram, 98.7 % of the segmented crack pixels are within the same connected component. The corresponding number for the absorption tomogram is 96.6 %. Each voxel has 6 faces, each of which has one neighbouring voxel. These neighbouring voxels can either be segmented as cracks or not cracks. A voxel face is considered *exposed* if its neighbour is not a crack voxel. It should be noted that one-voxel thin 2D structures are expected to have approximately 2 exposed surfaces per voxel, depending on the orientation and curvature of the 2D surface. In our case, the cracks are often thicker than one voxel, and we have frequent crack intersections, both effects leading to lower average exposures. Thus, a crack voxel can have anywhere between 0 and 6 (both numbers included) exposed faces. The dark-field-detected crack voxels on average had 1.83 exposed faces. The absorption-detected voxels had 2.36 exposed faces on average.

3.1 Volume renderings

The volume renderings of the segmented results shown in Figs. 7 and 8 support the interpretation of the results in Table 4 and Fig. 6 of two highly interconnected segmentations. Figure 7 shows the intersection of dark-field and absorption-detected pixels. These are clearly highly

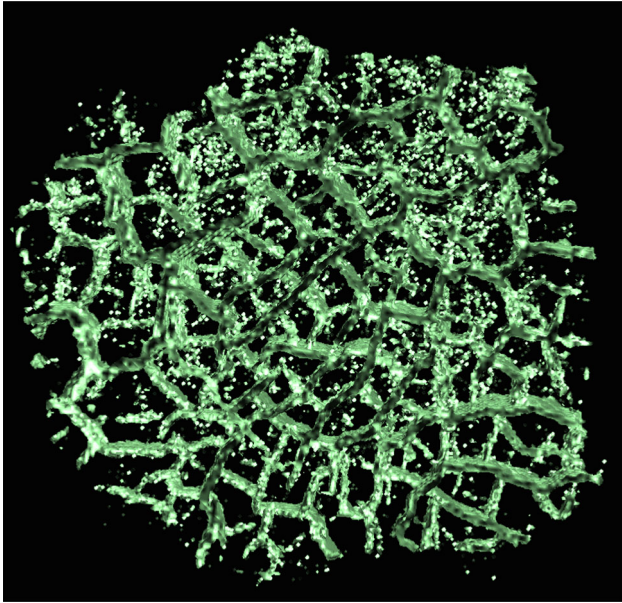


Fig. 7 Volume rendering of a $20 \times 20 \times 5$ mm segmented piece of stearin. Only pixels segmented as crack pixels in both the absorption tomogram and the dark-field tomogram are in green. The tomogram sub-volume shown in this figure, and the angle at which it is shown, is exactly the same as in Fig. 8

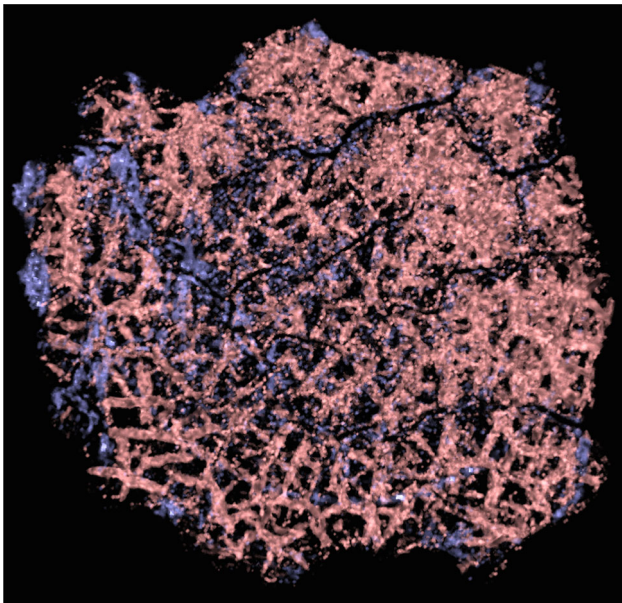


Fig. 8 Volume rendering of a $20 \times 20 \times 5$ mm segmented piece of stearin. Voxels segmented as crack voxels in the absorption tomogram but not in the dark-field tomogram are *blue*. Voxels segmented as crack voxels in the dark-field tomogram but not in the absorption tomogram are *red*. All other pixels are not shown. The tomogram sub-volume shown in this figure, and the angle at which it is shown, is exactly the same as in Fig. 7

interconnected. Figure 8 shows a high level of interconnection of the “pure” dark-field-segmented pixels (red), and a seemingly lesser degree of interconnection of the

“pure” absorption-detected pixels (blue), which is in agreement with the results in Table 4.

4 Discussion

The dark-field signal from an X-ray grating interferometer can be used as a measure of the scattering properties of a sample. We have used this scattering signal to reconstruct a 3D map of the scattering properties of the sample. The sample was a bulk piece of highly crack-affected stearin. Our investigations show that dark-field imaging reveals a larger total crack volume than traditional absorption imaging. Using the dark-field signal, we classified 1.65 times as many crack voxels as we did with the absorption signal. The uniquely dark-field-detected voxels (those only detected by the dark-field signal) tend to lie in continuation of the absorption-detected crack lines. Thus, we interpret them as being part of the same crack lines as their absorption-detected continuations, but too narrow to be detected in the absorption signal. The dark-field-detected crack voxels on average are less exposed to non-crack voxels than the absorption-detected ones, with both numbers being quite low (1.83 and 2.36, respectively). Together with visual inspection of the volume renderings, these numbers indicate that the crack voxels in both segmentations tend to cluster together in 2D-like structures.

5 Conclusion

We have shown that X-ray dark-field tomography is sensitive to detect cracks that in size are below the resolution of the absorption tomogram (and hence invisible). Hence, the scattering from fine cracks detected in the dark-field signal can be used to visualize the finer crack structure invisible to the absorption technique due to resolution limitations typical for large samples. This opens up new possibilities to detect the formation of cracks in materials under wear and stress much earlier than today with traditional X-ray inspection.

Acknowledgements We acknowledge Maria Thomsen, Mikkel Schou Nielsen and Katrine R. Rosenmejer Nielsen (all from University of Copenhagen) for their help and assistance. We also thank the Danish Strategic Research Council for support from the NEXIM project and we also thank support from the CIA-CT project.

References

1. T. Suzuki, M. Aoki, M. Ohtsu, Damage identification of cracked concrete by X-ray computed tomography method. In: Proceedings of FraMCoS-7, May 23–28, (2010), pp. 1143–1148

2. B.D. Metscher, Biological applications of X-ray microtomography: imaging microanatomy, molecular expression and organismal diversity. *Microsc. Anal.* **27**(2), 13–16 (2013)
3. W.A. Kalender, X-ray computed tomography. *Phys. Med. Biol.* **51**, R29–R43 (2006)
4. F. Beckmann, R. Grupp, A. Haibel, M. Huppmann, M. Nöthe, A. Pyzalla, W. Reimers, A. Schreyer, R. Zettler, In-situ synchrotron X-ray microtomography studies of microstructure and damage evolution in engineering materials. *Adv. Eng. Mater* **9**(11), 939–950 (2007)
5. F. Pfeiffer, M. Bech, O. Bunk, P. Kraft, E.F. Eikenberry, Ch. Bronniman, C. Grunzweig, C. David, Hard-X-ray dark-field imaging using a grating interferometer. *Nat. Mater.* **7**, 134–137 (2008)
6. M. Bech, O. Bunk, T. Donath, R. Feidenhans'l, C. David, F. Pfeiffer, Quantitative X-ray dark-field computed tomography. *Phys. Med. Biol.* **55**, 5529–5539 (2010)
7. W. Cong, F. Pfeiffer, M. Bech, G. Wang, X-ray dark-field imaging modeling. *J Opt. Soc. Am. A* **29**(6), 908–912 (2012)
8. V. Revol, I. Jerjen, C. Kottler et al., Sub-pixel porosity revealed by X-ray scatter dark field imaging. *J. Appl. Phys.* **110**, 044912 (2011)
9. W. Yashiro, A. Momose, Effects of unresolvable edges in grating-based X-ray differential phase imaging. *Opt. Express* **23**(7), 9233–9251 (2015)
10. M. Bech, X-ray imaging with a grating interferometer. PhD Thesis, University of Copenhagen, 2009
11. Atsushi Momose, Shinya Kawamoto, Ichiro Koyama, Yoshitaka Hamaishi, Kengo Takai, Yoshio Suzuki, Demonstration of X-ray Talbot Interferometry. *Jpn. J. Appl. Phys.* **42**(7B), 866 (2003)
12. Atsushi Momose, Phase-sensitive imaging and phase tomography using X-ray interferometers. *Opt. Express* **11**(19), 2303 (2003)
13. C. David, T. Weitkamp, F. Pfeiffer, A. Diaz, J. Bruder, T. Rohbeck, A. Groso, O. Bunk, M. Stampanoni, P. Cloetens, Hard X-ray phase imaging and tomography using a grating interferometer. *Spectrochim. Acta Part B* **62**, 626–630 (2007)
14. C. David, B. Nöhammer, H.H. Solak, E. Ziegler, Differential X-ray phase contrast imaging using a shearing interferometer. *Appl. Phys. Lett.* **81**, 3287 (2002)
15. F. Pfeiffer, C. Kottler, O. Bunk, C. David, Hard X-ray phase tomography with low-brilliance sources. *Phys. Rev. Lett.* **98**, 108105 (2007)
16. Timm Weitkamp, Ana Diaz, Christian David, Franz Pfeiffer, Marco Stampanoni, Peter Cloetens, Eric Ziegler, X-ray phase imaging with a grating interferometer. *Opt. Express* **12**(16), 6296 (2005)
17. J. Herzen, T. Donath, F. Pfeiffer, O. Bunk, C. Padeste, F. Beckmann, A. Schreyer, C. David, Quantitative phase-contrast tomography of a liquid phantom using a conventional X-ray tube source. *Opt. Express* **17**(12), 10010–10018 (2009)
18. M.S. Nielsen, T. Lauridsen, M. Thomsen, T.H. Jensen, M. Bech, L.B. Christensen, E.V. Olsen, M. Hviid, R.K. Feidenhans'l, F. Pfeiffer, X-ray tomography using the full complex index of refraction. *Phys. Med. Biol.* **57**(19), 5971–5979 (2012)
19. M. Willner, J. Herzen, S. Grandl, S. Auweter, D. Mayr, A. Hipp, M. Chabior, A. Sarapata, K. Achterhold, I. Zanette, T. Weitkamp, A. Sztrókay, K. Hellerhoff, M. Reiser, F. Pfeiffer, Quantitative breast tissue characterization using grating-based X-ray phase-contrast imaging. *Phys. Med. Biol.* **59**(7), 1557–1571 (2014)
20. W. Yashiro, Y. Terui, K. Kawabata, A. Momose, On the origin of visibility contrast in X-ray Talbot interferometry. *Opt. Express* **18**(16), 16890 (2010)
21. F. Yang, F. Prade, M. Griffa, I. Jerjen, C. Di Bella, J. Herzen, A. Sarapata, F. Pfeiffer, P. Lura, Dark-field X-ray imaging of unsaturated water transport in porous materials. *Appl. Phys. Lett.* **105**, 154105 (2014)
22. Andreas Dominik Malecki, X-ray Tensor Tomography. PhD Thesis, Technische Universität München (2013)
23. Z. P. Bazant, H. Ohtsubo, K. Aoh, Stability and post-critical growth of a system of cooling or shrinkage cracks. *Int. J. Fract.* **15**(5), 443–456 (1979)
24. S. Tarasovs, A. Ghassemi, Self-similarity and scaling of thermal shock fractures. *Phys. Rev. E* **90**, 012403 (2014)
25. D.P.H. Hasselman, Unified theory of thermal shock fracture initiation and crack propagation in brittle ceramics. *J. Am. Ceram. Soc.* **52**(11), 600–604 (1969)
26. F. Pfeiffer, T. Weitkamp, O. Bunk, C. David, Phase retrieval and differential phase-contrast imaging with low-brilliance X-ray sources. *Nat. Phys.* **2**, 258–261 (2006)

A.2

Mapping misoriented fibers using X-ray dark field tomography

Applied Physics A (2014)

T. Lauridsen, E. M. Lauridsen, R. Feidenhans'l

Appl. Phys. A (2014) 115: 741–745

Mapping misoriented fibers using X-ray dark field tomography

Torsten Lauridsen · Erik M. Lauridsen ·
Robert Feidenhans'l

Received: 5 March 2014 / Accepted: 18 March 2014 / Published online: 8 April 2014
© Springer-Verlag Berlin Heidelberg 2014

Abstract X-ray grating interferometers produce three distinct signals; an absorption signal, a differential phase signal and a dark field signal. Until now a method for successfully creating dark field tomograms of nonisotropic samples has not been demonstrated. In this paper we test a method for creating such tomograms on a highly nonisotropic sample, i.e. a five layer “sandwich” of oriented carbon fibers. The fibers are parallel within the individual sandwich layers, but perpendicular to the fibers in the adjacent layers. We show that by choosing a rotation axis parallel to the grating stepping direction (i.e. a horizontal rotation axis in most setup configurations) it is possible to produce a darkfield tomogram where fibers parallel to the probed scattering direction appear to have no dark field signal. The method produces a tomogram in the form of a scalar field of dark field scattering values.

1 Introduction

Fiber reinforced materials have many applications in today’s society. In products where stiffness and low weight are crucial (e.g. wind turbine blades, high end bicycle frames and car chassis) glass- or carbon-fibers reinforced materials are often applied. To maximize strength and stiffness the fiber orientation of the fibers is crucial. Misaligned fibers have a devastating impact on the compressive

strength of such materials, and the detection of misaligned fibers is therefore of great interest [1]. Visual inspection by microscopy gives only the fiber orientation distribution at the surface [2] and not the fiber orientation distribution in the interior. 3D techniques based on X-ray absorption microtomography have been developed [3, 4, 8] allowing for determination of interior fiber orientations. However, as typical sizes of glass- and carbon-fibers are in the range of 5–20 μm , and every fiber needs to be resolved with such techniques, it quickly becomes impractical for sample sizes exceeding a few millimeters. Grating interferometry based X-ray tomography uses the microstructure of the material as a contrast mechanism for dark field imaging. The method is sensitive to small structures (e.g. carbon fibers a few micrometers wide) decreasing the coherence of the X-ray beam, but images the resulting coherence signal with a pixel size much larger than the microstructure (e.g. a hundred micrometers or more), thus allowing us to map average scattering in samples much larger than what would have been possible if every component (e.g. individual carbon fibers) of the microstructure had to be within the resolution range of our detector. With this technique it has been demonstrated that the overall orientational characteristics in materials can be visualized but so far only in two-dimensional projections [5]. Here we propose a new setup of the grating interferometry method that utilizes the insensitivity of the grating interferometry setup for fibers oriented along the grating direction. This is achieved by a simple tilt of the sample rotation axis 90° relative to the traditional setup geometry. With this new setup aligned fibers become almost invisible to the grating interferometer dark field signal, whilst non-aligned fibers clearly stand out, thereby allowing 3D tomographic reconstructions of the spatial distribution of fibers misoriented with respect to the main axis given by the grating.

T. Lauridsen (✉) · R. Feidenhans'l
Niels Bohr Institute, University of Copenhagen,
Copenhagen, Denmark
e-mail: torstenl@nbi.ku.dk

E. M. Lauridsen
Department of Energy Conversion and Storage, Technical
University of Denmark, Kongens Lyngby, Denmark

2 Sample

2.1 Experimental method

In the X-ray grating interferometer a partially coherent X-ray beam produces a Talbot interference pattern by passing through an X-ray phase grating [6]. The interference pattern amplitude relative to the total beam intensity is called the visibility, and will depend on the coherence of the beam. The sample will introduce distortions in the interference pattern. The total intensity in the interference pattern will be lowered due to absorption, the fringes will be distorted due to refraction in the sample and the fringe visibility in the pattern will be lowered due to small angle scattering from the sample [7]. Hence, imaging the lowering of the visibility is a measure of the small angle scattering strength and hence the technique is called X-ray dark field imaging [7], which we will focus on the remaining part of the paper.

Briefly, the experimental setup consisted of six main components in a laboratory-based X-ray grating interferometer as shown in the top part of Fig. 1. The source was a rotating Cu anode with an effective spot size of 1×1 mm. The source grating was an Au slit grating introduced to minimize the effective source size of the X-rays. The period of the source grating was $14.1 \mu\text{m}$. The phase

grating was a Si grating introducing a π phase shift in half the beam, and thus producing a Talbot interference pattern. The period of this grating was $3.5 \mu\text{m}$. The sample was mounted on a rotation stage between the phase grating and the absorption grating. The absorption grating was a Au absorption grating with a period of $2.0 \mu\text{m}$ matched to the period of the phase grating, while taking magnification of the beam into account. The detector was a Pilatus two-dimensional detector with a pixel size of $172 \mu\text{m}$. The distance from the source grating to the phase grating was 140 cm, and the distance from the phase grating to the absorption grating was 20 cm. The center of the rotation stage was placed 10 cm from both phase and absorption grating.

The absorption grating in front of the detector is stepped along the grating direction in order to detect changes in the interference pattern. Changes in the visibility can only be observed along this direction and not perpendicular to it. Hence the sensitivity is highly directional and well suited to detect, i.e. the orientation of fibers [5]. In the standard setup the sample rotation axis is perpendicular to the grating stepping direction, see Fig. 1, left image. We proposed a modified setup for tomographic mapping of mis-oriented fibers, see Fig. 1, right image. Since the grating stepping direction is the direction along which the incoherent scattering is probed in a dark field image, this setup

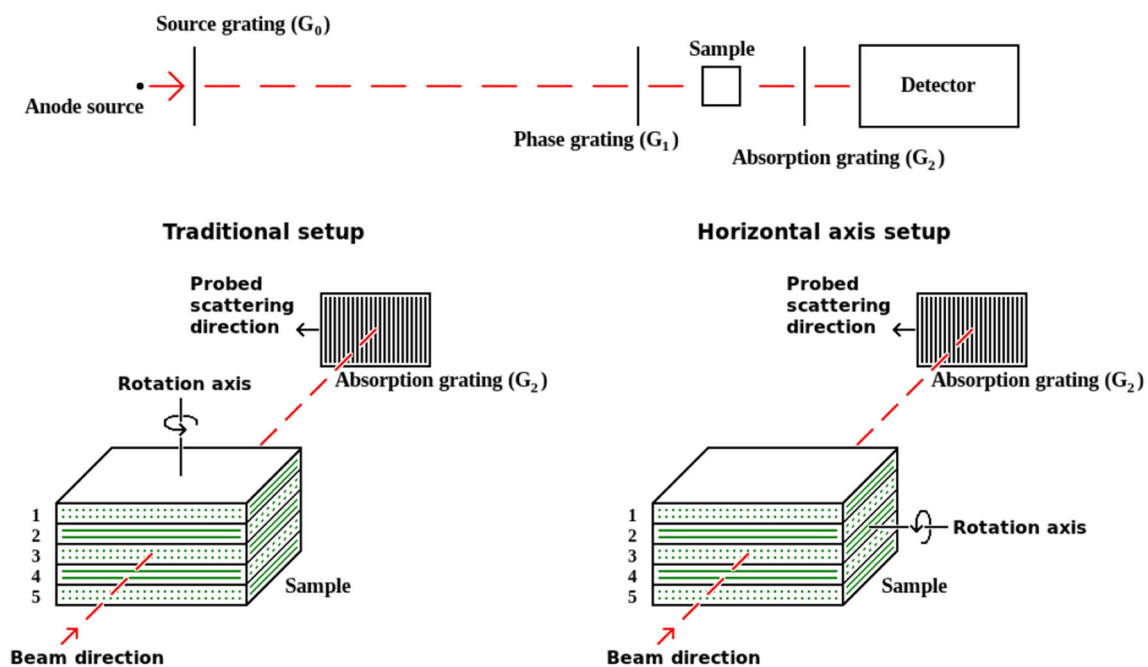


Fig. 1 Sketch of a traditional setup (*left*) and a horizontal rotation axis setup (*right*). The sample shown has two different fiber orientations. The absorption grating is shown above the sample and to the right. The probed scattering direction is marked by an *arrow*. In the horizontal axis setup, the rotation axis is parallel to the probed scattering direction. The fiber orientations in the five layers of the sample are indicated with

green lines. For three of the layers (layers 1, 3 and 5), the fibers are perpendicular to the rotation axis in either setup, and for two of the layers (layers 2 and 4), the fibers are parallel to the rotation axis, but only in the horizontal rotation axis setup. It is seen that the fibers of layers 2 and 4 remain parallel to the probed scattering direction in the horizontal rotation axis setup and hence invisible in the dark field image

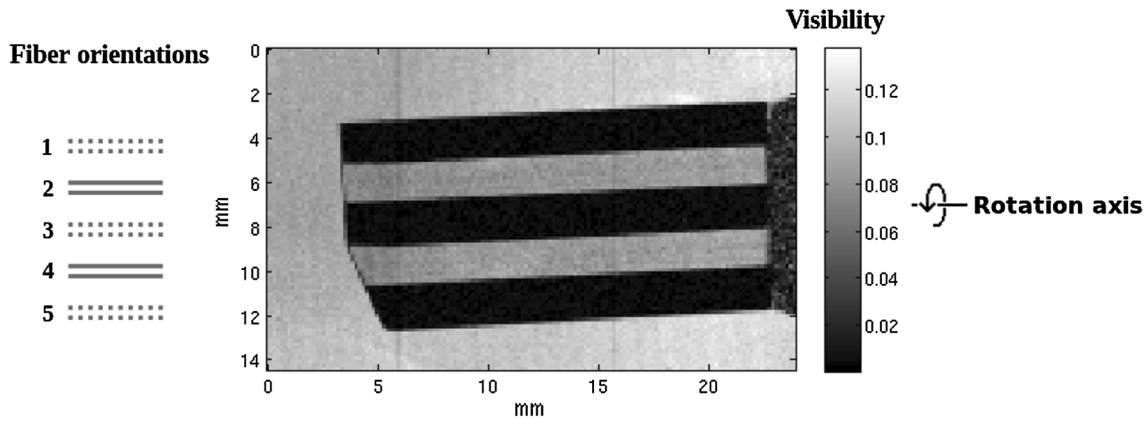


Fig. 2 Visibility projection of the sample. The projection is taken when the sample is rotated so that the five layers in the sample are horizontally aligned (See Fig. 1, right). The fiber orientations of the

individual layers are sketched to the left of the image. The fibers in layers 2 and 4 are invisible due to their orientation, while the layers 1, 3 and 5 scatter strongly

kept the probed scattering direction constant within the sample, as the sample is rotated, which is not the case in a traditional vertical rotation axis setup. Beam decoherence occurs in the direction perpendicular to the fibers. Hence, in order to make a main direction of fibers invisible in dark field imaging, the fibers must be oriented along the grating direction and keep this direction during sample orientation. Hence, the rotation axis must be rotated 90° as shown in Fig. 1, right.

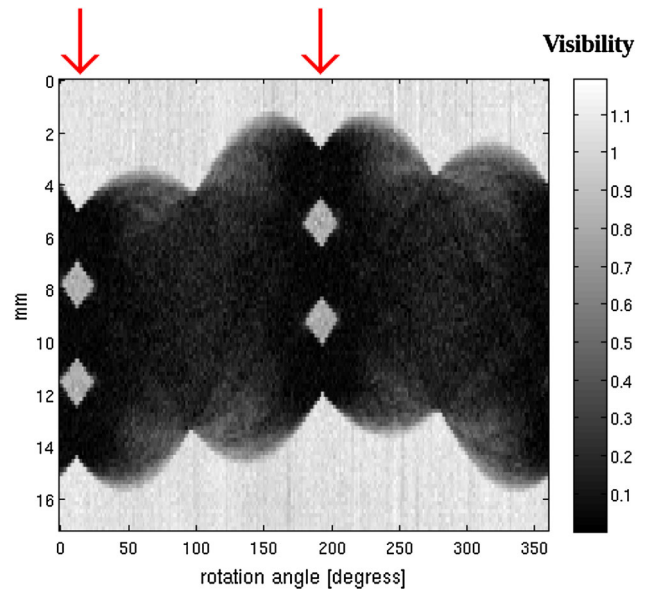
(Fig. 1), which is the direction that produces small angle (Fig. 2) scattering.

3 Results

Although the probed scattering direction remains constant under sample rotation, the beam propagation direction through the sample does not. The aligned fibers in layers 2 and 4 are kept parallel with respect to the rotation axis and hence remain invisible. But the fibers in layers 1, 3 and 5 are not parallel with the rotation axis. This means that the magnitude of the scattering produced by these layers may fluctuate as the sample is rotated. This may violate the basic assumption in the reconstruction algorithm used to produce the tomogram. But if the fluctuations are sufficiently small compared to the difference between the signal from the aligned and misaligned fibers, this may not compromise the validity of reconstruction of the tomogram.

The dark field signal is computed as the relative visibility in a given pixel in the detector (the visibility in the sample image divided by the visibility in a flat field image). Sinograms were produced by plotting the dark field signals in individual vertical pixel lines as a function of rotation angle. A typical sinogram is shown in Fig. 3.

As a reference, a scan with a traditional vertical rotation axis setup, was also performed. The setup and the geometry used for the two scans were exactly the same, except for the changed rotation axis.



In the setup with a horizontal rotation axis, the fiber orientations in layers 2 and 4 were parallel to the grating stepping direction regardless of the rotation angle of the sample (see Fig. 1, right). This meant that the magnitude of the scattering was always probed along the fibers' longitudinal direction. In layers 1, 3 and 5 the fibers were perpendicular to the probed incoherent scattering direction, meaning that the incoherent scattering was always probed perpendicular to the fibers' longitudinal direction (see

Fig. 3 Sinogram of vertical pixel line number 100. Note how the non-scattering layers 2 and 4 are visible at two different angles (15° and 195°, with 180° between them, marked with red arrows). These two angles produce visibility images similar to the one in Fig. 3

The reconstruction was done by performing a filtered back projection of the negative logarithm of the sinogram values.

A 3D-rendering of the dark field tomogram from the vertical rotation axis setup is seen in Fig. 4, bottom. This tomogram is more noisy than the corresponding horizontal axis tomogram, and the different fiber orientations are harder to detect.

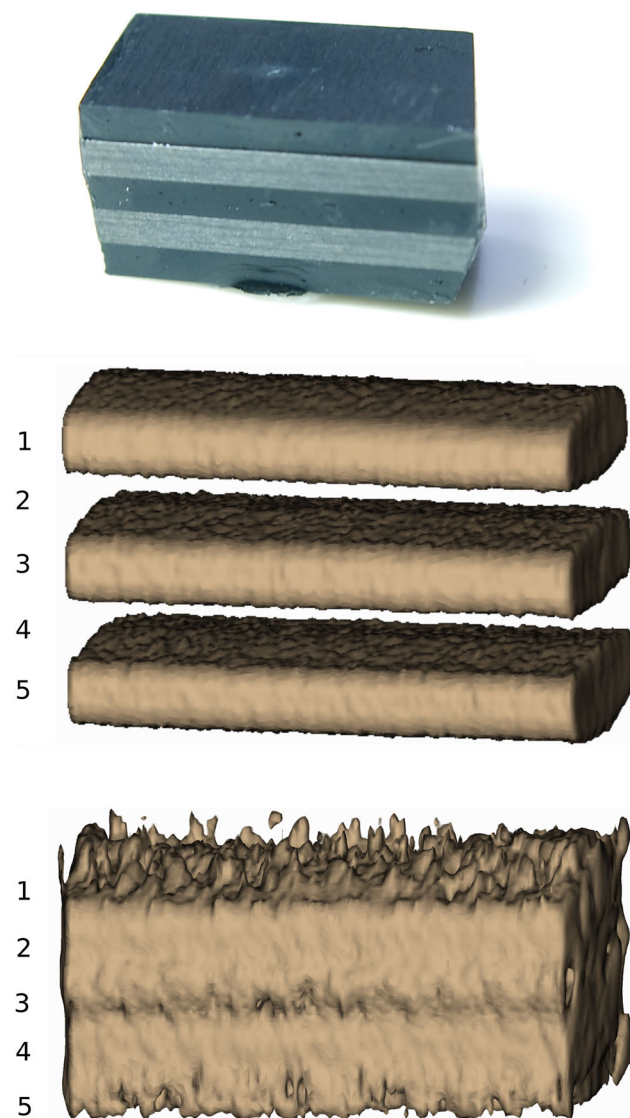


Fig. 4 Three images of the sample. *Top image*: a photograph. The different orientations of the fibers give the layers different colors. The fiber orientations are just visible in the layers 2 and 4. *Middle image*: tomogram from the horizontal axis setup. The layers 2 and 4 appear transparent. *Bottom image*: tomogram from the vertical axis setup. It is difficult to distinguish the different layers. The same threshold has been applied for the volume ray casting used to create the two tomogram visualizations

4 Discussion

The assumption of the filtered back projection is that the signal (in our case the signal is the beam decoherence) from each voxel volume of the sample is constant under rotation. This is not generally true for dark field scattering, but despite this, the reconstructions in our case are of a quality good enough to distinguish fibers of different orientations.

5 Conclusion

We have shown that horizontal axis setup allows us to map misaligned fibers. Specifically, we were able to distinguish volumes of misaligned fibers from volumes of aligned fibers within our sample.

6 Outlook

The scalar field this method produces can easily be extended to give a tensor field of the incoherent scattering in various directions for each volume element. This would only be a matter of rotating the sample along another axis than the sample stage rotation axis (in order to probe scattering in another direction), and then perform the tomogram measurement for the new scattering direction. This would enable us to probe incoherent scattering in several directions, and in this way investigate more complicated samples than the current, or alternatively for the sample used in this experiment, we could map not only the location of the misoriented fibers, but also their orientation.

Acknowledgments The authors would like to thank Mikkel Schou Nielsen, Niels Bohr Institute, University of Copenhagen for his help with the setup. We would also like to thank the Center for Industrial Application of CT scanning as well as the Carlsberg Foundation for their financial support.

References

1. B. Budiansky, N.A. Fleck, Compressive failure of fibre composites. *J. Mech. Phys. Solids* **41**, 183–211 (1993)
2. K.K. Kratmann, M.P.F. Sutcliffe, L.T. Lilleheden, R. Pyrz, O.T. Thomsen, A novel image analysis procedure for measuring fibre misalignment in unidirectional fibre composites. *Compos. Sci. Technol.* **69**, 228–238 (2009)
3. A. Axelson, Estimating 3D fibre orientation in volume images. *ICPR*, 1–4 (2008)
4. M. Krause, J.M. Hausherr, B. Burgeth, C. Herrmann, W. Krenkel, Determination of the fibre orientation in composites using the structure tensor and local X-ray transform. *J. Mater. Sci.* **45**, 888–896 (2010)

5. T.H. Jensen, M. Bech, O. Bunk, T. Donath, C. David, R. Feidenhans'l, F. Pfeiffer, Directional x-ray dark-field imaging. *Phys. Med. Biol.* **55**, 3317–3323 (2010)
6. T. Weitkamp, A. Diaz, C. David, F. Pfeiffer, M. Stampanoni, P. Cloetens, E. Ziegler, X-ray phase imaging with a grating interferometer. *Opt. Express* **13**(16), 6296–6304 (2005)
7. F. Pfeiffer, M. Bech, O. Bunk, P. Kraft, E.F. Eikenberry, Ch. Brönnimann, C. Grünzweig, C. David, Hard-X-ray dark-field imaging using a grating interferometer. *Nat. Mat.* **7**, 134–137 (2008)
8. K. Robb, O. Wirjadi, K. Schladitz, Fiber orientation estimation from 3D image data: practical algorithms, visualization, and interpretation. *Hybrid Intell. Syst.* 320–325 (2007)

A.3

Visualisation by high resolution synchrotron X-ray phase contrast micro-tomography of gas films on submerged superhydrophobic leaves

Journal of Structural Biology (2014)

T. Lauridsen, K. Glavina, T. D. Colmer, A. Winkel, S. Irvine, K. Lefmann, R. Feidenhans'l, O. Pedersen

Journal of Structural Biology (2014) 188: 61–70



Visualisation by high resolution synchrotron X-ray phase contrast micro-tomography of gas films on submerged superhydrophobic leaves



Torsten Lauridsen^a, Kyriaki Glavina^a, Timothy David Colmer^b, Anders Winkel^{b,c}, Sarah Irvine^{d,e,f}, Kim Lefmann^a, Robert Feidenhans'l^a, Ole Pedersen^{b,c,g,*}

^aNiels Bohr Institute, University of Copenhagen, Universitetsparken 5, 2100 Copenhagen, Denmark

^bSchool of Plant Biology, The University of Western Australia, 35 Stirling Highway, Crawley, 6009 WA, Australia

^cThe Freshwater Biological Laboratory, University of Copenhagen, Universitetsparken 4, 3rd Floor, 2100 Copenhagen, Denmark

^dLaboratory for Macromolecules and Bioimaging, Paul Scherrer Institut, 5232 Villigen PSI, Switzerland

^eFaculty of Biology and Medicine, University of Lausanne, 1015 Lausanne, Switzerland

^fLaboratory for Dynamic Imaging, Monash University, 3800 VIC, Australia

^gInstitute of Advanced Studies, The University of Western Australia, 35 Stirling Highway, Crawley, 6009 WA, Australia

ARTICLE INFO

Article history:

Received 25 April 2014

Received in revised form 8 August 2014

Accepted 15 August 2014

Available online 28 August 2014

Keywords:

Aerenchyma

Air film

CT scanning

X-ray phase contrast

Halophyte

Internal aeration

Leaf gas film

Hydrophobicity

Spartina anglica

Submergence tolerance

Tomogram

Wetland plant

ABSTRACT

Floods can completely submerge terrestrial plants but some wetland species can sustain O₂ and CO₂ exchange with the environment via gas films forming on superhydrophobic leaf surfaces. We used high resolution synchrotron X-ray phase contrast micro-tomography in a novel approach to visualise gas films on submerged leaves of common cordgrass (*Spartina anglica*). 3D tomograms enabled a hitherto unmatched level of detail regarding the micro-topography of leaf gas films. Gas films formed only on the superhydrophobic adaxial leaf side (water droplet contact angle, $\Phi = 162^\circ$) but not on the abaxial side ($\Phi = 135^\circ$). The adaxial side of the leaves of common cordgrass is plicate with a longitudinal system of parallel grooves and ridges and the vast majority of the gas film volume was found in large $\sim 180 \mu\text{m}$ deep elongated triangular volumes in the grooves and these volumes were connected to each neighbouring groove via a fine network of gas tubules ($\sim 1.7 \mu\text{m}$ diameter) across the ridges. In addition to the gas film retained on the leaf exterior, the X-ray phase contrast micro-tomography also successfully distinguished gas spaces internally in the leaf tissues, and the tissue porosity (gas volume per unit tissue volume) ranged from 6.3% to 20.3% in tip and base leaf segments, respectively. We conclude that X-ray phase contrast micro-tomography is a powerful tool to obtain quantitative data of exterior gas features on biological samples because of the significant difference in electron density between air, biological tissues and water.

© 2014 Elsevier Inc. All rights reserved.

1. Introduction

X-ray micro-tomography is a powerful non-destructive visualisation tool in biological sciences. Within plant sciences, visualisation of plant roots in soils *in situ* in pots is an example of application of X-ray micro-tomography to reveal 3D plant structures in an otherwise hidden environment (Mooney et al., 2012). Sand and clay soil particles are both highly X-ray attenuating as compared with the water-filled cells of roots, and so absorption-based X-ray micro-tomography shows contrast between roots

and soil (Kuka et al., 2013; Tracy et al., 2010). X-ray micro-tomography has also been used to visualise porosity (gas volume per unit tissue volume) of plant tissues (Mendoza et al., 2007) where the contrast is achieved between water-filled cells and gas-filled intercellular spaces. 3D visualisation is required to model e.g., O₂ diffusion and distribution in tissues since gases diffuse 10,000-fold faster in air than in water; examples include studies of O₂ distribution in fruits (e.g., Ho et al., 2009) and in roots (e.g., Verboven et al., 2012). However in contrast to studies of 3D root architecture in soils, alternative techniques, such as conventional light microscopy, can also enable assessments of tissue structure to underpin modelling of O₂ movement in plants (e.g., Armstrong, 1979) although visualisation of light microscopy slides and their 3D reconstruction is a time-consuming process and lacks the sophisti-

* Corresponding author at: The Freshwater Biological Laboratory, University of Copenhagen, Universitetsparken 4, 3rd Floor, 2100 Copenhagen, Denmark.

E-mail address: opedersen@bio.ku.dk (O. Pedersen).

cated software now available for the tomographic reconstructions and interpretations (Mendoza et al., 2007; Verboven et al., 2012, 2013).

In the present study, we used high resolution synchrotron X-ray phase contrast micro-tomography in a novel approach to visualise gas films retained on superhydrophobic leaves when submerged. In plant science, water repellence is characterised using the contact angle of a water droplet with the underlying surface (Adam, 1963; Brewer and Smith, 1997); contact angles above 150° implies superhydrophobicity (Koch et al., 2008; Neinhuis and Barthlott, 1997). The leaves of many wetland plants possess superhydrophobic leaf cuticles and during submergence, which can happen in the tidal zone (Winkel et al., 2011) as well as during overland floods (e.g., rice Colmer et al., 2014), such leaves are covered in a thin gas film (Pedersen and Colmer, 2012; Raskin and Kende, 1983). Leaf gas films greatly enhance the gas exchange between leaf surface and floodwater (CO₂ and O₂ in the light and O₂ during darkness) and hence, contribute to the flood tolerance of these wetland plants (Colmer et al., 2011; Verboven et al., 2014). During the day, the better CO₂ uptake from the floodwater results in enhanced rates of underwater photosynthesis (production of carbohydrates as well as O₂) and during the night, the better O₂ uptake sustains internal aeration of the shoot as well as of belowground tissues via internal O₂ movement via aerenchyma (Colmer and Pedersen, 2008; Pedersen and Colmer, 2012; Teakle et al., 2014; Winkel et al., 2011, 2013). Interestingly, the crop species rice (*Oryza sativa*) possesses superhydrophobic leaves (Pedersen et al., 2009; Winkel et al., 2013) and so do many wetland plants of ecological interest e.g., *Spartina anglica*, *Phragmites australis*, *Thypha latifolia*, and *Phalaris arundinacea* (Colmer and Pedersen, 2008; Winkel et al., 2011), so an in-depth understanding of the functioning and structure of leaf gas films is of importance to understand plant submergence tolerance in agricultural and ecological systems.

Characterisation of leaf gas film dimensions has previously been achieved using two contrasting approaches. The most accessible method involves buoyancy measurements of leaf segments before and after removal of the gas film; the hydrophobicity of the leaf surface can be greatly reduced by brushing it with a dilute detergent (Colmer and Pedersen, 2008; Raskin and Kende, 1983). The difference in buoyancy corresponds to the volume of gas film, and the average gas film thickness can then be estimated from the total area of the leaf segment – either for both surfaces (Pedersen et al., 2009) or one surface (Winkel et al., 2011), as appropriate. Application of the buoyancy method has shown that the average gas film thickness varies between 50 and 67 μm for the two species measured, *S. anglica* and rice (Pedersen et al., 2009; Winkel et al., 2011, 2013). However, an estimate of gas film thickness based upon this approach is unable to account for the surface microtopography, which likely results in great variation in actual gas film thickness. The spatial variation in gas film thickness can partly be captured using microelectrodes (Pedersen et al., 2009; Verboven et al., 2014). Pedersen et al. (2009) showed that gas film thickness of rice ranged from 10 to 140 μm by using O₂ microelectrodes to profile various locations on the leaf surface. Because of the high diffusivity in air, the gas film could be detected as a layer with no O₂ concentration gradient just above the leaf surface when submerged in darkness so that respiratory activity was consuming O₂ (Pedersen et al., 2009; Verboven et al., 2014).

In order to achieve improved characterisation of leaf gas films, here we used high resolution X-ray phase contrast micro-tomography to visualise the external gas layer on the superhydrophobic leaves of common cordgrass (*S. anglica*) when submerged. Using phase contrast micro-tomography instead of the conventional absorption-based methods resulted in much better contrast allowing for a more robust segmentation. Common cordgrass possesses a gas film only on the adaxial side of its leaves as the abaxial side is

not sufficiently hydrophobic to retain a gas layer when under water (Winkel et al., 2011). The average gas film thickness on leaves of common cordgrass is approximately 50 μm (Winkel et al., 2011) so in order to capture any effects of leaf microtopography upon gas layer thickness, we aimed for μm resolution to match data obtained with O₂ microelectrodes from rice (see above). We hypothesised that with such a sample, despite relatively low differences in X-ray attenuation, the large difference in electron density between air and water would yield significant X-ray phase contrast to enable distinction between water, external gas trapped on the superhydrophobic leaf surface, the much denser cells making up plant tissues and the internal gas-filled spaces within the leaf tissues.

2. Materials and methods

2.1. Source of sample material

Turfs of common cordgrass (*S. anglica*, CE Hubbard) were collected from populations at the Bay of Ho, Denmark, at multiple time points during the summer months. For details regarding the natural growth conditions of this population of common cordgrass, see Winkel et al. (2011). The turfs were maintained outdoors in Hillerød, Denmark, under natural light and temperature conditions as waterlogged cultures in 5 L buckets until used in experiments. Specimens used for high resolution X-ray micro-tomography were gently washed out of the natural sediment, transported in moist paper towels to the facility in Switzerland and studied within 4 d.

2.2. Scanning electron microscopy

Scanning electron microscopy (SEM) was performed with a JEOL JSM-6320F scanning microscope in high vacuum. Leaf samples were dehydrated in Petri dishes at room temperature to avoid evaporation of water in the vacuum chamber and a subsequent build-up of charge. Moreover, the leaves were coated with gold to enhance the natural conductivity of the cuticle surface. Dry leaf segments were fixed using double adhesive carbon tape on top of a silicon wafer. Leaf segments from the lower third of the youngest fully expanded leaf (subsequently referred to as 'base') were coated with a layer of 20 nm gold and viewed at a voltage of 5 keV, whereas samples from the upper third of the leaf (subsequently referred to as 'tip') were coated with 15 nm of gold and viewed at 10 keV.

2.3. Contact angle and hysteresis

Contact angle of water droplets (1 μL droplet of deionised water; radius ~0.625 μm) was used to assess wettability of the leaf surface (Adam, 1963). On a rough and chemically heterogeneous biological surface, the Cassie and Baxter model predicts that water droplets are suspended across surface protrusions, and tiny air pockets are thus formed between water and surface of the material (Shirtcliffe et al., 2005). Using water to measure the contact angle between droplet and surface of material enables classification into hydrophobic (contact angle > 90°) or hydrophilic (contact angle < 90°). Koch et al. (2008) subdivided the two categories further and defined materials as superhydrophobic when the contact angle exceeded 150°.

A water repellent surface can also be categorised as self-cleansing when an applied water droplet rolls off the surface at a tilting <10° (Koch et al., 2008). Rolling of a droplet occurs when the hysteresis is small and is defined as:

$$\text{Hysteresis} = \theta_{\text{advancing}} - \theta_{\text{receding}} \quad (1)$$

Measurements of contact angle and hysteresis were performed with an Intel Play QX3 Computer microscope at 60 \times magnification. A 1 μ L water droplet (at air-equilibrium dissolved gas) was applied to leaf segments from both base and tip (see above) using a micropipette. A goniometer was placed in front of the camera with a fixed glass slide on which the leaf segments were fixed with double-sided tape. Angles were subsequently measured using Image J (Schneider et al., 2012).

2.4. High resolution X-ray phase contrast micro-tomography

Biological samples have been studied using X-ray micro-tomography before, both using absorption-only reconstruction (Verboven et al., 2008), and holotomography (Cloetens et al., 2006). In the present study, only a single-distance phase retrieval method was used and furthermore the sample (a leaf segment) was submerged in water. Given the water-submerged sample, the single-distance phase retrieval method was the only feasible method. Phase-retrieval was essential because the absorption-contrast between plant and water proved insufficient to distinguish surrounding water from plant tissue in absorption images only, although the experiment originally was planned to be an absorption contrast experiment only.

All measurements involving high resolution X-ray phase contrast micro-tomography were carried out at the Paul Scherrer Institute at the TOMCAT beamline of the Swiss Light Source. Samples were prepared as follows. Cut surfaces of the leaf segments were sealed with capillary wax in order to reduce the possibility of water infiltration into the gas filled structures of the tissues. Samples were fixed using a Styrofoam stopper in a 3 mL Eppendorf (diameter of the lumen = 10 mm) tube filled with de-gassed water resulting in a detector-sample distance of 15–40 mm. The water was de-gassed to reduce movements and vibrations due to bubble formation, which would otherwise form during exposure to high-intensity radiation. Replicate leaf segments of the leaf tip ($n = 3$) and the leaf base ($n = 3$) were scanned (average scan time of 10 min) and they all showed a similar structure of the leaf gas film as the two leaf segments that were eventually segmented and presented in the present study.

The TOMCAT beamline uses a [Ru/C]100 double crystal multi-layer monochromator, with a photon energy bandwidth of 2–3% of the peak photon energy. We chose a peak photon energy of 12 keV, which gave us an acceptable transmission rate (~ 0.1 through the centre of the water-filled sample) while offering reasonable contrast between the low density materials in our sample. During X-ray exposure, samples were placed a few mm from the detector and rotated through 180 $^\circ$ in 2001 equiangular steps. A scintillator-based optical 2048 \times 2048 pixel CCD detector with an effective pixel size of 0.375 \times 0.375 μ m² was used (at 20 \times magnification).

Individual projections were corrected for refraction effects (evident in the form of phase contrast fringes at the interface between materials) by applying an algorithm for simultaneous phase and amplitude retrieval (Paganin et al., 2002). From the refraction corrected projections, tomograms were reconstructed using a filtered back-projection algorithm with computations performed in MATLAB. Applying the phase retrieval algorithm proved essential for creating tomograms of a sufficiently good quality to allow a satisfactory segmentation of the different components (plant tissue, water and air). Initial attempts at segmenting tomograms using a traditional absorption-only reconstruction algorithm proved fruitless, mainly due to refraction-induced edge enhancements artefacts. The Paganin phase retrieval algorithm takes refraction effects into account, at the cost of an assumption of a constant δ/β -ratio of the refractive index throughout the sample (Paganin et al., 2002); additional details in Supplementary Material. This

assumption can be described as a “single component at different densities-assumption”. With the elementary composition of plant tissue and (salt) water being quite similar, the sample was a nearly ideal system for applying the Paganin algorithm.

3. Results

3.1. Hydrophobicity and surface structure

The hydrophobicity of plant surfaces can be assessed using combined measurements of contact angle to tissue surface and hysteresis of a 1 μ L droplet of deionised water (Adam, 1963; Neinhuis and Barthlott, 1997). The adaxial side of the leaf (the anatomical upper side) had average contact angles ($^\circ$) of 162 \pm 3 (mean \pm SE, $n = 8$) and average hysteresis of 6.1 \pm 2 (mean \pm SE, $n = 7$). Consequently, according to Koch et al. (2008), the adaxial side can be classified as superhydrophobic with the contact angle exceeding 150 $^\circ$ and according to Koch et al. (2008) categorised as self-cleansing as the tilting angel causing the droplet to roll was $<10^\circ$. This adaxial side possessed a gas film when submerged (visual inspection). In contrast, the abaxial side (the anatomical lower side) was hydrophobic with average contact angles of 135 \pm 4 $^\circ$ (mean \pm SE, $n = 3$); the hysteresis of the abaxial side was not determined. This abaxial side did not retain a gas film when submerged (visual inspection).

The superhydrophobic feature of the adaxial side was caused by a hierarchy of surface structures spanning three scales. The plicate nature of the leaf with macroscopic features of alternating grooves and ridges parallel to longitudinal axis of the leaf resulted in hydrophobicity as illustrated by Cassie and Baxter's model where water droplets are suspended on such surface structures (Fig. 1). On the microscale, surface roughness was provided by papillose epidermal cells forming small buds, and finally the entire cuticle was covered by three-dimensional epicuticular waxes of the platelets type (Fig. 1); see Neinhuis and Barthlott (1997) for classification of cuticular wax nano-structures. On the abaxial side, however, all three roughness features present on the adaxial side were absent and the surface appeared smooth (Fig. 1). Stomata were only observed at the adaxial side and only inside the grooves at a density of approximately 300 mm⁻² and trichomes were absent from both leaf sides.

3.2. Tomogram resolution

The 3D data from the tomographic reconstructions were composed of cubic voxels with a size of 0.375 \times 0.375 \times 0.375 μ m resulting in a voxel volume of 0.053 μ m³. The actual resolution is a combined result of the source size, detector response, the filters used for reconstruction and, most significantly in this case, the phase-retrieval algorithm (which is also a low-pass filter, Paganin et al., 2002). In order to assess this resolution, we compared a 2D tomogram slice of 50 \times 50 μ m with a SEM image of a similar area inside one of the grooves of the adaxial side of the basal part of the leaf (Fig. 2). On the SEM image, the papillae are clearly evident and even the contour of the wax crystals are perceptible (Fig. 2A). Exact measurements of average papilla width and height based upon the SEM micrographs revealed a mean width of 3 μ m and mean height of 4 μ m. On the tomogram, the papillae are also clearly evident but contours of wax crystals on the sub- μ m scale are not visible (Fig. 2B). Estimates of mean papilla width and height (3 and 4 μ m, respectively) were similar to those based upon the SEM micrographs.

The excellent resolution of a few μ m is retained also after segmentation although with some minor loss of details (Fig. 2C and D). The contour reconstruction of surface tissue inside a groove reveals

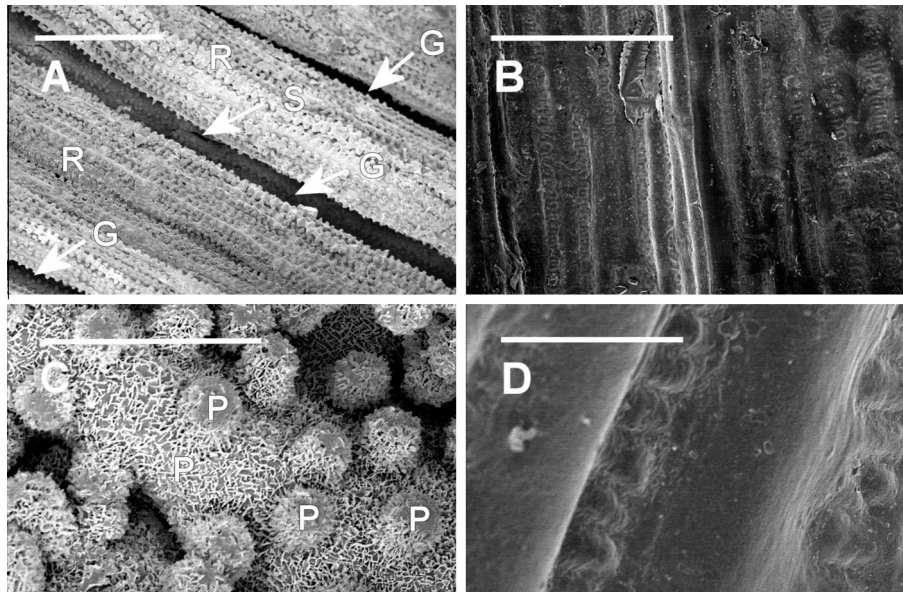


Fig. 1. Surface scanning electron micrographs of the youngest fully expanded leaf of common cordgrass (*Spartina anglica*); micrographs are from the middle part of the leaf. Micrographs are shown for the adaxial side (A and C) and the abaxial side (B and D) at two magnifications (scale bars in (A and B) 100 μm ; in (C and D) 10 μm). R = ridge, G = groove, S = stoma and P = papilla.

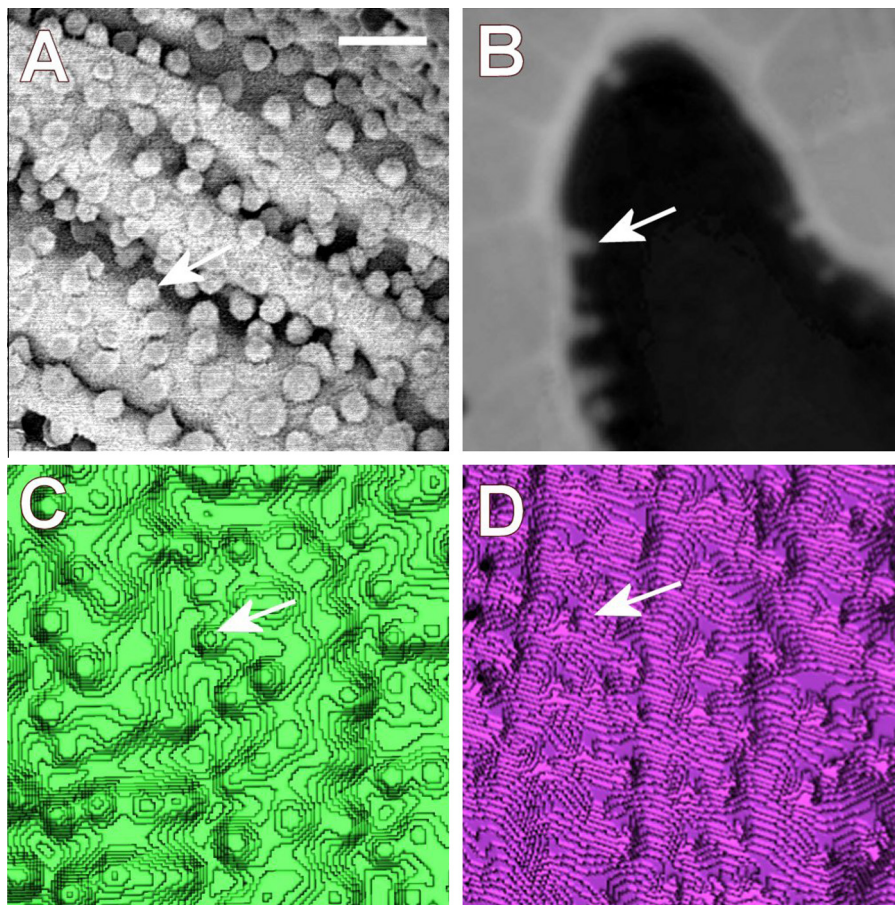


Fig. 2. Scanning electron micrograph (A), high resolution X-ray micro-tomogram slice (B), 3D reconstruction of surface tissues (C) and 3D reconstruction of gas film (D) of a $50 \times 50 \mu\text{m}$ section of the adaxial side of the youngest fully expanded leaf (base segment) of common cordgrass (*Spartina anglica*). In (A) the sub- μm wax crystals covering the leaf cuticle are barely visible. In (B) light shades of grey represent electron-dense tissues whereas the darker shades of grey represent gas. In (C and D) the contours show the reconstruction of the papillae (indicated by arrows in all four panels); in (C) as small elevations on the surface and in (D) as small dents in the gas film (the leaf segment in (B–D) was submerged into water during X-ray measurements). Scale bar = 10 μm .

most of the papillae but it also seems that some are lost in the segmentation algorithm (Fig. 2C). Similarly, contour reconstructions of the gas film reveal the papillae as tiny imprints (Fig. 2D).

3.3. Qualitative analysis of 3D tomograms

The 3D tomograms clearly showed the spatial distribution of gas inside the tissues as well as gas on the leaf surface, the leaf gas film, when submerged in water. On both base and tip leaf segments, the gas film filled the surface tissue grooves, forming elongated triangular volumes of gas on the superhydrophobic adaxial side of the leaf (Figs. 3 and 4). These gas layers of relatively high volume within each groove were connected to each other via a fine network of gas film covering the tissue ridges between each of the grooves (Figs. 3 and 4) resulting in gas phase connection of all observed external gas volume. In contrast, no gas films were observed on the abaxial side of the leaf.

Internal gas-filled structures were equally well segmented as compared to the external leaf gas films (Figs. 3 and 4). However, the internal gas-filled structures differed greatly between base and tip leaf segments. Within base segments, the internal gas-filled components were distributed into large bulky cavities referred to as lacunae or aerenchyma (Armstrong, 1979) and into a much finer internal network of intercellular gas-filled spaces (Fig. 3). The large

aerenchyma lacunae were separated by tissues with the veins (i.e., areas with vascular tissues) in the leaf lamina. In contrast, the tip segment only contained a network of fine intercellular gas-filled spaces but no lacunae (Fig. 4). Higher spatial resolution (cf. greater ‘magnification’) revealed details of gas-filled micro-structures inside the leaf tissues, and sub-stomatal cavities (zones of high gas volumes) were well connected via this fine network of gas-filled intercellular spaces (Fig. 5). However, we could not resolve gas-connectivity across stomata (detection limit of any gas-filled channel of 0.375 μm in diameter) under the present conditions, but such connectivity must exist in natural conditions (e.g., submerged field plants in Winkel et al., 2011, 2013; modelling data of Verboven et al., 2014). Animation videos of base and tip segments as well as close-ups of internal gas-filled spaces and gas films are shown in Supplementary Material, Videos 1S, 2S, 3S and 4S.

3.4. Quantitative estimates derived from 3D tomograms

Previous studies of leaf gas films were limited to relatively crude estimates regarding quantitative dimensions such as thickness (see Section 1). These were derived from measurements of external gas volume (based on buoyancy measurements before and after removal of the leaf gas film with a dilute detergent)

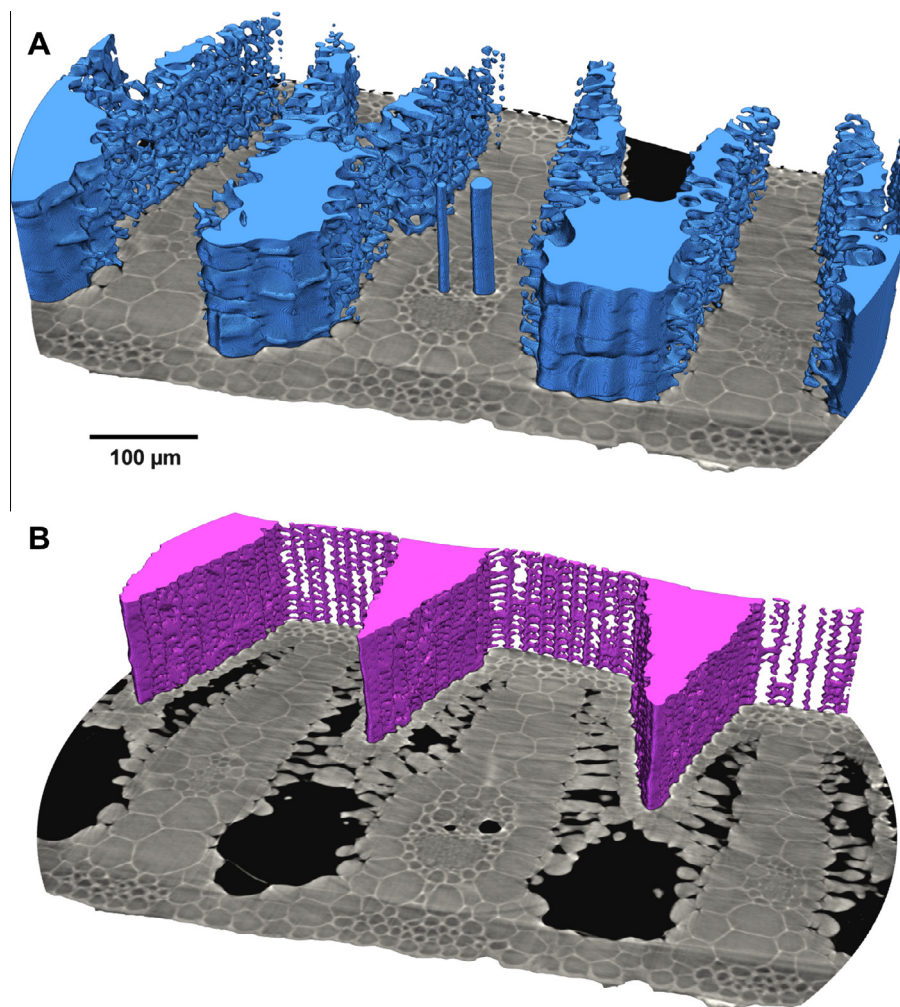


Fig. 3. 3D tomograms of the basal part of the youngest fully expanded leaf of common cordgrass (*Spartina anglica*) obtained by X-ray phase contrast micro-tomography. Internal gas-filled spaces (A, blue) projected onto a slice of the tomogram of leaf tissue (grey); black indicates external gas film. The leaf segment was submerged into water and the superhydrophobic adaxial side of the leaf retained a thin gas film (B, purple); black on the slice indicates internal gas-filled spaces. Two xylem vessels had embolized and are visible as blue pillars in (A) and as two black spots inside the vascular bundle in (B).

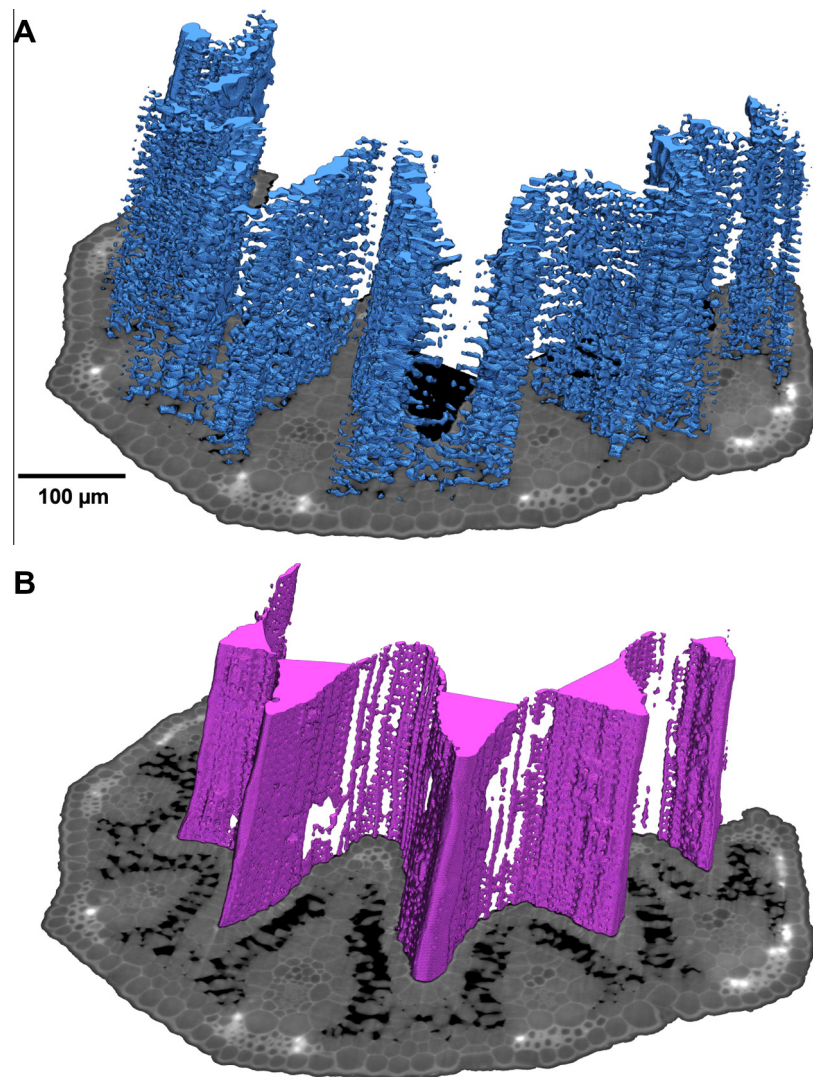


Fig. 4. 3D tomograms of the tip part of the youngest fully expanded leaf of common cordgrass (*Spartina anglica*) obtained by X-ray phase contrast micro-tomography. Internal gas-filled spaces (A, blue) projected onto a slice of the tomogram of leaf tissue (grey); black indicates external gas film. The leaf segment was submerged into water and the superhydrophobic adaxial side of the leaf retained a thin gas film (B, purple); black indicates internal gas-filled spaces. (For interpretation of the references to colour in this figure legend, the reader is referred to the web version of this article.)

and area of the leaf segment analysed, or microelectrode profiling under certain conditions. The present approach using high-resolution X-ray micro-tomography enabled us to obtain much more detailed quantitative information on the spatial distribution of leaf gas films with a resolution of a few μm or less (see tomogram resolution above).

A detailed view of the network structure connecting the gas-filled tissue surface grooves is provided in Fig. 6. The average diameter of the tubules forming the network across the 'ridges' was 1.7 and 1.4 μm (base and tip segment, respectively), and the gas trapped in the tubules made up only 2.8% to 6.1% (base and tip segment, respectively) of the total volume of leaf gas film. In contrast, the depth of the triangular structures ranged from 180–191 and 32–77 μm (base and tip segment, respectively), and the gas present in these structures made up 97.2% to 93.9% (base and tip segment, respectively) of the total volume of leaf gas film. The dimensions of these two contrasting volumes underlines spatial 3D variability of the leaf gas film. For comparison, Winkel et al. (2011) provided a mean gas film thickness of 50 μm on the superhydrophobic adaxial leaf side (Table 1). A similar estimate can also be derived from the tomograms in Figs. 3–6 using measurements

of external gas volume and projected adaxial leaf area, resulting in a mean gas film thickness of 45 and 21 μm for base and tip segments, respectively. Furthermore, if instead of projected surface area the actual surface area of the superhydrophobic adaxial leaf side is estimated based upon the microtopography of the leaf surface and used to calculate the mean gas film thickness, the mean gas films thickness is 13.9 and 6.7 μm for base and tip segments, respectively.

The internal gas spaces can also be quantified and compared to more conventional measurements of tissue porosity (for methods, see Raskin, 1983). As outlined above, the base segments contained more internal gas-filled volume than the tip segments because the base segment, in addition to the fine gas-filled intercellular network of spaces, also contained aerenchyma lacunae. Thus, the overall tissue porosity was 15.9% in the base segments but only 5.3% in the tip, as compared to 7% reported by Winkel et al. (2011) and measured on the middle part of the leaf but excluding the midrib. The gas film to total leaf gas volume ratio did not differ between base and tip leaf segments (Table 1). The relevance of this parameter is related to (i) the physics/physiology of underwater photosynthesis where the vast volume of external gas can function

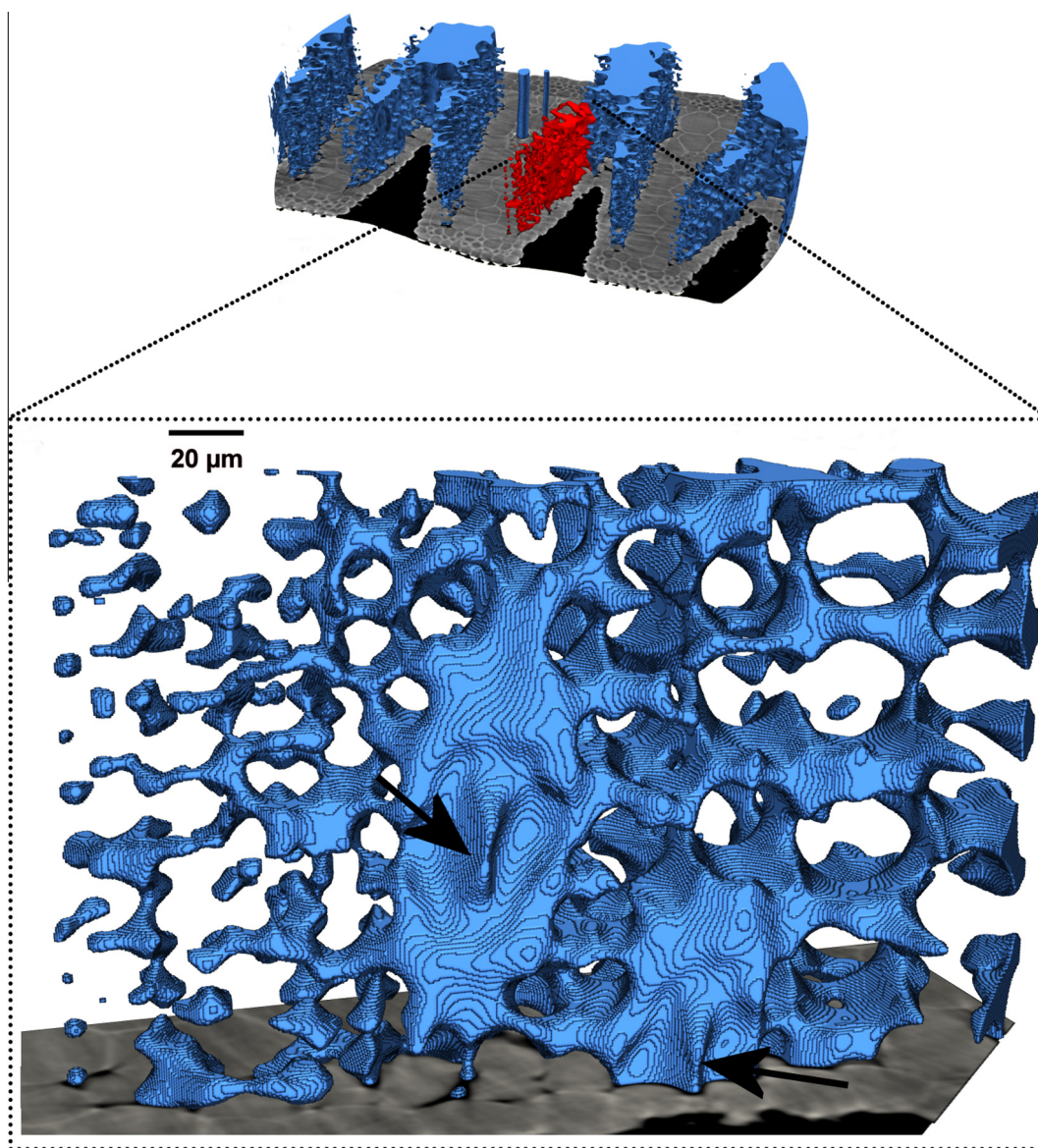


Fig. 5. 3D tomograms of the basal part of the youngest fully expanded leaf of common cordgrass (*Spartina anglica*) obtained by X-ray phase contrast micro-tomography. Close-up on internal gas spaces (blue) projected upon a 2D cross-section of leaf tissue (grey); target area for zooming is indicated in red. The arrows show areas with sub-stomatal cavities. (For interpretation of the references to colour in this figure legend, the reader is referred to the web version of this article.)

as a short term buffer/reservoir of CO_2 and O_2 (Sand-Jensen et al., 2005) and (ii) methods involving porosity measurements or measurements of underwater photosynthesis where a large fraction of external gas can influence the calculations. Finally, the proportions of gas volumes inside and outside leaves are also of interest for situations with longitudinal gas diffusion e.g., if leaf tips are emergent above water (Beckett and Armstrong, 1992), but that situation was not studied here so this parameter is not subsequently discussed in any further detail.

In summary, the 3D tomograms enabled a hitherto unmatched level of details regarding the micro-topography of the gas films on the surface of the submerged leaves.

4. Discussion

High resolution synchrotron X-ray phase contrast micro-tomography was shown to successfully visualise gas films on the superhydrophobic surface of leaves when submerged, using the interesting example of the wetland plant common cordgrass (*S.*

anglica). The large difference in electron density between air and water enabled the required contrast between water, external gas, cells and tissues and internal gas-filled spaces revealing the gas-filled network. Below, we discuss in further detail (i) the functional aspects of the superhydrophobic properties being restricted to the adaxial side of the leaf, (ii) the spatial information on leaf gas films obtained in the present study and compare it with information obtained with other methods for the same and one other species, and (iii) the surface structure leading to hydrophobicity in common cordgrass.

The present study confirmed that common cordgrass possesses a gas film only on the adaxial side of its leaves (Winkel et al., 2011) as the abaxial side is not sufficiently hydrophobic to retain a gas layer when under water. This observation was achieved using a combined approach of X-ray micro-tomography to visualise the leaf gas films under water, SEM to characterise the leaf surface structure and water droplets (1 μL) with image analyses to measure contact angle to the leaf surface. The abaxial side appeared smooth and lacked the fine wax platelets that covered the adaxial

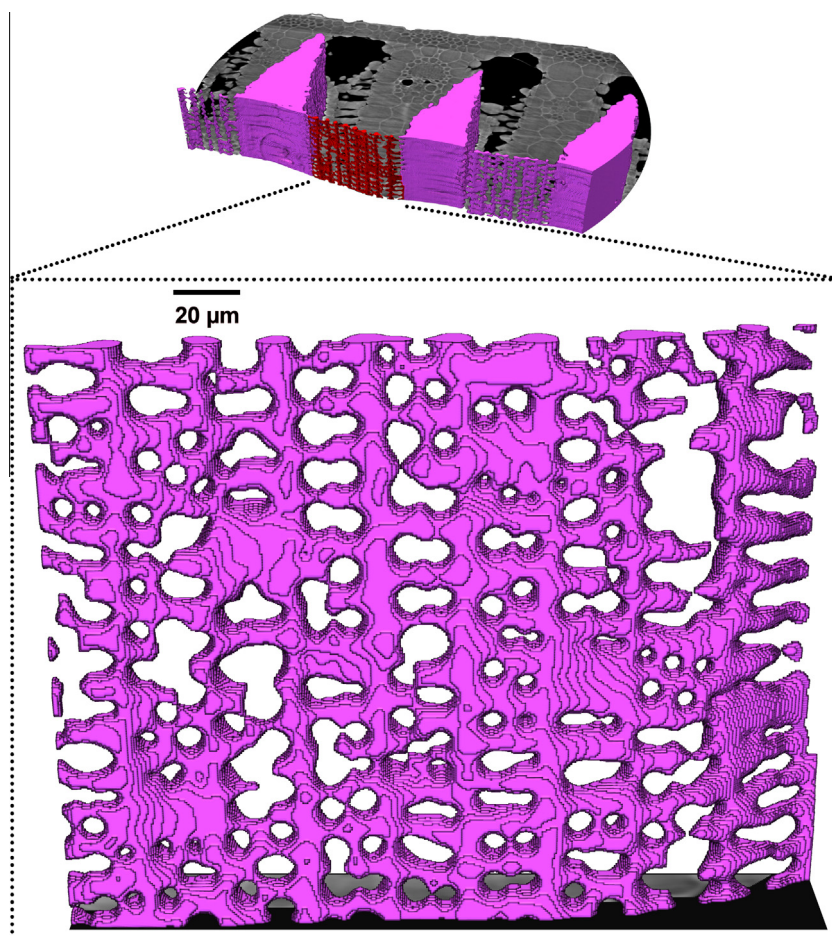


Fig. 6. 3D tomograms of the basal part of the youngest fully expanded leaf of common cordgrass (*Spartina anglica*) obtained by X-ray phase contrast micro-tomography. The leaf segment was submerged into water and the superhydrophobic adaxial side of the leaf retains a thin gas film (purple) projected onto a 2D cross-section of leaf tissue (grey). Close-up on a ridge with target area for zooming indicated in red. The gas film inside the grooves is connected via the ridges by a thin network of gas. (For interpretation of the references to colour in this figure legend, the reader is referred to the web version of this article.)

Table 1
Key tissue and gas film parameters as determined by high-resolution X-ray phase contrast micro-tomography on submerged leaf segments of common cordgrass (*Spartina anglica*). Data from leaf base (mid lower third of leaf) and leaf tip (mid upper third of leaf) based on the present study as well as on literature data (mean \pm SE, n = number of replicates). Estimates of gas film properties are based on total volumes of the 3D tomograms (base: 0.066 μ L and tip: 0.089 μ L) of tissue, internal gas and external gas, whereas estimates of tissue porosity and gas film to total leaf gas volume ratio are based both on whole 3D tomograms and tomogram slices. Different letters indicate significant differences ($P < 0.05$, t -test) between leaf base and leaf tip.

	Leaf base	Leaf tip	Literature values
Tissue porosity (% gas of total volume)	15.9 ^a \pm 3.2	5.3 ^b \pm 0.8	7 \pm 1, n = 5 (Winkel et al., 2011) [*]
Mean gas film thickness (μ m)	45 ¹	21 ¹	50 \pm 4, n = 5 (Winkel et al., 2011) [*]
Max. gas film thickness in tissue surface grooves (μ m)	184 ^a \pm 5, n = 6	92 ^b \pm 5, n = 6	n.a.
Max. gas film thickness on tissue surface ridges (μ m)	5.0 ^a \pm 1.6, n = 20	3.4 ^a \pm 0.9, n = 18	n.a.
Gas film to total leaf gas volume ratio	0.50 ^a \pm 0.05	0.66 ^a \pm 0.14	n.a.

¹ n = 1.

^{*} This value was taken from the middle of the leaf but excluding the midrib.

leaf surface. In contrast, the adaxial leaf side was superhydrophobic as it possessed hierarchal structures at the macro-, micro- and nano-levels together resulting in large contact angles (162°) when probed with the water micro-droplet method; this is 14° more than reported by Winkel et al. (2011) suggesting that these properties can vary somewhat within a species and/or at different sampling times as the same common cordgrass population was used in both studies. The functional aspects of hydrophobicity confined to only one side of the leaf is likely related to the fact that the vast majority of stomata in common cordgrass are located on the adaxial side with very few on the wettable abaxial leaf side. Inter-

estingly, salt glands are reported to occur on both leaf sides of common cordgrass (Maricle et al., 2009). In its natural habitat, common cordgrass is often submerged twice a day during high tides (Winkel et al., 2011). Hence, the superhydrophobic adaxial leaf side ensures that a gas film is formed when under water (Figs. 3–6) enhancing gas exchange with the environment, via the gas films and stomata (Verboven et al., 2014; Winkel et al., 2011).

The surface structures leading to the superhydrophobic properties of common cordgrass are similar to those reported for rice (*O. sativa*). The contact angle between the leaf surface and tiny water droplets in rice is similarly steep (157–162°) and the leaves are

longitudinally grooved with papillose epidermis covered by wax platelets (Guo and Liu, 2007; Neinhuis and Barthlott, 1997), but on both sides so that rice leaves retain gas films on both surfaces when submerged (Pedersen et al., 2009; Raskin and Kende, 1983; Setter et al., 1989). The steep contact angle along with low hysteresis reported in the present study (6.1°) renders the leaves of both common cordgrass (adaxial) and rice (both sides) are self-cleansing (Bhushan et al., 2009), a phenomenon referred to as the 'Lotus Effect' (Barthlott and Neinhuis, 1997). Habitats of both common cordgrass growing in salt marshes (Maricle et al., 2009) and rice which originated from tropical wetlands (Londo et al., 2006) are prone to submergence events (common cordgrass, Winkel et al., 2011; rice, Colmer et al., 2014). Self cleansing leaf surfaces would be beneficial when in air to prevent wetting of the leaves and thus clogging of the stomata by water if it were otherwise retained on the surface (Brewer and Smith, 1997), and when under water it would reduce the deposition on the leaf surface of suspended particles as these settle in floodwaters. The importance of self-cleansing for the floating (horizontal) leaf of the sacred lotus is evident (Neinhuis and Barthlott, 1997), whereas leaf angles in common cordgrass are above the horizontal, but not as erect as for modern rice varieties (personal observations).

Superhydrophobicity of the leaf surfaces results in retention of a gas film when plants are submerged by water, and our study has characterised the gas film on leaves of a wetland species with details that have not previously been achieved. Microelectrode profiling showed gas film thickness on rice leaves varied spatially between $<10\ \mu\text{m}$ and up to $140\ \mu\text{m}$ (Pedersen et al., 2009), but this method does not enable direct associations with the underlying surface structure. The triangular volumes filling the leaf surface grooves of common cordgrass (see Section 3.4) varied between $32\ \mu\text{m}$ (tip segments) and $191\ \mu\text{m}$ (base segment) in depth and the tubules forming the network covering the ridges were on average $<2\ \mu\text{m}$ thick. Considering that rice has a similar plicate leaf morphology as common cordgrass with alternating grooves and ridges, the present detailed images of leaf gas films in the present study suggest that the earlier measured variation by Pedersen et al. (2009) for rice would presumably derive from similar surface gas features on the rice leaves as documented here for common cordgrass.

It has recently been shown that leaf gas films on rice submerged in a field situation eventually collapse (i.e., cease to exist) after some time of submergence as presumably the superhydrophobic properties are lost (Winkel et al., 2014). From the present study, it seems that the fine network of gas film covering the ridges might be particularly prone to lose the gas trapped in the tubules (Fig. 6). The loss of the network may not be crucial for the gas film functioning under water since the stomata in common cordgrass are primarily located towards the bottom of the surface grooves (Maricle et al., 2009), and underwater photosynthesis in submerged rice was initially unaffected by the decline in overall gas film volume until a point where the gas film was apparently almost completely lost and then the underwater photosynthesis declined (Winkel et al., 2014). However, the experimental variation may mask the potential relationship between total gas collecting area (projected area of network) and projected area of the triangular volumes filling the grooves, and a modelling approach is required to unravel the functioning of the gas-filled network now that the more detailed spatial variability in gas film dimensions is known for common cordgrass, and particularly so if the gas volume reduces with time of submergence as documented for rice by Winkel et al. (2013). For the presently available modelling of the function of leaf gas films see (Verboven et al., 2014).

Our study on 3D visualisation of leaf gas films demonstrates the need to survey more contrasting species to better understand these traits for various wetland and crop species, as leaf gas films are

important for gas-exchange, growth and potentially the survival of terrestrial wetland plants during periods of submergence (Colmer and Pedersen, 2008; Pedersen et al., 2009; Teakle et al., 2014). The present qualitative combination of high resolution X-ray micro-tomography and scanning electron microscopy would enable an understanding of the structural changes in the cuticle that occur with time of submergence and how these changes affect hydrophobicity and the capacity to retain a gas film under water. Moreover, there is a need to integrate the 3D structure of the gas film in models describing O_2 and CO_2 exchange with floodwater; such level of complexity is currently not included the models (Verboven et al., 2014). To achieve these goals, a cross-disciplinary approach is needed – and without such an approach, we would not have been able to achieve this hitherto unmatched level of details regarding the micro-topography of the gas films on the leaves of submerged common cordgrass.

Acknowledgments

This work was funded by a University of Western Australia International Postgraduate Research Scholarship to Anders Winkel, the Danish Council for Independent Research Grant No. 09-072482 and through the Danish Centre (DANSCATT) for the use of Synchrotron X-ray and Neutron facilities for travel support. We thank the UWA Institute of Advanced Studies for hosting Ole Pedersen during his visits to UWA. We also thank PSI for providing beam time and staff support at the TOMCAT facility.

Appendix A. Supplementary data

Supplementary data associated with this article can be found, in the online version, at <http://dx.doi.org/10.1016/j.jsb.2014.08.003>.

References

- Adam, N.K., 1963. Principles of water repellency. In: Molliet, J. (Ed.), *Waterproofing and Water Repellency*. Elsevier, Amsterdam, pp. 1–23.
- Armstrong, W., 1979. Aeration in higher plants. *Adv. Bot. Res.* 7, 225–332.
- Barthlott, W., Neinhuis, C., 1997. Purity of the sacred lotus, or escape from contamination in biological surfaces. *Planta* 202, 1–8.
- Beckett, P.M., Armstrong, W., 1992. The modelling of convection and diffusion-driven aeration in plants. In: Egginton, S., Ross, H.F. (Eds.), *Oxygen Transport in Biological Systems*. Cambridge University Press, Cambridge, pp. 253–293.
- Bhushan, B., Jung, Y.C., Koch, K., 2009. Micro-, nano- and hierarchical structures for superhydrophobicity, self-cleaning and low adhesion. *Philos. Trans. R. Soc. A* 367, 1631–1672.
- Brewer, C.A., Smith, W.K., 1997. Patterns of leaf surface wetness for montane and subalpine plants. *Plant Cell Environ.* 20, 1–11.
- Cloetens, P., Mache, R., Schlenker, M., Lerbs-Mache, S., 2006. Quantitative phase tomography of *Arabidopsis* seeds reveals intercellular void network. *Proc. Natl. Acad. Sci. U.S.A.* 103, 14626–14630.
- Colmer, T.D., Armstrong, W., Greenway, H., Ismail, A.M., Kirk, G.J.D., Atwell, B.J., 2014. Physiological mechanisms of flooding tolerance in rice: transient complete submergence and prolonged standing water. *Prog. Bot.* 75, 255–307.
- Colmer, T.D., Pedersen, O., 2008. Underwater photosynthesis and respiration in leaves of submerged wetland plants: gas films improve CO_2 and O_2 exchange. *New Phytol.* 177, 918–926.
- Colmer, T.D., Winkel, A., Pedersen, O., 2011. A perspective on underwater photosynthesis in submerged terrestrial wetland plants. *AoB PLANTS* 2011, plr030.
- Guo, Z., Liu, W., 2007. Biomimicry from the superhydrophobic plant leaves in nature: binary structure and unitary structure. *Plant Sci.* 172, 1103–1112.
- Ho, Q.T., Verboven, P., Mebatsion, H.K., Verlinden, B., Vandewalle, S., Nicolai, B., 2009. Microscale mechanisms of gas exchange in fruit tissue. *New Phytol.* 182, 163–174.
- Koch, K., Bhushan, B., Barthlott, W., 2008. Diversity of structure, morphology and wetting of plant surfaces. *Soft Matter* 4, 1943–1963.
- Kuka, K., Illerhaus, B., Fox, C.A., Joschko, M., 2013. X-ray computed microtomography for the study of the soil–root relationship in grassland soils. *Vadose Zone J.* <http://dx.doi.org/10.2136/vzj2013.2101.0014>.
- Londo, J.P., Chiang, Y.-C., Hung, K.-H., Chiang, T.-Y., Schaal, B.A., 2006. Phylogeography of Asian wild rice, *Oryza rufipogon*, reveals multiple independent domestications of cultivated rice, *Oryza sativa*. *Proc. Natl. Acad. Sci.* 103, 9578–9583.

- Maricle, B.R., Koteyeva, N.K., Voznesenskaya, E.V., Thomasson, J.R., Edwards, G.E., 2009. Diversity in leaf anatomy, and stomatal distribution and conductance, between salt marsh and freshwater species in the C₄ genus *Spartina* (Poaceae). *New Phytol.* 184, 216–233.
- Mendoza, F., Verboven, P., Mebatsion, H., Kerckhofs, G., Wevers, M., Nicolai, B., 2007. Three-dimensional pore space quantification of apple tissue using X-ray computed microtomography. *Planta* 226, 559–570.
- Mooney, S.J., Pridmore, T.P., Helliwell, J., Bennett, M.J., 2012. Developing X-ray computed tomography to non-invasively image 3-D root systems architecture in soil. *Plant Soil* 352, 1–22.
- Neinhuis, C., Barthlott, W., 1997. Characterization and distribution of water-repellent, self-cleaning plant surfaces. *Ann. Bot.* 79, 667–677.
- Paganin, D., Mayo, S., Gureyev, T.E., Miller, P.R., Wilkins, S.W., 2002. Simultaneous phase and amplitude extraction from a single defocused image of a homogeneous object. *J. Microsc.* 206, 33–40.
- Pedersen, O., Colmer, T.D., 2012. Physical gills prevent drowning of many wetland insects, spiders and plants. *J. Exp. Biol.* 215, 705–709.
- Pedersen, O., Rich, S.M., Colmer, T.D., 2009. Surviving floods: leaf gas films improve O₂ and CO₂ exchange, root aeration, and growth of completely submerged rice. *Plant J.* 58, 147–156.
- Raskin, I., 1983. A method for measuring leaf density, thickness and internal gas. *Hortscience* 18, 698–699.
- Raskin, I., Kende, H., 1983. How does deep water rice solve its aeration problem? *Plant Physiol.* 72, 447–454.
- Sand-Jensen, K., Pedersen, O., Binzer, T., Borum, J., 2005. Contrasting oxygen dynamics in the freshwater isoetid *Lobelia dortmanna* and the marine seagrass *Zostera marina*. *Ann. Bot.* 96, 613–623.
- Schneider, C.A., Rasband, W.S., Eliceiri, K.W., 2012. NIH Image to ImageJ: 25 years of image analysis. *Nat. Methods* 9, 671–675.
- Setter, T.L., Waters, I., Wallace, I., Bekhasut, P., Greenway, H., 1989. Submergence of rice. I. Growth and photosynthetic response to CO₂ enrichment of floodwater. *Aust. J. Plant Physiol.* 16, 251–263.
- Shirtcliffe, N.J., McHale, G., Newton, M.I., Perry, C.C., 2005. Wetting and wetting transitions on copper-based super-hydrophobic surfaces. *Langmuir* 21, 937–943.
- Teakle, N.L., Colmer, T.D., Pedersen, O., 2014. Leaf gas films delay salt entry and enhance underwater photosynthesis and internal aeration of *Melilotus siculus* submerged in saline water. *Plant Cell Environ.* <http://dx.doi.org/10.1111/pce.12269>.
- Tracy, S.R., Roberts, J.A., Black, C.R., McNeill, A., Davidson, R., Mooney, S.J., 2010. The X-factor: visualizing undisturbed root architecture in soils using X-ray computed tomography. *J. Exp. Bot.* 61, 311–313.
- Verboven, P., Herremans, E., Borisjuk, L., Helfen, L., Ho, Q.T., Tschiersch, H., Fuchs, J., Nicolai, B.M., Rolletschek, H., 2013. Void space inside the developing seed of *Brassica napus* and the modelling of its function. *New Phytol.* 199, 936–947.
- Verboven, P., Kerckhofs, G., Mebatsion, H.K., Ho, Q.T., Temst, K., Wevers, M., Cloetens, P., Nicolai, B.M., 2008. Three-dimensional gas exchange pathways in pome fruit characterized by synchrotron X-ray computed tomography. *Plant Physiol.* 147, 518–527.
- Verboven, P., Pedersen, O., Herremans, E., Ho, Q.T., Nicolai, B.M., Colmer, T.D., Teakle, N., 2012. Root aeration via aerenchymatous phellem: three-dimensional micro-imaging and radial O₂ profiles in *Melilotus siculus*. *New Phytol.* 193, 420–431.
- Verboven, P., Pedersen, O., Ho, Q.T., Nicolai, B.M., Colmer, T.D., 2014. The mechanism of improved aeration due to gas films on leaves of submerged rice. *Plant Cell Environ.* <http://dx.doi.org/10.1111/pce.12300>.
- Winkel, A., Colmer, T.D., Ismail, A.M., Pedersen, O., 2013. Internal aeration of paddy field rice (*Oryza sativa* L.) during complete submergence – importance of light and floodwater O₂. *New Phytol.* 197, 1193–1203.
- Winkel, A., Colmer, T.D., Pedersen, O., 2011. Leaf gas films of *Spartina anglica* enhance rhizome and root oxygen during tidal submergence. *Plant Cell Environ.* 34, 2083–2092.
- Winkel, A., Pedersen, O., Ella, E.S., Ismail, A.M., Colmer, T.D., 2014. Gas film retention and underwater photosynthesis during field submergence of four contrasting rice genotypes. *J. Exp. Bot.* 65, 3225–3233.

A.4

Virtual histology uncertainty in Synchrotron x-ray micro-Computed Tomography evaluation

Submitted to Journal of Cranio-Maxillo-Facial Surgery

T. Lauridsen, R. Feidenhans'l, E. M. Pinholt

Submitted to Journal of Cranio-Maxillo-Facial Surgery

TITLE PAGE

“Virtual histology uncertainty in Synchrotron x-ray micro-Computed Tomography evaluation”

Authors:

T Lauridsen¹, PhD student, cand. Scient.

R Feidenhans'l², Professor, PhD, cand.scient.

EM Pinholt³, Professor, DDS, MSci, dr.odont. (DOS)

1: Niels Bohr Institute, University of Copenhagen, Blegdamsvej 19, 2100 Copenhagen Ø, Denmark

2: XFEL, Hamburg, Germany

3: University of Southern Denmark, Faculty of Health Sciences, Institute of Regional Health Research & Research Center South West Denmark, Esbjerg, Denmark

Corresponding author:

Torsten Lauridsen,

Niels Bohr Institute,

University of Copenhagen,

D309,

Universitetsparken 5,

2100 Copenhagen Ø

Denmark.

Phone: 0045 53396638

Email: torstenl@nbi.ku.dk

Abstract

A 3-dimensional (3 D) X-ray tomogram evaluation gives a full view of the bone distribution around an entire implant in contrast to the often used 2 - dimensional (2D) histological methods. High-resolution x-ray absorption tomography was used to evaluate the 3- D bone growth around dental implants in an experimental goat mandible reconstruction model. The tomogram allows for the construction of virtual histological cross sections, which can be used to evaluate the statistical uncertainty of the histologic methods, which was the purpose of this paper. The virtual 2 D histological results showed a significantly higher uncertainty within the same sample than did the full 3 D volume results.

Keywords

Uncertainty, Synchrotron Radiation micro Computed Tomography, Virtual histology, 2 dimensional, 3 dimensional, bone, osseointegration, dental implant, x-ray imaging

Introduction

Light- or electron microscopy histology are the traditional methods for evaluating implant integration in bone. These methods have two major disadvantages: They only supply information in 2 D of the bone to implant distribution along a single line through the sample. Furthermore, the specimens are cut during the preparation technique resulting in a limited number of histological sections per sample to be used for the evaluation of mean values of the peri-implant osseous formation. Synchrotron μ CT (SR μ CT) techniques have been performed during several years (Peyrin et al. 2001; Bernhardt et al. 2004; 2005; Bernhardt 2006; Bernhardt 2012 ; Stiller et al. 2009; Neldam & Lauridsen et al. 2015) and have revealed superior 3 Dimensional (3 D) results in evaluation of dental implant integration (Sarve et al. 2013). In these studies the results have usually been given as volume fractions of bone and at a certain distance from the implant surface, 11 μ m (Sarve et al. 2013) and 18 μ m (Bernhardt et al. 2012). This 3 D measure can be useful, however, due to the lack of description of the geometrical distribution along the dental implant it is not sufficient in order to describe the integration of the implant into the bone. Bernhardt et al. 2012 compared certainty in evaluating bone to implant contact (BIC) and bone to implant volume (BOV) by histological sections and 3 D images from x-ray absorption SR μ CT in a mini-pig study. Comparing 3-4 histological slices per implant to appropriate 3-4 SR μ CT slices, he showed a non-significant difference in uncertainty of evaluations between 2 D and 3 D histology in bone to

implant contact (BIC) as well as in bone to implant volume (BOV). Sarve et al., 2013 compared dental implant integration obtained from 1440 stepped, artifact corrected radiograms, which were reduced in numbers by animation to 350 slides per turn and presented by a “thread-fly-through”. In virtual 2 D- compared to virtual 3 D histology on SR μ CT images of 11x11x11 μ m resolution and at a distance of 11 μ m from the dental implant surface. Sarve, 2013 evaluated BIC by two dimensional quantification to be 21 % less than by three dimensional quantification.

When evaluating tomograms it is essential to use the same parameters as used in ordinary histological methods. Results given both as full 3 D averages and as virtual 2D histological results are beneficial in understanding the integration and geometrical distribution of bone in dental implant osseointegration. In the method of radial analysis in dental implant integration (Neldam & Lauridsen et al. 2015) we have shown a standardized routine for analyzing implants in 3 D of arbitrary geometries instead of having to choose which 3 D volume to analyze (Bernhardt et al 2004, Neldam & Sporning et al. 2017). It is well known, that voxel values represent the absorption coefficients of the volumes represented by actual voxels, however due to measurement deviations, voxel values have some uncertainty. Furthermore, refraction phenomena at interfaces between regions with very different electron densities can create deviations in voxel values including negative absorption coefficients. So far no one has utilized the unique possibility of tomographic data to study the deviation in the results obtained by different 2 D plane sections in the same sample, virtual histologic cross sections. Such a study would reveal the inherent statistical uncertainty in histological investigations deriving from the choice of cutting plane.

Aim of study

The aim of this study was to evaluate the inherent statistical uncertainty in histological investigations comparing virtual histology of 2 D plane sections to full 3 D volume results performed on the same samples.

Hypothesis

The inherent uncertainty in the results obtained by different 2 D plane sections in the same sample, virtual histologic cross sections, is the same obtained from those of 3 D volume results.

Materials & methods

The specimens used for evaluation were cylindrical bone samples containing a titanium dental implant in an experimental goat mandible Critical Size reconstruction Defect model. The samples in the present publication comprised the controls of a previous described surgical project (Neldam & Lauridsen et al. 2015), which was developed and operated by the senior author. For presentation of measurement certainty of the used histological x-ray method, as presented in this paper, the three groups of samples, representing the controls of the vertical augmentation around an Astra dental implant was used. These controls comprised immediate vertical defect reconstruction by particulated, autologous bone, some covered with and some without, a thin titanium membrane (Riemsers Artzen Mittle AG, Greifswald, Insel Riems, Germany), and left empty and covered with a thin titanium membrane, respectively. Seven healthy mature female (Landbred) goats, 4 year of age and weighing 40 - 50 kg were housed at the research facilities at the Foulum Agricultural Center of Research, University of Aarhus, Denmark (Danish Animal Research Council Approval No: 2006-561-1130). On each base of the seven goat mandibles, five Critical Size defects were surgically created and an Astra Osseospeed dental implant (Astra Tech, Molndal, Sweden) was immediately installed. Reconstruction for purpose of new bone formation was performed in order to fill up the defect around the implants. Two defects were reconstructed with Synthetic resorbable *in situ* hardening and Synthetic partially resorbable *in situ* hardening biphasic calcium phosphate (GUIDOR *easy-graft* – and *easy graft* CRYSTAL, Sunstar Suisse SA, Etoy, Switzerland), respectively and used for studying BIC and BVF by another evaluation method than the present (Neldam & Sporning et al. 2017). The design of the Astra Osseospeed dental implant (Astra Tech, Molndal, Sweden) comprises a section of macrothreads, installed into the recipient bone, and a section of microthreads, penetrating into the reconstructed defect, which was the interest of this paper (Fig. 1).

The x-ray acquisitions were carried out at the ID-19 beamline, at the European Synchrotron Radiation Facility, Grenoble, France. The ID-19 beamline, which is specialized in micro-tomography, has a high angular coherence and a small beam size. A monochromatic 67.4 keV x-ray beam was used and the detector was a 2048x 2048 pixel scintillator detector with a pixel size of 5µm. Reconstruction into 3 D was performed using a radon transform algorithm on the beamline server. The full size of the reconstructed tomograms was 2048 x 2048 x 2048 voxels, however, for the data analysis only sections containing newly formed bone i.e. around the microthreads of the dental implant (Fig. 1) was chosen. The analyzed sections comprised a resolution of 2048 x 2048 x 500 voxels. The voxels were cubic with a side length of 5 µm, subsequently the tomogram sections

covered a volume of $10.24 \times 10.24 \times 2.5 \text{ mm}^3$. Each tomogram volume contained one implant with its long axis oriented along the z-direction with subsequent orientation of the horizontal slice (transverse plane) of the implant approximately as an elliptical cross section (Fig. 2).

Data analysis

The data analysis was performed on a slice-by-slice basis. For each slice, the center-of-mass of the titanium implant was identified (Fig. 2). Using the screws center-of-mass coordinates as origo, a polar coordinate system was defined in each tomogram slice. The polar coordinate system had two coordinates, the angular coordinate (theta) and the radial distance from Origo (r). At a given angle, theta, the distance from the origo to the edge of the implant along the radial direction was marked. Such radial center-to-edge distances were found for 2000 angles and defined the edge of the implant. To define the Region of Interest (ROI) for our measurements the outer limit of the radial dimension was set to $1000 \mu\text{m}$ beyond the implant edge, which is equivalent to 200 pixels. In this way the area between this outer radius and the implant edge represented the first mm of bone and cavities surrounding the implant, referred to as the circle band because of its approximately circular shape.

The slice-by-slice conversion from 2 D cartesian coordinates to 2 D polar coordinates as described above was performed as a linear pixel value interpolation. The result of converting the tomogram to polar coordinates is not isometric due to the circumference of the inner circle representing the threads of the implant edge is not parallel to the outer circle. However, the radial distance dimension is preserved, which is the dimension of interest for our evaluation of results and subsequent calculation of the inherent uncertainty.

In the analysis performed along the radial dimension of the polar coordinate system, '(Web ref.1)', four parameters were derived: 1) Implant-bone distance was the average distance from the implant edge to the first detected bone along the radial distance. 2) Radial bone fraction was the average occurrence of bone along the radial lines. 3) Bone free surface was implant surface without any bone within the analyzed radial distance of 1 mm. 4) Contact fraction was the fraction of the implant surface that was covered by bone within a contact region, defined as the first $50 \mu\text{m}$ along the radial dimension (Neldam & Lauridsen et al. 2015).

Virtual histology-equivalent results were created by adding up the radial analysis results along a given polar angle for all slices representing the summed result of virtual histologic data corresponding to one vertical slice of the implant.

Virtual histology variations across different samples were performed on tomograms presenting the three groups of samples, representing the controls of the vertical augmentation around the Astra dental implant using autologous bone covered with and without a thin titanium membrane (Riemser Artzen Mittle AG, Greifswald, Insel Riems, Germany), and left empty covered with a thin titanium membrane, respectively.

For the statistical hypothesis testing, we assumed Gaussian distributed samples with different variances. A 95% two-tailed confidence interval was chosen.

Results

Histologic variations across different samples were performed on tomograms presenting the three control groups of each six, six and five samples representing the above mentioned vertical augmentation, respectively

The tomographic measurements were performed on seven samples, representing the seven goats, in each group, and a total of four samples were discarded (1, 1 and 2 in the different groups, respectively) in the following data analysis due to misalignments and apart-broken implants, which prevented a meaningful analysis.

The key numbers and their standard deviations in the histologic cross sections for each of the samples are shown in Tables 1, 2 and 3. The key parameters of bone integration showed significant variation along the theta-angle in all samples. For all four parameters, implant-bone distance, radial bone fraction, bone free surface and contact fraction, the virtual histology standard results and deviations are shown in Tables 4, 5 and 6. The variations in the virtual histologic cross sections were significantly higher than the variations in the full volume results, Table 4. Even within a single volume sample the standard deviation of the virtual histology results, Table 3, was often higher than the standard deviation of the full volume results (second line of Table 4). For all three sets of samples, Tables 4, 5 and 6, the volume results showed significantly smaller standard deviations than the virtual histology results. Typically the difference between the two was around a factor of two. The larger standard deviations for the virtual histological results in Tables 1-6 represent statistical

effects. The limited sampling area tested by a single virtual histology cross section increased the variance of the measurement results compared with the full volumetric results. This effect was illustrated by considering the radial bone fraction in Tables 1-6 and by use of the Welch's t-test with a 95% confidence interval to test if the three sets were significantly different, Table 7. Welch's t-test has been chosen since the variances across sample types vary too much to be assumed constant, and since we don't have data to support an abandonment of a Gaussian distribution model. The results from performing the corresponding t-test for an average set of virtual histological cross sections, using the same number of samples assuming the same mean values, but using the larger variances found for the virtual histological results in Tables 4-6, are shown in Table 8. The t-test revealed a significant difference between the results of full volume bone fractions obtained by reconstruction with autologous bone covered by the membrane in contrast to reconstruction with autologous bone not covered by a membrane and the empty but membrane-covered cavity. Using the average virtual histology result in the same t-test, the two sample groups were not significantly different. Hence, with the present samples, a full volumetric analysis revealed a significant difference, which the average virtual histology examination did not detect.

Discussion

A useful algorithm for deriving standard histologic parameters from 3 D SR μ CT tomograms was used to evaluate crucial parameters in dental implant osseointegration. Upon comparing 3 D volume data concerning implant-bone distance, radial bone fraction, bone free surface and contact fraction with virtual histologic cross sections of the tomograms, we have shown that the uncertainty in the full 3 D analysis results was significantly lower than the uncertainty in the virtual histology results. Subsequently our hypothesis was dismissed. The key numbers in bone integration and their standard deviations in the virtual histology cross sections for each of the samples as shown in Tables 1, 2 and 3 showed significant variation along the theta-angle in all samples. This indicates that traditional histological evaluations of bone volume and contact area fractions have a significantly higher uncertainty than what can be obtained by SR μ CT. The lower uncertainty of the SR μ CT is a statistical effect. SR μ CT deals with the whole 2 D surface of the implant, whereas the traditional histologic method only considers a one dimensional vertical line on the implant surface. For all three sets of samples, the volume 3 D results showed significantly smaller standard deviations than the virtual histology results. Typically the difference between the two was around a factor of two.

Previous studies have compared single histological results with corresponding single 2 D plane sections of tomographic results and full 3 D results (Bernhardt et al. 2004 , Stiller et al. 2009).

Uncertainty in results within 2 D histology compared to 3 D full volume readings was discussed by Sarve et al ,2013 who observed a 2 D quantification of 21 % BIC less of that observed in full volume readings of 350 slices per turn of the dental implants. In contrast Rebaudi et al, 2004 found an increase of 20 % in bone to implant apposition in 2 D histomorphometry compared to full volume observations obtained with micro CT.

This may imply that the observed variations are statistical effects of the reduced sampling performed in 2 D histology compared to the vast number of samplings in 3 D full volume evaluations, which in our case comprised 2000 readings of each specimen.

SR μ CT has superior characteristics such as high resolution, minimal artifacts, a high voltage making penetration of the titanium dental implant possible and 360 ° rotation at acquisition. Due to acquisition at each 0.2°, a very high number of tomograms become available for the evaluation. This method therefore supplies us with results given both as full volume averages and as virtual 2 D histological results and is beneficial in understanding the integration and geometrical distribution of bone in dental implant osseointegration. The significantly smaller inherent uncertainty in full volume SR μ CT compared to 2 D virtual histology underlines the strength of this method as today's gold standard in dental implant – and periimplant bone evaluation. To further elaborate on the increased statistical power from 3 D relative to 2 D, we have used the found means and variances from the different sample groups to determine the expected two-tailed p-values for different numbers of samples. These results are shown in Fig. 3-5. For all three sample groups the expected two-tailed p-values are higher for SR μ CT analysis than for virtual histology. This is a purely statistical effect: By inspecting the full 3 D volume, we will inevitably lower the observed variances, resulting in improved p-values. If derived parameters were constant for all possible histology cross sections, we subsequently would observe an unchanged variance going from 2 D to 3 D evaluations. However, this is hardly a realistic scenario and therefore decreased variances always should be expected in 3 D evaluations in contrast to 2 D observations.

Conclusion

Using an algorithm for finding full volume averages of standard histology parameters in SR μ CT tomograms and by comparing these with virtual histology cross section data of the tomograms, we

have shown that the uncertainty in the full 3 D analysis results is significantly lower than the uncertainty in the virtual histology results.

Tables:

sample #	implant-bone distance [μm]	radial bone fraction [%]	bone free surface [%]	contact fraction [%]
770	69.7 ± 13.9	66.5 ± 6.7	0.0 ± 0.1	55.9 ± 9.0
775	130.7 ± 49.2	61.1 ± 6.4	6.1 ± 4.8	48.5 ± 14.8
780	87.9 ± 59.5	70.0 ± 5.7	2.3 ± 5.4	64.1 ± 10.7
785	89.0 ± 43.4	69.3 ± 9.3	1.9 ± 3.9	59.8 ± 9.5
811	68.1 ± 32.0	75.1 ± 5.0	1.4 ± 2.5	65.9 ± 12.4
816	89.5 ± 62.1	59.5 ± 11.9	3.1 ± 4.9	68.4 ± 10.8

Table 1. Data from the six samples with autologous bone covered by the membrane. For each sample the mean across all 2000 virtual histology cross sections, and their standard deviations are given as “mean \pm std”. E.g for sample 770, the mean implant bone distance is 69.7 μm , and the standard deviation among the virtual histology cross sections is 13.9 μm .

sample #	implant-bone distance [μm]	radial bone fraction [%]	bone free surface [%]	contact fraction [%]
773	128.7 ± 116.5	63.8 ± 12.5	8.3 ± 12.3	65.1 ± 11.1
778	72.7 ± 38.0	57.3 ± 10.7	1.8 ± 3.8	63.9 ± 12.0
788	211.9 ± 112.2	36.6 ± 12.0	16.0 ± 12.8	59.4 ± 8.3

814	115.9 ± 30.2	55.6 ± 5.5	6.3 ± 3.7	66.5 ± 6.7
819	51.0 ± 13.4	67.0 ± 5.2	0.3 ± 0.5	71.7 ± 9.6

Table 2. Data from the five samples with autologous bone without the membrane. For each sample the mean across all 2000 virtual histology cross sections, and their standard deviations are given as “mean ± std”.

sample #	implant-bone distance [μm]	radial bone fraction [%]	bone free surface [%]	contact fraction [%]
769	162.8 ± 78.7	55.0 ± 8.6	10.3 ± 7.3	59.4 ± 11.5
774	159.5 ± 83.2	40.7 ± 9.2	10.0 ± 6.8	59.7 ± 16.0
779	148.2 ± 84.6	59.1 ± 9.4	9.6 ± 8.2	61.7 ± 12.6
784	106.7 ± 67.0	59.6 ± 13.1	5.8 ± 7.4	63.5 ± 7.8
810	195.6 ± 119.7	48.7 ± 18.7	11.0 ± 11.2	48.7 ± 13.2
815	112.7 ± 99.4	42.3 ± 14.5	7.1 ± 10.3	74.4 ± 9.9

Table 3. Data from the six empty samples. For each sample the mean across all 2000 virtual histology cross sections, and their standard deviations are given as “mean ± std”.

	implant-bone distance [μm]	radial bone fraction [%]	bone free surface [%]	contact fraction [%]
mean result	89.2	66.90	2.50	60.40
deviation of volume results	20.6	5.30	1.90	6.70
deviation of virtual	50.8	9.50	4.50	13.20

histology results				
-------------------	--	--	--	--

Table 4. Mean result and standard deviations for the six samples with autologous bone covered by the membrane. The deviations are *measured standard deviations*, as they are based on the biased sample variance, see appendix A1. The *deviation of volume results* is found by comparing the six volumetric averages from Table 1. E.g. for the implant bone distance, the standard deviation of the set {69.7; 130.7; 87.9; 89.0; 68.1; 89.5} is 20.6. If, instead of using the 6 volumetric averages, we compare all the 12,000 virtual histology cross sections from the six samples (2000 cross sections per sample), we get a standard deviation of 50.8 μm . This number is then called the *deviation of the virtual histology results*.

	implant-bone distance [μm]	radial bone fraction [%]	bone free surface [%]	contact fraction [%]
mean result	116.0	56.10	6.50	65.30
deviation of volume results	55.6	10.60	5.60	4.00
deviation of virtual histology results	94.0	14.40	10.00	10.50

Table 5. Mean result and standard deviations for the six samples with autologous bone without the membrane. The deviations are *measured standard deviations* as they are based on the biased sample variance. For the t-test calculations shown later the *unbiased sample variance* is used.

	implant-bone distance [μm]	radial bone fraction [%]	bone free surface [%]	contact fraction [%]
mean result	147.6	50.90	9.00	61.20
deviation of volume results	30.5	7.60	1.90	7.50

deviation of virtual histology results	95.3	14.90	8.90	14.30
--	------	-------	------	-------

Table 6. Mean result and standard deviations for the empty samples. The deviations are *measured standard deviations* as they are based on the biased sample variance. For the t-test calculations shown later the *unbiased sample variance* is used.

	Auto no membrane	Empty control
Autologous bone with membrane	P=0.886	P=0.996
Autologous bone without membrane		P=0.562

Table 7: Two-tailed p-values for Welch's t-test (variances assumed not to be equal) on the volumetric bone fraction results in tables 1-3. For the t-test calculations the *unbiased variance estimator* is used, see appendix A2.

	Autologous bone without membrane	Empty control
Autologous bone with membrane	P=0.806	P=0.944
Autologous o without membrane		P=0.425

Table 8: Two-tailed p-values for Welch's t-test (variances assumed not to be equal) on average histological cross sections as found in Tables 1-3.

Acknowledgements

Vi have received fundig from the Excellence Programme for interdisciplinary research UCPH 2016, CoNEXT, and from Innovationsfonden, grant number 0603-00491B (NEXIM).

Goat and titanium dental implants were kindly provided by Astra Tech Company, Mölndal, Sweden

Scannings, bone substitutes and histology preparations were kindly provided by the former Degradable Solutions, Schlieren, Switzerland, now Sunstar Company, Etoy, Switzerland.

References

Bernhardt R, Scharnweber D, Muller B, Thurner P, Schliephake H, Wyss P, Beckmann F, Goebbels J, Worch H . Comparison of microfocus- and synchrotron X-ray tomography for the analysis of osteointegration around Ti6Al4V implants. *Eur Cell Mater* 7: 42-51; 2004.

Bernhardt B, Dolder J, Bierbaum S, Beutner R, Scharnweber D, Jansen J, Beckmann F, Worch H. Osteoconductive modifications of Ti-implants in a goat defect model: characterization of bone growth with SR μ CT and histology. *Biomaterials* 26 ;3009–3019 ; 2005.

Bernhardt R, Scharnweber D, Muller B, Beckmann F, Goebbels J, Jansen J, Schliephake H, Worch H . 3D analysis of bone formation around titanium implants using micro computed tomography (μ CT): *Developments in X-Ray Tomography V*, edited by Ulrich Bonse, v. 6318, 631807; 2006.

Bernhardt R, Kuhlisch E, Schultz MC, Eckelt U, Stadlinger B. Comparison of bone-implant contact and bone-implant volume between 2 D- histological sections and 3 D-SR μ CT slices . *Eur Cell Mater* 23; 237-248;2012.

Neldam CA, Lauridsen T, Rack A, Lefolii TT, Jørgensen NR, Feidenhansl R, Pinholt EM . Application of high resolution synchrotron micro-CT radiation in dental implant osseointegration. *J Cranio- Max Fac Surg* 43;5:682-87; 2015.

Neldam CA, Sporring J, Rack A, Lauridsen T, Hauge EM, Jørgensen HL, Jørgensen NR, Feidenhansl R, Pinholt EM . Synchrotron radiation μ CT and histology evaluation of bone-to-implant contact. *J Craniomaxillofac Surg*. 2017 Jun 3. pii: S1010-5182(17)30185-3. doi: 10.1016/j.jcms.2017.05.019. [Epub ahead of print]

Peyrin F, Muller C, Carillon Y, Nuzzo S, Bonnassie A, Briquet A . Synchrotron radiation μ CT: a reference tool for the characterization of bone samples. *Adv in Experiment Med Biol* 496; 129-142; 2001.

Rebaudi A, Koller B, Laib A, Trisi P . Microcomputed tomographic analysis of the peri-implant bone. *Int J Periodontics Restorative Dent* 24:316-325; 2004.

Sarve, H, Friberg B, Borgefors G, Johansson CB . Introducing a Novel Analysis Technique for Osseointegrated Dental Implants Retrieved 29 Years Postsurgery. Clin Implant Dent Relat Res 15: 538-549; 2013.

Stiller M, Rack A, Zabler S, Goebbels J, Dalugge O, Jonscher S, Knabe C . Quantification of bone tissue regeneration employing beta-tricalcium phosphate by three-dimensional non-invasive synchrotron micro-tomography--a comparative examination with histomorphometry. Bone 44: 619-628; 2009.

Web reference:

1. Lauridsen T (2017). www.fys.ku.dk/~torstenl/implant_bone_analysis.m

Figure list

Fig 1:

3 D-renderings of the tomogram of sample number 770. The implant in white is visible in all three renderings. a) all bone surrounding the implant is visible. b) only the bone surrounding the implant's microthread is visible (i.e. the bone analyzed in this publication). c) only leaves the implant visible. Ring artefacts from the reconstruction are seen in the top of a) and b).

Fig 2.

Slice through the middle of the analyzed section of the tomogram of sample 770 (see Fig 1). The implant is seen as an approximately circular white shape in the centre of the slice. The bone is the lighter grey surrounding the impant. The darker grey is bone cavities and external air. The four corners are greyed out in the reconstruction, since they are not completely angularly covered in the scanning. Some arbitrary virtual histology cross section is illustrated by the red line. For this virtual histology cross section, various parameters can be found. If we compare the parameters from a lot of different cross sections, we can find their means and their standard deviations.

Fig 3.

Comparison of expected p-values if comparing autologous bone samples with and without membrane. As input are used the found variances from virtual histology and full 3 D CT analysis. The lower variances in the full CT analysis result in increased p-values, and a 95 % confidence will be reached with 8 samples. For the variances found in the virtual histology analysis, 10 samples would be necessary to reach 95 % confidence.

Fig 4.

Comparison of expected p-values if comparing autologous bone samples covered with a membrane with the empty samples with no membrane. As input are used the found variances from virtual histology and full 3 D CT analysis. The lower variances in the full CT analysis result in increased p-values, and a 95 % confidence will be reached with 4 samples. For the variances found in the virtual histology analysis, 5 samples would be necessary to reach 95 % confidence.

Fig 5.

Comparison of expected p-values if comparing the empty samples and the uncovered autologous bone samples. As input are used the found variances from virtual histology and full 3 D CT analysis. The lower variances in the full CT analysis result in increased p-values, and a 95 % confidence will be reached with 32 samples. For the variances found in the virtual histology analysis, 48 samples would be necessary to reach 95 % confidence.

Appendix.

A1: biased sample variance

The biased sample variance used for calculating the measured standard deviations used in Tables 1-6 is given by:

$$\sigma^2 = \frac{1}{N} \sum_{n=1}^N (\mu - X_n)^2$$

Where X is the stochastic variable in question, N is the number of occurrences in the set and μ is the mean value, defined as:

$$\mu = \frac{1}{N} \sum_{n=1}^N X_n$$

From the biased sample variance, the measured standard deviation is found as:

$$\sigma = \sqrt{\sigma^2}$$

A2: unbiased variance estimator

The unbiased variance estimator used for calculating the p-values in Tables 7-8 is given by:

$$s^2 = \frac{1}{N-1} \sum_{n=1}^N (\mu - X_n)^2$$

Where X is the stochastic variable in question, N is the number of occurrences in the set and μ is the mean value, defined as above.

Figure
[Click here to download high resolution image](#)

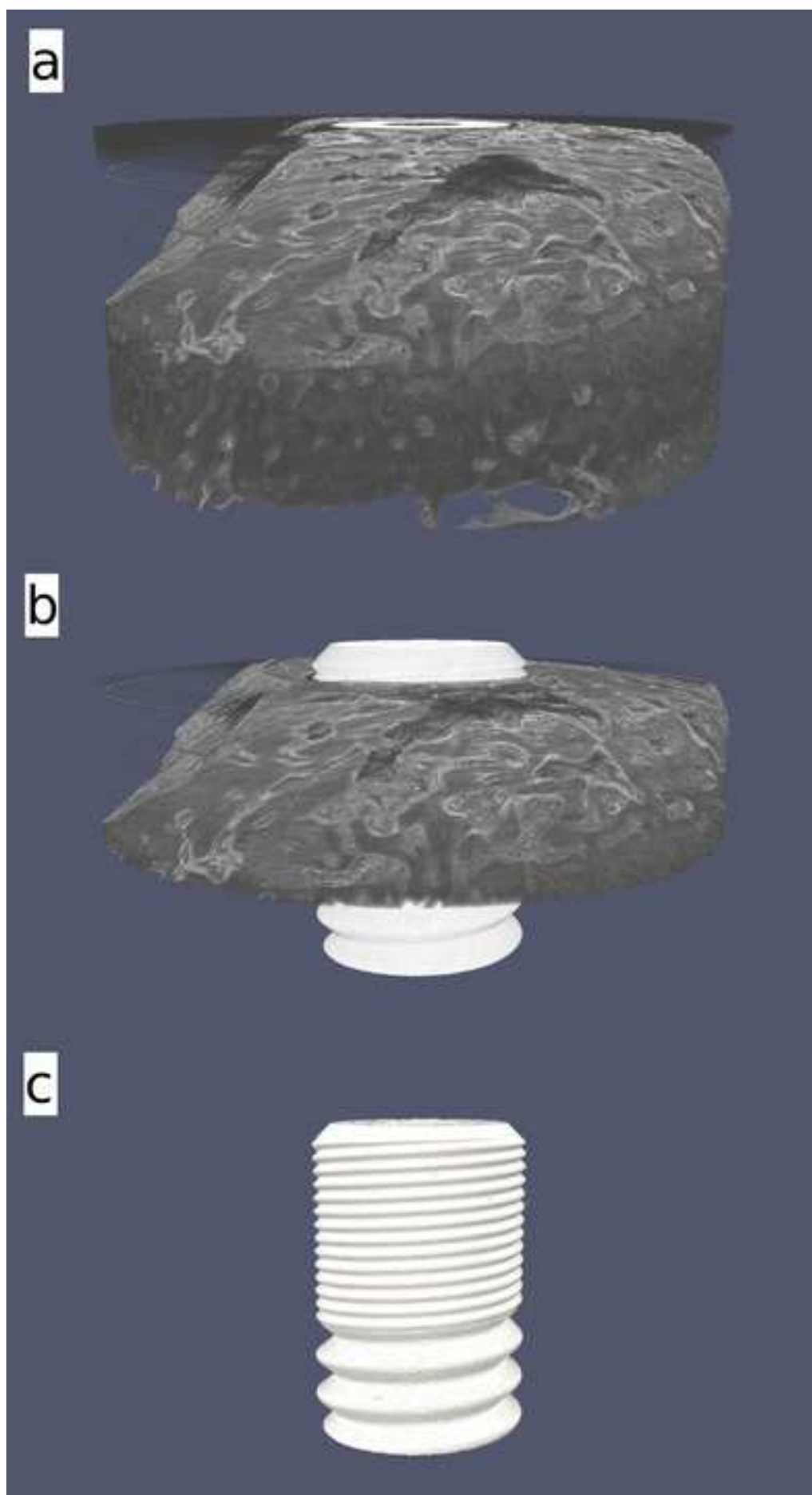


Figure
[Click here to download high resolution image](#)

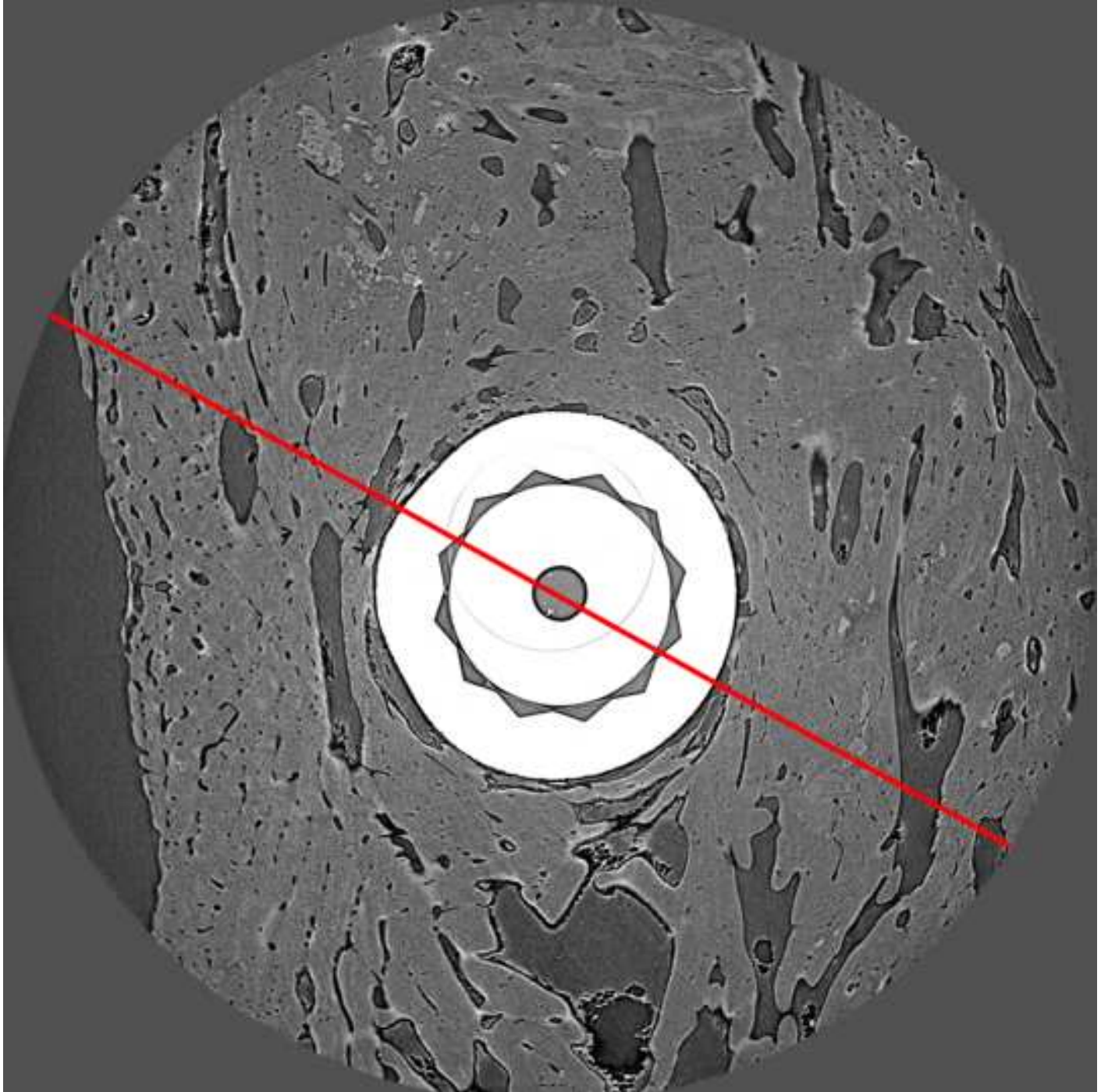


Figure
[Click here to download high resolution image](#)

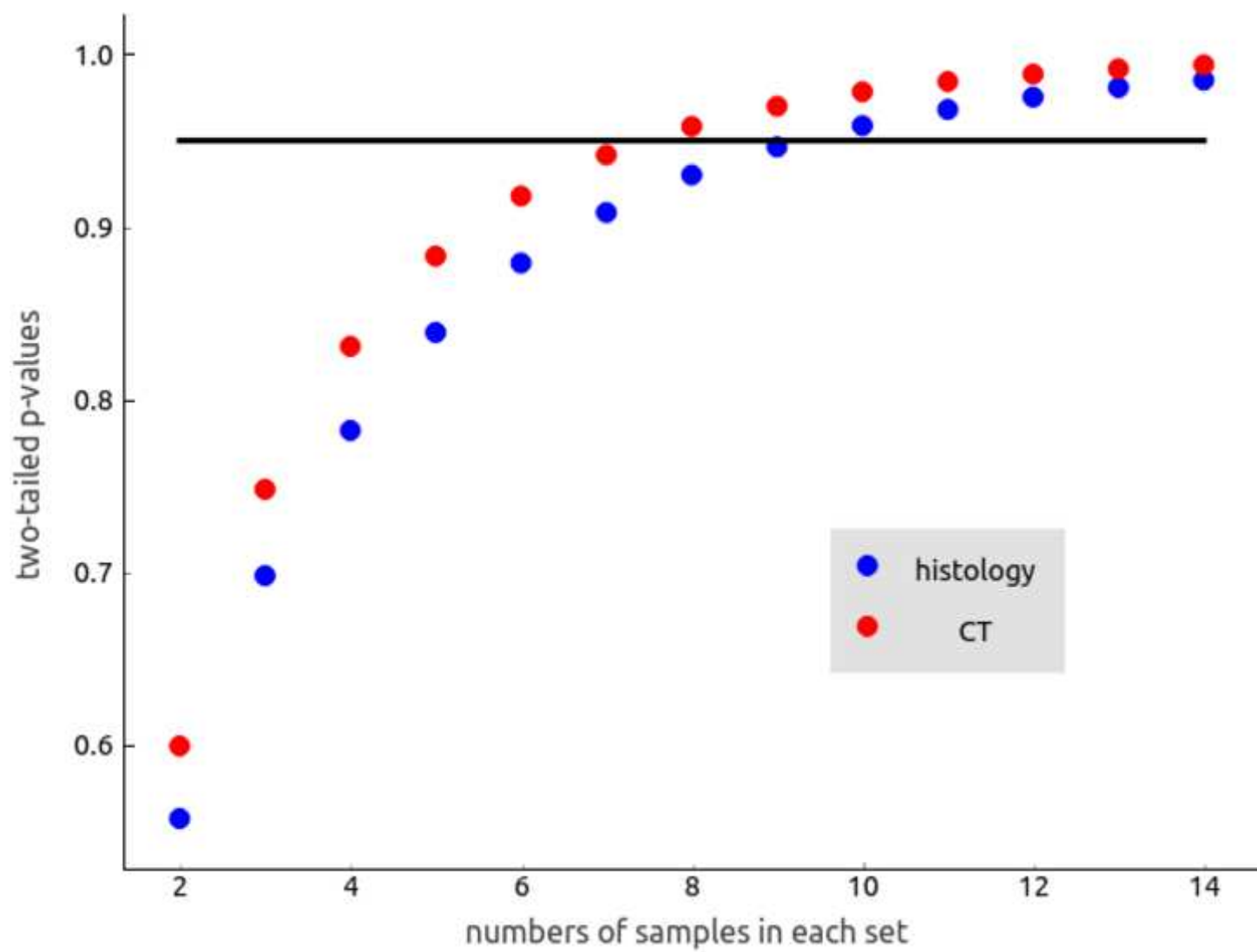


Figure
[Click here to download high resolution image](#)

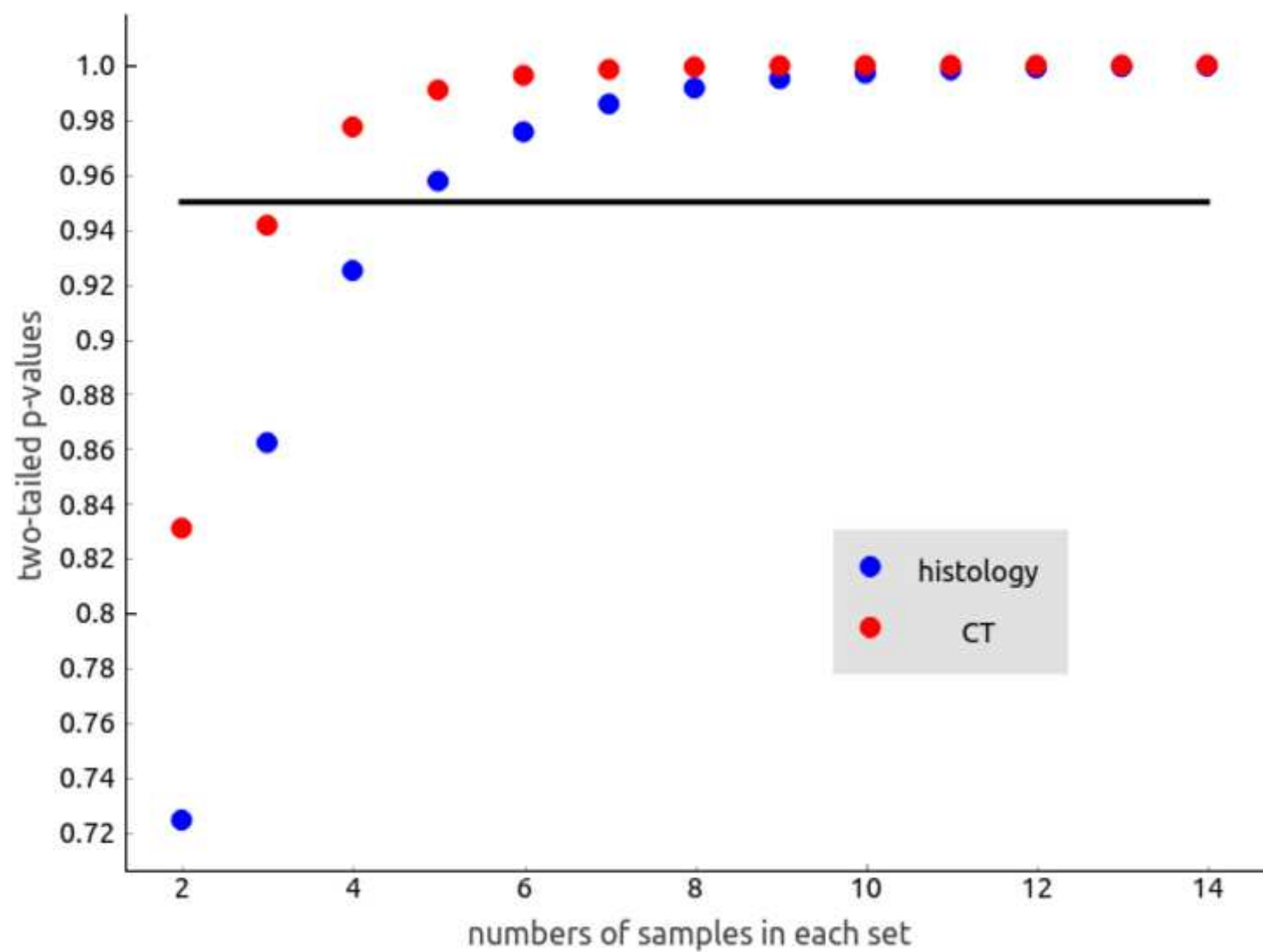
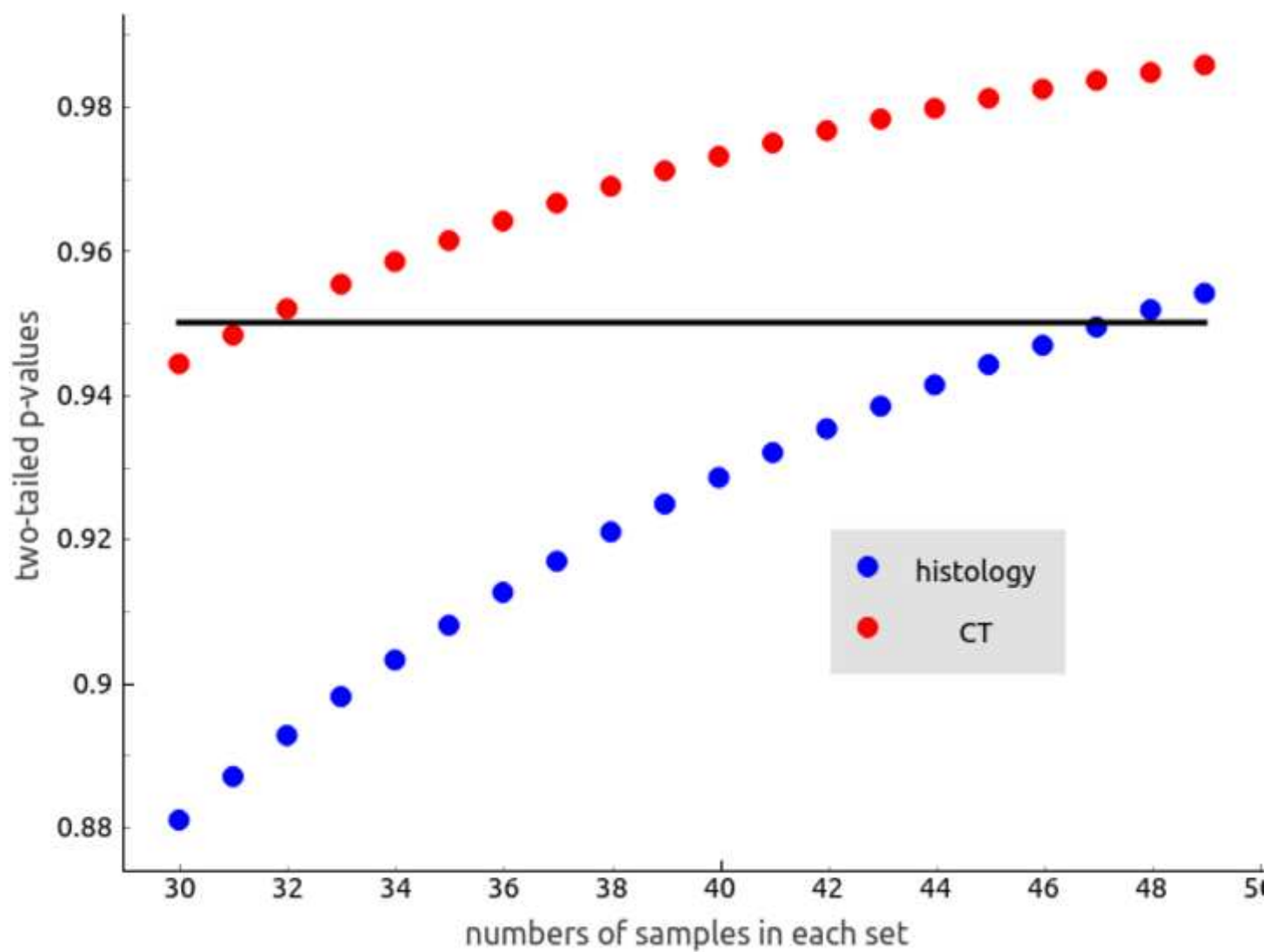


Figure
[Click here to download high resolution image](#)



A.5

Application of high resolution synchrotron micro-CT radiation in dental implant osseointegration

Journal of Cranio-Maxillo-Facial Surgery (2015)

C. A. Neldam, T. Lauridsen, A. Rack, T. T. Lefolii, N. R. Jørgensen, R. Feidenhans'l, E. M. Pinholt

Journal of Cranio-Maxillo-Facial Surgery (2015) 43: 682-687

Contents lists available at [ScienceDirect](http://www.sciencedirect.com)

Journal of Cranio-Maxillo-Facial Surgery

journal homepage: www.jcmfs.com

Application of high resolution synchrotron micro-CT radiation in dental implant osseointegration

Camilla Albeck Neldam ^{a, b, *}, Torsten Lauridsen ^e, Alexander Rack ^c, Tore Tranberg Lefolii ^d, Niklas Rye Jørgensen ^{a, b}, Robert Feidenhans'l ^e, Else Marie Pinholt ^f^a Research Center for Ageing and Osteoporosis, Departments of Diagnostics and Medicine, Copenhagen University Hospital Glostrup, Glostrup, Denmark^b Institute of Clinical Medicine, University of Copenhagen, Copenhagen, Denmark^c European Synchrotron Radiation Facility, Grenoble, France^d Department of Oral and Maxillofacial Surgery, University Hospital of Copenhagen (Rigshospitalet), Copenhagen, Denmark^e Nano Science Center, Niels Bohr Institute, University of Copenhagen, Copenhagen, Denmark^f Faculty of Health Sciences, Institute for Regional Health Sciences, University of Southern Denmark, Denmark

ARTICLE INFO

Article history:

Paper received 23 November 2014

Accepted 18 March 2015

Available online 25 March 2015

Keywords:

Bone structure

Dental implants

Evaluation

High resolution

Osseointegration

Synchrotron radiation micro-CT

ABSTRACT

The purpose of this study was to describe a refined method using high-resolution synchrotron radiation microtomography (SRmicro-CT) to evaluate osseointegration and peri-implant bone volume fraction after titanium dental implant insertion. SRmicro-CT is considered gold standard evaluating bone microarchitecture. Its high resolution, high contrast, and excellent high signal-to-noise-ratio all contribute to the highest spatial resolutions achievable today. Using SRmicro-CT at a voxel size of 5 μm in an experimental goat mandible model, the peri-implant bone volume fraction was found to quickly increase to 50% as the radial distance from the implant surface increased, and levelled out to approximately 80% at a distance of 400 μm . This method has been successful in depicting the bone and cavities in three dimensions thereby enabling us to give a more precise answer to the fraction of the bone-to-implant contact compared to previous methods.

© 2015 European Association for Cranio-Maxillo-Facial Surgery. Published by Elsevier Ltd. All rights reserved.

1. Introduction

X-ray micro-computed tomography (micro-CT) (Bonse and Busch, 1996) combined with synchrotron radiation X-ray sources enables spatial resolution in the micrometre regime for three-dimensional (3D) imaging of bone microarchitecture combined with a high level of image sensitivity. In combination with X-ray optical elements the resolution can be further increased up to the nanometre scale (Withers, 2007). A synchrotron source is a large-scale facility: the common design comprises an electron gun; a linear accelerator or microtron, where free electrons are accelerated to a medium energy; a circular accelerator, the actual synchrotron, in which the electrons are raised to their final energy in the GeV regime; and a storage ring where they are maintained at a constant

energy. The actual radiation used for the experiments is generated in the storage ring: synchrotron radiation refers to the electromagnetic radiation produced when relativistic electrons circulating in the storage ring are deflected by strong magnetic fields (Wiedemann, 2002), with subsequent synchrotron light being emitted in a narrow beam at a tangent to the curved trajectory of the electrons in the storage ring (Wiedemann, 2002). Beamlines, where experiments can be carried out, surround the storage ring. Commonly their design is highly adapted to the experimental techniques used, such as X-ray diffraction, X-ray fluorescence or X-ray imaging.

To achieve high spatial resolution for synchrotron radiation micro-CT (SRmicro-CT) indirect detectors are commonly used; the luminescent image of a scintillator screen is captured by magnifying visible light optics and a charge-coupled device or complementary metal-oxide-semiconductor (CMOS)-based cameras. The effective pixel size of the detector needs to be adapted to the desired spatial resolution according to Shannon's theorem (Bonse and Busch, 1996). Such detectors operated at high spatial resolution commonly offer limited detection efficiency due to the thin

* Corresponding author. Departments of Clinical Biochemistry and Medicine, Copenhagen University Hospital Glostrup, Nordre Ringvej 57, 2600 Glostrup, Denmark.

E-mail address: camillaneldam@hotmail.com (C.A. Neldam).

scintillators required which make them less attractive for laboratory-based micro-CT. SRmicro-CT enables efficient use of high-resolution indirect detectors and consequently offers several advantages in contrast to micro-CT. The high photon flux density allows for high spatial resolution with SRmicro-CT and at the same time the narrow bandwidth of radiation for illumination also increases the contrast. SRmicro-CT is considered the gold standard of imaging for the bone microstructure (Peyrin et al., 2010), and is nowadays accessible as a standard tool on many synchrotron light sources located around the globe (Rack et al., 2011). Due to the quasi-parallel beam geometry at a synchrotron light source, the tomographic reconstruction can be done on a slice-by-slice basis, without the need of interpolation steps, which are frequently required when working in cone-beam geometry. It is the combination of high resolution, a high signal-to-noise ratio, and the different contrast modalities that renders SRmicro-CT an excellent analytical tool suited for studies in the biomedical field (Bernhardt et al., 2004; Feldkamp et al., 1989; Rack et al., 2011; Ritman, 2004; Ruegsegger et al., 1996; Ruhli et al., 2007; Stiller et al., 2009).

The application of SRmicro-CT in the bio-medical field has recently been evaluated in a review by Neldam and Pinholt (2014). The review depicted that SRmicro-CT has been used to evaluate osseointegration of titanium implants (Bernhardt et al., 2004), visualization of the vascular canals in cortical bone, micro-architecture of osteoporotic bone, and osseous microcracks (Bousson et al., 2004; Cooper et al., 2011; Larrue et al., 2011; Voide et al., 2009).

Studies have depicted osseointegration with bone-to-implant contact of 60–80% when using light microscopy (Albrektsson, 2008; Shah et al., 2014). Thus, if parts of the implant surface are not in direct contact with bone, it is relevant to measure the implant–bone distance. Volume images obtained with SRmicro-CT make it possible to distinguish between different material phases within a sample, i.e. bone, titanium implant and cavities containing either air, blood vessels or fibrous tissue, by their different densities (Rack et al., 2006, 2011; Stiller et al., 2009) due to the high contrast given by the intense photon flux density. Classic histomorphometry enables evaluation of different levels of mineralization while micro-CT/SRmicro-CT visualizes bone with a certain threshold of mineralization. At the 5–10 μm scale, SRmicro-CT makes it possible to assess bone mineralization simultaneously with bone microstructure in both trabecular and cortical bone in 3D (Bonse et al., 1994; Peyrin, 2009).

The peri-implant bone volume fraction is defined as the bone surrounding an implant. Peri-implant bone volume contact fraction

is the area in close proximity to the implant surface including the contact area, which is another important measure of osseointegration of dental implants. The peri-implant bone volume contact fraction is often evaluated within a threshold of 50 μm radial distances from the implant surface (Davies, 1996). Visual inspection within this distance may define the maximum width of the artificial absorption coefficient lowering at the edge of the implant, originating from a refraction-based artefact.

1.1. Aim of the study

The aim of this study was to present the application of high-resolution 3D SRmicro-CT images at a 5 μm voxel size in evaluating the peri-implant bone volume contact fraction, bone-to-implant contact (BIC), and the peri-implant bone volume fraction, in an experimental goat mandible model, representing recipient and grafted bone after vertical augmentation.

2. Materials and methods

2.1. Bone sample

One bone sample containing a titanium dental implant (Astra-Tech OsseoSpeed, ST Molndal, Sweden) 8 mm long \times 3.5 mm in diameter and comprising macro threads for the lower 5.5 mm and micro threads for the upper 2.5 mm was used for evaluation. The implant was installed according to the manufacturer's instructions, in a critical size defect of a goat's mandible (Fig. 1). Immediate vertical bone augmentation was performed with bone chips of $0.5 \times 3 \times 1 \text{ mm}^3$ – $0.5 \times 5 \times 1 \text{ mm}^3$ in size processed in bone mills (Liebinger, Freiburg, Germany; Quentin, Leimen, Germany), and the defect was covered by a titanium membrane (Riemser Artzen mittle AG, Insel Riems, Germany). After 20 weeks of healing the bone sample including the dental implant was taken, fixated in 10% formaldehyde (Rigshospitalets Apotek, Rigshospitalet, Denmark), dehydrated in graded alcohol solutions and finally embedded in Technovit in an acrylic cylinder, 12 mm in diameter and 20 mm in height (Donath, 1993). The sample was left uncut for scanning purposes.

The region of interest (ROI) for this study was defined as the part of the sample that included bone and the micro threads of the implant representing newly formed bone around the original defect (Fig. 2). For comparison, the macro thread area surrounded by the recipient bone was used. The peripheral limitation of the ROI

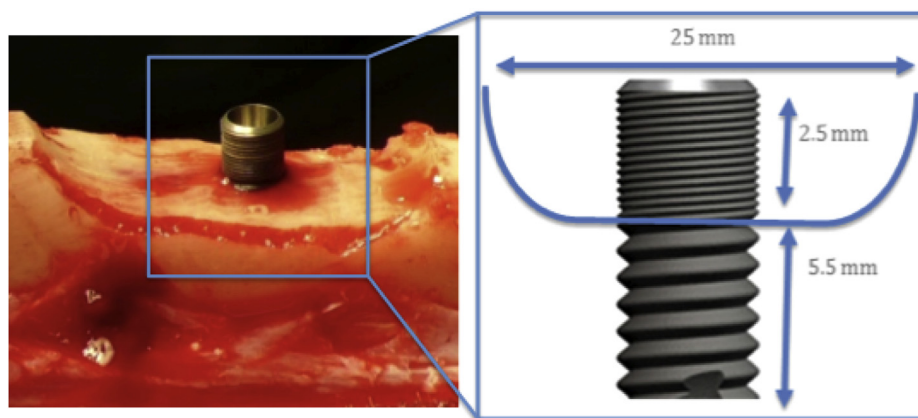


Fig. 1. Illustration of the critical size defect and the titanium implant before reconstruction with bone graft. The cartoon illustrates the implant installation; where the upper part present the area of grafted autologous bone and the area below the blue line present the recipient bone.

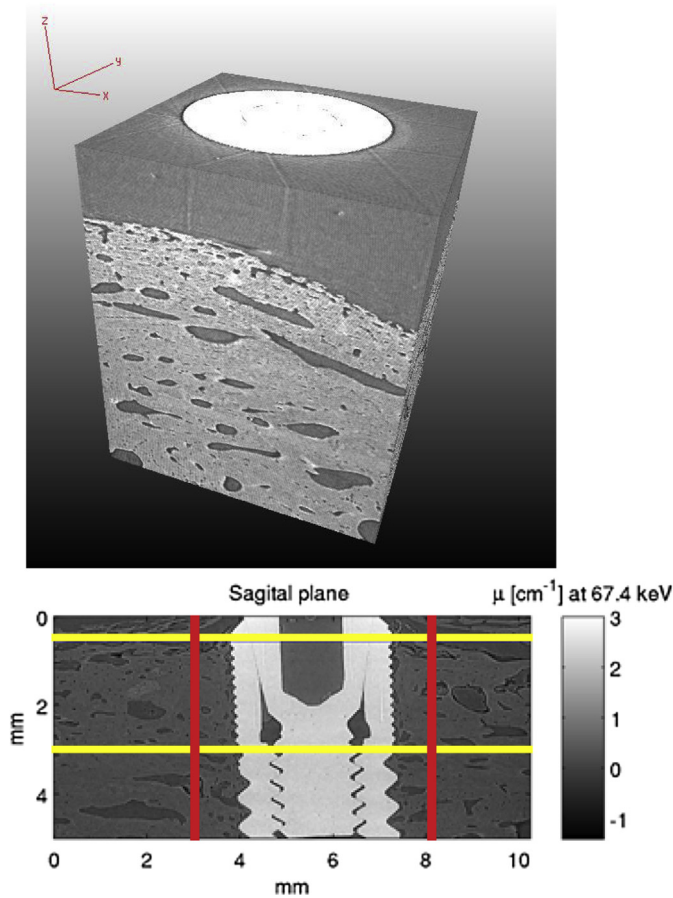


Fig. 2. Slice of a vertical tomogram. The yellow lines indicate the ROI in a horizontal plane with the grafted area between the two lines and recipient bone below the lowest yellow line. The red lines indicate the ROI in a vertical plane.

was bounded by a circular band placed 2000 μm away from the implant surface (Fig. 3).

2.2. Synchrotron radiation facility

The SRmicro-CT scans were carried out at the ID19 beamline, at the European Synchrotron Radiation Facility (ESRF) in Grenoble, France. ID19 is ideally suited for such an experiment, as it offers a sufficiently high photon flux density and sufficient coherence properties at higher energies. Furthermore, the flexible layout of the experimental setup allows one to exploit propagation-based phase contrast with sample-detector distances of up to several metres. As the sample for X-ray imaging included a dental implant made from titanium, a comparatively high photon energy of approximately 67 keV (pink) was chosen, i.e. the emitted radiation of a wiggler insertion device (a magnetic device) was filtered to produce a narrower bandwidth. An indirect detector (lens-coupling of a scintillator to a camera incorporating a charge-coupled device with 2048×2048 pixels), with a pixel size of $5 \mu\text{m}$ acquired tomographic scans of the region of interest (ROI), which was slightly smaller (10 mm wide) than the sample (~ 20 mm wide). The sample was continuously rotated over 360° , as 1999 equiangularly spaced radiographic images were taken.

The tomograms were reconstructed at the ID19 beamline. A standard filtered projection algorithm was applied via the ESRF in-house developed software PyHST (Mirone et al., 2014). The size of the reconstructed tomogram was $2048 \times 2048 \times 1024$ voxels. Voxel

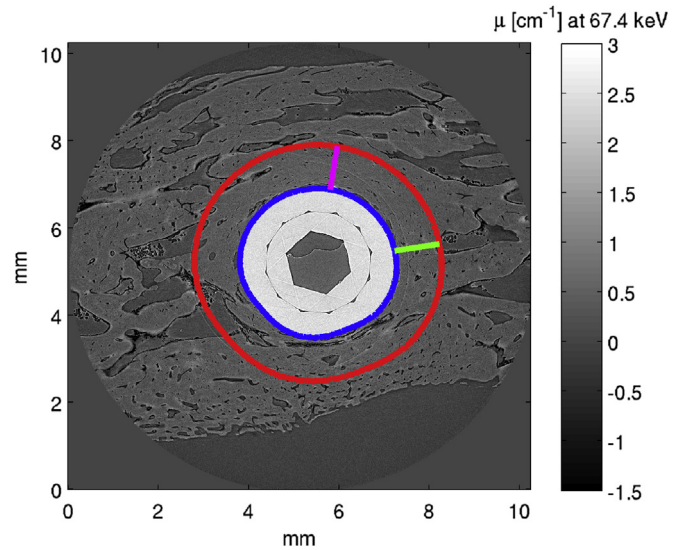


Fig. 3. Tomogram slice showing the two circle bands used for the circle band analysis. The radial lines (green and magenta) are illustrating two out of 1999 radial lines used to create the polar coordinate system.

values represented the common Gaussian spread i.e. noise, overlapped with refraction phenomena, which were present at interfaces such as implant–bone interfaces, an effect known as edge-enhancement (Cloetens et al., 1996). The segmentation was performed using VG Studio Max 2.1 (Volume Graphics GHBM, Heidelberg, Germany) also at the ESRF in Grenoble, France.

The tomogram height was 1024 pixels since only half of the detector height was necessary to obtain data from the ROI (Fig. 2). The vertical height of the tomograms was reduced to 500 voxels, i.e. 2.5 mm, which was done by inclusion of the part of the tomogram containing the ROI of the implant (Fig. 2).

3. Results and data analysis

3.1. Data analysis

Analysis of a given slice consisted of three steps:

1. Segmentation, followed by.
2. Circular-band construction, and.
3. Bone fraction determination.

- 1) *Segmentation*: The sample consisted of three major components; the titanium dental implant, the surrounding bone and the cavities, which were distinguished by, and segmented by different absorption coefficients. Due to the implant's low-noise high-intensity in the image volume it was easily segmented by thresholding.
- 2) *Circular-band construction*: This data analysis evaluated the bone distribution of the 1999 radial lines radiating from the implant surface in one dimension (Fig. 3), representing the bone distribution along the radial dimension at the 1999 places on the implant surface. The segmentation of the tomographic data was done on 2D horizontal sections.

Two lines were defined representing the outer perimeter and the implant surface. A circular band of 2000 μm in width was defined around the dental implant, representing the area between the implant surface (blue circle) and the outer periphery at 1 mm radial distance (red circle). Due to the presence of implant threads the image of the implant was not strictly circular (Fig. 3).

3) *Bone fraction determination*: The bone fraction was determined by the bone segmentation within the circular band and presented as a function of radial distance. Data analysis for the two areas was performed in 2D and reconstructed in 3D. After segmentation and reconstruction of the bone sample, cavities along the implant surface were visualized.

3.2. *Sample data*

This section gives the full volume results for the one sample comprising the two areas. The tomographic 3D voxel size was 5 μm. For each of the 1999 different angles in the ROI, the peri-implant bone volume fraction and BIC were evaluated.

3.2.1. *Grafted bone area*

The peri-implant bone volume contact fraction was 62.2% (Table 1). The BIC was approximately 4% (Table 1), (Figs. 4 and 5a), and within the first 65 μm the peri-implant bone volume fraction increased to approximately 50% (Fig. 5a). At a distance of 285 μm from the implant surface—the peak of the curve—the peri-implant bone volume fraction was approximately 82%. The peri-implant bone volume fraction levelled out at 400 μm distance to approximately 78% (Fig. 5a). The mean peri-implant bone volume fraction was 75.6%, and the maximum peri-implant bone volume fraction was 82%. The total peri-implant bone volume fraction was 75.9%.

3.2.2. *Recipient bone*

The peri-implant bone volume contact fraction was 63.3% (Table 1). The BIC was approximately 3.5% (Table 1), (Fig. 5b), and within the first 50 μm the peri-implant bone volume fraction was approximately 50% (Fig. 5b). At a distance of 285 μm from the implant surface—the peak of the curve—the peri-implant bone volume fraction was approximately 76%. The peri-implant bone volume fraction levelled out at 400 μm distance to approximately 80–85% (Fig. 5b). The mean peri-implant bone volume fraction was 79.3%, and the maximum peri-implant bone volume fraction was 85%. The total peri-implant bone volume fraction was 80.7%.

4. Discussion

The present study introduces a 3D high-resolution method for evaluating the bone volume fraction at the surface and at different distances from a titanium dental implant, and is based on SRmicro-CT. Analysis of the circular area around the implant enables 3D evaluation to be carried out in the ROI. The experimental model used a dental titanium implant in an augmented vertical critical size defect in the mandible of a goat, simulating an atrophic mandibular alveolar process mainly comprising cortical bone. The aim was to present SRmicro-CT images as a high-resolution 3D method, at a voxel size of 5 μm, evaluating peri-implant bone volume fraction and BIC in recipient and de novo formed bone.

The peri-implant bone volume contact fractions were 62.2% and 63.3%, the BIC were approximately 4% and 3.5%, the mean peri-implant bone volume fraction were 75.6% and 79.3%, and the maximum peri-implant bone volume fraction were 82% and 85% for the grafted and the recipient regions, respectively.

Table 1

The table shows the key measures from the two different regions, i.e. the grafted area at the micro thread region and the recipient bone at the macro thread region.

Sample area	Peri-implant bone volume contact fraction	Bone-to-implant contact (BIC)	Peri-implant bone volume fraction
Grafted area	62.2%	4%	75.9%
Recipient bone	63.3%	3.5%	80.7%

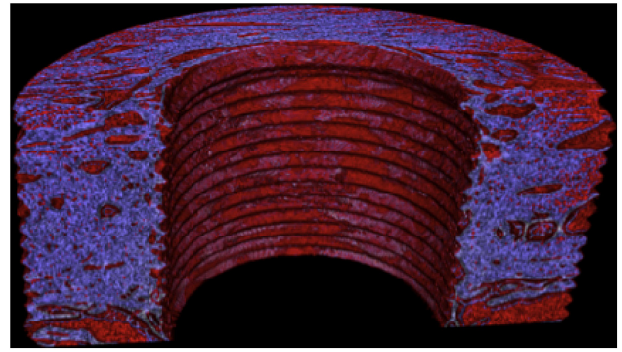


Fig. 4. Illustrating BIC in the grafted area in half the sample. Red represents cavities. Blue represents bone. The implant has been removed to depict the area in proximity to the implant.

The BIC in the present study was approximately 3–4%. The value of BIC has been discussed in many studies representing different evaluation modalities. Sarve et al. (2013) found a BIC of 54–69%, at a pixel size of 4.40 μm on two samples in human bone, 29 years

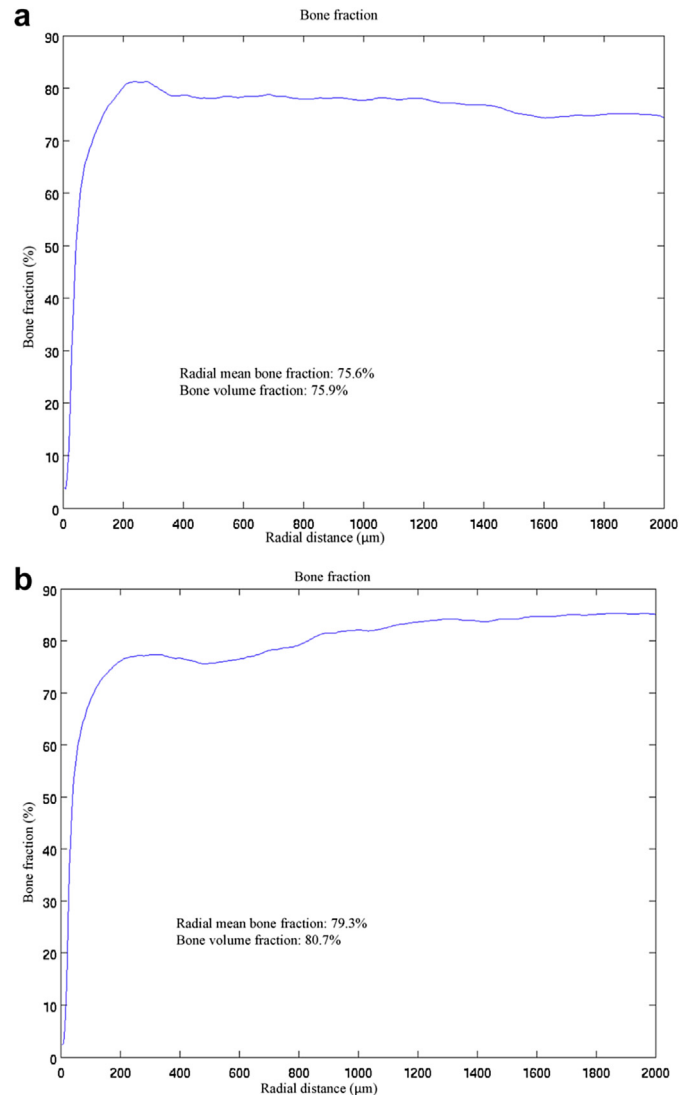


Fig. 5. a: Peri-implant bone fraction in grafted area. Bone volume fraction as a percentage as a function of the radial distance. b: Peri-implant bone fraction in recipient bone area. Bone volume fraction as a percentage shown as a function of the radial distance.

post-surgery and scanned at the HASYLAB, DESY in Hamburg. [Bernhardt et al. \(2004\)](#), found a BIC of approximately 30%, 4 weeks after implant installation, at voxel size 6.4 μm on a single sample in a beagle dog scanned at the HASYLAB, DESY in Hamburg. In rats, [Sarve et al. \(2011\)](#) found a BIC of 45.8–70.1%, 4 weeks after implant installation, at a pixel size of 4.40 μm scanned at the HASYLAB, DESY in Hamburg. In goats, [Bernhardt et al. \(2006\)](#) found a BIC ranging between 44 and 70%, 12 weeks after implant installation, at voxel size 10 μm , of 16 bone samples evaluated at the HASYLAB, DESY in Hamburg.

The discussion of BIC values is important in the quality assessment of the surface of the titanium dental implant represented by the presence or lack of artefacts. The BIC is most often evaluated in a 2–3 pixel size zone, which in the present study comprised 10–15 μm . SRmicro-CT was used with a photon flux density at an X-ray photon energy sufficient to transmit the images of the dental implants free of artefacts and with a high contrast and signal-to-noise ratio. In order to acquire tomographic images at high photon energies, the ID19 beamline of the ESRF was chosen. ID19 presents parallel beam geometry and a high number of photons accessible for hard X-ray imaging using a wiggler insertion device. The acquired images allow for an estimate and precise bone detection.

BIC evaluation is also dependent on the segmentation of the resin used for preparation of the specimens, which gives image noise, and the osteoid of newly formed bone can cause difficulties in the segmentation procedure. However, the formation of mineralized tissue in the present study was secured by an observation time of 20 weeks.

The peri-implant bone volume fraction in the present study in the grafted and in the recipient bone was 50% at a distance of 50–65 μm , and 82 and 76% at a distance of 285 μm away from the implant surface, respectively. This is comparable to other studies ([Rebaudi et al., 2004](#); [Sarve et al., 2013](#)). This implies that our experimental study model is representative. [Bernhardt et al. \(2006\)](#) found a bone volume ranging between 40 and 67% after 12 weeks of healing of implants in a goat defect model at a distance of 0–700 μm .

Histomorphometry comprises a 2D fraction of a 3D structure and only represents a number of 10 μm thick sections in a process of cutting and grinding with subsequent loss of tissue in the preparation procedure. By performing 3D evaluation by the SRmicro-CT method, it is possible to obtain data from the entire surface in a bone cylinder. When using SRmicro-CT the resolution can be reduced due to refraction artefacts at the interfaces between materials of different electron densities ([Rack et al., 2006, 2011](#); [Stiller et al., 2009](#)). It can be challenging to compare bone volume results evaluated by classical histomorphometry (2D) and results obtained from micro-CT and SRmicro-CT. In the study by [Rebaudi et al. \(2004\)](#), bone volume differences evaluated by histology and by micro-CT ranged between 9 and 16%. In the study by [Bernhardt et al. \(2004\)](#) the difference in bone quantification was non-significant and less than 1% using SRmicro-CT, however, when looking at the BIC the difference was about 10%. [Bernhardt et al. \(2012\)](#) found a difference in the BIC of 4.9%, and a bone-implant-volume difference of 1.2% for histomorphometry (with 3–4 histological sections) compared with SRmicro-CT. The number of histological sections, which they were able to compare directly with SRmicro-CT, could explain the small differences. They conclude that 3–4 histological sections could be sufficient to evaluate bone-implant-volume with only minor discrepancies to 3D measurements.

Evaluation of BIC with SRmicro-CT can cause some challenges due to the partial volume effect (PVE) which forces BIC measurements to be performed at a minimum of 1–2 pixels away from the implant surface. The PVE appears when structures are the same size or smaller than the pixel size and therefore are not correctly

detected. Consequently, the PVE can be reduced at higher resolutions i.e. lower pixel size. SRmicro-CT requires high contrast for detecting bone in proximity to a titanium surface; the bone needs to be fully mineralized to be detected correctly ([Bernhardt et al., 2012](#)). When the implant surface is covered by a thin layer of mineralized tissue the PVE may arise because the absorption coefficients will be a mixture of bone and implant. Subsequently, PVE will always be found near interfaces and result in an underestimation of the bone, however this has not been found to be significant ([Bernhardt et al., 2012](#); [Mangano et al., 2013](#); [Sarve et al., 2013](#)). [Bernhardt et al. \(2012\)](#) defined a distance of 18 μm , 5 pixels, from the implant surface to be the position to obtain BIC values in SRmicro-CT slices. [Mangano et al. \(2013\)](#) performed their BIC evaluations at 2 pixels, 15 μm , from the implant surface. [Sarve et al. \(2013\)](#) performed BIC measurements 11 μm from the surface, i.e. 1 pixel from the surface. This present study has a resolution of 5 μm , hence, it is possible to evaluate the BIC even closer to the implant surface than in previous studies.

Our data represented by peri-implant bone volume fractions are in accordance with the leading studies within the field of 3D evaluation. Therefore the BIC difference in the present paper is assumed to be due to the higher performance of SRmicro-CT with subsequent higher resolution, a larger number of images and consequently an expected higher level of precision.

5. Conclusion

A semi-automatic computer algorithm to determine the peri-implant bone volume fraction of the ROI in three dimensions was presented. In close proximity to the implant surface, the BIC was 3–4%; at 400 μm away from the dental implant the peri-implant bone volume fraction showed a steady level of nearly 80%. This kind of study, with immediate vertical bone augmentation around a dental implant, has not been performed before and evaluated at a spatial resolution of 5 μm . As shown in this study, there is a tremendous difference in the peri-implant bone volume fraction, which comprise 50% when looking at a distance from the implant surface of 50–65 μm , compared with a bone fraction of 4% at a distance of 5 μm from the implant surface.

The method has been successful in depicting the bone and cavities in three dimensions thereby enabling us to give a much more precise answer to the fraction of the BIC compared with previous methods. The next step will be to further develop our method to give an even more accurate image of the bone fraction in very close proximity to the dental implant (0–50 μm).

Whether the peri-implant bone volume fraction of 3–4% is an actual image of BIC or is due to the surgical design is unknown, and not the aim of this study, but will be evaluated in a future publication, which is in progress.

Acknowledgement

We would like to thank the staff at the ESRF, beamline ID 19, Grenoble, France: Paul Tafforeau and Elodie Boller for performing the scans, the reconstructions and their generous help during our visits to the research facilities.

Degradable Solutions, Sun Star Company, Schlieren, Switzerland, is thanked for the financial support for the histological preparation of specimens. The authors and the Company were by signed contract kept out of conflicting interests.

References

- Albrektsson T: Hard tissue implant interface. *Aust Dent J* 53(Suppl. 1): S34–S38, 2008

- Bernhardt R, Kuhlisch E, Schulz MC, Eckelt U, Stadlinger B: Comparison of bone-implant contact and bone-implant volume between 2D-histological sections and 3D-SRmicro-CT slices. *Eur Cell Mater* 23: 237–248, 2012
- Bernhardt R, Scharnweber D, Müller B, Beckmann F, Goebbels J, Jansen J, et al. In: Bonse Ulrich (ed.), 3D analysis of bone formation around titanium implants using micro computed tomography (μ CT): Developments in X-ray tomography V, vol. 6318; 2006, 631807, 2006
- Bernhardt R, Scharnweber D, Müller B, Thurner P, Schliephake H, Wyss P, et al: Comparison of microfocus- and synchrotron X-ray tomography for the analysis of osteointegration around Ti6Al4V implants. *Eur Cell Mater* 7: 42–51, 2004
- Bonse U, Busch F: X-ray computed microtomography (microCT) using synchrotron radiation (SR). *Prog Biophys Mol Biol* 65: 133–169, 1996
- Bonse U, Busch F, Günnewig O, Beckmann F, Pahl R, Dellling G, et al: 3D computed X-ray tomography of human cancellous bone at 8 μ m spatial and 10^{-4} energy resolution. *Bone Miner* 25: 25–38, 1994
- Bousson V, Peyrin F, Bergot C, Hausard M, Sautet A, Laredo JD: Cortical bone in the human femoral neck: three-dimensional appearance and porosity using synchrotron radiation. *J Bone Miner Res* 19: 794–801, 2004
- Cloetens P, Barrett R, Baruchel J, Guigay JP, Schlenker M: Phase objects in synchrotron radiation hard x-ray imaging. *J Phys D* 29: 133–146, 1996
- Cooper DM, Bewer B, Wiebe S, Wysokinski TW, Chapman D: Diffraction enhanced X-ray imaging of the distal radius: a novel approach for visualization of trabecular bone architecture. *Can Assoc Radiol J* 62: 251–255, 2011
- Davies JE: In vitro Modelling of the Bone/implant interface. *Anat Rec* 245: 426–445, 1996
- Donath K: Preparation of histologic sections- by cutting-Grinding technique for hard tissue and other material not suitable to be sectioned by routine methods. In: Equipment and methodical performance, vol. 34. Norderstedt: EXAKT-Kulzer-Publication, 1993
- Feldkamp LA, Goldstein SA, Parfitt AM, Jesion G, Kleerekoper M: The direct examination of three-dimensional bone architecture in vitro by computed tomography. *J Bone Miner Res* 4: 3–11, 1989
- Larrue A, Rattner A, Peter ZA, Olivier C, Laroche N, Vico L, et al: Synchrotron radiation micro-CT at the micrometer scale for the analysis of the three-dimensional morphology of microcracks in human trabecular bone. *PLoS One* 6: e21297, 2011
- Mangano C, Adriano P, Mangano F, Rustichelli F, Shibli JA, Iezzi G, et al: Histological and synchrotron radiation-based computed microtomography study of 2 human-retrieved direct laser metal formed titanium implants. *Implant Dent* 22: 175–181, 2013
- Mirone A, Guillard E, Brun E, Tafforeau P, Kieffer J: PyHST2: an hybrid distributed code for high speed tomographic reconstruction with iterative reconstruction and a priori knowledge capabilities. *Nucl Instrum & Meth B* 324: 41–48, 2014
- Neldam CA, Pinholt EM: Synchrotron μ CT imaging of bone, titanium implants and bone substitutes—a systematic review of the literature. *J Craniomaxillofac Surg* 42: 801–805, 2014
- Peyrin F: Investigation of bone with synchrotron radiation imaging: from micro to nano. *Osteoporos Int* 20: 1057–1063, 2009
- Peyrin F, Attali D, Chappard C, Benhamou CL: Local plate/rod descriptors of 3D trabecular bone micro-CT images from medial axis topologic analysis. *MedPhys* 37: 4364–4376, 2010
- Rack A, Knabe C, Stiller M, Koch C, Seligmann H, Zabler S, et al: Synchrotron-Tomography for Evaluation of Bone Tissue Regeneration using rapidly Resorbable Bone Substitute Materials Proc. 9th European Conference on Nondestructive Testing (ECNDT2006), Berlin; 2006, DGZFP Proceedings BB 103-CD (ISBN 3-931381-86-2)
- Rack A, Stiller M, Dalugge O, Rack T, Knabe C, Riesemeier H: Developments in high-resolution CT: studying bioregeneration by hard x-ray synchrotron-based microtomography. In: Duchenne P, Healy KE, Hutmacher DW, Grainger DW, Kirkpatrick CJ (eds), *Comprehensive biomaterials*. Elsevier Science, 2011
- Rebaudi A, Koller B, Laib A, Trisi P: Microcomputed tomographic analysis of the peri-implant bone. *Int J Periodontics Restorative Dent* 24: 316–325, 2004
- Ritman EL: Micro-computed tomography-current status and developments. *Annu Rev Biomed Eng* 6: 185–208, 2004
- Rueggsegger P, Koller B, Muller R: A microtomographic system for the nondestructive evaluation of bone architecture. *Calcif Tissue Int* 58: 24–29, 1996
- Ruhli FJ, Kuhn G, Evison R, Muller R, Schultz M: Diagnostic value of micro-CT in comparison with histology in the qualitative assessment of historical human skull bone pathologies. *Am J Phys Anthropol* 133: 1099–1111, 2007
- Sarve H, Friberg B, Borgefors G, Johansson CB: Introducing a novel analysis technique for osseointegrated dental implants retrieved 29 years postsurgery. *Clin Implant Dent Relat Res* 15: 538–549, 2013
- Sarve H, Lindblad J, Borgefors G, Johansson CB: Extracting 3D information on bone remodeling in the proximity of titanium in SR μ CT image volumes. *Comput Methods Programs Biomed* 102: 25–34, 2011
- Shah FA, Nilson B, Brånemark R, Thomsen P, Palmquist A: The bone-implant interface—nanoscale analysis of clinically retrieved dental implants. *Nanomedicine: Nanotechnol, Biol Med* vol. 10(8): 1729–1737, 2014
- Stiller M, Rack A, Zabler S, Goebbels J, Dalugge O, Jonscher S, et al: Quantification of bone tissue regeneration employing beta-tricalcium phosphate by three-dimensional non-invasive synchrotron micro-tomography—a comparative examination with histomorphometry. *Bone* 44: 619–628, 2009
- Voide R, Schneider P, Stauber M, Wyss P, Stampanoni M, Sennhauser U, et al: Time-lapsed assessment of microcrack initiation and propagation in murine cortical bone at submicrometer resolution. *Bone (Germany)* 45: 164–173, 2009
- Wiedemann H: Synchrotron radiation. Berlin, Heidelberg: Springer-Verlag, 1–268, 2002
- Withers PJ: X-ray nanotomography. *Mater today* 10: 26–34, 2007

A.6

Synchrotron radiation μ CT and histology evaluation of bone-to-implant contact

Journal of Cranio-Maxillo-Facial Surgery (2017)

C. A. Neldam, J. Sporning, A. Rack, T. Lauridsen, E.-M. Hauge, H. L. Jørgensen, N. R. Jørgensen, R. Feidenhansl, E. M. Pinholt

Journal of Cranio-Maxillo-Facial Surgery (2017) 45: 1448-1457



Contents lists available at ScienceDirect

Journal of Cranio-Maxillo-Facial Surgery

journal homepage: www.jcmfs.comSynchrotron radiation μ CT and histology evaluation of bone-to-implant contact[☆]

Camilla Albeck Neldam^{a,*}, Jon Sporning^b, Alexander Rack^c, Torsten Lauridsen^d,
Ellen-Margrethe Hauge^e, Henrik L. Jørgensen^f, Niklas Rye Jørgensen^{a,g,1},
Robert Feidenhansl^h, Else Marie Pinholtⁱ

^a Department of Clinical Biochemistry, Rigshospitalet Glostrup, Copenhagen, Denmark

^b Department of Computer Science, University of Copenhagen, Copenhagen, Denmark

^c European Synchrotron Radiation Facility, Grenoble, France

^d Niels Bohr Institute, University of Copenhagen, Denmark

^e Department of Rheumatology, Aarhus University Hospital, Aarhus, Denmark

^f Department of Clinical Biochemistry, Bispebjerg Hospital, Denmark

^g OPEN, Odense Patient Data Explorative Network, Odense University, Hospital/Institute of Clinical Research, University of Southern Denmark, Odense, Denmark

^h European XFEL GmbH, Hamburg, Germany

ⁱ University of Southern Denmark, Faculty of Health Sciences, Department of Regional Health Research, Odense, Denmark

ARTICLE INFO

Article history:

Paper received 11 September 2016

Accepted 22 May 2017

Available online 3 June 2017

Keywords:

Synchrotron radiation micro-CT

Osseointegration

Bone-to-implant contact

Dental implant

Graft

Histology

ABSTRACT

The purpose of this study was to evaluate bone-to-implant contact (BIC) in two-dimensional (2D) histology compared to high-resolution three-dimensional (3D) synchrotron radiation micro computed tomography (SR micro-CT). High spatial resolution, excellent signal-to-noise ratio, and contrast establish SR micro-CT as the leading imaging modality for hard X-ray microtomography. Using SR micro-CT at voxel size 5 μ m in an experimental goat mandible model, no statistically significant difference was found between the different treatment modalities nor between recipient and reconstructed bone. The histological evaluation showed a statistically significant difference between BIC in reconstructed and recipient bone ($p < 0.0001$). Further, no statistically significant difference was found between the different treatment modalities which we found was due to large variation and subsequently due to low power. Comparing histology and SR micro-CT evaluation a bias of 5.2% was found in reconstructed area, and 15.3% in recipient bone. We conclude that for evaluation of BIC with histology and SR micro-CT, SR micro-CT cannot be proven more precise than histology for evaluation of BIC, however, with this SR micro-CT method, one histologic bone section is comparable to the 3D evaluation. Further, the two methods complement each other with knowledge on BIC in 2D and 3D.

© 2017 European Association for Cranio-Maxillo-Facial Surgery. Published by Elsevier Ltd. All rights reserved.

1. Introduction

Bone-to-implant contact (BIC) in loaded implants is proven to be 60–70% when using light microscopy, and 10% less in unloaded

[☆] Sunstar Suisse SA, Etoy, Switzerland, is thanked for the financial support for the histological preparation of specimens, and for the tuition for the Ph.D. school. The authors and the Company were by signed contract kept out of conflict of interests.

* Corresponding author.

E-mail address: camillaneldam@hotmail.com (C.A. Neldam).

¹ Attribution to: Departments of Clinical Biochemistry, Blegdamsvej 9, 2100 København Ø, Rigshospitalet Glostrup, Denmark.

implants (Albrektsson, 2008). However, histology studies in mini-pigs, pigs, and dogs show comparable BIC in unloaded implants ranging between 49% and 77.2% after healing periods of 2–4 months (Stadlinger et al., 2009; Bressan et al., 2012; Botzenhart et al., 2015). Attainment of osseointegration and primary stability is essential for implant success. A high BIC is a prerequisite for implant stability and is vital in order to generate secondary stability (Brånemark, 1983; Albrektsson, 2008).

Osseointegration and bone structure are classically investigated in a 2D manner by histology (Brånemark et al., 1969). Three-dimensional (3D) evaluation of bone quantification, structure, and

mineralization has been performed with micro computed tomography (micro-CT) and with synchrotron radiation micro-CT (SR micro-CT) (Bonse et al., 1994; Britz et al., 2010; Peyrin et al., 2010; Sarve et al., 2011, 2013; Bernhardt et al., 2012; Stalder et al., 2014; Neldam et al., 2015). Micro-CT and SR micro-CT are non-destructive techniques, providing 3D images of bone *in vitro* (Nuzzo et al., 2002; Jung et al., 2003; Bernhardt et al., 2004). However, beam hardening is inevitable with polychromatic beams used in micro-CT, which is not an issue with SR micro-CT, where a monochromatic beam is used (Nuzzo et al., 2002). SR micro-CT exploits the parallel-beam geometry, offers high spatial resolution, excellent signal-to-noise ratio, and, due to narrow bandwidth illumination, reduced artefacts and increased contrast. The strength of SR micro-CT lies in its 3D evaluation of the entire implant surface and, hence, the information it provides, including the geometry and distribution of peri-implant tissues (Bernhardt et al., 2012). Titanium implants have a higher X-ray absorption than bone. However, newly formed bone with a low mineral content can be difficult to detect at the implant interface due to its reduced absorption signal (Bernhardt et al., 2012). Furthermore, the partial volume effect (PVE), which is dependent on the CT resolution expressed by voxel size, provides challenges when materials with very different absorption coefficients are sampled in the very same voxel, resulting in a measured beam attenuation proportional to only the average value of the two (Höhne and Bernstein, 1986; Ito et al., 2003; Bernhardt et al., 2012).

Histology is two-dimensional (2D), but can be transformed into 3D using stereology. The availability of a wide range of contrast agents offers superb sensitivity, but histology is basically a highly destructive technique (Bonse et al., 1994). SR micro-CT acquisition is presented in a 2D, slice-by-slice manner and subsequently reconstructed into 3D X-ray images. The methods are used to evaluate, in a non-destructive way, the implant contact with the surrounding tissues, including: bone, marrow spaces, grafting material, and fibrous tissue (Stiller et al., 2009; Rack et al., 2011; Neldam and Pinholt, 2014; Neldam et al., 2015).

In preparation for SR micro-CT scanning, and in contrast to preparation for histology, it is not necessary to reduce the size specimens in our study by cutting and grinding. Polishing of the bone specimens for histology may result in titanium particles dispersed throughout the specimen and embedding material, hence making BIC evaluation difficult. However, histology does offer important information on bone vitality, because it is not possible to visualize cells or osteoid in X-ray tomography.

Tooth loss is associated with bone loss; on average 40–60% bone loss is evident within the first 3 years after extraction (Tallgren, 1972; Schropp et al., 2003). Consequently, alveolar ridge augmentation can be necessary prior to implant installation. Although autologous bone is considered gold standard for augmentation, it has some inherent disadvantages, including limited quantities, and donor site morbidity (Ono et al., 2011). Consequently, bone augmentation procedures using synthetic bone substitute materials have become significantly more common. However, not many studies exist concerning SR micro-CT evaluation of different augmentation materials and titanium dental implants. Alloplastic materials such as hydroxyapatite (HA) and β -tricalcium phosphate (β -TCP) are promising materials due to their synthetic nature and their osteoconductive (HA, β -TCP) abilities and unlimited quantities (Kim et al., 2012; Leventis et al., 2016).

In this study, a goat model with a critical-sized defect (CSD) was used for evaluation of osseointegration in the mandible after immediate vertical bone augmentation. 35 bone specimens with five different augmentation procedures were used for evaluation. Additionally, a 3D imaging technique was applied and complemented with a 2D histological evaluation. The aim of the study

was to evaluate BIC using 2D histology and 3D SR micro-CT after immediate vertical bone augmentation.

2. Material and Methods

2.1. Experimental animals and critical size defects

Seven healthy female adult goats (land-bred), 4-years of age, and weighing 40–50 kg, whose metabolism and bone formation are comparable with those of a human (Anderson et al., 1999), were chosen for this experimental study. A standardized CSD at the mandibular base of the goat bicortical, 25 mm in length, was chosen to represent the atrophic defect (Viljanen et al., 1996; Gao et al., 1997; Anderson et al., 1999) within the skeletal envelope (Lundgren et al., 1995; Slotte and Lundgren, 2002). The goats were housed and operated on at the research facilities of the Foulum Agricultural Center of Research, University of Aarhus, Denmark. National guidelines for use and care of laboratory animals were followed, and the study was approved by the Danish Veterinary Ethical Committee (permit no: 2006/561-1130).

2.2. Experimental design

Under general anesthesia, using Ketamine (Pfizer Aps., Ballerup, Denmark) and Streptocillin, pre- and post-operatively, i.m. 5 mL \times 5 days (Boehringer Ingelheim A/S, Copenhagen, Denmark), five bone defects mimicking the atrophic alveolar process were created at the base of the mandible via an external bilateral approach. CSDs were created by reduction of the cortical basal part of the mandible, measuring 25 mm in length, 4 mm in height, and bicortical in width (Anderson et al., 1999). Insertion of 3.5 mm \times 8 mm dental titanium implants (Astra Tech OsseoSpeed, ST Molndal, Sweden) with cover screws was performed centrally into each defect ad modum Astra, leaving 3.5 mm ejecting into the defect (Fig. 1).

Randomized, immediate, vertical, peri-implant augmentation was performed in each defect ($n = 35$) using one of the following reconstructive methods:

- i. Synthetic, resorbable, *in situ* hardening β -TCP, 0.4 mL (GUIDOR easy-graft CLASSIC, Sunstar Suisse SA, Etoy, Switzerland).
- ii. Synthetic, partially resorbable, *in situ* hardening biphasic calcium phosphate (ratio HA/ β -TCP: 60/40), 0.4 mL (GUIDOR easy-graft CRYSTAL, Sunstar Suisse SA, Etoy, Switzerland).



Fig. 1. Goat mandible with the critical sized defects and reconstruction material.

- iii. Autologous bone augmentation by bone chips of between $0.5 \times 3 \times 1 \text{ mm}^3$ and $0.5 \times 5 \times 1 \text{ mm}^3$ in size, processed in bone mills (Liebinger, Freiburg, Germany; Quentin, Leimen, Germany). The defect was covered by a titanium membrane (Riemser Artzen mittle AG, Greifswald, Insel Riems, Germany), fixed with titanium alloy osteosynthesis self-tapping screws, 2.4 mm in diameter and 6 mm in length (Synthes, Solothurn, Switzerland).
- iv. Autologous bone chips of between $0.5 \times 3 \times 1 \text{ mm}^3$ and $0.5 \times 5 \times 1 \text{ mm}^3$ in size, processed in bone mills (Liebinger, Freiburg, Germany; Quentin, Leimen, Germany), without a membrane.
- v. Empty defect covered by a titanium membrane (Riemser Artzen mittle AG, Greifswald, Insel Riems, Germany), fixed with titanium alloy osteosynthesis self-tapping screws, 2.4 mm in diameter and 6 mm in length (Synthes, Solothurn, Switzerland).

2.3. Bone graft substitutes

Synthetic β -TCP (GUIDOR easy-graft CLASSIC, Sunstar Suisse SA, Etoy, Switzerland) and synthetic biphasic calcium phosphate (BCP) (GUIDOR easy-graft CRYSTAL, Sunstar Suisse SA, Etoy, Switzerland), with particle diameters of 0.5–1 mm and 0.45–1 mm respectively, were used. The BCP comprises 40% β -TCP and 60% HA, with every granule composed of a sintered mixture of both materials. The calcium phosphate granules are coated with a thin layer of resorbable polymer (poly(lactide-co-glycolide)). Prior to application, the granules were mixed with N-methyl-2-pyrrolidone (NMP) according to the company's instructions, which plasticizes the coating, making the mass of granules formable. This hardens upon contact with blood and forms a stable scaffold after rinsing with sterile saline.

2.4. Harvesting and preparation of bone specimens

After 20 weeks, the goats were anesthetized with isoflurane (Baxter, Allerød, Denmark) and euthanized by an overdose of pentobarbital i.v. (100 mg/kg, Le Vet B.V. Oudewater, The Netherlands). The specimens were harvested, fixed in 10% formaldehyde (Rigshospitalets Apotek, Rigshospitalet, Denmark), and dehydrated in graded alcohol solutions, for non-decalcified specimen preparation. The specimens were finally embedded in a cylinder, 12 mm in diameter, with methylmethacrylate (Technovit 9100 neu[®], Heraeus Kulzer, Wehrheim, Germany) ad modum Donath (Donath and Breuner, 1982). This represented a dental implant – 3.5 mm in diameter – surrounded radially by 4 mm of bone. Before cutting and grinding for microscopic slide preparation the specimens were scanned in SR micro-CT. Finally, the specimens were cut and grinded for microscopic slide preparation in the Department of Biomaterials, Sahlgrenska Academy, University of Gothenburg, Sweden to produce non-decalcified specimens.

2.5. Synchrotron-based microtomography

Tomographic data were acquired at the ID19 beam line of the European Synchrotron Radiation Facility (ESRF) in Grenoble, France. As described in previous work (Neldam et al., 2015), high photon energy of 67.4 KeV was chosen in order to sufficiently transmit titanium implant material (Grodzins et al., 1983). A 2048×2048 pixel indirect scintillator detector, with a pixel size of $5 \mu\text{m}$, acquired tomographic scans of only the region of interest (ROI) – i.e. not the complete sample was scanned (local

tomography). Reconstruction was performed onsite using a filtered projection algorithm via the ESRF in-house developed software PyHST (Mirone et al., 2014). Full-size tomograms were $2048 \times 2048 \times 1024$ pixels and the scanning was performed at 1999 angles (for complete descriptions see Neldam et al., 2015).

In order to evaluate BIC, a Matlab (MathWorks Inc., Massachusetts, USA) program was developed to semi-automatically segment the tomograms into implant, bone, and cavity, and to derive statistical data on these segments. For each tomogram, the following were applied: 1) a combined segmentation and bias correction, 2) identification of a coordinate system defined by the central axis of the implant, and 3) analysis of the volume of bone and cavity as a function of height and distance to the implant surface. In detail, each step was as follows:

1. Due to the large amount of data, the original tomograms were down-sampled by a factor of 4 in the x -, y -, and z -directions in the tomogram's coordinate system, which resulted in isotropic voxel size of $20 \mu\text{m}$ (Fig. 2). Subdivision of the tomograms to avoid down-sampling was not possible due to the noise reduction in proximity to the implant. Subsequently, the segmentation was performed by manually identifying the location of an implant, a cavity, and a bone voxel, where both the cavity and bone voxels were outside

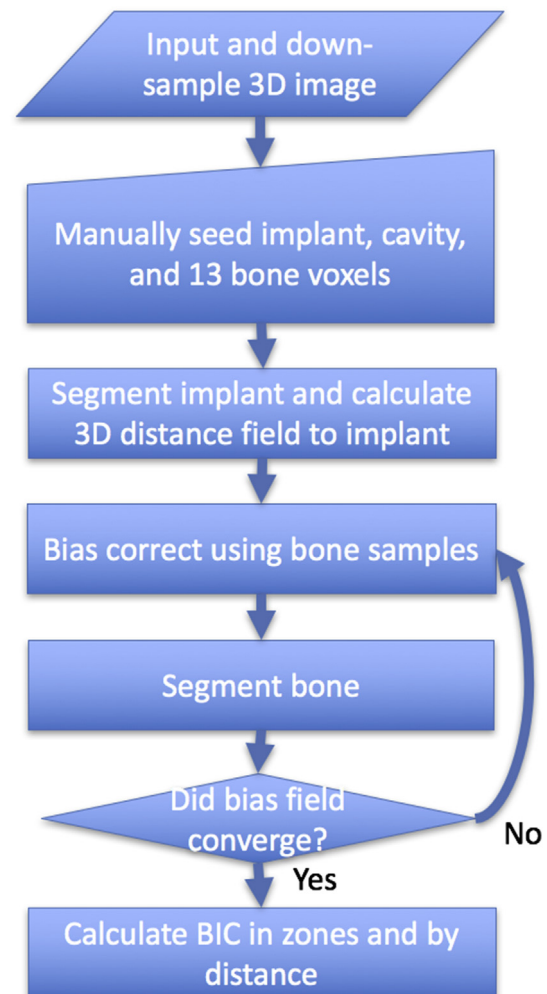


Fig. 2. Flowchart illustrating the acquisition of data, from down sampling to BIC analysis.

but near the implant surface. The threshold was found using the average intensity value between bone and implant, and was used to segment the implant. Furthermore, 12 seed location voxels, spread throughout the full tomogram, were manually identified. The down-sampled tomogram was smoothed, and the bias field was fitted to these values. The bias field, comprising an inhomogeneity in the CT, caused different levels of gray, representing, for example, bone. In the column to the right (Fig. 2), the bias field was subtracted from non-implant voxels, and the average bias-corrected intensity values between the initial bone and cavity locations were used as threshold values to segment bone and cavity. The segmented bone locations were then taken as seed locations, and the procedure was repeated until convergence.

2. Since the tomograms were given in non-standardized coordinate frames, an implant-centered coordinate system was identified as follows. Firstly, the centers of mass of the segmented implant voxels were used as origins. Then four points on the surface of the implant were manually identified (the direction from macro to micro thread is denoted up):
 - i. The end point of the valley of the micro thread in the first ridge of the macro thread (Fig. 3) denoted the reference point.
 - ii. The micro thread above the reference point.
 - iii. The peak of the 13th micro thread above the reference point.
 - iv. The ridge of the first macro thread below the reference point.

Since the threads of the implants have the shape of a torus, it was not possible to define a plane that separated the micro and macro threads. Subsequently, zones were defined by the implant's vertical axis: the micro thread area was initiated from ii) to iii), and the macro thread area was demarcated by ii) and iv). To analyze the BIC, the bone and cavity volumes were evaluated in a 3D volume band from 0 to 10 μm perpendicular to the implant surface in both micro and macro thread areas.

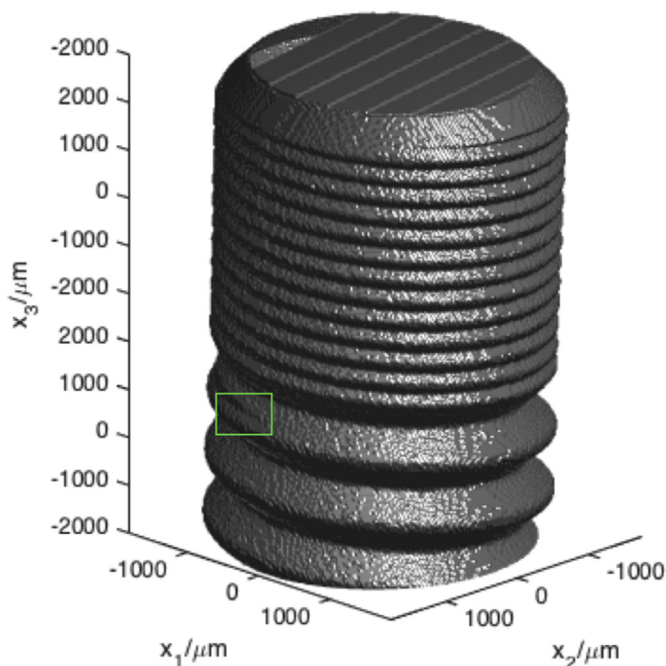


Fig. 3. The specific point that demarcates the micro and macro thread areas.

2.6. Definition of region of interest

The region of interest (ROI) was defined as the peri-implant bone covering the implant surface. The implant was divided into two vertical zones (Fig. 4):

1. The micro thread area: comprising the different treatment modalities.
2. The macro thread area: comprising recipient bone at the two first macro threads, serving as measures for recipient bone.

2.7. Definition of BIC

Histologically, BIC is defined as bone in direct contact with the implant surface. Furthermore, marrow, graft, and fibrous tissue were also evaluated when in contact with the implant surface. Additionally, BIC was evaluated by SR micro-CT within the nearest two voxels of the surface.

2.8. Histology evaluation

After scanning at the ESRF the undecalcified bone specimens were cut and stained in the Department of Biomaterials, Sahlgrenska Academy, University of Gothenburg, Sweden ad modum Donath (Donath and Breuner, 1982). The tissue blocks were cut into sections after random rotation around the vertical axis of the implant center. The sections with a thickness of approximately 100 μm were cut and ground down to a thickness of 10 μm (Donath and Breuner, 1982) and surface-stained with toluidine blue.

BIC was measured using a microscope (Nikon ECLIPSE 80i, Tokyo, Japan) equipped with a motorized Proscan 11 stage (Prior, Cambridge, UK), a MT1201 microcator (Heidenhain, Traunreit, Germany), and a DP72 digital camera (Olympus, Tokyo, Japan) connected to a PC with the stereological software newCAST (version 3.4.1.0, Visiopharm, Hørsholm, Denmark). The measurements were performed in the Department of Rheumatology, Aarhus University, Aarhus, Denmark.

BIC was evaluated using cycloid test lines parallel to the vertical axis, generating isotopic, uniformly random, intersection points with the structure of interest (Baddeley et al., 1986). Full-length grid lines were used to evaluate the intersections between the different tissues and the surface of the dental implant. The evaluation was performed at a magnification of $\times 462$, with a line spacing of 30 μm , and sampling fraction of 200% in the two ROIs. Quantitative measurement of BIC was the primary outcome variable and measured as bone in direct contact with the implant surface. Furthermore, direct contact between the implant surface and graft, bone marrow, and fibrous tissue was measured.

2.9. Statistics

The results from the 2D histology tests were presented as mean and standard deviation (SD) for each bone specimen. The analyses were performed using Excel version 2010 (Microsoft Corporation, WA, USA). The statistical model used for comparison of data from the different treatment modalities ($n = 5$), and a comparison of peri-implant tissue volume in micro and macro thread areas, was performed, using mixed-model analyses, with the statistical software SAS (SAS Institute, Inc., NC, USA). p -values < 0.05 were considered significant. Furthermore, in order to measure the difference in BIC between the gold standard treatment – autologous bone with a membrane – and easy-graft CLASSIC and easy-graft CRYSTAL, post-hoc analyses in both the micro and macro thread areas, using <https://www.stat.ubc.ca/~rollin/stats/ssize/n1.html>,

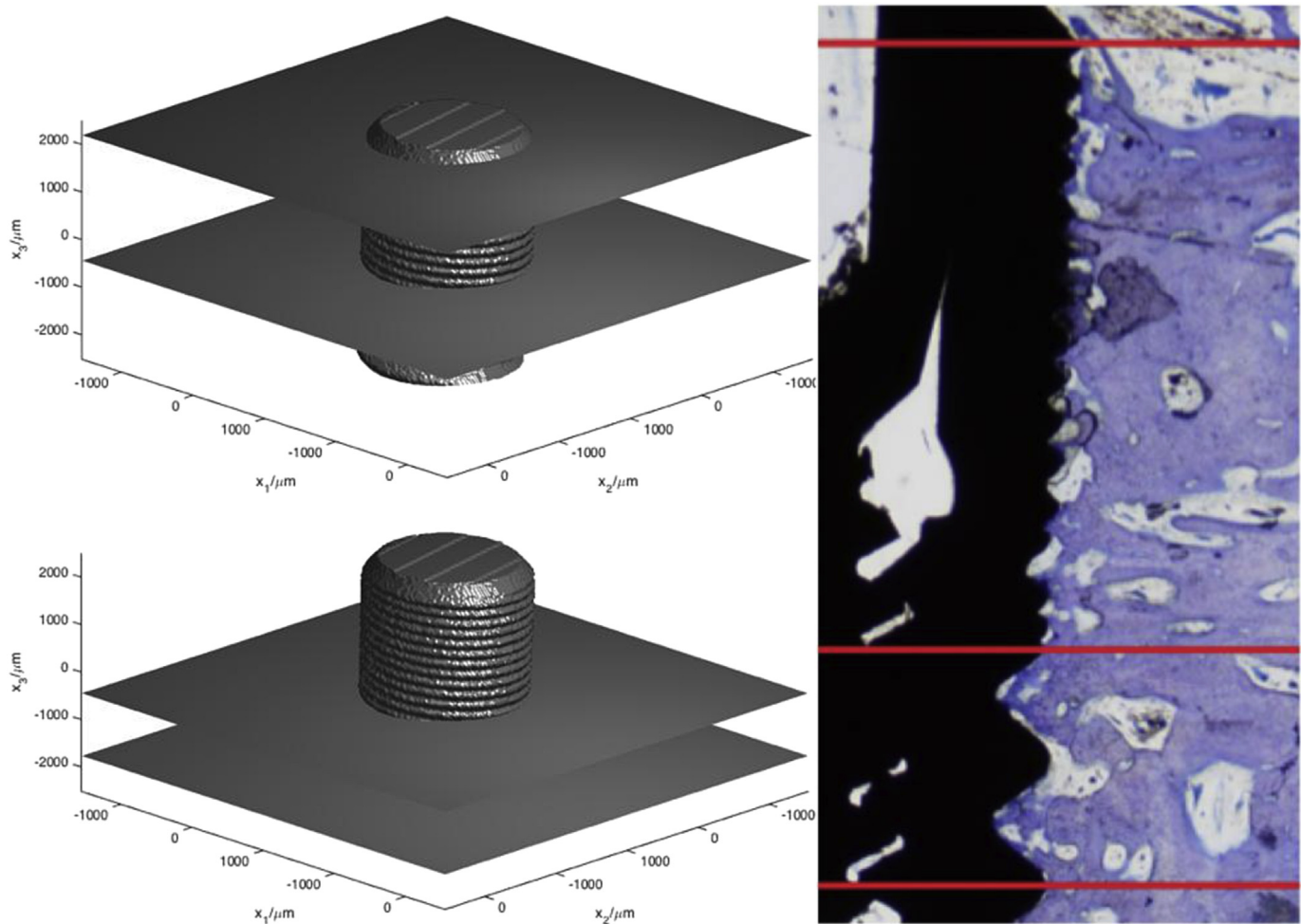


Fig. 4. The region of interest, divided into a micro and macro thread area, to the left with SR micro-CT and to the right with histology.

were performed. Coincidence between the two methods was determined by correlation analysis, and presented as a Bland–Altman plot (Altman and Bland, 1983). In our case, histology was considered gold standard and thus the difference between the two methods was calculated by subtracting the SR micro-CT results from the histologic measurements.

3. Results

The animals revealed normal wound healing and the observation period was uneventful, no implants were lost, and all implants healed submerged, without exposure. In the micro thread area, four samples had to be excluded due to off-center cutting of the samples. In the macro thread area three samples were excluded.

3.1. Histological evaluation of BIC

In the micro thread area (augmented area) four specimens had to be excluded due to off-center cutting, hence 31 specimens were evaluated. In the macro thread area (recipient bone) three specimens had to be excluded due to off-center cutting, hence 32 specimens were evaluated. Histological measures concerning mean BIC, SD, and p -values can be found in Table 1. The 2D evaluation showed a statistically significant difference in BIC between micro and macro thread areas ($p < 0.0001$). No statistically significant

difference was found between the different treatment modalities in either the micro or macro thread areas, when evaluating the different tissues. In general, high variation was found in both micro and macro thread areas.

Power calculations between easy-graft and autologous bone with a membrane revealed a power of 59%, in the micro thread area, with this study's sample size ($n = 12$). For a power of 80% a sample size of 20 would have been required. In the macro thread area, a power of 9% was found ($n = 12$). Again, for a power of 80% a sample size of 245 would have been required. When comparing easy-graft CRYSTAL with autologous bone with a membrane, a power of 16% was found in the micro thread area ($n = 14$). For a power of 80% a sample size of 118 would have been required. In the macro thread area, a power of 79% was found ($n = 14$), but for a power of 80% a sample size of 15 would have been required.

The coefficient of variation (CV%) in the micro thread area, for five randomly chosen bone sections, 1 year after the first evaluation, was 5.1%.

3.2. SR micro-CT evaluation of BIC

SR micro-CT measures concerning mean BIC, SD, and p -values can be found in Table 2. The 3D evaluation showed no statistically significant difference between the micro and macro thread areas ($p = 0.1530$). No statistically significant difference was found

Table 1

Shows the histology BIC percentage evaluation for the augmented area (micro thread area) and recipient bone (macro thread area), mean and standard deviation (SD), for bone, marrow, fibrous tissue, and graft for each treatment modality. The macro thread area is not augmented but represents recipient bone corresponding to the reconstructed CSD in the micro thread area. The *p*-values represent comparisons between the different treatment modalities in the micro thread area. In the macro thread area the *p*-value is used to assess whether the augmentation performed in the micro thread area influenced the macro thread area. MV: missing value, since no graft is evident in the macro thread area.

Treatment mean (SD)	Bone		Marrow		Fibrous tissue		Graft	<i>p</i> -value	
	Micro	Macro	Micro	Macro	Micro	Macro	Micro	Micro	Macro
Easy-graft CLASSIC	21.3% (13.7%)	42.5% (30.3%)	27.2% (14.2%)	56.9% (30.1%)	51.5% (18.4%)	0.7% (1.5%)	0% (0%)	Bone 0.8470	Bone 0.8193
Easy-graft CRYSTAL	23.4% (23.1%)	38.8% (20.6%)	47% (17.4%)	58% (14.3%)	29.3% (23.7%)	3.3% (8%)	0.4% (0.9%)	Marrow 0.8470	Marrow 0.8193
Autologous bone with a membrane	30% (18.5%)	47.7% (24.3%)	45.2% (22.6%)	52.3% (24.3%)	24.8% (16.2%)	0% (0%)		Fibrous tissue 0.2715	Fibrous tissue 0.6724
Autologous bone without a membrane	19.7% (18.1%)	31% (25.7%)	28.1% (24.3%)	63.2% (32%)	52.2% (36.5%)	5.8% (14.2%)		Graft 0.5132	Graft MV
Empty	18.4% (15%)	42.4% (19.3%)	32.4% (17.2%)	51.3% (21.6%)	33.4% (28%)	6.3% (13.5%)			

Table 2

Shows the SR micro-CT BIC percentage evaluation for the augmented area (micro thread area) and recipient bone (macro thread area), mean and standard deviation (SD), for bone and cavity for each treatment modality. The macro thread area is not augmented, however, it represents recipient bone corresponding to the reconstructed CSD in the micro thread area. The *p*-values represent comparison between the different treatment modalities in the micro thread area. In the macro thread area the *p*-value is used to assess whether the augmentation performed in the micro thread area influenced the macro thread area.

Treatment mean (SD)	Bone		Cavity		<i>p</i> -value	
	Micro	Macro	Micro	Macro	Micro	Macro
Easy-graft CLASSIC	17.2% (13.4%)	19.5% (12.4%)	82.8% (13.4%)	80.5% (12.4%)	Bone 0.2499	Bone 0.8978
Easy-graft CRYSTAL	25.7% (14.8%)	22.8% (14.2%)	74.3% (14.8%)	77.2% (14.2%)		
Autologous bone with a membrane	14.8% (4.9%)	19.2% (6.4%)	85.2% (4.9%)	80.8% (6.4%)	Marrow 0.2499	Marrow 0.8978
Autologous bone without a membrane	21.5% (14.9%)	25.7% (18%)	78.5% (14.9%)	74.3% (18%)		
Empty	12.1% (8.2%)	21.2% (14.6%)	87.9% (8.2%)	78.8% (14.6%)		

between the different treatment modalities in the micro and macro thread areas – $p = 0.2499$ and $p = 0.8978$ respectively. In general, a large variation was observed both in the micro and macro thread areas.

3.3. Comparison of methods

The correlation analysis revealed relatively weak correlation between the two methods, with correlation coefficients (*r*) of 0.34 and 0.39 in the micro and macro thread areas, respectively (Fig. 5 and Fig. 7). The agreement analysis showed a bias of 5.2% and 15.3% in the micro- and macro thread areas, respectively, for SR micro-CT when compared with histology (Figs. 6 and 8).

4. Discussion

The aim of this study was to compare the histomorphometric evaluation of BIC, which has been used for decades, with more recent 3D SR micro-CT technology. High BIC is considered a prerequisite for implant stability and survival, and a functional dental reconstruction. The use of a CSD with immediate implant installation and bone augmentation was chosen. In this study, 35 bone specimens with five different augmentation procedures were used. No statistically significant difference in BIC was found between defects reconstructed with autologous bone and with the different grafting materials easy-graft CLASSIC and easy-graft CRYSTAL. Nevertheless, the histological evaluation revealed a statistically significant difference between the micro and macro thread areas; this was not evident in the SR micro-CT evaluation.

This study is, to our knowledge, the first to document and evaluate BIC after immediate vertical bone augmentation consisting of autologous bone, β -TCP (easy-graft CLASSIC), and the BCP bone graft material easy-graft CRYSTAL (β -TCP and HA), comparing SR micro-CT quantitative results with conventional histology. Histological evaluation revealed that cavities reconstructed with autologous bone with a membrane had the highest mean BIC, with

30% in the grafted area. Differences in healing resulting from autologous bone, which is considered the gold standard for bone augmentation (Ono et al., 2011), were not statistically significant when compared with the other treatment modalities in this study. The lack of statistically significant differences could be due to large variability and subsequently low power. Intra-observer variation of 5.1% (CV%), evaluated 1 year after the initial histological analysis, was acceptable.

Evaluation of BIC with SR micro-CT has been performed in several studies. However, a comparison is difficult because of a large variability in methods used, and none of the evaluated studies are in reconstructed bone (Bernhardt et al., 2004, 2012; Sarve et al., 2013). In our study, a comparison in the micro thread area of SR micro-CT and histology presented a bias of 5.2%, which is considered minor. Bernhardt et al. (2012) found a comparable, non-significant difference of 4.9% when comparing four bone sections with 3D SR micro-CT scans. Furthermore, evaluation of the Bland–Altman plot revealed a lower bias when BIC was <20% compared with higher BIC values. This indicates that an uncertainty exists when evaluating large amounts of bone in close proximity to the implant surface or maybe the single bone section evaluated is not representative of the entire bone sample. Furthermore, in this study a bias of 15.3% in the macro thread area was found, which might be due to differences in size of the macro thread area in 2D and 3D (Fig. 4). The ROI in the macro thread area was demarcated at the lower border by the next macro thread in accordance with the transition between micro and macro thread. This resulted in evaluation of 1–2 macro threads, because the implant shape was a helix. Since the histological sections were rotated in an unbiased way, it was decided to evaluate one complete macro thread and the peak of the next thread for approximation of comparable ROIs in 2D and 3D. Evaluation of the Bland–Altman plot in the macro thread area revealed large variabilities between SR micro-CT and histology, which we believe is caused by the differences in size of the evaluated macro thread area, in this study.

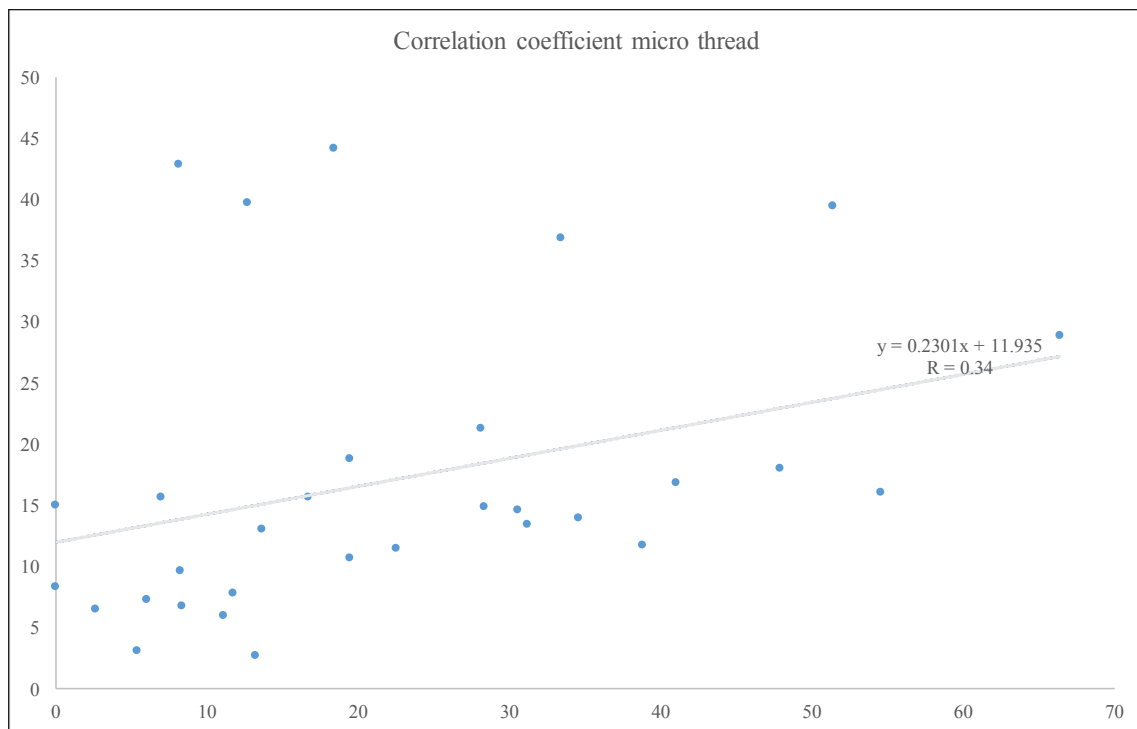


Fig. 5. The BIC correlation analysis between histology and SR micro-CT in the micro thread area (augmented area).

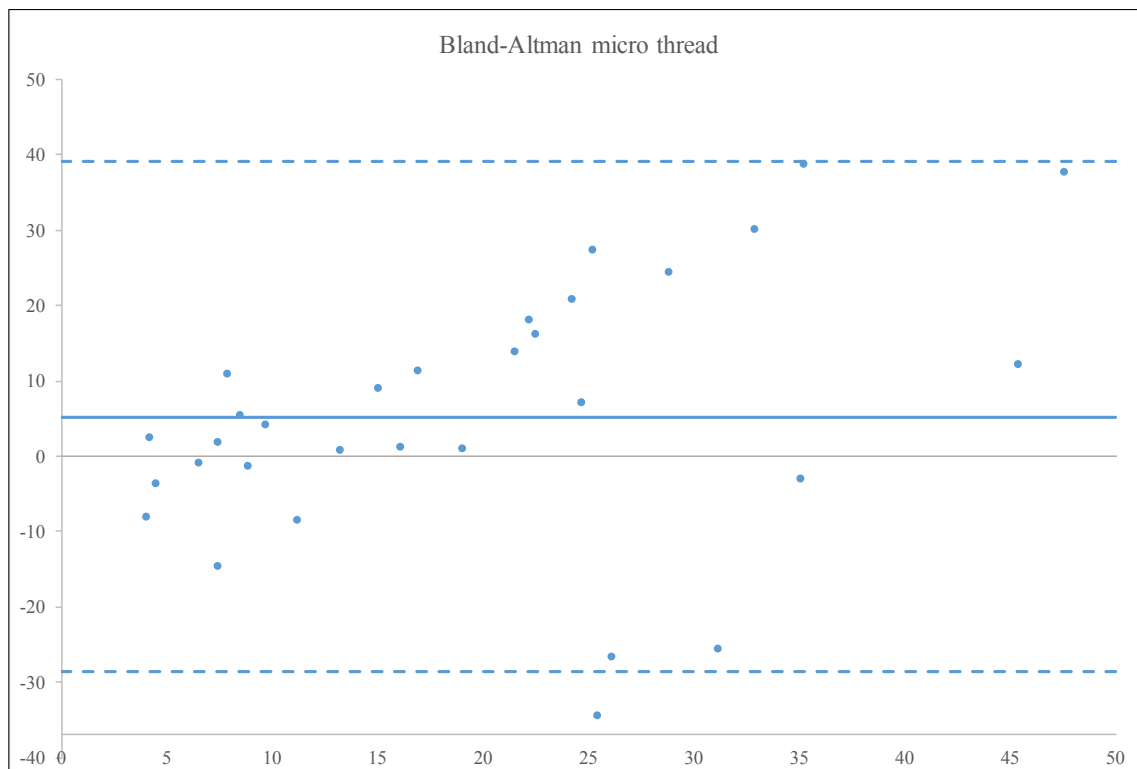


Fig. 6. The agreement analysis showed a bias of 5.2% in the micro thread area for SR micro-CT compared with histology.

According to [Bernhardt et al. \(2004, 2012\)](#) and [Sarve et al. \(2013\)](#), the PVE influences the BIC in the SR micro-CT scan because the evaluation is performed 1–2 pixels away from the surface, while in the histologic evaluation the BIC is measured at the implant surface, resulting in an allegedly different BIC with the

SR micro-CT scans compared with histology. Furthermore, thin, separated regions of mineralized tissue in proximity to the implant surface might be underestimated in SR micro-CT but included in histology ([Bernhardt et al., 2004](#)). However, we believe that refraction, which is an artefact in CT scans, influences the BIC

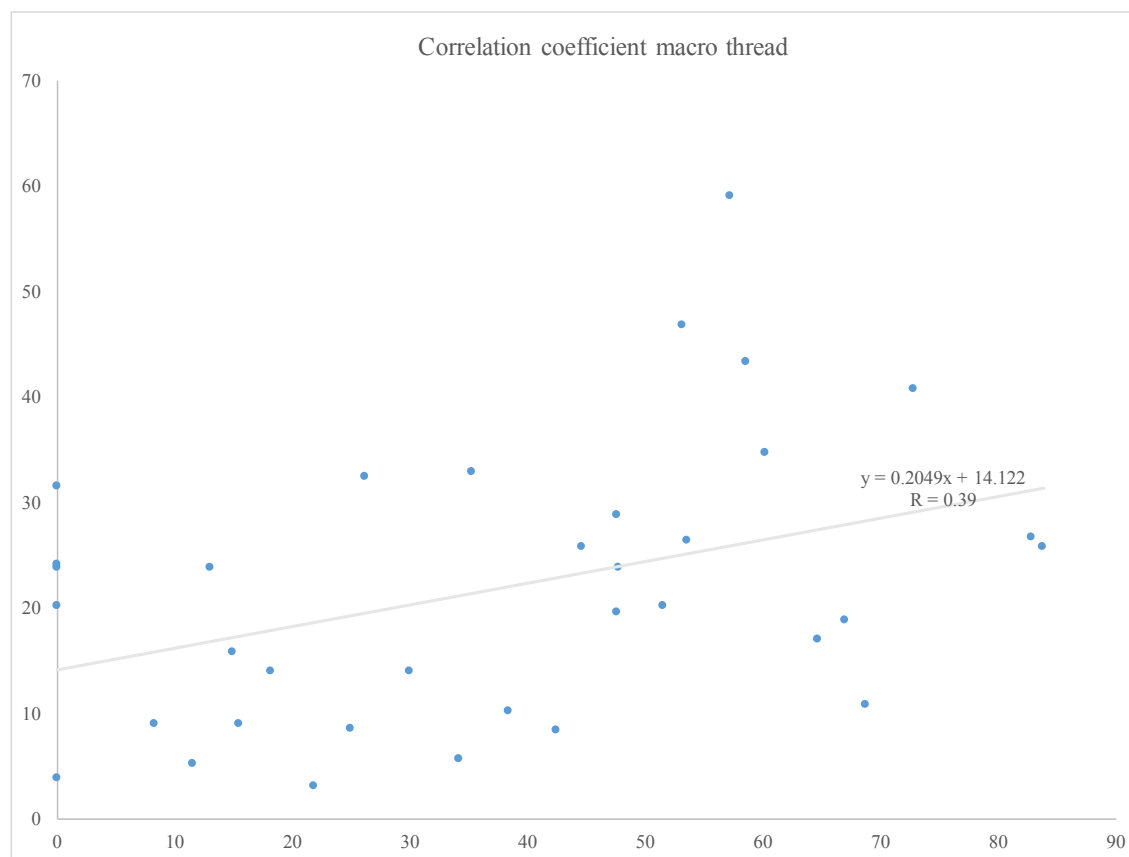


Fig. 7. The BIC correlation analysis between histology and SR micro-CT in the macro thread area (recipient bone).

evaluation. Refraction effects can disturb absorption tomography images. Refraction is strongest at interfaces between materials with very different refractive indexes. At interfaces between two materials of very different densities, e.g. the interface between a titanium implant and the much less dense surrounding tissue, refraction will typically enhance the contrast difference between the two materials, as demonstrated by (Liu et al., 2009), leading to edge enhancement in the image. Ito et al. (2003) evaluated bone samples with micro-CT and SR micro-CT and found that the PVE was not evident on the SR micro-CT evaluation (voxel size 6 μm), whereas the micro-CT revealed a blurred border between bone and cavity. In our study, when evaluating the titanium implant in the center of a bone sample, a bright line was visible at the edge of the implant (Fig. 9). The algorithm used in this study aimed to compensate for refraction, and with a difference of 5.2% between histology and SR micro-CT in reconstructed bone, this was considered acceptable.

The segmentation of bone in histological specimens can be hindered by preparation artifacts. Small titanium particles were evident in some of the specimens, but not in close proximity to the implant surface. Minor movements and preparation artefacts (cutting and polishing) in histology are excluded when using SR micro-CT. Ring artifacts and star-like structures are evident in the SR micro-CT scans, and the high absorption of implants compared with bone provides reconstructive challenges (Bernhardt et al., 2004). Nevertheless, the parallel beam of the SR micro-CT provides a slice-by-slice reconstruction of the tomograms, with absorption coefficients giving a Gaussian shape, which consequently makes it rather simple to determine the threshold for the different components such as bone, implant, and embedding material, even if the related peaks overlap (Bernhardt et al., 2004).

Generally, bone was underestimated using the 3D evaluation. Non-mineralized or low-mineralized tissue is invisible with SR micro-CT when using high voltage for evaluation of highly absorbent titanium implants in close proximity to bone. The BIC in this study was evaluated as volume in a band 0–10 μm from the implant surface, and the threshold in proximity to the implant was amended to adjust for refraction. Our findings are in accordance with Bernhard et al. (2004), and the BIC found in this study was low compared with that found by Bernhardt et al. (2012) and Sarve et al. (2013).

A disadvantage of 3D evaluation for BIC is the low lateral resolution compared with histology. In our study a 5 μm pixel size was used, and the BIC evaluation in 3D was applied to a volume 0–10 μm perpendicular to the implant surface, hence not a 'true' BIC. This was comparable to previous studies in which BIC was measured from 10 to 18 μm from the surface (Bernhardt et al., 2004, 2012; Sarve et al., 2013). The PVE can hinder histological measurements if the slides are too thick (Johansson and Morberg, 1995). Sections with a thickness over 30 μm were found to overestimate true bony contacts due to over-projection (Johansson and Morberg, 1995). However, the sections used in this study were 10 μm thick. The challenge when evaluating BIC, which is a 2D factor, is that we want to obtain those data using 3D measurements. Histologically, BIC is measured as tissue intersections at the implant surface and thus not in 3D. Furthermore, down sampling of the tomograms – which is necessary for handling the large amount of data, in this study – makes it challenging to determine exactly which type of tissue is in direct contact with the implant surface. Nevertheless, the algorithm used revealed a difference between histology and SR micro-CT of 5.2% when comparing 3D with one bone section.

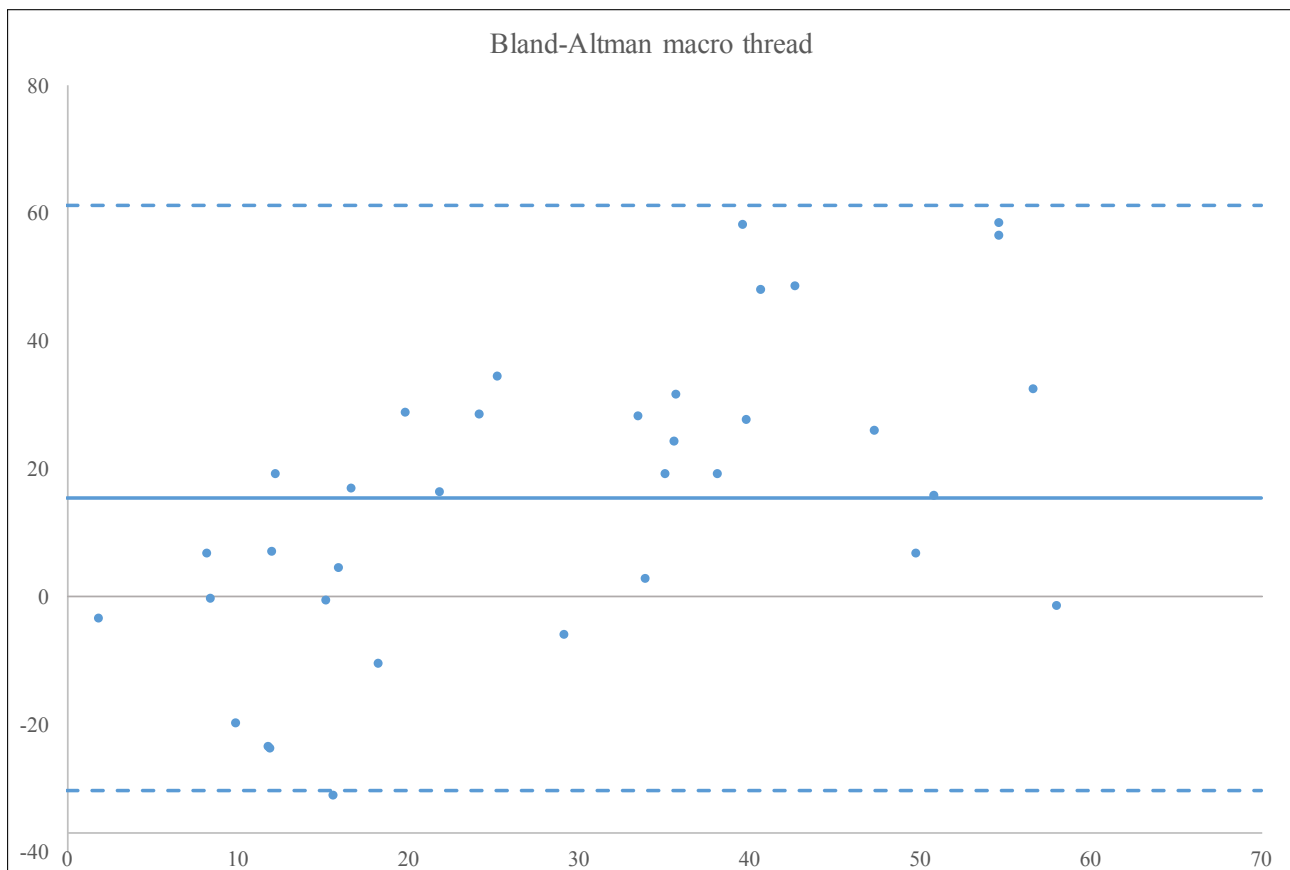


Fig. 8. The agreement analysis showed a bias of 15.3% in the macro thread area for SR micro-CT compared with histology.

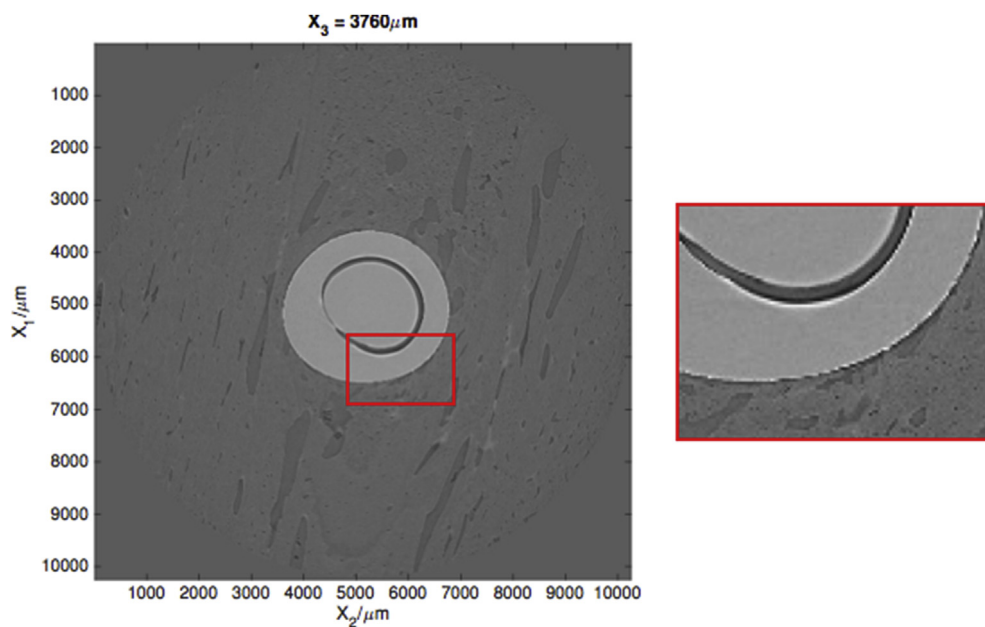


Fig. 9. Tomographic slice of an implant with surrounding bone (left). The magnified area (right) shows bright lines visible at the edge of the implant, verifying that the refraction effect enhances the contrast edges of the implant.

5. Conclusion

In conclusion, 3D evaluation is effective when applied to bone micro architecture due to its non-destructive nature. However,

when it comes to assessing BIC, this technique has shown limitations. Generally, SR micro-CT underestimates bone compared with histology and cannot be considered more effective than histology for evaluation of BIC. However, the SR micro-CT method used in this

study was highly comparable to histological evaluation. No statistically significant differences were found between the different treatment modalities, which we found were due to large variability and subsequently low power. When comparing 2D and 3D, a bias of 5.2% was found in reconstructed bone, quite in agreement with previous studies (Müller et al., 1998; Stiller et al., 2009; Bernhardt et al., 2012). One important issue when evaluating in 2D or 3D is the spatial resolution – distinguishing bone, graft, and cavity is dependent on the voxel size, so a higher resolution might provide more information. The resolution is improving at the synchrotron sources, but the limiting factor could be the capacity to handle the enormous amounts of data that come with high-resolution imaging.

Conflicts of interest

None.

Acknowledgement

We would like to thank the staff at the ESRF, beamline ID19, Grenoble, France: Paul Tafforeau and Elodie Boller for performing the scans, the reconstructions and their generous help during our visits to the research facilities.

Sunstar Suisse SA, Etoy, Switzerland is thanked for the financial support for the histological preparation of specimens, and for the PhD tuition.

References

- Albrektsson T: Hard tissue implant interface. *Aust Dent J* 53(suppl 1): 34–38, 2008
- Altman DG, Bland JM: Measurements in medicine: the analysis of method comparison studies. *Statistician* 32: 307–317, 1983
- Anderson ML, Dhert WJ, de Bruijn DJ, Dalmeijer RA, Leenders H, van Blitterswijk CA, et al: Critical size defect in goat's os ilium. A model to evaluate bone grafts and substitutes. *Clin Orthop Relat Res* 364: 213–239, 1999
- Baddeley AJ, Gundersen HJG, Cruz-Orive LM: Estimation of surface area from vertical sections. *J Micro* 142(3): 259–276, 1986
- Bernhardt R, Scharnweber D, Müller B, Thurner P, Schliephake H, Wyss P, et al: Comparison of microfocus and synchrotron X-ray tomography for the analysis of osteointegration around Ti6Al4V-implants. *Eur Cells Mater* 7: 41–51, 2004
- Bernhardt R, Kuhlisch E, Schulz MC, Eckelt U, Stadlinger B: Comparison of bone-implant contact and bone-implant volume between 2D histological sections and 3D SR micro-CT slices. *Eur Cells Mater* 23: 237–248, 2012
- Bonse U, Busch F, Günnewig O, Beckmann F, Pahl R, Dellling G, et al: 3D computed X-ray tomography of human cancellous bone at 8 μm spatial and 10^{-4} energy resolution. *Bone Mineral* 25: 25–38, 1994
- Botzenhart U, Kunert-Keil C, Heinemann F, Gredes T, Seiler J, Berniczek-Roykó A, et al: Osseointegration of short titanium implants: a pilot study in pigs. *Ann Anat* 199: 16–22, 2015
- Bressan E, Sivolella S, Urrutia ZA, Salata LA, Lang NP, Botticelli D: Short implants (6 mm) installed immediately into extraction sockets: an experimental study in dogs. *Clin Oral Implants Res* 23: 536–541, 2012
- Britz HM, Jokihaara J, Leppänen OV, Järvinen, Cooper DML: 3D visualization and quantification of rat cortical bone porosity using a desktop micro-CT system: a case study in tibia. *J Microsc* 240(1): 32–37, 2010
- Brånemark PI, Adell R, Breine U, Hansson BO, Lindström J, Hallen O, et al: Intraosseous anchorage of dental prostheses I. Experimental studies. *Scand J Plast Reconstr Surg* 3: 81–100, 1969
- Brånemark PI: Osseointegration and its experimental background. Research and education. *J Prosthet Dent* 50(3): 399–410, 1983
- Donath K, Breuner G: A method for the study of undecalcified bones and teeth with attached soft tissues: the Säge-Schliff (sawing and grinding) technique. *J Oral Path* 11: 318–326, 1982
- Gao TJ, Lindholm TS, Kommonen B, Ragni P, Parozini A: Stabilization of an inserted tricalcium phosphate spacer enhances the healing of a segmental tibial defect in sheep. *Arch Orthop Trauma Surg* 116: 290–294, 1997
- Grodzins L: Optimum energies for X-ray transmission tomography of small samples: applications of synchrotron radiation to computerized tomography I. *Nucl Instrum Methods* 206: 541–545, 1983
- Höhne KH, Bernstein R: Shading 3D-images from CT using gray-level gradients. *IEEE Trans Med Imaging* 5: 45–47, 1986
- Ito M, Ejiri S, Jinnai H, Kono J, Ikeda S, Nishida A, et al: Bone structure and mineralization demonstrated using synchrotron radiation computed tomography (SR-CT) in animal models: preliminary findings. *J Bone Miner Metab* 21: 287–293, 2003
- Johansson CB, Morberg P: Importance of ground section thickness for reliable histomorphometrical results. *Biomaterials* 16: 91–95, 1995
- Jung H, Kim HJ, Kim KD, Moon HS, Je JH, Hwu Y: Osseointegration assessment of dental implants using a synchrotron radiation imaging technique: a preliminary study. *Int J Oral Maxillofac Impl* 18(1): 121–126, 2003
- Kim DM, Nevins M: Schupbach. Alveolar ridge reconstruction with a composite alloplastic biomaterial. *Int J Periodontics Restorative Dent* 32(6): 204–209, 2012
- Leventis MD, Fairbairn P, Kakar A, Leventis AD, Margaritis V, Lückenrath W, et al: Minimally invasive alveolar ridge preservation utilizing an *in situ* hardening β -tricalcium phosphate bone substitute: a multicenter case series. *Int J Dent* 125406736, 2016
- Liu PT, Pavlicek WP, Peter MB, Spanghel MJ, Roberts CC, Paden RG: Metal artifact reduction image reconstruction algorithm for CT of implanted metal orthopedic devices: a work in progress. *Skeletal Radiol* 38: 797–802, 2009
- Lundgren D, Lundgren AK, Sennerby L, Nyman S: Augmentation of intramembraneous bone beyond the skeletal envelope using an occlusive titanium barrier. An experimental study in the rabbit. *Clin Oral Implants Res* 6: 67–72, 1995
- Mirone A, Gouillart E, Brun E, Tafforeau P, Kieffer J: PyHST2: an hybrid distributed code for high speed tomographic reconstruction with iterative reconstruction and a priori knowledge capabilities. *Nucl Instrum Meth B* 324: 41–48, 2014
- Müller R, Van Campenhout H, Van Damme B, Van Der Perre G, Dequeker J, Hildebrand T, et al: Morphometric analysis of human bone biopsies: a quantitative structural comparison of histological sections and micro-computed tomography. *Bone* 23: 59–66, 1998
- Neldam CA, Pinholt EM: Synchrotron μCT imaging of bone, titanium implants, and bone substitutes – a systematic review of the literature. *J Cranio-MaxilloFac Surg* 42: 801–805, 2014
- Neldam CA, Lauridsen T, Rack A, Lefolii TT, Jørgensen NR, Feidenhansl R, et al: Application of high-resolution synchrotron micro-CT radiation in dental implant osseointegration. *J Cranio-Maxillo-Facial Surg* 43(5): 682–687, 2015
- Nuzzo S, Peyrin F, Cloetens P, Baruchel J, Boivin G: Quantification of the degree of mineralization of bone in three dimensions using synchrotron radiation microtomography. *Med Phys* 29(11): 2672–2681, 2002
- Ono D, Jimbo R, Kawachi G, Ioku K, Ikeda T, Sawase T: Lateral bone augmentation with newly developed β -tricalcium phosphate block: an experimental study in rabbit mandible. *Clin Oral Implants Res* 22: 1366–1371, 2011
- Peyrin F, Attali D, Chappard C, Benhamou CL: Local plate/rod descriptors of 3D trabecular bone micro-CT images from medial axis topologic analysis. *Med Phys* 37: 4364–4376, 2010
- Rack A, Stiller M, Dalugge O, Rack T, Knabe C, Riesemeier H: Development in high-resolution CT: studying bioregeneration by hard X-ray synchrotron-based microtomography. In: Duchenne P, Healy KE, Hutmacher DW, Grainger DW, Kirkpatrick CJ (eds), *Comprehensive Biomaterials*. Elsevier Science, 2011
- Sarve H, Lindblad J, Borgefors G, Johansson CB: Extracting 3D inf bone remodeling in the proximal titanium implant in SR micro-CT image volumes. *Comput Meth Programs Biomed* 102: 25–34, 2011
- Sarve H, Friberg B, Borgefors G, Johansson CB: Introducing a novel analysis technique for osseointegrated dental implants retrieved 29 years postsurgery. *Clin Impl Dent Rel Res* 15: 539–549, 2013
- Schropp L, Wenzel A, Kosopoulos L, Karring T: Bone healing and soft tissue contour changes following single-tooth extraction: a clinical and radiographic 12-month prospective study. *Int J Periodontics Res Dent* 23(4): 313–323, 2003
- Slotte C, Lundgren D: Impact of cortical perforations of contiguous donor bone in a guided bone augmentation procedure: an experimental study in the rabbit skull. *Clin Implant Dent Relat Res* 4: 1–10, 2002
- Stalder AK, Ilgenstein B, Chicherova N, Deyhle H, Beckmann F, Müller B, et al: Combined use of micro computed tomography and histology to evaluate the regenerative capacity of bone grafting materials. *Int J Mater Res* 105: 679–691, 2014
- Stadlinger B, Bierbaum B, Grimmer S, Schulz MC, Kuhlisch E, Scharnweber D, et al: Increased bone formation around coated implants. *J Clin Periodontol* 36: 698–704, 2009
- Stiller M, Rack A, Zabler S, Goebbels J, Dalügge O, Jonscher S, et al: Quantification of bone tissue regeneration employing β -tricalcium phosphate by three-dimensional non-invasive synchrotron micro-tomography – a comparative examination with histomorphometry. *Bone* 44: 619–628, 2009
- Tallgren A: The continuing reduction of the residual alveolar ridges in complete denture wearers: a mixed longitudinal study covering 25 years. *J Prosthet Dent* 25: 21–43, 1972
- Viljanen VV, Gao TJ, Lindholm TC, Lindholm TS, Kommonen B: Xenogeneic moose (*Alces alces*) bone morphogenetic protein (mBMP)-induced repair of critical-size skull defects in sheep. *Int J Oral Maxillofac Surg* 25: 217–222, 1996

A.7

Injection of high dose botulinum-toxin A leads to impaired skeletal muscle function and damage of the fibrillar and non-fibrillar structures

Nature, Scientific Reports (2017)

Jessica Pingel, Mikkel Schou Nielsen, Torsten Lauridsen, Kristian Rix, Martin Bech, Tine Alkjaer, Ida Torp Andersen, Jens Bo Nielsen, R. Feidenhansl

Nature, scientific reports (2017) 7: 14746

SCIENTIFIC REPORTS

OPEN

Injection of high dose botulinum-toxin A leads to impaired skeletal muscle function and damage of the fibrillar and non-fibrillar structures

Jessica Pingel¹, Mikkel Schou Nielsen¹, Torsten Lauridsen², Kristian Rix², Martin Bech³, Tine Alkjaer¹, Ida Torp Andersen¹, Jens Bo Nielsen¹ & R. Feidenhansl^{2,4}

Botulinum-toxin A (BoNT/A) is used for a wide range of conditions. Intramuscular administration of BoNT/A inhibits the release of acetylcholine at the neuromuscular junction from presynaptic motor neurons causing muscle-paralysis. The aim of the present study was to investigate the effect of high dose intramuscular BoNT/A injections (6 UI = 60 pg) on muscle tissue. The gait pattern of the rats was significantly affected 3 weeks after BoNT/A injection. The ankle joint rotated externally, the rats became flat footed, and the stride length decreased after BoNT/A injection. Additionally, there was clear evidence of microstructural changes on the tissue level by as evidenced by 3D imaging of the muscles by Synchrotron Radiation X-ray Tomographic Microscopy (SRXTM). Both the fibrillar and the non-fibrillar tissues were affected. The volume fraction of fibrillary tissue was reduced significantly and the non-fibrillar tissue increased. This was accompanied by a loss of the linear structure of the muscle tissue. Furthermore, gene expression analysis showed a significant upregulation of COL1A1, MMP-2, TGF- β 1, IL-6, MHCIIA and MHCIIx in the BoNT/A injected leg, while MHVIIB was significantly downregulated. In conclusion: The present study reveals that high dose intramuscular BoNT/A injections cause microstructural damage of the muscle tissue, which contributes to impaired gait.

Botulinum toxin (BoNT/A) is among the most potent toxins to humans that are known^{1,2}. One gram of crystalline preparation of BoNT/A can potentially kill 1.000.000 people. In several incidents its use as a biological weapon has been attempted³. Nevertheless, BoNT/A is the first biological toxin that has been licensed for treatment of human disease after the pioneering work of the ophthalmologist Alan Scott who used BoNT/A for the treatment of strabismus⁴. Today, the list of diseases that are treated by using BoNT/A is long and includes cervical dystonia⁵, blepharospasm⁶, urinary incontinence⁷, anal fissure⁸ and numerous movement disorders⁹, including cerebral palsy¹⁰, migraine¹¹, depression¹², mandibular recontouring¹³ and, fascial wrinkles¹⁴. Furthermore, BoNT/A continues to be the most common minimally invasive procedure performed by plastic surgeons and has during the past decade grown into a billion dollar industry¹⁵.

BoNT/A injection is also commonly used against the development of contractures in patients with central motor lesions. However, only a few studies have investigated the effect of BoNT/A injections on the muscle at tissue level. Skeletal muscle consists of the contractile proteins myosin and actin, which are incorporated into thick and thin filaments, respectively. Together they form arrays in longitudinally repeated banding patterns termed sarcomeres. Sarcomeres in series form myofibrils, and many parallel myofibrils exist in each fiber. A muscle contraction occurs when an action potential reaches the presynaptic terminal of a motor neuron. This activates voltage-dependent calcium channels and allows calcium ions to enter the neuron. Calcium ions bind to proteins (synaptotagmin) on synaptic vesicles, triggering vesicle fusion with the cell membrane and subsequent neurotransmitter release from the motor neuron into the synaptic cleft. The motor neurons then release acetylcholine (ACh), which diffuses across the synaptic cleft and binds to nicotinic acetylcholine receptors (nAChRs) on the cell membrane of the muscle fiber, also known as the sarcolemma. The binding of ACh to the receptor

¹Center for Neuroscience, University of Copenhagen, Copenhagen, Denmark. ²Niels Bohr Institute, University of Copenhagen, Copenhagen, Denmark. ³Medical Radiation Physics, Clinical Sciences, Lund University, Lund, Sweden. ⁴Present address: European XFEL, Hamburg, Germany. Correspondence and requests for materials should be addressed to J.P. (email: jpingel@sund.ku.dk)

depolarizes the muscle fiber, and triggers a series of molecular events that includes the binding of calcium to the muscle-regulatory proteins, and causes the interaction between myosin and actin filaments, and subsequently the formation of cross-bridges causing muscle contraction.

Botulinum toxin works by blocking the release of acetylcholine from presynaptic motor neurons, and this chemical denervation causes a cascade of downstream events in the muscle thus causing muscle paralysis¹⁶. BoNT/A asserts its effect by proteolysis of the SNARE protein synaptosome-associated protein of 25 kDa (SNAP25) in the synapses of the motor neurons¹⁷. SNAP25 is a cytoplasmic protein, which is crucial in the fusion between the membranes of the vesicles containing ACh and the cell membrane at the axon terminal. When BoNT/A is injected into muscle tissue, the proteolysis of SNAP25 prevents the exocytosis of ACh, and effectively leads to muscle paralysis^{2,18,19}.

Muscle atrophy has been noted as a common side effect as a result of denervation^{20,21}. Furthermore, considerable fiber atrophy has been observed after BoNT/A (5–10 UI) injections into the longissimus dorsi muscle of rabbits²². One rat study investigated changes in different muscle proteins after BoNT/A injections (dosage of 5 units/kg body weight) and observed that the expression of various proteins changed after injection when compared to saline injections²³. In fact, thirty-eight proteins were associated with alterations of energy metabolism, contractile function of the muscle, transcription and translation, cell proliferation and cellular stress response²³. In addition, intramuscular BoNT/A injections (Each dose was 6 U/kg, in a 100 μ L volume) have been shown to induce significant changes of fiber type composition with a shift from faster to slower isoforms²⁴. Nonetheless, it is still unclear whether or not the fibrillar structure of the muscle fibers is damaged as a result of BoNT/A injections. To resolve this issue a 3D visualizations of the tissue is required. Standard lab-based X-ray tomography does not have the sufficient X-ray brilliance to resolve the details of tissue at microstructural level within a reasonable time frame. However, Synchrotron Radiation X-ray Tomographic Microscopy (SRXTM) dramatically improves the sensitivity within biomedical applications^{25,26}. The tunable-energy monochromatic beam allows us to achieve high sensitivity to small variations in mass densities. This makes SRXTM well-suited for imaging biological tissue in contrast to conventional X-ray CT²⁵. Within medical science, the modality has been successfully applied to study the microstructure of a range of tissues such as the 3D brain anatomy in murine model²⁷, the microvascular network and thrombi in hepatocellular carcinoma²⁸ and hyaline cartilage in human knees²⁹. Hence, the SRXTM is ideal for the purpose to monitor tissue changes in muscles after high dose BoNT/A injections. In this study, x-ray attenuation and phase contrast was taken into consideration by implementation of the Paganin approach³⁰. The aim of the present study was to explore the effects of high dose intramuscular BoNT/A injections on healthy muscle tissue using SRXTM. This was done to confirm whether or not the muscle tissue maintained its integrity and microstructure following BoNT/A injections. In Fig. 1 an example of a 3D reconstruction of the fibrillar and the non-fibrillar tissue is shown for a BoNT/A injected muscle and the corresponding control. The scale is 400 μ m \times 400 μ m \times 700 μ m. It is clearly seen that the BoNT/A injection causes significant changes in the microstructure of the tissue. Most obvious is that the ratio between fibrillary and non-fibrillar tissue changes and that the linear structure of the muscle tissue is lost. In order to quantify these changes we calculate the volume fraction of the fibrillary tissue and the isotropy index as defined below. As secondary study aims we also investigated the effects of high dose BoNT/A injections on both the gait pattern and the gene expression profile in healthy rats.

Results

Volume fraction. The muscle tissue organization was severely affected by the BoNT/A injections 3 weeks after injection (Figs 1 and 2) of 20 pg BoNT/A per muscle head (60 pg in total). The amount of the fibrillar tissue significantly decreased ($p = 0.02$), while the non-fibrillar tissue was significantly increased ($p = 0.02$).

Muscle atrophy. Three weeks after BoNT/A injection the wet weight of the triceps surae was decreased significantly ($p = 0.00005$) by 45% (BoNT/A injected leg (BoNT/A): 0.78 ± 0.03 g and Contralateral saline injected leg (Con): 1.43 ± 0.07 g) in the BoNT/A injected leg. A 2D image of the muscle crosssections displays the atrophy observed in the BoNT/A leg (Fig. 3).

Anisotropy. The isotropy index from the star length distribution (SLD) analysis significantly increased ($p = 0.002$) after the BoNT/A injections (3 weeks post injection), which indicates a loss of linear structure of the muscle tissue. This was further supported by visualization of the 3D orientation of the muscle tissue using rose diagrams (Fig. 4). The diagram displays the strength of directions of the non-fibrillar tissue in the volume of interest (VOI). For linearly structured tissues, the diagram will take the shape of a strongly elongated ellipsoid whereas isotropic tissues with uniformly distributed directions will take the shape of a sphere. As seen from Fig. 4, the BoNT/A injection has resulted in a loss of directionality of the non-fibrillar tissue.

Gait pattern analysis. The gait pattern of the rats was significantly affected. There was a significant main effect of both time ($p < 0.0001$) and leg ($p = 0.0008$) on the stride length but not of the interaction. Across time, the stride length was significantly reduced for the BoNT/A leg compared to the non BoNT/A leg ($p = 0.0006$). Across legs, the second pre-test stride length value was significantly higher than any post-test values ($p < 0.0006$ for all comparisons). No significant differences were observed between the post-tests. There was a significant main effect of time, leg and the time-leg interaction on the foot length ($p < 0.0001$ in all cases) indicating that the rats became flat footed after BoNT/A injections. The post hoc test revealed that for the BoNT/A leg the foot length was significantly increased in all post-test observations when compared to the pre-test observation ($p < 0.0001$ in all cases). For the non BoNT/A leg, the foot length was significantly shorter at the pre-test compared to the first three post-tests ($p = 0.004$, $p = 0.012$ and $p = 0.028$, respectively). However, the last post-test foot length did not differ significantly from the pre-test. The foot length of the BoNT/A leg was significantly greater at all post-tests compared to the non BoNT/A leg ($p < 0.0001$ in all cases). The foot angle was measured as indicated in Fig. 5.

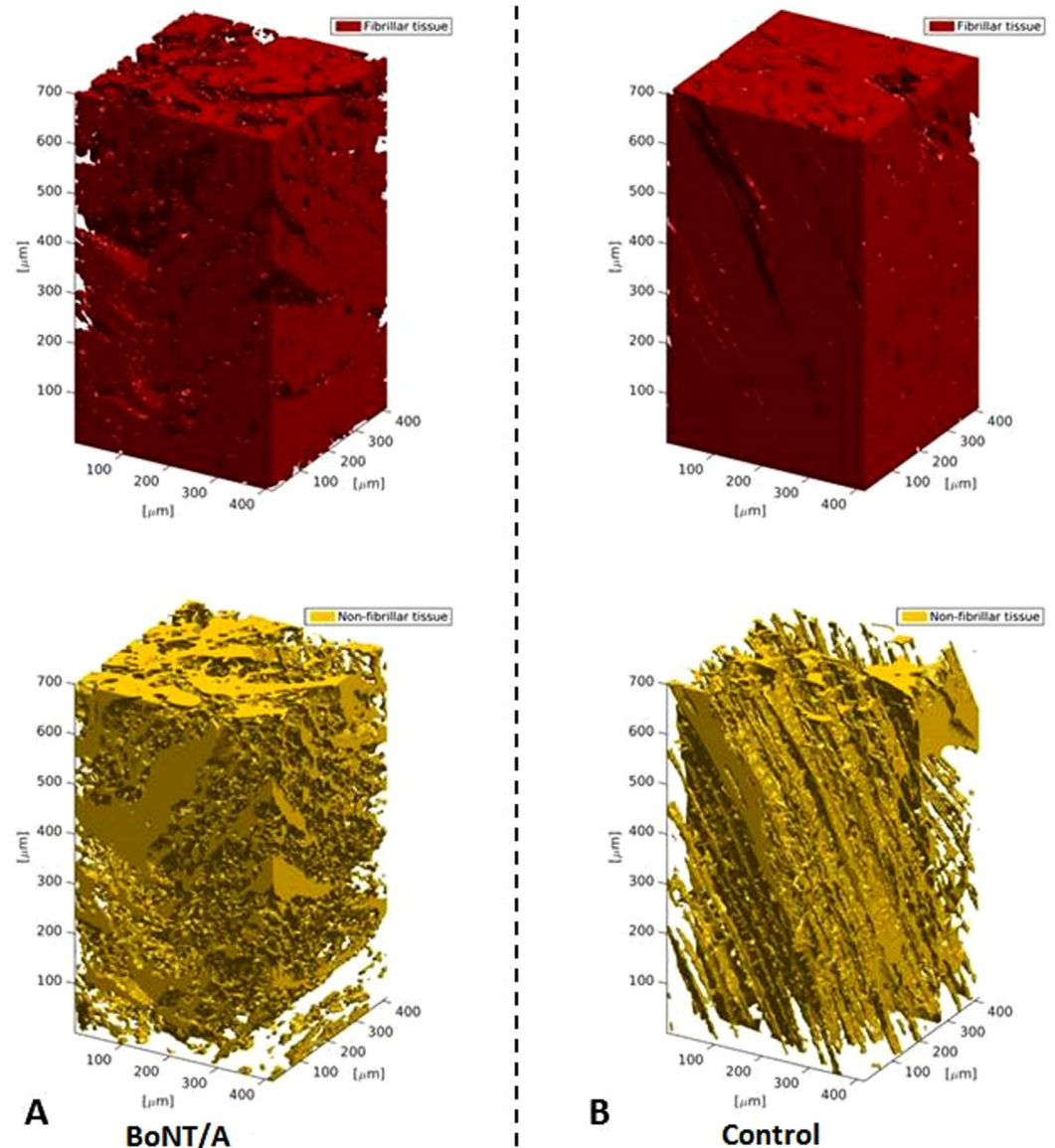


Figure 1. 3D visualizations of tomograms from the SRXTM measurements. Shown are the fibrillar (red) and non-fibrillar tissue (yellow) of the muscle in BoNT/A injected (A) and control leg (B) of one of the rats (3 weeks post injection of 6UI BoNT/A (3×20 pg BoNT (2UI)/a ~ 60 pg BoNT/A in total)). The SRXTM data indicate that BoNT/A injection causes damage to the muscle tissue structure and organization.

A positive foot angle indicates external rotation, and a negative foot angle indicates an internal rotation of the foot. There was a significant main effect of time, leg and the time-leg interaction on the foot angle ($p < 0.0001$ in all cases). The post hoc test revealed that for the BoNT/A leg all post-test observations were significantly larger than the pre-test observation ($p < 0.002$ in all cases). For the non BoNT/A leg, the foot angle did not significantly change from the pre-test to the post-tests. The foot angle of the BoNT/A leg was significantly greater at all post-tests compared to the non BoNT/A leg (Fig. 6).

Clinical score assessment. The clinical score dropped significantly already 24 h post injection ($p = 0.0001$) and reached the lowest level on day 3 post injection ($p = 0.00001$). The rats never recovered during the protocol and the clinical score was still decreased three weeks post injection. There was a significant main effect of time on the clinical score ($p < 0.0001$). The post hoc test revealed that all post-test observations were significantly lower compared to the pre-test observation ($p < 0.0001$ in all cases) (Fig. 6).

Gene expression. The gene expression of seventeen gene targets were analyzed in $n = 8$ rats (Fig. 7). Specific gene targets were selected covering the areas of muscle structure, muscle metabolism, Extracellular matrix components, connective tissue breakdown and muscle fiber types. There was a significant main effect of both BoNT/A treatment ($p < 0.001$) and gene ($p < 0.001$) on the gene expressions and a significant interaction ($p < 0.001$). Post

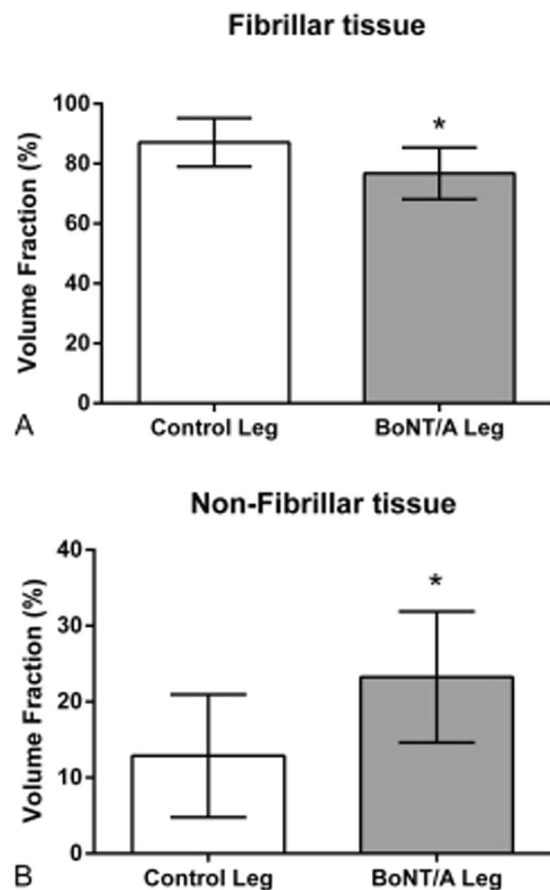


Figure 2. Volume fraction in percent of the fibrillar (A) and non-fibrillar tissue (B) of the muscle. All data are shown as Mean \pm SEM. *Indicates a significant difference between BoNT/A and Con leg. Dose of injection 6UI BoNT/A (3×20 pg BoNT (2UI)/a ~ 60 pg BoNT/A in total). The level of significance was $p < 0.05$.

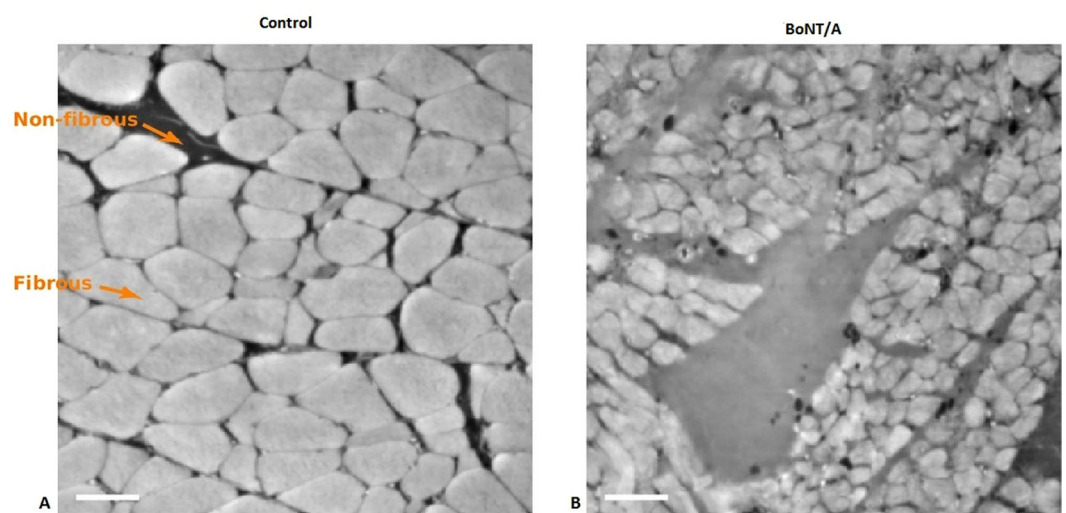


Figure 3. 2D images of muscle cross sections. Left image control leg, right image BoNT/A injected muscle (3 weeks post-injection). The BoNT/A injected muscle contains smaller muscle fibers than the control muscle, indicating muscle atrophy. Arrows are indicating fibrous and non-fibrous tissue. Dose of injection 6UI BoNT/A (3×20 pg BoNT (2UI)/a ~ 60 pg BoNT/A in total). The scale bar equals $50 \mu\text{m}$.

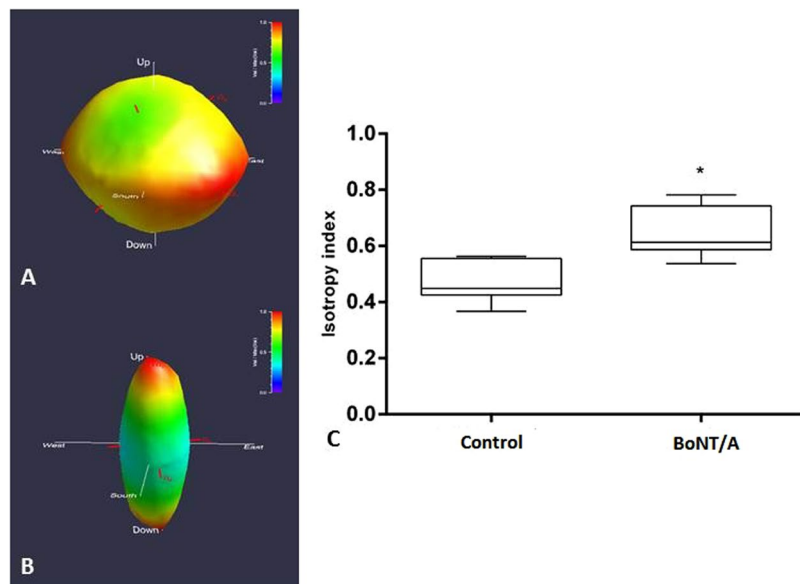


Figure 4. Star length distribution (SLD) rose diagrams depicting non-fibrillar tissue orientation in BoNT/A (**A**) and control (**B**) muscle from one of the rats (3 weeks post injection). Dose of injection 6UI BoNT/A (3×20 pg BoNT (2UI)/a ~ 60 pg BoNT/A in total). Distance from origin and colour (violet = minimum, red = maximum) indicate relative component value. Red axes show principal component directions and relative magnitudes. The boxplot (right **C**) shows the isotropy index of $n = 6$ rats shown as Mean \pm SEM. *Indicates a significant difference between BoNT/A and Con leg, showing an significantly increased anisotropy index after the BoNT/A injections, which indicates a loss of linear structure of the muscle tissue. The level of significance was $p < 0.05$.

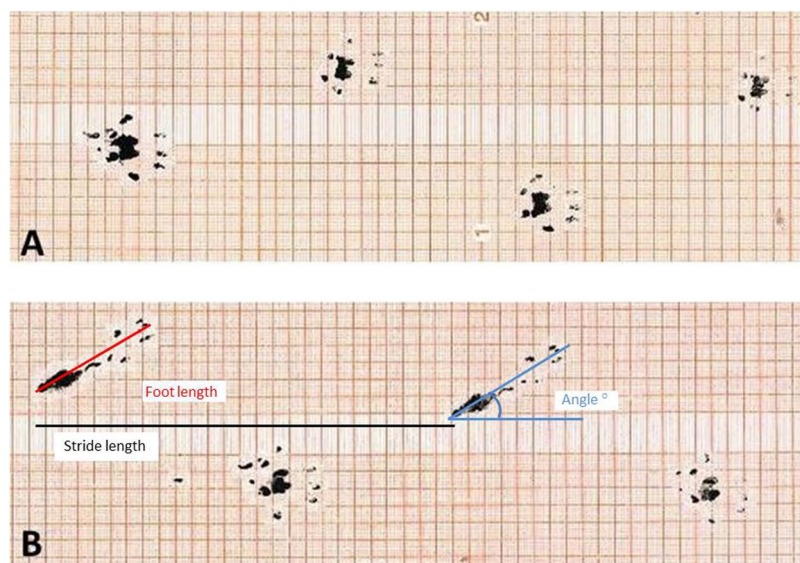


Figure 5. Foot step analysis. The hind paws were dipped in ink and the rats ran over graph paper at (**A**) baseline (2 days pre injection), and (**B**) post (21 days) after BoNT/A injection into the left triceps surae. Dose of injection 6UI BoNT/A (3×20 pg BoNT (2UI)/a ~ 60 pg BoNT/A in total). The stride length, foot angle and the foot length were analyzed. All parameters were significantly affected in the BoNT/A leg when compared to baseline and the control leg ($p < 0.05$).

hoc tests revealed a significant upregulation of gene expression in: collagen type 1 (*COL1A1*), interleukin 6 (*IL-6*), transforming growth factor beta 1 (*TGF- β 1*), matrix metalloproteinase 2 (*MMP-2*), myosin heavy chain IIA (*MHCIIA*) and myosin heavy chain IIX (*MHCIIX*). Myosin heavy chain IIb (*MHCIIB*) was significantly down-regulated in the BoNT/A leg compared with the control leg.

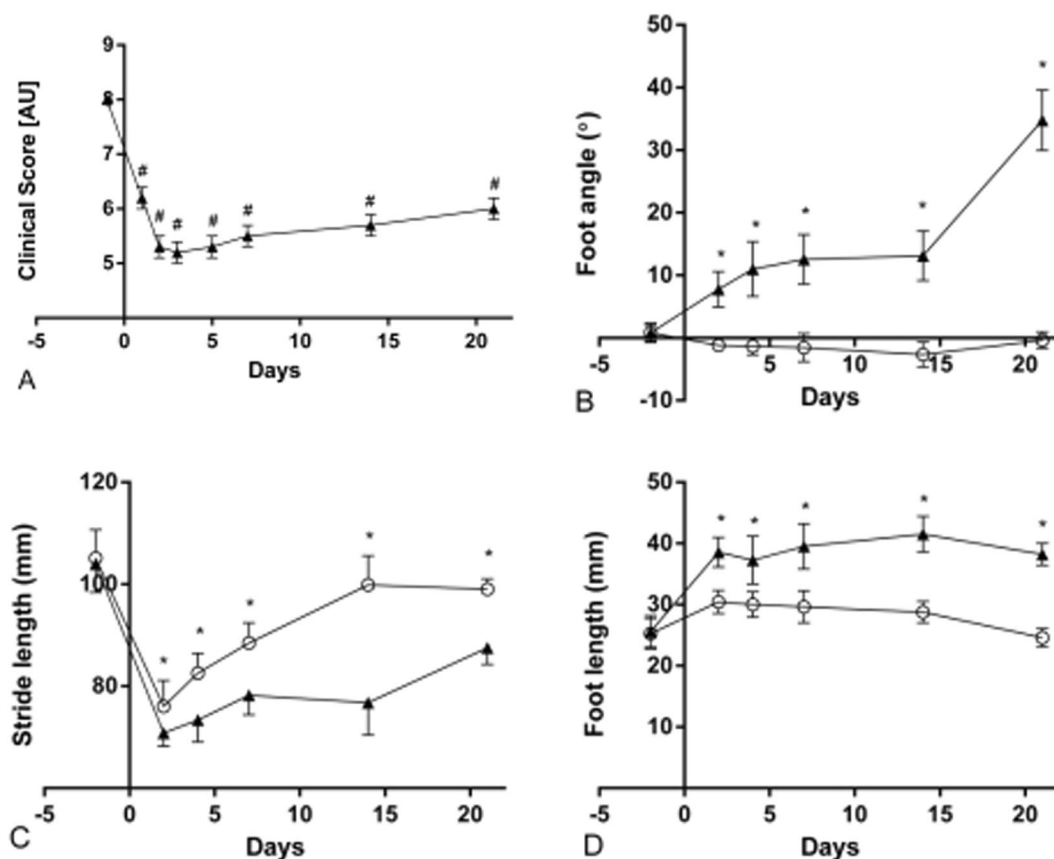


Figure 6. The stride length, foot angle and foot length was analyzed as indicated on Fig. 5. The clinical score (A) shows all animals in arbitrary units AU. The foot angle (B) is shown in degrees (°). The stride length (C) is shown in mm. And the foot length is shown in mm. In both B,C and D the black triangles represent the BoNT/A injected leg, and the open circles represent the contralateral Con injected leg. Dose of injection 6UI BoNT/A (3 × 20 pg BoNT (2UI)/a ~60 pg BoNT/A in total). All data are shown as Mean ± SEM. *Indicates a significant difference between BoNT/A and Con leg, #indicates a significant difference from baseline. The level of significance was $p < 0.05$.

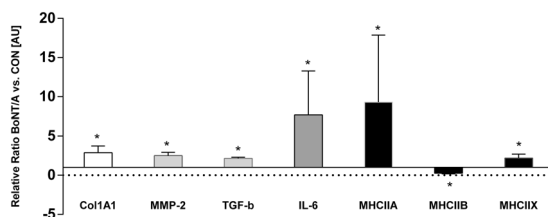


Figure 7. The relative changes of gene expression after botulinum toxin injection. The control leg equals 1 and all expressions are shown relative to the expression of the control leg. All data are shown as Geo Mean ± SEM. *Indicates a significant difference between BoNT/A and Con leg. Dose of injection 6UI BoNT/A (3 × 20 pg BoNT (2UI)/a ~60 pg BoNT/A in total). The level of significance was $p < 0.05$.

Body weight. The development of the body weight differed significantly between the BoNT/A injected animals and the Control group ($p < 0.0001$) (Fig. 8). In addition both groups changed significantly over time (after 1 week) ($p < 0.0001$).

Discussion

The main finding of the present study is that the microstructure of the skeletal muscle showed signs of muscle damage following high dose BoNT/A injections (3 × 20 pg BoNT (2UI)/a ~60 pg BoNT/A in total (6UI)), both at the fibrillar- and non fibrillar level of the tissue. The 3D tomographs showed that the tissue lost its linear structure, and that the structural composition was clearly affected. The anisotropy analysis of the tomograms gives further

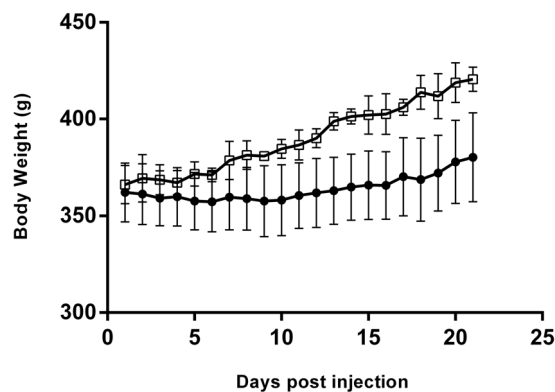


Figure 8. The development of the body weight of the rats after botulinum toxin injection. The open squares represent control rats ($n = 2$), and the black dots represent BoNT/A rats ($n = 6$). All data are shown as Mean \pm SEM. *Indicates a significant difference between BoNT/A and Con leg. The level of significance was $p < 0.05$.

support to these indications. The isotropy index increased after high dose BoNT/A injection, which indicates that the muscle tissue was more randomly oriented following high dose BoNT/A injections.

Botox is used in several different disciplines with many different purposes. In addition, it is becoming more and more common for healthy individuals to receive BoNT/A injections, not to cure a disease, but in order to improve the appearance. BoNT/A is among others used to sculpt different muscles of the body, including the masseter muscles for mandibular recontouring (used for when individuals complaint of a “squared” lower face³¹ or the medial and lateral gastrocnemius for calf recontouring (for when individuals complaint of prominent calf muscles)³¹. However, recent studies have expressed some concerns regarding the use of BoNT/A^{32–34}.

The chemical denervation induced by BoNT/A injection prevents muscle contraction and causes a cascade of downstream events in the muscle e.g. inflammation, satellite cell activation, oxidative stress, atrophy and metal ion imbalance^{35,36}. Whether BoNT/A also has a direct effect on the muscle tissue is unclear. However, it has been shown that repeated BoNT/A injections (once a day for 28 days at doses of 1, 3, and 9 ng kg⁻¹ day⁻¹) result in pronounced muscle atrophy³⁷ and muscle weakness. In the present study we observed a loss of 45% muscle wet weight after three weeks, and we have previously shown that muscle force drops significantly after BoNT/A injection using the same dose as in the present study³³. In fact several studies report muscle weakness as the most common treatment-related adverse event³¹. Furthermore it has been shown that side effects are temporary and often related to usage of high doses³⁸. Even though the use of BoNT/A has been reported to be safe and many patients are treated without complications, some studies report unwanted side effects^{39,40}. One study by Blaszczyk *et al.* examined unwanted side effects (adverse events AEs) after BoNT/A injections in 79 cerebral palsy patients⁴¹. Altogether 95 AE's were reported in 45 patients. Nineteen patients reported muscle weakness, and four patients did report severe adverse events including speech disorders, swallowing difficulties and respiratory troubles. These findings indicate that side effects after BoNT/A injection are quite common⁴¹. Cerebral palsy patients are often treated with BoNT/A in order to improve gait function, and several studies have shown that this treatment is safe and without side effects^{10,42}. However, we suggest that the success of the treatment should be evaluated with care. We propose that even though patients do not report any unwanted side effects, this does not mean that the BoNT/A treatment was successful in these patients per se. In the present study we observed that BoNT/A injections had a significant effect on the gait pattern of the present rats. The rats developed a flatfoot on the BoNT/A injected leg (Fig. 5). Furthermore the clinical score dropped already after 24 hours and did not return to baseline within three weeks (Fig. 6). The same observation has been made previously by Ozawa *et al.*⁴³ after BoNT/A injection (dose 5 units/mL). In addition, the BoNT/A injection caused an external rotation of the foot possibly to regain balance (Fig. 6). Furthermore, it appears that more and more people question whether the few positive effects achieved by BoNT/A injection are actually overcome by the negative effects it has on the muscles^{32,33,44}.

The affected gait after 24 hours is a result of the reduced presynaptic acetylcholine release that follows Botulinum toxin injection. BoNT/A cleaves a SNARE protein SNAP25, which is required for exocytosis and as a result several downstream events are affected including muscle atrophy. The muscle atrophy induces weakness, and the weakness affects the gait pattern. Thus while the gait pattern and clinical score at the early time points reflect the neural effects of BoNT/A, atrophy and muscle weakness is likely to contribute to the impairment of gait function at the later time points (3 weeks post injection).

Eamus *et al.* (1999) have shown that a single injection of BoNT/A into the calf increased the length of gastrocnemius during gait⁴⁵. Furthermore, gait analysis of ninety-seven CP patients revealed that muscle strength was highly related to muscle function and explained more of the gait variance than spasticity⁴⁶. Based on the present findings we suggest that the desired outcome of BoNT/A treatment in cerebral palsy patients should be reconsidered, and future studies should focus on finding a better treatment instead of improving a drug that does not entail the desired effects.

Furthermore, whether muscle contouring of the calf muscles influences the gait pattern in humans has not yet been investigated, but based on the present findings we suggest that it might be an important point to focus on in future investigations as well.

The damage that occurs in the muscle after high dose BoNT/A injection requires a comprehensive remodeling process. This is reflected in gene expressions of the present study (Fig. 7). Both the collagen synthesis and collagen breakdown is upregulated after BoNT/A injection. This finding is in agreement with previous observations showing increased collagen synthesis at gene expression level three weeks after muscle injury in rats⁴⁷. On the other hand, immobilization causes a decrease of collagen expression⁴⁸. Thus, the increased collagen synthesis might indicate an accelerated tissue remodeling after muscle damage rather than being a result of the denervation due to BoNT/A injection (Fig. 7). The anisotropy findings of the present study indicate a loss of tissue orientation, which further indicates that the microstructure of the muscle is undergoing an extensive remodeling process. Furthermore, the inflammation marker IL-6 was upregulated in the present study. IL-6 is a pleiotropic cytokine involved in tissue regeneration and remodeling, indicating an inflammatory response after BoNT/A injection in the muscle⁴⁹. A significantly up-regulation of IL-6 following muscle injury, coinciding with the active period of muscle regeneration has been observed previously in mice⁴⁸. The present upregulation of IL-6 in the BoNT/A injected muscle underlines that the high dose BoNT/A injection caused muscle damage. Furthermore, one study observed a significant increase of satellite cells after intramuscular botox injections in rabbits⁵⁰. In resting muscle satellite cells remain quiescent, while muscle injury and trauma invokes activation of satellite cells^{51,52}. Numerous studies have shown that skeletal muscle satellite cells are essential for muscle fiber repair and regeneration^{53–55}. Muscle wasting occurs in a variety of conditions, including muscular dystrophies, cancer cachexia and sarcopenia⁵⁶. In the present study the intramuscular BoNT/A injection caused a decrease of muscle mass of (45%). In addition, muscle atrophy can affect specific fiber types, involving predominantly slow type 1 or fast type 2 muscle fibers (slow-to-fast or fast-to-slow fiber type shift)⁵⁷. Age related muscle wasting (sarcopenia) induces a fast-to-slow fibertype shift^{58,59}. Spinal cord injury patients on the other hand experience a type 1 fiber atrophy with a slow-to-fast fiber type shift due to disuse⁶⁰. In the present study a significant upregulation of myosin heavy chain IIA and myosin heavy chain Ix expression was demonstrated, while MHC I was unchanged and MHC IIb was downregulated (Fig. 7). These results indicate that BoNT/A injections cause a slow-to-fast fibertype shift due to upregulation of fast fiber type expression rather than due to atrophy of type 1 fibers. This might be a compensatory process in order to compensate for a significant loss of muscle force and mass after BoNT/A injections which has been observed previously after a single injection of 100 µL of BoNT/A of 6.0 units/kg⁶¹. However, the present findings are in contrast to previous findings showing that BoNT/A injection in the gastrocnemius muscle of rats caused a fast-to-slow fibertype shift when rats received either 3,6,12 or 18 UI of BoNT/A¹⁸. These contradictory findings may be explained by the difference in how long after the BoNT/A injection the tissue was analyzed. The present findings reflect the early regeneration phase (3 weeks after injury), while the study by Dodd *et al.* demonstrates the long term effect of the damage after BoNT/A injection¹⁸. Furthermore, the present study investigated mRNA levels only. To clarify whether BoNT/A injections cause a fibertype shift both short- and longterm should rather be investigated using proper fibertyping methods, than mRNA expression only. In addition Fig. 3 shows qualitative transectional images of the microstructure of the muscle, and makes the effect of BoNT/A visible by eye showing that the muscle fibers in the BoNT/A injected leg are smaller and appear with blurred edges, indicating muscle atrophy of all present muscle fibers. By using Synchrotron Radiation X-ray Tomographic Microscopy (SRXTM) the present study revealed that the microstructure of skeletal muscle tissue was significantly damaged three weeks after a single injection of BoNT/A in rats. However, whether repeated injections would lead to even further damage needs further investigations.

Whether repeated injections of BoNT/A might have unwanted and irreversible effects is still unclear for several different treatments. There are to date unfortunately only few studies that have examined the effects on the muscle tissue after repeated injections. However, Minamoto *et al.* investigated the effect of repeated BoNT/A injections into the tibialis anterior muscle in rats and observed that a single injection of BoNT/A caused a 50% decrease of muscle torque, while a second injection of botox decreased the muscle torque to 95% when compared to the pre injection level⁶¹. The authors concluded that a second BoNT/A injection caused a profound and persistent loss in muscle function and altered muscle structure⁶¹. Unwanted side effects have also been reported in cosmetic medicine where cumulative and repeated injections into the masseter muscle for lower face contouring can cause different adverse effects including difficulty chewing, speech disturbances and muscle fatigue³¹.

In addition, the loss of bodyweight after BoNT/A injections might also be characterized as an unwanted side effect. In the present study, when the body weight of the rats that were injected with BoNT/A was compared with the bodyweight of healthy untreated control rats, it was observed that the body weight was significantly lower in the BoNT/A rats one week after the botox injection until the end of the protocol (Fig. 8). This indicates that a high dose of BoNT/A affects the bodyweight development of the rats, which might reflect an inhibited growth of the rats. Whether this is only experienced after injection of a high dose BoNT/A is unknown, but it is possible that a high dose of BoNT/A injection causes systemic effects which are reflected by the body weight of the rats. However, there is increasing evidence that BoNT/A inhibits growth both in rats and in humans^{32,62,63}. Gough *et al.* has previously claimed that BoNT/A injections inhibit muscle growth⁶⁴. In addition, it has been shown that the skeletal muscle tissue in rabbits did not fully recover six month post injection (3.5 UI/kg)⁶⁵. When translating this finding into human years this would mean that the skeletal muscle tissue has not fully recovered 16 years after injection. However, there is no infallible mathematical formula to calculate the human age of a rabbit because its growth and physiological changes during its life are very different from the development seen in humans. And the existing age equivalence charts are usually based on observations of ages of rabbits from veterinarians. Nevertheless, the finding that high dose BoNT/A injections affect both bodyweight development, microstructure of the muscle and has an influence on the gait pattern of rats, raises a series of questions towards the rationale of BoNT/A as a treatment against muscle contractures.

One major limitation of the present study is that the synchrotron data are only analysed at one single time-point (3 weeks post BoNT/A injection). This limits the ability to draw any major conclusions regarding the use of BoNT/A, since we cannot rule out that all the effects we observe here are fully reversible. Thus, long-term observations at several time-points are necessary in order to elucidate the recovery of the muscle tissue following BoNT/A injections. Furthermore, this study only reflects effects on the muscle tissue after one single injection. Future studies should investigate whether additional injections cause additive damage to the microstructure and the tissue. Another important issue in the present study is the fact that the injection volume is quite high (100 μ l) compared to other studies where only 20 μ l injection volume has been used⁶⁶. The high injection volume has certainly produced some edema within the muscle tissue. However, the contralateral leg was injected with 100 μ l saline as well and showed no signs of muscle damage 3 weeks after injection. However, it should be remembered that a high injection volume might increase the risk of systemic effects due to unintended spread of BoNT/A. One previous study has shown that high dose injections of botulinum toxin caused sporadic SNAP25 expression in distal muscles of rats indicating systemic spread but without evidence of transcytosis (dose: 20 μ l of BoNT/A (3, 10, 30 U/kg)⁶⁷. Unfortunately we were not able to investigate whether there was any systemic spread of BoNT/A in the present rats. However, it is possible that the high dose of BoNT/A injection and the high injection volume used in the present study might have caused systemic effects. These might be reflected by the reduced increase of body weight in the rats. On the other hand, the reduced increase of body weight in the BoNT/A injected rats may also be explained by reduced mobility of the rat due to the impaired muscle function caused by the local effect of the injection, but we cannot exclude that it may also be related to a systemic effect of the injection, although there were no visible signs of this.

The rats of present study did not lose much bodyweight; they rather showed a reduction of growth, unlike the animals used in the pilot study (Supplementary Material Figure 1). This difference in weight loss might be due to differences in age and baseline bodyweight. Unlike the rats that were used in the pilot study (Supplementary Material Figure 1) the rats from the present protocol were still growing, and this process might have counteracted the weight loss that was induced by the high dose BoNT/A injections.

Conclusion

The present study leads to serious concerns regarding BoNT/A treatment because of the significant effect it has on the micro structure of the muscle tissue and tissue organization. Furthermore the results of the present study highlight that it is possible that intramuscular high dose BoNT/A injections might cause unwanted side effects such as muscle atrophy, and fatigue which causes an extensive remodeling process in the muscle tissue. The present findings indicate that high dose BoNT/A injections causes damage of the microstructure of the muscle tissue. Furthermore the present study shows that the physical capabilities are significantly reduced and the gait is significantly compromised 3 weeks after a high dose BoNT/A injection into the calf.

Materials and Methods

Animals. All experiments were conducted in accordance with the guidelines of EU Directive 2010/63/EU and were approved by the Danish Animal Experiments Inspectorate. 23 samples in the form of male Sprague Dawley rats (weight: 360 g) were used for the present experiment (n = 4 pilot gait analysis and clinical score (Baseline + 21 days post injection); n = 8 gait analysis and clinical score (21 days), n = 8 gene expression analysis and volume fraction (21 days post injection), n = 1 sham injection (Saline) gene expression normalization, and n = 2 control rats for body weight assessment. The rats were caged two by two (2 rats in each cage) in a 12/12 light dark cycle with access to water and food ad libitum. All recommended procedures for safe and proper handling, storage and preparation for experimental use, and disposal of Botulinum Toxin were complied. (https://www.cdc.gov/biosafety/publications/bmbl5/bmbl5_sect_viii_g.pdf). The entire medial gastrocnemius (including the injection site) of the muscle was dissected and harvested 21 days after BoNT/A injection and was used for gene expression analyses and volume fraction measurements. The tissue was harvested while the animals were anesthetized by 2% isoflurane. After the harvest the animals were euthanized using pentobarbital injections into the heart while the animals still were under anesthesia (2% isoflurane).

Gait pattern analysis. The paws of both hind limbs of the rats were dipped in ink on a stamp pad. Then they were put down on a piece of graph paper and run through a plastic tunnel into a dark box. This procedure was then repeated three times. All paper strips were digitalized and analyzed using ImageJ (<http://imagej.net/Welcome> University of Wisconsin-Madison). The measurements of stride length, foot angle and foot length was done as indicated in Fig. 5.

Tissue preparation. The rats were anesthetized by 2% isoflurane. The medial gastrocnemius was removed and dissected into smaller pieces with a scalpel (Swann-Morton, Mediq danmark A/S). The wet weight of the triceps surae was measured immediately after removal. One piece of the medial gastrocnemius was snap frozen in liquid nitrogen and stored at -80°C for further PCR analysis. Another piece was fixed in Bouin's fluid for 24 h and kept at 4°C in 1.5 ml Eppendorf tubes. The tissue were then transferred into fresh tubes with 96% ETOH and remained at 4°C until subsequently analysis.

The Clinical score assessment and gait analysis were conducted in four rats in a pilot study where baseline measurements and 21 days post measurements were obtained (Fig. 6). Subsequently eight rats were followed closely for 21 days and the clinical score and gait analysis was assessed every second day to monitor the acute effects over time after BoNT/A injection (Fig. 6).

Injections. In order to test the dosage and injection volume a pilot study was conducted to test the optimal dosage (The optimal dose was defined as the smallest dose that would cause the desired effect of muscle atrophy, without causing any distress for the animals) (Results shown in Supplementary Material Figure 1). All animals

Gene	Sense	Anti sense	P-values
<i>RPLP0</i>	AGGGTCTGGCTTTGTCTGTGG	AGTGCAGGAGCAGCAGTGG	<0.001*
<i>GAPDH</i>	CCATTCTTCCACCTTTGATGCT	TGTTGCTGTAGCCATATTCATTGT	<0.001*
<i>Col1A1</i>	ATCAGCCCAAACCCCAAGGAGA	CGCAGGAAGGTCAGCTGGATAG	0.006*
<i>Col3A1</i>	TGATGGGATCCAATGAGGGAGA	GAGTCTCATGGCCTTGCGTGTFT	0.059
<i>DCN</i>	CACTCCAGGAGCTTCGACTCCAC	AGTGGGTTGCCGCCAGTTC	0.131
<i>FMOD</i>	CCGTCAACACCACTGGAGAA	CGTGCAGAACTGCTGATGGAGA	0.262
<i>FNI</i>	GGGCTTTGGCAGTGGTCATTT	CTCATCCGCTGGCCATTTTCTC	0.055
<i>GLUT4</i>	CTTCATCGTTGGCATGGGTTC	CAAATGTCCGGCCTCTGGTTTC	0.594
<i>Iga7</i>	GCTGAGAAGAGAAACGTGAC	GTAGAGTGGCAGCTGAATA	0.135
<i>Prep</i>	CACCTGTACTCAACAACAATA	GAAGTCATGGAAGGCCACTA	0.142
<i>IL6</i>	GACAAAGCCAGAGTCATTCAGAGCA	GAGCATTGGAAGTTGGGGTAGGA	<0.001*
<i>MMP2</i>	CTGGGTTTACCCCTGATGTCC	AACCGGGTCCATTTTCTCTTT	0.017*
<i>TGFb1</i>	CCCCTGGAAAGGGCTCAACAC	TCCAACCAGGTCTCTCTAAAGTC	0.046*
<i>MHC1b</i>	ATTGCCGAGTCCCAGGTCAACA	GCTCCAGGTCTCAGGGCTTCAC	0.161
<i>MHCIIA</i>	GAAGAGCCGCGAGGTTACACAC	GGGACATGACCAAGGCTTCACA	<0.001*
<i>MHCIIIB</i>	GCCGAGTCCCAGGTCAACAAG	TGTGATTCTTCTGTACCTTTCAAC	<0.001*
<i>MHCIIIX</i>	GCCGAGTCCCAGGTCAACA	CTCATCTCTTGGTCACTTTCTCTGCT	0.042*

Table 1. PCR primers.

were anesthetized with 2% isoflurane. Both hind limbs were shaved, and the skin was disinfected. Then a high dose of BoNT/A was injected (1 BoNT/A Unit = 10 picogram). The present high dose injection was 6 UI in total (6 UI = 60 pg in total) and (2 UI = 20 pg per 100 μ l saline was injected per muscle head (Botulinum-toxin A (BoNT/A[®] Allergan INC. Irvine CA)) of was injected into the triceps surae (medial gastrocnemius, the lateral gastrocnemius and soleus) muscle using a 0.5 ml syringe (Omnican[®] 20 BRAUN, Germany), and 100 μ l saline was injected per muscle head in the contralateral control leg. Each rat thereby received a total of 300 μ l and 6UI of BoNT/A. Until termination of the experiment the welfare of the rats were routinely checked (e.g. for signs of dehydrations or distress). The rats were weighed every day following the injection in order to monitor weight loss. When any weight loss occurred the rats got 5 ml subcutaneous saline injections twice a day until the body weight was regained. The rats used in Clinical locomotion score assessment: The clinical evaluation system by (Malmsten 1983) was used to estimate the time course of improvement of motor performance in the hind limbs following BoNT/A injections⁶⁸. The animals were tested at the following timepoints: 2 days pre injection and 2 days, 4 days, 7 days, 14 days and 21 days post injection. This is a system which scores the movement ability on a scale from 1 to 8 (1: no active movements of the limb, 2: few involuntary movements when handling the animal, 3: few uncontrolled gait movements with long breaks, 4: leg is used for locomotion without control, 5: leg is used for locomotion with little control, 6: leg is used for locomotion with increasing control, 7: Abnormal movements are only seen during close observation, 8: normal gait). The animals are observed while they walk voluntarily around in their cages for approx 3 minutes, and the same observer rates the clinical score from 1 to 8.

RNA extraction and real time-PCR analysis. Total RNA isolation: Total RNA was extracted from frozen muscle samples from n = 8 BoNT/A rats by using 1 ml of TRI Reagent (Molecular Research Centre, Cincinnati, OH) 5 steel beads (2.3 mm) and 1 silica bead (1.0 mm Silicon Carbide Beads (454 grams) BioSpec Products Inc.). Extracted RNA was precipitated from the aqueous phase with isopropanol and was washed with ethanol (75%), dried and suspended in 10 μ l of nuclease-free water. The RNA concentration was determined using a RiboGreen RNA Quantitation kit 200–2000 Assays, Molecular Probes USA. RNA quality was determined on the basis of a RNA 6000 nano Chip assay kit, Agilent Technologies, Germany. The RNA samples were stored frozen at –20 °C until subsequent use in real-time RT-PCR procedures. To test the quality of the extracted RNA an electrophoresis in an agarose gel was made. The RNA quality was suggested to be satisfactory for further analysis.

cDNA synthesis. 150 ng RNA was reverse transcribed for each muscle sample in a total volume of 20 μ l by using the Qiagen Omniscript RT Kit at 37 °C for 1 hour followed by 70 °C for 15 minutes. The resulting cDNA was diluted twenty times in dilution buffer (10 mM Tris EDTA buffer: Sigma Germany) + Salmon Testes DNA (1 ng/ μ l; Sigma Germany), and samples were stored at –20 °C until used in the PCR reactions for specific mRNA analysis.

Polymerase Chain Reaction. The Real-time PCR-method using Glyceraldehyde 3-phosphate dehydrogenase (GAPDH) and 60S acidic ribosomal protein P0 (RPLP0) as reference genes to study specific mRNAs of interest was applied. However, since both reference genes were significantly affected of the BoNT/A injections, all data were normalized to the median values of the control samples of all animals. The primers were purchased from MWG Biotech. For each target cDNA the PCR reactions were carried out under identical conditions by using 5 μ l diluted cDNA in a total volume of 25 μ l QuantiTect SYBR Green PCR Mix (Qiagen) and 100 nM of each primer (Table 1). The amplification was monitored in real-time using a MX3005 P real-time PCR machine (Stratagene, CA). The threshold cycle (C_t) values were related to a standard curve made with cloned PCR products

to determine the relative difference between the unknown samples, accounting for the PCR efficiency. The specificity of the PCR reaction was confirmed by melting curve analysis after amplification. The real-time PCR conditions were as follows: to denature the DNA strands the reaction mix was heated above the melting temperature of DNA (95 °C) for 10 minutes, followed by 50 cycles each of 15 seconds at 95 °C, followed by the annealing step where optimal primer hybridization conditions were obtained by lowering the temperature to 58 °C for 30 seconds, and the extension step, where the reaction mix was heated to 63 °C for 90 seconds.

Synchrotron radiation x-ray tomographic microscopy (SRXTM). The SRXTM measurements were carried out at the TOMCAT (TOMographic Microscopy and Coherent rAdiology experimenTs) beamline at the Swiss Light Source⁶⁹. The X-ray source is a superbending magnet radiation source located 25 m from the sample. A double crystal multilayer monochromator was placed 7 m downstream of the source to extract monochromatic X-ray photons at 25 keV. The detector system consisted of a 100 µm thick, Ce-doped LuAG (Lutetium Aluminum Garnet) scintillator which converted the transmitted X-rays into visible light, a high numerical-aperture microscope which gave a 20 fold magnification, and a pco.edge5.5 16-bit CMOS (Complementary metal-oxide-semiconductor) based camera to record the images. The resulting field-of-view (FoV) was 0.832 mm × 0.702 mm (width × height), and the effective pixel size was 325 nm. Muscle biopsies were placed in a 96% ETOH buffer in a small 0.2 ml Eppendorf tube and soldered to a holder with beeswax. The sample was placed 63 mm in front of the scintillator. Since the sample was larger than the FoV, local tomographic measurements were conducted by collecting 1501 projections of 600 ms exposure time over a 180 degree rotation. Flat-beam images (i.e., images taken with no sample) and dark images (i.e., images taken with no beam) were obtained in order to correct the projections. The total measuring time for all 21 samples took about 24 hours including sample mounting.

The 63 mm distance between sample and detector, combined with an effective pixel size of 325 nm, lead to refraction-induced intensity effects in the images. In order to account for this, refraction corrections were performed in using a local implementation at TOMCAT of a single image first order refraction correction algorithm. The algorithm used the Paganin approach with the assumption that the object consisted of a homogeneous soft tissue material and that the propagation distance was sufficiently short for the transport-of-intensity-equation to apply³⁰. For tomographic reconstruction, a filtered back-projection based algorithm was applied.

Image analysis. The background of the slices in the reconstructed tomogram suffered from a low-frequency bias-field. A correction was applied by first subtracting a constant plane and then subtracting a linear radial profile. The two correction functions were found by applying a least-squares fit to the mean of the tomogram stack slices.

For segmentation into a non-fibrillar and fibrillar phase, an alpha-level Markov random field (MRF) segmentation was applied to the tomograms as described by Pedersen *et al.*⁷⁰. First, the data was modeled as a mixture of distribution functions by assigning a probability distribution to each phase. After assigning probability distributions, the spatial information of the data was incorporated into the segmentation process by modeling the data as an isotropic MRF⁷¹. The MRF smoothing parameter was set to 0.5. To find the optimal segmentation solution the multi-labeling problem was solved using graph cuts with alpha expansions as described in Boykov *et al.*⁷².

BoNT/A is expected to alter the microstructural tissue of the muscle and changes the fibrillary organization. This is evident from Fig. 1, where typical images are shown. Clearly, the ratio between the non-fibrillar and fibrillar structure is change significantly which indicates muscle atrophy and tissue damage. Furthermore, the anisotropy in the tissue structure is altered (3 weeks post BoNT/A injection, when compared to the contralateral control leg). In order to quantify these changes we have evaluated the tomograms.

Volume fraction (percent object volume). The tomograms visualize the muscle tissue around the injection site. From the segmented tomograms (3 weeks post BoNT/A injection, when compared to the contralateral control leg), volume fractions for the identified non-fibrillar and fibrillar phases were calculated as the percent object volume (POV) values. Image analysis as well as visualization of the tomograms was performed using custom made software implemented in MATLAB (Mathworks, Inc., Natick, MA).

Anisotropy. The anisotropy analysis was performed 3 weeks post BoNT/A injection, and compared to the contralateral control leg, with a star length distribution (SLD) analysis using the Quant3D software as described elsewhere^{73,74}. A volume of interest (VOI) from the non-fibrillar segmentation was used as an input to the SLD in Quant3D. For the orientation parameters, a uniform setting with 513 orientations, random rotations, and dense vectors were applied using 10,000 random points for calculating the SLD. The SLD analysis produces a number of anisotropic descriptors as described in⁶⁸. As a measure of the orientation of the non-fibrillar tissue, the isotropy index was used. A value of one reflects a completely isotropic structure whilst zero reflects an anisotropic one. An assumption for the anisotropy analysis is that all the connected non-fibrillar tissue has been identified in the segmentation of the tomograms. Since the segmentation can have difficulties for samples with a very low non-fibrillar volume fraction, a lower threshold of 5% has been set. Two samples with a volume fraction below this threshold were excluded.

Data availability. Due to the enormous amount of data, the datasets generated during and/or analysed during the current study are available from the corresponding author on reasonable request.

Statistics. All data are presented as Mean ± SEM. Level of significance was set at 5% ($p < 0.05$).

Clinical score. Changes in the clinical score from the second pre-test to the seventh post-test were investigated using an ANCOVA for repeated measures with time as an independent factor and the first pre-test value as a covariate. In case of significant main effect, a post hoc test was applied with Tukey correction for multiple comparisons. Gait analysis: Changes from the second pre-test to the fourth post-test in gait function measures (stride

length, foot angle and foot length) were investigated using an ANCOVA for repeated measures with time and leg (BoNT/A leg and non BoNT/A leg) as independent factors and an interaction of time and leg. The first pre-test value was set as a covariate. In case of a significant main effect, a post hoc test was applied with Tukey correction for multiple comparisons. Volume fraction and anisotropy: Volume fraction and anisotropy was analyzed using a paired Students T-Test. Gene expression: Changes in gene expression between the BoNT/A leg and the control leg were investigated using a 2-Way ANOVA analysis with gene targets and leg (BoNT/A leg and control leg) as independent factors and an interaction of gene targets and leg. In case of a significant main effect, a post hoc test was applied with Tukey correction for multiple comparisons. All p-values from the post hoc tests are shown in Table 1. Changes in the development of body weight were investigated using a 2-Way ANOVA analysis with treatment and time as independent factors and an interaction of treatment and time. All PCR data are presented as the geo mean \pm backtransformed SEM. Statistics software: Statistical calculations for gait analysis and the clinical score were performed in SAS Enterprise Guide (SAS Institute Inc. NC, USA 2015, version 7.11). The statistical calculations for changes in gene expressions and volume fraction were performed in Sigma Plot (Systat Software Inc. USA, version 12.5). Figures 1, 4 and 6 were generated in graphpad Prism 6.04 (GraphPad Software, Inc. CA, USA).

References

- Swaminathan, S. & Eswaramoorthy, S. Structural analysis of the catalytic and binding sites of Clostridium botulinum neurotoxin B. *Nature structural biology* **7**, 693–699 (2000).
- Lalli, G., Bohnert, S., Deinhardt, K., Verastegui, C. & Schiavo, G. The journey of tetanus and botulinum neurotoxins in neurons. *Trends in microbiology* **11**, 431–437 (2003).
- Arnon, S. S. *et al.* Botulinum toxin as a biological weapon: medical and public health management. *JAMA* **285**, 1059–1070 (2001).
- Scott, A. B. Botulinum toxin injection of eye muscles to correct strabismus. *Transactions of the American Ophthalmological Society* **79**, 734–770 (1981).
- Camargo, C. H., Cattai, L. & Teive, H. A. Pain Relief in Cervical Dystonia with Botulinum Toxin Treatment. *Toxins* **7**, 2321–2335, <https://doi.org/10.3390/toxins7062321> (2015).
- Dashtipour, K., Chen, J. J., Frei, K., Nahab, F. & Tagliati, M. Systematic Literature Review of AbobotulinumtoxinA in Clinical Trials for Blepharospasm and Hemifacial Spasm. *Tremor and other hyperkinetic movements (New York, N.Y.)* **5**, 338, <https://doi.org/10.7916/d8cj8cvr> (2015).
- Hsieh, P. F., Chiu, H. C., Chen, K. C., Chang, C. H. & Chou, E. C. Botulinum toxin A for the Treatment of Overactive Bladder. *Toxins* **8**, <https://doi.org/10.3390/toxins8030059> (2016).
- Dat, A. *et al.* Botulinum toxin therapy for chronic anal fissures: where are we at currently? *ANZ journal of surgery*. <https://doi.org/10.1111/ans.13329> (2015).
- Simpson, D. M. *et al.* Assessment: Botulinum neurotoxin for the treatment of movement disorders (an evidence-based review): report of the Therapeutics and Technology Assessment Subcommittee of the American Academy of Neurology. *Neurology* **70**, 1699–1706, <https://doi.org/10.1212/01.wnl.0000311389.26145.95> (2008).
- Balaban, B., Tok, F., Tan, A. K. & Matthews, D. J. Botulinum toxin a treatment in children with cerebral palsy: its effects on walking and energy expenditure. *American journal of physical medicine & rehabilitation/Association of Academic Physiatrists* **91**, 53–64, <https://doi.org/10.1097/PHM.0b013e31823caae1> (2012).
- Schaefer, S. M., Gottschalk, C. H. & Jabbari, B. Treatment of Chronic Migraine with Focus on Botulinum Neurotoxins. *Toxins* **7**, 2615–2628, <https://doi.org/10.3390/toxins7072615> (2015).
- Magid, M. *et al.* Treatment of major depressive disorder using botulinum toxin A: a 24-week randomized, double-blind, placebo-controlled study. *The Journal of clinical psychiatry* **75**, 837–844, <https://doi.org/10.4088/JCP.13m08845> (2014).
- Carruthers, J. & Carruthers, A. Botulinum toxin in facial rejuvenation: an update. *Dermatologic clinics* **27**, 417–425, v, <https://doi.org/10.1016/j.det.2009.08.001> (2009).
- El-Domyati, M. *et al.* The use of Botulinum toxin-a injection for facial wrinkles: a histological and immunohistochemical evaluation. *Journal of cosmetic dermatology* **14**, 140–144, <https://doi.org/10.1111/jocd.12144> (2015).
- Cosmetic Surgery National Data Bank Statistics. *Aesthetic surgery journal* **36** Suppl 1, 1–29, https://doi.org/10.1093/asj/36.Supplement_1.1 (2016).
- Nigam, P. K. & Nigam, A. Botulinum toxin. *Indian journal of dermatology* **55**, 8–14, <https://doi.org/10.4103/0019-5154.60343> (2010).
- Blasi, J. *et al.* Botulinum neurotoxin A selectively cleaves the synaptic protein SNAP-25. *Nature* **365**, 160–163, <https://doi.org/10.1038/365160a0> (1993).
- Dodd, S. L., Selsby, J., Payne, A., Judge, A. & Dott, C. Botulinum neurotoxin type A causes shifts in myosin heavy chain composition in muscle. *Toxicon: official journal of the International Society on Toxinology* **46**, 196–203, <https://doi.org/10.1016/j.toxicon.2005.03.022> (2005).
- Dressler, D., Saberi, F. A. & Barbosa, E. R. Botulinum toxin: mechanisms of action. *Arquivos de neuro-psiquiatria* **63**, 180–185, doi: S0004-282x2005000100035 (2005).
- Hastings-Ison, T. & Graham, H. K. Atrophy and hypertrophy following injections of botulinum toxin in children with cerebral palsy. *Developmental medicine and child neurology* **55**, 778–779, <https://doi.org/10.1111/dmcn.12231> (2013).
- Williams, S. A., Reid, S., Elliott, C., Shipman, P. & Valentine, J. Muscle volume alterations in spastic muscles immediately following botulinum toxin type-A treatment in children with cerebral palsy. *Developmental medicine and child neurology* **55**, 813–820, <https://doi.org/10.1111/dmcn.12200> (2013).
- Borodic, G. E., Ferrante, R., Pearce, L. B. & Smith, K. Histologic assessment of dose-related diffusion and muscle fiber response after therapeutic botulinum A toxin injections. *Movement disorders: official journal of the Movement Disorder Society* **9**, 31–39, <https://doi.org/10.1002/mds.870090106> (1994).
- Han, N. *et al.* Proteomic changes in rat gastrocnemius muscle after botulinum toxin a injection. *Annals of rehabilitation medicine* **37**, 157–166, <https://doi.org/10.5535/arm.2013.37.2.157> (2013).
- Thacker, B. E. *et al.* Passive mechanical properties and related proteins change with botulinum neurotoxin A injection of normal skeletal muscle. *Journal of orthopaedic research: official publication of the Orthopaedic Research Society* **30**, 497–502, <https://doi.org/10.1002/jor.21533> (2012).
- Bravin, A., Coan, P. & Suortti, P. X-ray phase-contrast imaging: from pre-clinical applications towards clinics. *Physics in medicine and biology* **58**, R1–35, <https://doi.org/10.1088/0031-9155/58/1/r1> (2013).
- Zhou, S. A. & Brahme, A. Development of phase-contrast X-ray imaging techniques and potential medical applications. *Physica medica: PM: an international journal devoted to the applications of physics to medicine and biology: official journal of the Italian Association of Biomedical Physics (AIFB)* **24**, 129–148, <https://doi.org/10.1016/j.ejmp.2008.05.006> (2008).

27. Marinescu, M. *et al.* Synchrotron radiation X-ray phase micro-computed tomography as a new method to detect iron oxide nanoparticles in the brain. *Molecular imaging and biology: MIB: the official publication of the Academy of Molecular Imaging* **15**, 552–559, <https://doi.org/10.1007/s11307-013-0639-6> (2013).
28. Jian, J. *et al.* Visualization of microvasculature and thrombi by X-ray phase-contrast computed tomography in hepatocellular carcinoma. *Journal of synchrotron radiation* **23**, 600–605, <https://doi.org/10.1107/S1600577516001016> (2016).
29. Grandl, S. *et al.* Evaluation of phase-contrast CT of breast tissue at conventional X-ray sources - presentation of selected findings. *Zeitschrift fur medizinische Physik* **23**, 212–221, <https://doi.org/10.1016/j.zemedi.2013.02.005> (2013).
30. Paganin, D., Mayo, S. C., Gureyev, T. E., Miller, P. R. & Wilkins, S. W. Simultaneous phase and amplitude extraction from a single defocused image of a homogeneous object. *Journal of microscopy* **206**, 33–40 (2002).
31. Durand, P. D. *et al.* Botulinum Toxin and Muscle Atrophy: A Wanted or Unwanted Effect. *Aesthetic surgery journal* **36**, 482–487, <https://doi.org/10.1093/asj/sjv208> (2016).
32. Gough, M. Does botulinum toxin prevent or promote deformity in children with cerebral palsy? *Developmental medicine and child neurology* **51**, 89–90, <https://doi.org/10.1111/j.1469-8749.2008.03247.x> (2009).
33. Pingel, J., Wienecke, J., Lorentzen, J. & Nielsen, J. B. Botulinum toxin injection causes hyperreflexia and increased muscle stiffness of the triceps surae muscle in the rat. *Journal of neurophysiology*, in 00452 02016, <https://doi.org/10.1152/jn.00452.2016> (2016).
34. Barber, L. *et al.* The effects of botulinum toxin injection frequency on calf muscle growth in young children with spastic cerebral palsy: a 12-month prospective study. *Journal of children's orthopaedics* **7**, 425–433, <https://doi.org/10.1007/s11832-013-0503-x> (2013).
35. Mukund, K. *et al.* Systems analysis of transcriptional data provides insights into muscle's biological response to botulinum toxin. *Muscle & nerve* **50**, 744–758, <https://doi.org/10.1002/mus.24211> (2014).
36. Tagerud, S., Libelius, R. & Thesleff, S. Effects of botulinum toxin induced muscle paralysis on endocytosis and lysosomal enzyme activities in mouse skeletal muscle. *Pflugers Archiv: European journal of physiology* **407**, 275–278 (1986).
37. Choi, W. H. *et al.* Skeletal muscle atrophy induced by intramuscular repeated dose of botulinum toxin type A in rats. *Drug and chemical toxicology* **30**, 217–227, <https://doi.org/10.1080/01480540701375091> (2007).
38. O'Flaherty, S. J., Janakan, V., Morrow, A. M., Scheinberg, A. M. & Waugh, M. C. Adverse events and health status following botulinum toxin type A injections in children with cerebral palsy. *Developmental medicine and child neurology* **53**, 125–130, <https://doi.org/10.1111/j.1469-8749.2010.03814.x> (2011).
39. Carraro, E., Trevisi, E. & Martinuzzi, A. Safety profile of incobotulinum toxin A [Xeomin((R))] in gastrocnemius muscles injections in children with cerebral palsy: Randomized double-blind clinical trial. *European journal of paediatric neurology: EJPN: official journal of the European Paediatric Neurology Society* **20**, 532–537, <https://doi.org/10.1016/j.ejpn.2016.04.008> (2016).
40. Papavasiliou, A. S. *et al.* Safety of botulinum toxin A in children and adolescents with cerebral palsy in a pragmatic setting. *Toxins* **5**, 524–536, <https://doi.org/10.3390/toxins5030524> (2013).
41. Blaszczyk, I., Foumani, N. P., Ljungberg, C. & Wiberg, M. Questionnaire about the adverse events and side effects following botulinum toxin A treatment in patients with cerebral palsy. *Toxins* **7**, 4645–4654, <https://doi.org/10.3390/toxins7114645> (2015).
42. Cosgrove, A. P., Corry, I. S. & Graham, H. K. Botulinum toxin in the management of the lower limb in cerebral palsy. *Developmental medicine and child neurology* **36**, 386–396 (1994).
43. Ozawa, J. *et al.* Interaction between gastrocnemius muscle weakness and moderate exercise deteriorates joint integrity in rat knee. *Scandinavian journal of medicine & science in sports* **25**, e11–19, <https://doi.org/10.1111/sms.12195> (2015).
44. Schroeder, A. S., Koerte, I., Berweck, S., Ertl-Wagner, B. & Heinen, F. How doctors think—and treat with botulinum toxin. *Developmental medicine and child neurology* **52**, 875–876, <https://doi.org/10.1111/j.1469-8749.2010.03692.x> (2010).
45. Eames, N. W. *et al.* The effect of botulinum toxin A on gastrocnemius length: magnitude and duration of response. *Developmental medicine and child neurology* **41**, 226–232 (1999).
46. Ross, S. A. & Engsberg, J. R. Relationships between spasticity, strength, gait, and the GMFM-66 in persons with spastic diplegia cerebral palsy. *Archives of physical medicine and rehabilitation* **88**, 1114–1120, <https://doi.org/10.1016/j.apmr.2007.06.011> (2007).
47. Hurme, T., Kalimo, H., Sandberg, M., Lehto, M. & Vuorio, E. Localization of type I and III collagen and fibronectin production in injured gastrocnemius muscle. *Laboratory investigation; a journal of technical methods and pathology* **64**, 76–84 (1991).
48. Ahtikoski, A. M., Koskinen, S. O., Virtanen, P., Kovanen, V. & Takala, T. E. Regulation of synthesis of fibrillar collagens in rat skeletal muscle during immobilization in shortened and lengthened positions. *Acta physiologica Scandinavica* **172**, 131–140, <https://doi.org/10.1046/j.1365-201X.2001.00848.x> (2001).
49. Pedersen, B. K. IL-6 signalling in exercise and disease. *Biochemical Society transactions* **35**, 1295–1297, <https://doi.org/10.1042/bst0351295> (2007).
50. Ugalde, I., Christiansen, S. P. & McLoon, L. K. Botulinum toxin treatment of extraocular muscles in rabbits results in increased myofiber remodeling. *Investigative ophthalmology & visual science* **46**, 4114–4120, <https://doi.org/10.1167/iovs.05-0549> (2005).
51. Snijders, T. *et al.* Satellite cells in human skeletal muscle plasticity. *Frontiers in physiology* **6**, <https://doi.org/10.3389/fphys.2015.00283> (2015).
52. Yablonska-Reuveni, Z. The Skeletal Muscle Satellite Cell: Still Young and Fascinating at 50. *Journal of Histochemistry and Cytochemistry* **59**, 1041–1059, <https://doi.org/10.1369/0022155411426780> (2011).
53. Lepper, C., Partridge, T. A. & Fan, C. M. An absolute requirement for Pax7-positive satellite cells in acute injury-induced skeletal muscle regeneration. *Development (Cambridge, England)* **138**, 3639–3646, <https://doi.org/10.1242/dev.067595> (2011).
54. McCarthy, J. J. *et al.* Effective fiber hypertrophy in satellite cell-depleted skeletal muscle. *Development (Cambridge, England)* **138**, 3657–3666, <https://doi.org/10.1242/dev.068858> (2011).
55. Murphy, M. M., Lawson, J. A., Mathew, S. J., Hutcheson, D. A. & Kardon, G. Satellite cells, connective tissue fibroblasts and their interactions are crucial for muscle regeneration. *Development (Cambridge, England)* **138**, 3625–3637, <https://doi.org/10.1242/dev.064162> (2011).
56. Cohen, S., Nathan, J. A. & Goldberg, A. L. Muscle wasting in disease: molecular mechanisms and promising therapies. *Nature reviews. Drug discovery* **14**, 58–74, <https://doi.org/10.1038/nrd4467> (2015).
57. Cicilioti, S., Rossi, A. C., Dyar, K. A., Blaauw, B. & Schiaffino, S. Muscle type and fiber type specificity in muscle wasting. *The international journal of biochemistry & cell biology* **45**, 2191–2199, <https://doi.org/10.1016/j.biocel.2013.05.016> (2013).
58. Gannon, J., Doran, P., Kirwan, A. & Ohlendieck, K. Drastic increase of myosin light chain MLC-2 in senescent skeletal muscle indicates fast-to-slow fibre transition in sarcopenia of old age. *European journal of cell biology* **88**, 685–700, <https://doi.org/10.1016/j.ejcb.2009.06.004> (2009).
59. Verdijk, L. B. *et al.* Reduced satellite cell numbers with spinal cord injury and aging in humans. *Medicine and science in sports and exercise* **44**, 2322–2330, <https://doi.org/10.1249/MSS.0b013e3182667c2e> (2012).
60. Burnham, R. *et al.* Skeletal muscle fibre type transformation following spinal cord injury. *Spinal cord* **35**, 86–91 (1997).
61. Minamoto, V. B., Suzuki, K. P., Bremner, S. N., Lieber, R. L. & Ward, S. R. Dramatic changes in muscle contractile and structural properties after 2 botulinum toxin injections. *Muscle & nerve* **52**, 649–657, <https://doi.org/10.1002/mus.24576> (2015).
62. Gough, M., Fairhurst, C. & Shortland, A. P. Botulinum toxin and cerebral palsy: time for reflection? *Developmental medicine and child neurology* **47**, 709–712, <https://doi.org/10.1017/s0012162205001453> (2005).
63. Chen, C. M., Stott, N. S. & Smith, H. K. Effects of botulinum toxin A injection and exercise on the growth of juvenile rat gastrocnemius muscle. *Journal of applied physiology (Bethesda, Md.: 1985)* **93**, 1437–1447, <https://doi.org/10.1152/jappphysiol.00189.2002> (2002).

64. Gough, M. & Shortland, A. P. Could muscle deformity in children with spastic cerebral palsy be related to an impairment of muscle growth and altered adaptation? *Developmental medicine and child neurology* **54**, 495–499, <https://doi.org/10.1111/j.1469-8749.2012.04229.x> (2012).
65. Fortuna, R., Vaz, M. A., Sawatsky, A., Hart, D. A. & Herzog, W. A clinically relevant BONT/A -A injection protocol leads to persistent weakness, contractile material loss, and an altered mRNA expression phenotype in rabbit quadriceps muscles. *Journal of biomechanics* **48**, 1700–1706, <https://doi.org/10.1016/j.jbiomech.2015.05.018> (2015).
66. Broide, R. S. *et al.* The rat Digit Abduction Score (DAS) assay: a physiological model for assessing botulinum neurotoxin-induced skeletal muscle paralysis. *Toxicon: official journal of the International Society on Toxinology* **71**, 18–24, <https://doi.org/10.1016/j.toxicon.2013.05.004> (2013).
67. Cai, B. B., Francis, J., Brin, M. F. & Broide, R. S. Botulinum neurotoxin type A-cleaved SNAP25 is confined to primary motor neurons and localized on the plasma membrane following intramuscular toxin injection. *Neuroscience* **352**, 155–169, <https://doi.org/10.1016/j.neuroscience.2017.03.049> (2017).
68. Malmsten, J. Time course of segmental reflex changes after chronic spinal cord hemisection in the rat. *Acta physiologica Scandinavica* **119**, 435–443, <https://doi.org/10.1111/j.1748-1716.1983.tb07359.x> (1983).
69. Stampanoni, M. *et al.* Tomographic Hard X-ray Phase Contrast Micro- and Nano-imaging at TOMCAT. *AIP Conference Proceedings* **1266**, 13–17, <https://doi.org/10.1063/1.3478189> (2010).
70. Pedersen, E. B. L. *et al.* Improving organic tandem solar cells based on water-processed nanoparticles by quantitative 3D nanoimaging. *Nanoscale* **7**, 13765–13774, <https://doi.org/10.1039/C5NR02824H> (2015).
71. Li, A. Z. *Markov Random Field Modeling in Image Analysis*. 3rd Edition edn (Springer, 2009).
72. Boykov, Y., Veksler, O. & Zabih, R. Fast Approximate Energy Minimization via Graph Cuts. *IEEE Trans. Pattern Anal. Mach. Intell.* **23**, 1222–1239, <https://doi.org/10.1109/34.969114> (2001).
73. Ketcham, R. A. & Ryan, T. M. Quantification and visualization of anisotropy in trabecular bone. *Journal of microscopy* **213**, 158–171 (2004).
74. Ryan, T. M. & Ketcham, R. A. The three-dimensional structure of trabecular bone in the femoral head of strepsirrhine primates. *Journal of human evolution* **43**, 1–26 (2002).

Acknowledgements

We thank Dr. Peter C. Raffalt for statistical advice and assistance. This project was funded by the Danish research Council (DFE-1333-00197), and the Elsass Foundation.

Author Contributions

All authors have contributed to this work and have approved the final version of the manuscript. All authors are designated as authors and are qualified for authorship, and are all listed as authors. Design and planning of the project: J.P., R.F., M.B., T.L. Applied for funding and ethical approval: J.P., J.B.N. Applied for Beam Time: J.P., R.F. Execution of rat experiments: J.P., I.T.A., T.A. Execution of synchrotron experiments: J.P., M.S.N., T.L., K.R., M.B., R.F. Execution of data and tissue analysis: J.P., M.S.N., T.A., I.T.A., T.L. Writing of the first draft of the manuscript: J.P. Correcting and improving the first draft of the manuscript: J.P., M.S.N., T.L., K.R., M.B., T.A., I.T.A., J.B.N., R.F.

Additional Information

Supplementary information accompanies this paper at <https://doi.org/10.1038/s41598-017-14997-3>.

Competing Interests: The authors declare that they have no competing interests.

Publisher's note: Springer Nature remains neutral with regard to jurisdictional claims in published maps and institutional affiliations.



Open Access This article is licensed under a Creative Commons Attribution 4.0 International License, which permits use, sharing, adaptation, distribution and reproduction in any medium or format, as long as you give appropriate credit to the original author(s) and the source, provide a link to the Creative Commons license, and indicate if changes were made. The images or other third party material in this article are included in the article's Creative Commons license, unless indicated otherwise in a credit line to the material. If material is not included in the article's Creative Commons license and your intended use is not permitted by statutory regulation or exceeds the permitted use, you will need to obtain permission directly from the copyright holder. To view a copy of this license, visit <http://creativecommons.org/licenses/by/4.0/>.

© The Author(s) 2017

Appendix B

Other publications

X-ray tomography using the full complex index of refraction

M S Nielsen¹, T Lauridsen¹, M Thomsen¹, T H Jensen¹, M Bech²,
L B Christensen³, E V Olsen³, M Hviid³, R Feidenhans¹ and F Pfeiffer²

¹ Niels Bohr Institute, University of Copenhagen, DK-2100 Copenhagen, Denmark

² Department of Physics and Institute for Medical Engineering, Technische Universität München, D-85748 Garching, Munich, Germany

³ Danish Meat Research Institute, Danish Technological Institute, DK-2630 Taastrup, Denmark

E-mail: schou@fys.ku.dk and robert@fys.ku.dk

Received 16 January 2012, in final form 12 July 2012

Published 11 September 2012

Online at stacks.iop.org/PMB/57/5971

Abstract

We report on x-ray tomography using the full complex index of refraction recorded with a grating-based x-ray phase-contrast setup. Combining simultaneous absorption and phase-contrast information, the distribution of the full complex index of refraction is determined and depicted in a bivariate graph. A simple multivariable threshold segmentation can be applied offering higher accuracy than with a single-variable threshold segmentation as well as new possibilities for the partial volume analysis and edge detection. It is particularly beneficial for low-contrast systems. In this paper, this concept is demonstrated by experimental results.

(Some figures may appear in colour only in the online journal)

1. Introduction

Since the development of x-ray computed tomography (CT), x-ray imaging has been used for studies of 3D structures by applying segmentation on the reconstructed tomograms, e.g., threshold segmentation using one or more threshold voxel values. However, for imaging biological tissues, consisting of low atom numbers, the limited absorption contrast makes this approach difficult and more advanced methods must be employed such as region-growing segmentation or edge-detection techniques together with image processing such as noise-reducing filters (Gonzalez and Woods 2008).

Recent advances in x-ray imaging have introduced new x-ray modalities such as phase-contrast imaging and dark-field imaging (Fitzgerald 2000, Momose 2005), which in many cases give an improved contrast in imaging biological tissue. One of the most recent techniques is grating-based interferometry (David *et al* 2002, Momose 2003, Weitkamp *et al* 2005), which can be adapted to laboratory-based setups (Pfeiffer *et al* 2006) and has already shown a potential for industrial applications (Kottler *et al* 2010). Grating-based interferometry has the advantage

that absorption, phase-contrast and dark-field images are obtained in a single measurement (Pfeiffer *et al* 2008, Bech *et al* 2010) allowing for direct comparison of absorptive, refractive and scattering properties on voxel basis.

So far these modalities have been applied separately in single-variable data processing. In this paper, we will show how a simple addition using both the absorption length and the electron density—obtained in absorption and phase-contrast tomography, respectively—for multivariable segmentation can give an improved threshold segmentation. For demonstration on biological tissue, two samples were chosen: a piece of pork backfat and a piece of beef muscle tissue (Longissimus Dorsi).

2. The full complex index of refraction

The full complex index of refraction describing both refraction and absorption of x-rays in matter is

$$n = 1 - \delta + i\beta, \quad (1)$$

where the real part δ accounts for the refraction and the imaginary part β accounts for the absorption. Above the atomic K-edge, these can be related to the electron (number) density ρ_e and absorption length μ , respectively, by (Als-Nielsen and McMorro 2001)

$$\delta = \frac{2\pi r_0 c^2 \hbar^2}{E^2} \rho_e, \quad \beta = \frac{\hbar c}{2E} \mu, \quad (2)$$

where r_0 is the Thomson scattering length, \hbar is Planck's constant divided by 2π , c is the speed of light in vacuum and E is the x-ray photon energy. The electron density ρ_e and absorption length μ of a compound depend on the atomic composition in different ways (Als-Nielsen and McMorro 2001):

$$\rho_e = \frac{ZN_A}{M} \rho_m, \quad \mu \propto \frac{Z^4}{E^3 M} \rho_m, \quad (3)$$

where Z is the number of electrons in the molecule, N_A is Avogadro's number, M is the molar mass and ρ_m is the mass density.

The strong dependence on the atomic number Z makes the absorption length μ more sensitive to the atomic composition than the electron density giving rise to complementary contrast abilities. This is illustrated for a number of common organic compounds in the scatter plot in figure 1, including three plastics; high-density polyethylene (HDPE), acrylonitrile butadiene styrene (ABS) and polymethyl methacrylate (PMMA). Tabular values, the chemical formulas and mass densities are given in table 1. The μ values are for an x-ray energy of 21.5 keV and were found following Chantler *et al* (2001). It is seen that compounds overlap in their values of either μ , such as acetic acid and PMMA, or ρ_e , such as formic acid and PMMA. Thus, even though the cross section for phase shift is higher than for absorption (Fitzgerald 2000, Momose 2005), phase-contrast imaging will not always yield a higher contrast of different components. Hence, in order to separate, i.e., acetic acid, formic acid and PMMA, it would be necessary to use both the absorption lengths and the electron densities by, e.g., using a bivariate plot.

3. Materials and methods

3.1. Experimental setup

The x-ray grating interferometer setup using a lab-based source is shown in figure 2 and has previously been described in detail elsewhere (Pfeiffer *et al* 2006). The grating interferometer

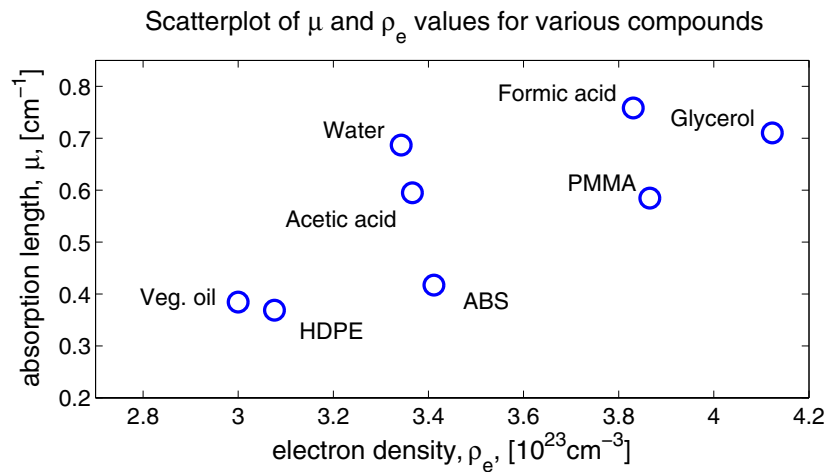


Figure 1. Bivariate plot showing values of absorption length and electron density for a number of organic compounds including three plastics: high-density polyethylene (HDPE), acrylonitrile butadiene styrene (ABS) and polymethyl methacrylate (PMMA).

Table 1. Tabular values for μ and ρ_e as well as chemical composition and mass density of a number of compounds. The compounds with relatively large amount of oxygen have the largest values of absorption length while components with a large mass density have large values of electron density. The μ values were found using a NIST database (Chantler *et al* 2001) for an x-ray energy of 21.5 keV.

Substance	Chemical formulas	ρ_m (g/cm^{-3})	μ (cm^{-1})	ρ_e (10^{23} cm^{-3})
ABS	$(\text{C}_8\text{H}_8)_x(\text{C}_4\text{H}_6)_y$ $(\text{C}_3\text{H}_3\text{N})_z$	1.05	0.417	3.41
Acetic acid	CH_3COOH	1.05	0.595	3.37
Formic acid	HCOOH	1.22	0.758	3.83
Glycerol	$\text{C}_3\text{H}_8\text{O}_3$	1.26	0.710	4.12
HDPE	$(\text{C}_2\text{H}_4)_n$	0.95	0.369	3.08
Water	H_2O	1.00	0.687	3.34
PMMA	$(\text{C}_5\text{O}_2\text{H}_8)_n$	1.19	0.585	3.87
Vegetable oil	–	0.9	0.384	3.00

itself consists of a phase-grating G1 and an absorption grating G2. Partial spatial coherence is required in the x -direction, perpendicular to the grating lines, and is obtained by introducing a third grating, G0. To analyze the interference pattern formed by G1 and distorted by the presence of the sample, one of the gratings is stepped through the pattern, typically G0 or G2. The absorption and refraction due to the sample are measured via the change in the interference pattern. Hence, the absorption and the refraction are recorded simultaneously. In figure 2(a), G0 is the stepped grating. The sample rotates around the vertical y -axis. Its angular position is denoted by ω .

3.2. Image acquisition and sample preparation

Two experiments were performed at the Technical University of Munich using an x-ray rotating anode source. The x-ray tube was operated at an acceleration voltage of 30 kV and a filament current of 80 mA, and had a molybdenum target. The interferometer used a $\frac{\pi}{2}$ phase grating for

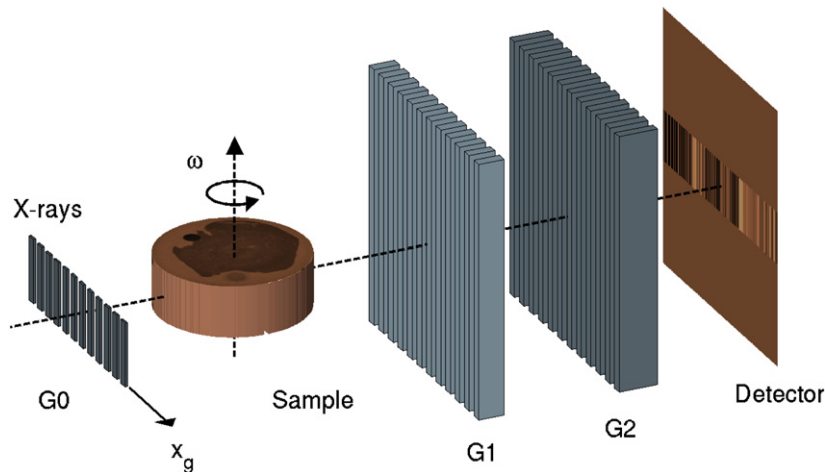


Figure 2. X-ray grating-based tomography setup with sample. The phase-grating G1 and absorption grating G2 form the interferometer. G0 acts as an array of line sources.

G1 with a period of $3.5 \mu\text{m}$, and the periods of G0 and G2 were 10 and $5.4 \mu\text{m}$, respectively, with a G0-to-G1 distance of 976 mm and a G1-to-G2 distance of 527 mm. The gratings were optimized for a photon energy of 23 keV. The images were recorded with a PILATUS detector with 195×487 pixels with an effective pixel size at the sample of $112 \mu\text{m}$. The detector was operated at a threshold energy of 15 keV in order to avoid double counting.

As typical examples of biological tissue, a piece of pork backfat and a piece of beef muscle tissue (*Longissimus Dorsi*) were chosen. The samples had an approximate size of $25 \text{ mm} \times 25 \text{ mm} \times 25 \text{ mm}$ and were measured with phase-stepping scans at 241 evenly spaced rotation angles in the interval $[0, 2\pi[$. The beef was measured with eight steps per scan at an exposure time of 10 s per frame and the pork with four steps per scan at an exposure time of 5 s per frame. Both samples were fixed in a solution of vegetable oil and held in a cylindrical HDPE plastic container to reduce refraction between the sample and its surroundings. Two references, a small HDPE plastic container with water and a PMMA plastic rod, were included with both samples in order to determine the effective energy of the setup. The measurements were performed in air.

3.3. Data processing

A parallel beam filtered back-projection algorithm was used in the tomographic reconstruction as described by Pfeiffer *et al* (2007).

Since both the absorption length and the real part of the refractive index depend on the photon energy, as seen from equations (2) and (3), an energy calibration was performed to obtain effective values for μ and ρ_e as the full energy spectrum from the anode was used. The calibration was performed on the entire tomogram using a linear regression between the measured mean values of the components and the tabulated values. The values of both μ and ρ_e for air were set to zero. For the absorption tomograms, the components were the background air, the HDPE container, the water reference and PMMA rod. Due to large refraction between the background air and the HDPE container, the HDPE value was not used for the phase-contrast tomograms. The effective energy for the absorption tomograms was 21.5 keV and, for the phase-contrast tomograms, it was 25.2 keV for the beef and 25.5 keV for the pork sample,

respectively. The difference in effective energy for the two signals is in agreement with that proposed by Engelhardt *et al* (2008). The R^2 value for all regressions was better than 0.99 and the RMSE was approximately 0.015 for the absorption slices and 0.04 for the phase-contrast slices.

3.4. Image segmentation

In multivariable threshold segmentation, the distance for each pixel $\mathbf{p}(i, j)$ to a specific point \mathbf{a} is calculated. The bold-face represents that each pixel has multiple variables and therefore is described by an n -dimensional vector, where n is the number of variables.

Different measures can be used for the distance calculation but a notable one is the well-known n -dimensional *Euclidean distance*, which will be used in the following. With this method, we segment the input image as follows (Gonzalez and Woods 2008):

$$q(i, j) = \begin{cases} 1, & \text{if } D(\mathbf{p}, \mathbf{a}) < T, \\ 0, & \text{otherwise,} \end{cases} \quad (4)$$

where it is noted that the pixels of the segmented image q have only one variable, as opposed to the n variables of the input image. In this way of calculating the distance, the equation $D(\mathbf{p}, \mathbf{a}) = T$ describes a hypersphere (in n -dimensions), and the thresholding can be seen as selecting all pixels with a set of values within this hypersphere. Other forms of thresholding criteria can be chosen that, for example, define a hyperellipse or a hypercube instead. The number of regions can be increased by defining more than one threshold.

4. Results and discussion

A slice of the reconstruction of the pork sample from the absorption and the phase-contrast tomogram is shown in figures 3(a) and (b), respectively. A slice of the beef sample is displayed in figures 4(a) and (b). The size of all slices is 291×291 voxels, corresponding to $32.6 \text{ mm} \times 32.6 \text{ mm}$. The blue parts represent air surrounding the container and in the form of air bubbles within the sample. The different components are labeled with text.

The absorption and phase-contrast signals can quantitatively be compared by depicting the bivariate voxel values in a 2D diagram (Tapfer *et al* 2011). In figures 3(c) and 4(c), this was done by dividing the range of absorption length and electron densities into 162×162 bins of size $(0.005 \text{ cm}^{-1}; 0.01 \times 10^{23} \text{ cm}^{-3})$, counting the number of voxels in each bin and plotting the resulting 2D histogram. The 1D histograms displayed on the axes use identical bins as in the 2D histograms. All histograms are on linear scale. The different parts of the distribution in the 2D histogram can be inspected by defining simple threshold boundary curves and performing multivariable segmentation by choosing the voxels whose values lie within the boundary. In figures 3(c) and 4(c), a four-sided polygon and ellipse-shaped boundaries are shown with the corresponding segmentations in figures 3(d) and 4(d), (e). These can be compared with the slices.

To demonstrate the improved capabilities of a simple multivariable analysis over a single variable, the multivariable threshold segmentation in figure 3(d) was compared to a single-variable threshold segmentation of the container, oil and fat part of the pork sample. The latter was performed by selecting threshold values in the 1D histograms. The threshold values are displayed with horizontal and vertical lines in figure 3(c) and the single-variable segmentations are shown in figures 3(e) and (f). Clearly, the horizontal and vertical lines intersect more than one component. The threshold boundary curves allow for more freedom in shaping the thresholds after the bivariate distribution. As a result, the multivariable analysis can give a better

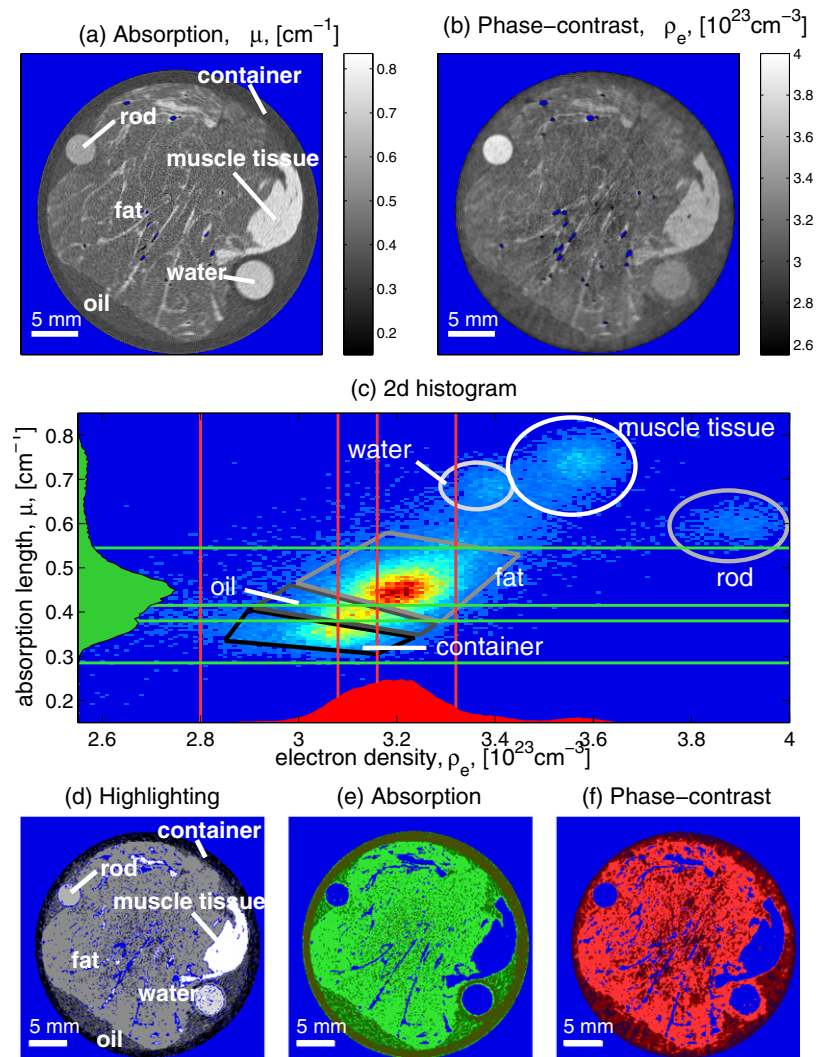


Figure 3. Pork sample. (a), (b) Absorption and phase-contrast slice of a piece of pork in oil with two references: a PMMA rod and water. The blue color represents air bubbles inside and the air surrounding the sample. (c) 2D histogram (linear scale) with 1D distributions (linear scale) on the axes. (d) Multivariable segmentation of the different components: HDPE container, oil, fat, water reference, muscle tissue and PMMA reference. (e), (f) Single-variable segmentation of the absorption and phase-contrast 1D histograms.

segmentation of the container, oil and fat components of the sample. The ability to separate vegetable oil and porcine fat would be relevant in meat science if x-ray imaging was applied for studying the effect of replacing animal fat with vegetable fat in, e.g., sausages, which has attracted attention in recent years (Jiménez-Colmenero 2007). Here, a simple multivariable analysis could give an improved threshold segmentation.

Another application with multivariable segmentation is to separate distributions that overlap in one or both of the two signals but are separated in the 2D representation. In figure 4(c), the electron density histogram shows only one combined peak for the oil and

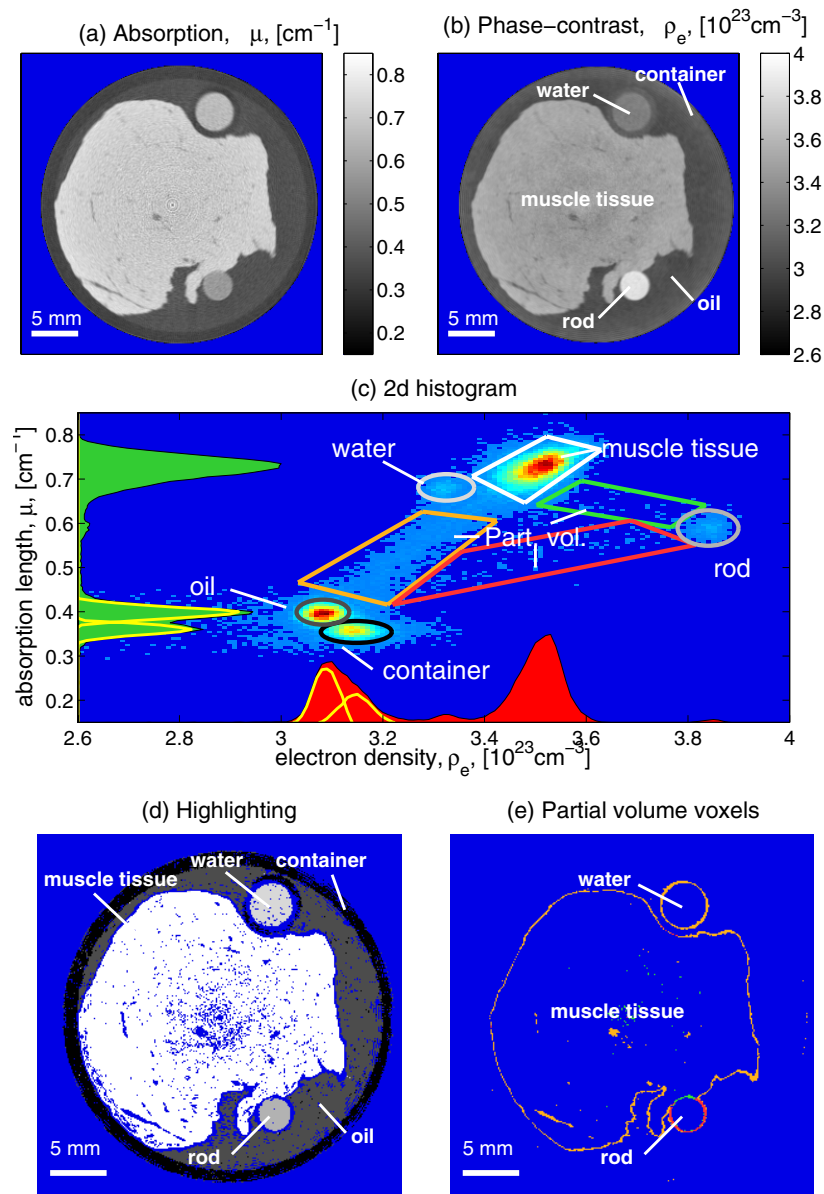


Figure 4. *Beef sample.* (a), (b) Absorption and phase-contrast slice of a piece of beef in oil with two references: a PMMA rod and water. The blue color represents air bubbles inside and the air surrounding the sample. (c) 2D histogram (linear scale) with 1D distributions (linear scale) on the axes. (d) Multivariable segmentation of the different components: HDPE container, oil, water reference, muscle tissue and PMMA reference. (e) Multivariable segmentation of the partial volume elements.

container components, whereas two separate peaks are seen in the 2D histogram. By using the multivariable segmentation, it is possible to identify the separate oil and container contributions to the electron density signal as depicted with the solid curves on the 1D histograms on the axes.

When comparing the two samples, it should be noted that, due to better counting statistics for the beef sample, the resolution in both the electron density and the absorption length is better than that for the pork. Besides this, there is a high degree of consistency in the range of values of the components. An exception is the electron density value of the HDPE container, which is lower for the pork sample than for the beef and is believed to be due to refraction effects at the air–container interface.

Another exception is that the pork sample consists mainly of fat, as shown in figure 3, whereas almost no fat is present in the beef. In the beef sample, this range of values is occupied by partial volume elements. These are located at the interface between two components and can as such be used for a visualization of edges. An application of this can be seen in figure 4(e), where different parts of the partial volume elements have been multivariable segmented using the boundary curves shown in figure 4(c). By comparing with the tomogram slices in figures 4(a) and (b), the segmented partial volume voxels are indeed found to be located at edges between components. In figure 4(e), it is possible to distinguish the mixed muscle tissue–oil edge and water–container edge from the rod–muscle tissue edge and from the rod–oil edge, which could only be done by using multivariable analysis.

5. Summary

In summary, we have demonstrated that multivariable analysis, using the full complex index of refraction, can give an improved threshold segmentation over standard thresholding. This is especially useful for low contrast x-ray lab sources. The technique also offers new possibilities for using partial volumes in edge detection. In this paper, tomography data were presented but multivariable segmentation could also be used in radiography. Multivariable segmentation can readily be expanded from two to three physical parameters by including the dark-field signal obtainable with grating-based interferometry.

Acknowledgments

The authors gratefully acknowledge the work by Marian Willner in building the experimental setup. The gratings were produced within a research collaboration by Dr Juergen Mohr, KIT for which the authors are deeply thankful. The authors acknowledge financial support from the innovation consortium CIA-CT. MB and FP acknowledge financial support through the DFG Cluster of Excellence Munich-Center (DFG EXC-158) for Advanced Photonics and the European Research Council FP7, starting grant number 24012.

References

- Als-Nielsen J and McMorrow D 2001 *Elements of Modern X-Ray Physics* 1st edn (New York: Wiley)
- Bech M, Bunk O, Donath T, Feidenhans'l R D C and Pfeiffer F 2010 Quantitative x-ray dark-field computed tomography *Phys. Med. Biol.* **55** 5529
- Chantler C, Olsen K, Dragoset R, Chang J, Kishore A, Kotochigova S and Zucker D 2001 X-ray form factor, attenuation and scattering tables <http://physics.nist.gov/PhysRefData/FFast/html/form.html>
- David C, Nöhammer B, Solak H and Ziegler E 2002 Differential x-ray phase contrast imaging using a shearing interferometer *Appl. Phys. Lett.* **81** 3287
- Engelhardt M, Kottler C, Bunk O, David C, Schroer C, Baumann J and Pfeiffer F 2008 The fractional Talbot effect in differential x-ray phase-contrast imaging for extended and polychromatic x-ray sources *J. Microsc.* **232** 145–57
- Fitzgerald R 2000 Phase-sensitive x-ray imaging *Phys. Today* **53** 23–6
- Gonzalez R C and Woods R E 2008 *Digital Image Processing* 3rd edn (Upper Saddle River, NJ: Pearson Prentice Hall)

- Jiménez-Colmenero F 2007 Healthier lipid formulation approaches in meat-based functional foods. Technological options for replacement of meat fats by non-meat fats *Trends Food Sci. Technol.* **18** 567–78
- Kottler C *et al* 2010 Phase sensitive x-ray imaging: towards its interdisciplinary applications *AIP Conf. Proc.* **1236** 213–8
- Momose A 2003 Phase-sensitive imaging and phase tomography using x-ray interferometers *Opt. Express* **11** 2303–14
- Momose A 2005 Recent advances in x-ray phase imaging *Japan. J. Appl. Phys.* **44** 6355–67
- Pfeiffer F, Bech M, Bunk O, Kraft P, Eikenberry E F, Brönnimann C, Grünzweig C and David C 2008 Hard-x-ray dark-field imaging using a grating interferometer *Nature Mater.* **7** 134–7
- Pfeiffer F, Kottler C, Bunk O and David C 2007 Hard x-ray phase tomography with low-brilliance sources *Phys. Rev. Lett.* **98** 108105
- Pfeiffer F, Weitkamp T, Bunk O and David C 2006 Phase retrieval and differential phase-contrast imaging with low-brilliance x-ray sources *Nature Phys.* **2** 258–61
- Tapfer A *et al* 2011 Development of a prototype gantry system for preclinical x-ray phase-contrast computed tomography *Med. Phys.* **38** 5910
- Weitkamp T, Diaz A, David C, Pfeiffer F, Stampanoni M, Cloetens P and Ziegler E 2005 Hard x-ray phase tomography with low-brilliance sources *Opt. Express* **13** 6296



X-ray dark-field imaging for detection of foreign bodies in food

Mikkel Schou Nielsen^{a,*}, Torsten Lauridsen^a, Lars Bager Christensen^b, Robert Feidenhans'l^a

^a Niels Bohr Institute, University of Copenhagen, 2100 Copenhagen, Denmark

^b DMRI/Danish Technological Institute, Roskilde, Denmark

ARTICLE INFO

Article history:

Received 17 January 2012

Received in revised form

13 August 2012

Accepted 21 August 2012

Keywords:

X-ray dark-field imaging

Image analysis

Foreign body detection

X-ray radiography

Meat

Dairy products

ABSTRACT

Conventional X-ray transmission radiography has long been used for online detection of foreign bodies in food products relying on the absorption contrast between the foreign body and food product. In this paper, we present a novel approach for detection of organic foreign bodies such as paper and insects in two food products using X-ray dark-field imaging with a grating interferometer. The ability to detect the foreign bodies is quantified using a measure of the contrast-to-noise ratio.

© 2012 Elsevier Ltd. All rights reserved.

1. Introduction

Screening for foreign bodies (FB) plays an important role in quality assurance of high quality food products. Particularly organic materials constitute a challenge in the modern food production because conventional methods, e.g. based on X-rays, are not able to detect organic residues from raw materials or packages due to the low contrast with X-ray absorption.

The presence of FBs is a major problem for the industry as shred fragments from production equipment may incidentally end up in the food product. Such fragments may be of organic or inorganic origin; the latter generating a high contrast in absorption detectors whereas the former often generate, at most, a subtle contrast that is difficult to detect in an automatic detection algorithm.

Thus a non-destructive, highly sensitive method for detection of organic materials is greatly needed. One strategy to increase absorption contrast is to apply low X-ray energies in the 10–25 keV range, in order to benefit from the higher attenuation. Such strategies, however, has to cope with an increase in the total attenuation thus implying lower scanning speed or high X-ray power levels.

During the last decade a dramatic evolution in X-ray imaging has taken place, involving introduction of techniques using several new X-ray modalities like phase-contrast and dark-field imaging with increased sensitivity to low Z elements and hence organic

materials (Fitzgerald, 2000; Momose, 2005; Pfeiffer et al., 2008). One of the most promising techniques is grating-based interferometry (David, Nöhammer, Solak, & Ziegler, 2002; Momose, 2003; Weitkamp et al., 2005) which can be adapted to laboratory-based setups (Pfeiffer, Weitkamp, Bunk, & David, 2006), and shows potential for industrial applications (Kottler et al., 2010). It has the advantage of simultaneously recording transmission, phase-contrast and dark-field images allowing for multiple independent mechanisms of contrast. Recently, the technique has been successfully applied for studying porcine fat and rind (Jensen et al., 2011), and the potential for detection of FBs has been demonstrated in the case of a piece of fabric from a worker's hairnet (Kottler et al., 2010).

In this study, we demonstrate identification of FBs consisting of organic materials using transmission and dark-field X-ray radiography with a grating-based interferometer.

2. Experimental method

The X-ray grating interferometer outlined in Fig. 1 has previously been described in detail (Pfeiffer et al., 2006; Weitkamp et al., 2005). It consists of an X-ray phase-grating G1 and an analyzer absorption grating G2. At laboratory setups a third grating, G0, is included to obtain satisfactory spatial coherence in the horizontal direction perpendicular to the grating lines.

The interference pattern is generated by G1, and creates a periodic intensity modulation at the position of G2. The latter is used to analyze the position, mean value and amplitude of the intensity

* Corresponding author. Tel.: +45 35320453; fax: +45 35320460.
E-mail address: schou@fys.ku.dk (M.S. Nielsen).

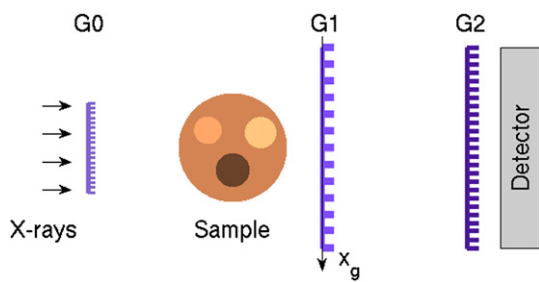


Fig. 1. Setup: X-ray grating-based setup with sample. The phase-grating, G1, and analyzer grating, G2, forms the interferometer. G0 acts as an array of line sources. G1 is the stepped grating.

modulation by moving one of the gratings in steps through the period of the pattern while recording an image at each step. In Fig. 1 the stepped grating is G1.

The presence of a sample distorts the interference pattern and the deviation can be calculated by analyzing the intensity modulations with and without the sample present (Pfeiffer et al., 2009). From these calculations, three different contrast mechanisms can be extracted of which two, transmission and dark-field, will be presented in this paper. Due to the normalization using the reference image without the sample present, the transmission and dark-field signal will have values in the range [0:1].

The contrast mechanisms map independent and complementary material properties, as the conventional transmission contrast is a measure of the absorbing properties of the sample whereas the dark-field contrast is a measure of the scattering properties of the sample due to microstructures within the sample (Bech, 2009).

3. Materials and measurements

3.1. Grating interferometer setup

The experiments were carried out at the Niels Bohr Institute at the University of Copenhagen using an X-ray rotating anode tube with a grating interferometer setup. The Rigaku rotation anode tube had a copper target and was set at an acceleration voltage of

40 kV and a filament current of 150 mA. The effective source size was $1 \text{ mm} \times 1 \text{ mm}$.

The interferometer used a π phase-grating for G1 with a period of $3.5 \mu\text{m}$, a G0 and G2 grating with periods of $14.1 \mu\text{m}$ and $2.0 \mu\text{m}$, respectively and was set up with a G0-to-G1 distance of 139 cm and a G1-to-G2 distance of 20 cm as described in (Bech, 2009). The gratings were optimized for 28 keV. The images were recorded with a PILATUS 100k detector with 195×487 pixels and an effective pixel size at the sample of $126 \mu\text{m} \times 126 \mu\text{m}$.

3.2. Sample preparation

Two food products were used in the experiments; minced beef meat consisting of 9–15 mass percent fat and a cultured sour cream product with 6 mass percent fat. The food products were stored in the laboratory refrigerator at $5 \text{ }^\circ\text{C}$ until just before measurements. The choice of food matrices cover two important industries, the meat and the dairy industry, where detection of foreign bodies is an issue. The examples here represent also a large difference in fibrous composition: the complex structure of muscle fibers in the minced meat vs. the highly homogeneous structure of the dairy product.

The FBs used were two sets of folded standard paper (4 and 8 layers), a cigarette butt, a piece of broken glass (1 mm thickness), a fly (*Musca domestica*) and a harlekin ladybug (*Harmonia axyridis*). The samples and FBs used for each can be seen in Fig. 2 panels a) and b).

The food product to be scanned was placed in a holder, and the FBs to be detected were inserted into the product. The minced meat, as seen in Fig. 2 panel a), was placed on a piece of paper and holes were made for the FBs. After insertion of the FBs, the meat was reformed to close the holes. The holder used for the sour cream was a small plastic cup with low absorbing and scattering properties as seen in Fig. 2 panel b). The FBs were lowered into the cream, and the samples were measured one at a time to minimize deterioration of the sample.

3.3. Measurements

For both sample and reference measurements, 14 phase-steps were used, as described in Section 2, with an exposure time of 5 s for each image recorded. The measurements were carried out with air as a reference using the setup described in Section 3.1.

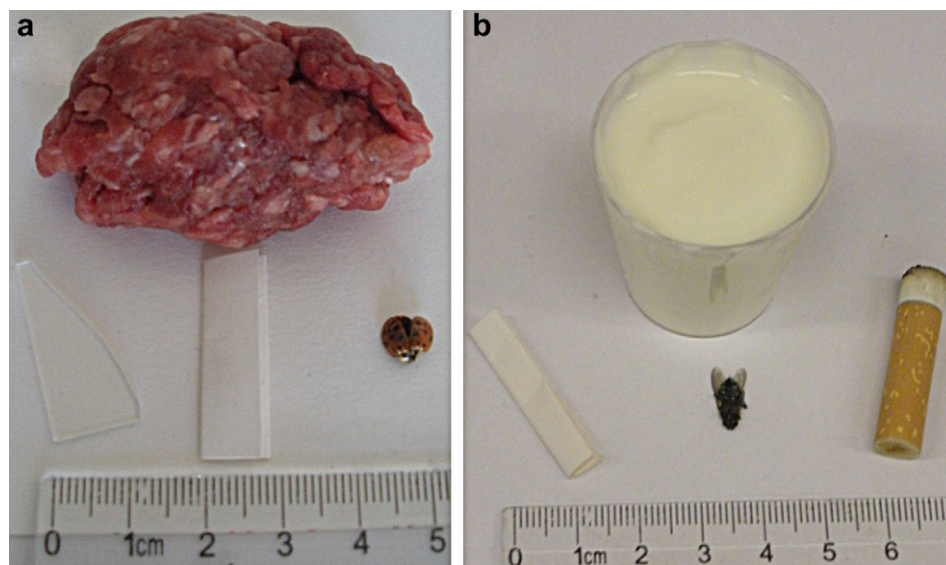


Fig. 2. Sample: the samples and FBs used for the measurements. a) Minced beef meat, a piece of glass, 8 layers of paper and a harlekin ladybug placed on a piece of paper. b) Cultured sour cream placed in a small plastic cup, 4 layers of paper, a fly and a cigarette butt.

The settings were the same for the two samples with similar background conditions of temperature and humidity of the air.

4. Image analysis

To compare the ability to detect the FBs in the transmission and dark-field signal, respectively, an image contrast measure is introduced in the form of a contrast-to-noise ratio (CNR) which is defined as (Song et al., 2004):

$$\text{CNR} = |\mu_{\text{FB}} - \mu_{\text{M}}| / (w_{\text{FB}}\sigma_{\text{FB}}^2 + w_{\text{M}}\sigma_{\text{M}}^2)^{1/2} \quad (1)$$

where μ denotes the mean value and σ^2 the variance of the FB and food matrix (M) in the transmission and dark-field images, respectively. Since the area covered by the FB and food matrix in the image may vary, the variances are weighted with the factor w which is the ratio of the number of pixels of the FB or food matrix, relative to the total number of the two.

A high CNR value means that the contrast between FB and food matrix is significantly higher than the noise in image whereas a low value means that there is no significant contrast.

5. Results

Transmission and dark-field radiograms of the minced meat containing three FBs are shown in Fig. 3 panels a) and b), respectively. The FBs are, from left to right: A piece of glass, 4 layers of paper and a ladybug.

As can be seen in the left side of the transmission radiogram (blue square in the web version), the glass is highly absorbing compared to the minced meat whereas there is no visible difference in absorption between the minced meat and the paper (green square in the web version) and ladybug (red squares in the web version) in the middle and right side of the image. In the dark-field radiogram, it is seen that both the paper and ladybug gives a higher degree of scattering than the minced meat resulting in a clear outline of these two FBs whereas only the edge of the glass can be seen in the left side.

To quantify the contrast, the CNR value, as defined in eq. (1), between foreign body and food product is calculated for both the transmission and dark-field image. In each image, areas covering the FBs and the food matrix were selected as basis for the calculation as shown in Fig. 3 with colored squares. The yellow (in the web version) squares indicate the minced meat food matrix with a total area of 11,513 pixels.

As seen from Table 1, the CNR value for the glass is highest in the transmission image, and for the paper and ladybug it is highest in the dark-field image confirming the qualitative analysis conducted above. This shows that transmission and dark-field radiography have complementary contrast properties, and can thus be used together for multiple detection purposes. A limitation for the contrast in both the transmission and dark-field signal is the large variance in pixel values of the minced meat due to the fibrous structure. This puts a limit on the CNR values obtainable.

In Fig. 4 panels a) and b) are shown the transmission and dark-field radiograms of the sour cream with three FBs from left to right; paper, a cigarette butt and a fly.

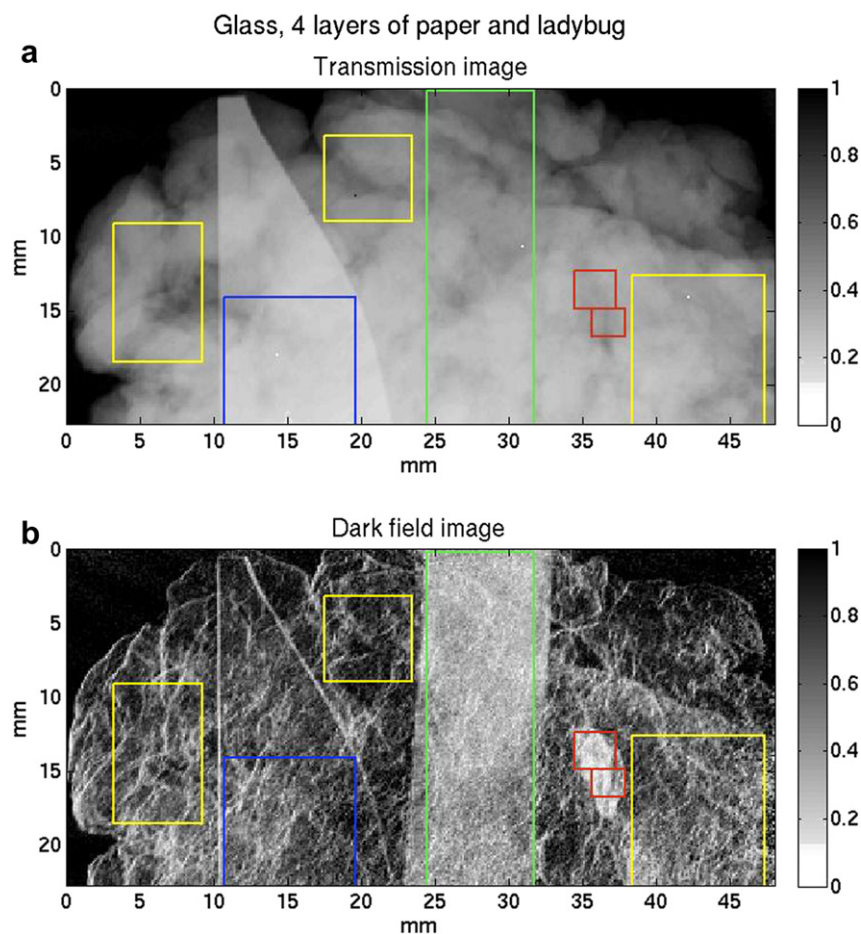


Fig. 3. Minced meat: X-ray images of minced meat with three FBs; glass (left), 4 layers of paper (middle) and a ladybug (right). a) Transmission radiogram. b) Dark-field radiogram.

Table 1
Contrast-to-noise ratios of foreign bodies in minced meat.

Material	Transmission CNR	Dark-field CNR	w_{FB}
Glass (1 mm)	2.3	0.0	0.30
4 Sheets paper	0.1	1.8	0.48
Ladybug (insect)	0.5	1.9	0.06

A visual comparison of panels a) and b) indicates that the dark-field radiogram gives a much higher contrast between the FBs and the sour cream than the transmission. This is especially the case for the paper (blue square in the web version) which is seen clearly in the left side of the dark-field radiogram even though the paper layers have unfolded after being inserted into the sour cream. Thus, it is possible to see different thicknesses of the paper. In the middle and right side of the dark-field radiogram, the cigarette butt (green square in the web version) and fly (red square in the web version) can be seen clearly whereas it is more difficult in the transmission radiogram.

To quantify the contrast, the CNR value between foreign body and food product is calculated in the same manner as above. The areas used for the calculations are indicated in Fig. 3 with colored squares. The yellow (in the web version) squares indicate the sour cream areas used which had a total area of 6579 pixels.

As seen from Table 2, the CNR values for the three FBs are highest in the dark-field image confirming the qualitative analysis conducted above. Note that in the dark-field radiogram, it is also possible to distinguish between the FBs and air bubbles in the sample as opposed to the transmission radiogram where the values

Table 2
Contrast-to-noise ratios of foreign bodies in sour cream.

Material	Transmission CNR	Dark-field CNR	w_{FB}
8 Sheets paper	0.4	2.8	0.59
Cigarette butt	0.7	6.3	0.44
Fly (insect)	0.2	2.9	0.08

are in the same range for air bubbles and FBs. The high contrast level improves the detection potential of the dark-field modality over conventional transmission based detection.

6. Discussion and outlook

The proof-of-principle experiments in our work demonstrate some of the potentials of dark-field radiography as a promising emerging modality for detection of “hard-to-find” FBs in food. For detection of paper, insects and other fibrous materials, dark-field X-ray radiography is outperforming the conventional transmission based systems with respect to improved contrast as the CNR values were a factor of 5–10 larger in the dark-field image for these kind of FBs.

As our approach generate both transmission and dark-field images simultaneously, the versatility of X-ray screening is optimized by combining the two modalities in one single detection system. This versatility may possibly be further improved if the differential phase-contrast images, also obtained by the scanning method, can be utilized for detection purposes.

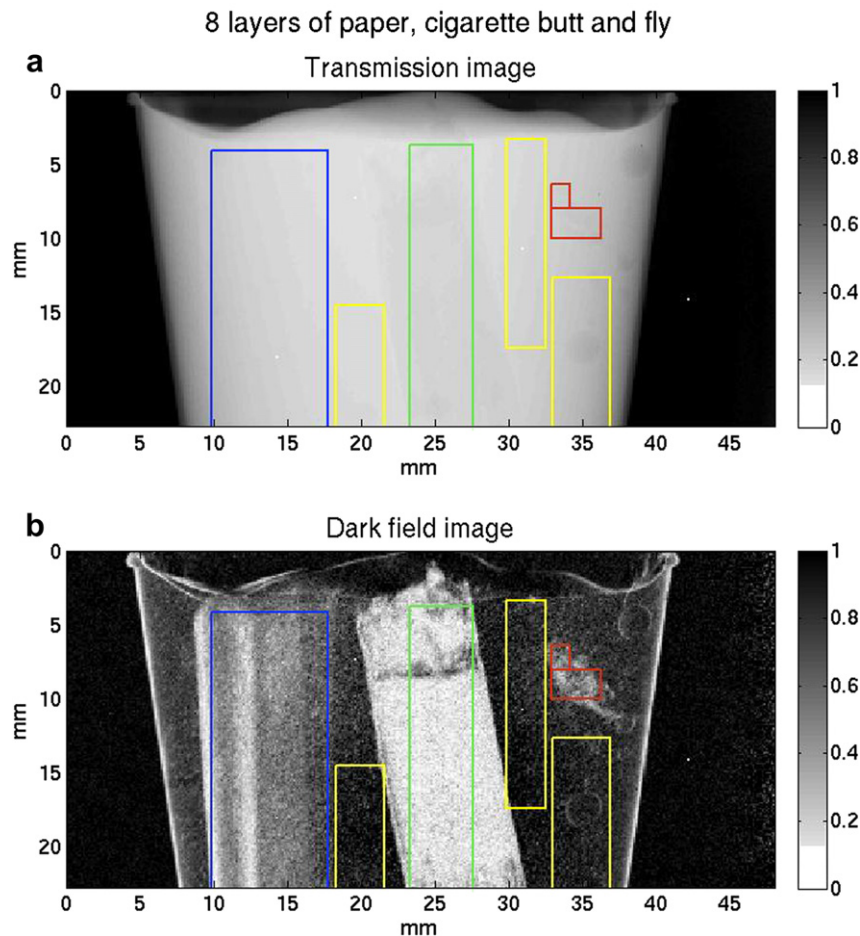


Fig. 4. Sour cream: X-ray images of sour cream with three FBs; 8 layers of paper (left), a cigarette butt (middle) and a fly (right). a) Transmission radiogram. b) Dark-field radiogram.

Extremely small FBs of fibrous material pose a challenge in some food matrices with a similar fibrous structure. The fibrous structure of the minced meat illustrates the challenge by comparison of the intensity variation of the dark-field compared to the transmission image.

A discussion of what level of CNR value would be needed for implementing this technique in an automatic detection system still remains.

Further work is needed before the technique can be used online at conveyor belt production lines but a proposal has already been made for a grating-based interferometry scanning system (Kottler, Pfeiffer, Bunk, Grüntzweig, & David, 2007) which uses a number of line detectors and the movement of the sample for imaging. Thus, grating-based interferometry has great potential for practical implementation.

References

- Bech, M. (2009). *X-ray imaging with a grating interferometer*. Ph.D. thesis, Graduate School of Science, University of Copenhagen.
- David, C., Nöhammer, B., Solak, H. H., & Ziegler, E. (2002). Differential X-ray phase contrast imaging using a shearing interferometer. *Applied Physics Letters*, *81*(17), 3287–3289.
- Fitzgerald, R. (2000). Phase-sensitive X-ray imaging. *Physics Today*, *53*(7), 23.
- Jensen, T. H., Böttiger, A., Bech, M., Zanette, I., Weitkamp, T., Rutishauser, S., et al. (2011). X-ray phase-contrast tomography of porcine fat and rind. *Meat Science*, *88*(3), 379–383.
- Kottler, C., Pfeiffer, F., Bunk, O., Grüntzweig, C., & David, C. (2007). Grating interferometer based scanning setup for hard X-ray phase contrast imaging. *Review of Scientific Instruments*, *78*, 043710.
- Kottler, C., Revol, V., Kaufmann, R., Urban, C., Knop, K., Sennhauser, U., et al. (2010). Phase sensitive X-ray imaging: towards its interdisciplinary applications. *AIP Conference Proceedings*, *1236*(1), 213–218.
- Momose, A. (2003). Phase-sensitive imaging and phase tomography using X-ray interferometers. *Optics Express*, *11*(19), 2303–2314.
- Momose, A. (2005). Recent advances in X-ray phase imaging. *Japanese Journal of Applied Physics, Part 1*, *44*, 6355.
- Pfeiffer, F., Bech, M., Bunk, O., Donath, T., Henrich, B., Kraft, P., et al. (2009). X-ray dark-field and phase-contrast imaging using a grating interferometer. *Journal of Applied Physics*, *105*(10), 102006.
- Pfeiffer, F., Bech, M., Bunk, O., Kraft, P., Eikenberry, E. F., Brönnimann, Ch., et al. (2008). Hard-X-ray dark-field imaging using a grating interferometer. *Nature Materials*, *7*, 134–137.
- Pfeiffer, F., Weitkamp, T., Bunk, O., & David, C. (2006). Phase retrieval and differential phase-contrast imaging with low-brilliance X-ray sources. *Nature Physics*, *2*, 258–261.
- Song, X., Pogue, B., Jiang, S., Doyley, M., Dehghani, H., Tosteson, T., et al. (2004). Automated region detection based on the contrast-to-noise ratio in near-infrared tomography. *Applied Optics*, *43*(5), 1053–1062.
- Weitkamp, T., Diaz, A., David, C., Pfeiffer, F., Stampanoni, M., Cloetens, P., et al. (2005). X-ray phase imaging with a grating interferometer. *Optics Express*, *13*(16), 6296–6304.